Unfolding Structure Formation in the Dark Universe via Weak Gravitational Lensing:
from Pixels to Cosmology in the Dark Energy Survey and Roman Space Telescope

by

Masaya Yamamoto

Department of Physics
Duke University

Defense Date: <u>   June 18, 2024   </u>

Approved:

<u>   </u>
Michael A. Troxel, Supervisor

<u>   </u>
Dan Scolnic

<u>   </u>
Arun Kannawadi

<u>   </u>
Robert Wolpert

<u>   </u>
Thomas Mehen

Dissertation submitted in partial fulfillment of the requirements for the degree of
Doctor of Philosophy in the Department of Physics
in the Graduate School of Duke University
2024

ABSTRACT

Unfolding Structure Formation in the Dark Universe via Weak Gravitational Lensing:
from Pixels to Cosmology in the Dark Energy Survey and Roman Space Telescope

by

Masaya Yamamoto

Department of Physics
Duke University

Defense Date: _____ June 18, 2024 _____

Approved:

_____
Michael A. Troxel, Supervisor

_____
Dan Scolnic

_____
Arun Kannawadi

_____
Robert Wolpert

_____
Thomas Mehen

An abstract of a dissertation submitted in partial fulfillment of the requirements for
the degree of Doctor of Philosophy in the Department of Physics
in the Graduate School of Duke University
2024

Abstract

Weak gravitational lensing (deflection of light from distant galaxies due to the gravitational potential of intervening mass) is one of the most exciting probes in cosmology as it is sensitive both to the growth of the large-scale structure and the expansion history of the Universe. We can measure the coherent distortion of galaxy shapes (which we call cosmic shear) and infer the matter distribution. With next-generation imaging surveys such as the Vera C. Rubin Observatory Legacy Survey of Space and Time (Rubin LSST) and the Nancy G. Roman Space Telescope (Roman), there is immense new promise in understanding the fundamental nature of dark matter and dark energy. With datasets from current experiments like the Dark Energy Survey (DES), we see apparent cosmological tensions between experiments that may either be real and indicate new physics or new systematics we do not yet understand. LSST and Roman will increase the number of galaxies we have observed by an order of magnitude, leading to improved constraints on our cosmological model by up to 300%. These experiments will have the potential to prove if these cosmological tensions are real. However, our control of systematic uncertainties must also improve by similar levels to achieve the promise of what these missions can deliver.

To achieve these scientific outcomes, the challenges of determining galaxy shapes and redshifts and modeling the impact of astrophysical effects must be solved. My PhD has focused on enabling weak lensing science in DES and Roman. I co-led the shear analysis teams in DES to produce the largest weak lensing galaxy sample, as well as the final DES cosmological analysis of cosmic shear. For Roman, I have led two papers characterizing and mitigating shear-related systematics with image simulations.

Contents

List of Tables

List of Figures

List of Abbreviations and Symbols

AGN Active Galactic Nuclei

CCD Charge-Coupled Device

CMB Cosmic Microwave Background

DES Dark Energy Survey with Blanco Telescope

DESY6 The analysis of six years of the Dark Energy Survey data

DM Dark Matter

FLRW Friedmann–Lemaître–Robertson–Walker

GGL Galaxy-Galaxy Lensing

GR General Relativity

ΛCDM Λ (Cosmological Constant)-Cold Dark Matter

HLIS High-Latitude Imaging Survey with Roman Space Telescope

HLWAS High-Latitude Wide Area Survey with Roman Space Telescope

IA Intrinsic Alignment

LSST Legacy Survey of Space and Time with Rubin Observatory

MEDS Multi-Epoch Data Structure

MCMC Markov Chain Monte Carlo

PSF Point Spread Function

SCA Sensor Chip Assembly

SNIa Type Ia Supernovae

WL Weak Lensing

2PCF Two-Point Correlation Function

Acknowledgements

I would not have made it this far without the trust and support of people from different research groups and collaborations. They are the reason I will continue in this field.

First and foremost, I would like to dedicate my appreciation to my advisor, Michael Troxel. Thank you for everything you have done for me. From academic advising to supporting me in experiencing many things, you have done so much for me. You are the most caring and patient advisor. Regardless of my lack of knowledge, skill, and experience, you were always there and patiently listened to me. Sometimes, I was stressed and frustrated, but I was able to enjoy my life and work throughout my Ph.D. years. I am glad you are my advisor, and I am proud to be your first student. On top of that, you have shown me how to care for people. Your attitude towards raising researchers will always help me navigate my life and career.

Matt Becker – Your diligence, dedication, and frankness have helped and supported me in navigating the collaborative work in DES. Watching you come up with good tests has shaped my mindset as a researcher. Thank you for guiding me as one of your "shear children."

Chris Hirata – Your wealth of insight and knowledge, together with a great amount of patience and thoughtfulness, has been very motivational. Your inspiration will always help me navigate my academic career.

To people and teams in the Dark Energy Survey,

Masao Sako – Your mentoring has inspired and motivated me to accomplish my work in DES and continue in academia as an international student. I hope to continue our bi-weekly

chat in the future.

Alex Drlica-Wagner – Thank you for giving me the opportunity to visit Chile and observe with the Blanco telescope for the DELVE survey. The experience in Chile was influential in helping me acquire a broader perspective on how data is delivered and how we conduct science with it.

Shear analysis team – I would like to first thank Theo Schutt for your help and support in co-leading the team with me. I greatly enjoyed our time being co-leads of the team. I would also like to thank all of the members in the team (Erin Sheldon, Mike Jarvis, Robert Gruendl, Marco Gatti, Gary Bernstein, Sid Mau, Vernon Wetzell, Brian Yanny) for your support and encouragement in driving our work forward.

Cosmic shear team – I would like to first thank Simon Samuroff for your help and support in co-leading the team with me. I am immensely thankful for your experience and knowledge, which guided me toward the analysis. Your thesis has also been very inspirational in helping me understand various concepts. I would also like to thank Alex Amon for your guidance in leading teams and analyzing results.

Y6 Key Project team – I would like to thank the team for all of your tremendous amount of remarkable work and encouragement, which is making our DES Y6 cosmological analysis possible.

To people in the Duke Cosmology group,

Dan Scolnic, Chris Walter – Thank you, Dan, for kindly having me in your social group and also reviewing and providing valuable comments on my job applications. Thank you, Chris, for hosting the weekly group meeting for the last five years and showing us how to ask good questions.

Erik Peterson, Rebecca Chen – To my cosmology cohort, thank you always for your support, entertainment, and cherished memories. I hope to see the three of us succeed in our careers as the first-gen in the Duke cosmology group.

Maria Acevedo – I appreciate the weekly dose of cat pictures at the group meetings. I will come back to Durham anytime to look after your girls. Thank you for supporting me

in choosing the coffee machine as well.

To my cohort in Duke Physics, Swapnil Patel, Jordan McCourt, Charlie Prior, Katherine Parham – thank you for always being kind friends to me throughout my life in Durham. I will not forget the moments of working on homework together during COVID, playing tennis, and Bull McCabes.

To my Englewood gangs, Brodie Popovic, Utsav Patel – I greatly enjoyed our time together under the same roof outside of work. All your shenanigans and our Halloween parties are deeply embedded in my heart. I will never want to lose a door to my room after a long flight, though.

To members of various Japanese communities, Tennis community – Thank you for creating a community where I can return to the same place every Sunday. Playing tennis with you on many Sunday mornings was my relaxation time.

Golf community – I will not forget all the memories of us playing golf at Hillandale, Duke, and Orlando. It made me realize golf can be a wonderful sport where I can meet with a great community anywhere in the world. Thank you for our moments together.

Student community – My life without "Nomikai" would not have been fun. I loved everything from listening to your research to chatting about stupid things, and spending many new years together making nabe. I would like to give a special thanks to Yuhi. You have supported me in many ways since the first year.

My friends and family have provided unconditional love and support throughout this journey. To my family in Japan, thank you always for your support in my decision. To my family in the US and friends from college, even though we have only seen each other once or twice a year for the past five years, spending time with you has always given me the energy to get through the year. Thank you for having a place where I can return anytime and feel at home.

Last but not least, to my partner, Marika, I cannot thank you more than enough over the past three years for always being with me and being supportive. I hope to continue inspiring each other both from the art and science worlds.

1

Introduction

Cosmology, the study of the Universe's origin, structure, evolution, and ultimate fate, has fascinated humanity for millennia, evolving from mythological narratives to precise science. The study of cosmology reflects humanity's deep curiosity to comprehend the vastness of the Universe and our place within it.

Ancient Greeks called the Universe *"cosmos"* – an entity that makes a regular movement and in an orderly systematic manner. Aristotle's Universe was finite and geocentric, with Earth at its center surrounded by concentric celestial spheres that carried the planets and stars, all made of a perfect, unchanging substance called aether. This model was further refined by Ptolemy, who introduced the epicycles to account for the apparent retrograde motion of planets. Despite their inaccuracies, these models persisted for centuries, deeply influencing the way humanity perceived the Universe. The Aristotelian and Ptolemaic cosmologies have dominated how people regarded the Universe for more than 2000 years.

The Scientific Revolution (16th – 17th Century) began during the Renaissance. This era witnessed the re-emergence of classical knowledge, combined with new discoveries and methodologies. The Renaissance set the stage for a more systematic and observational approach to understanding the heavens, transitioning from a geocentric model of the Universe

to a heliocentric model with the sun at the center. This shift was propelled by the work of Nicolaus Copernicus, whose heliocentric theory laid the foundation for modern astronomy, challenging the prevailing Aristotelian and Ptolemaic views and paving the way for future scientific inquiries. This was further advanced by astronomers such as Johannes Kepler, who eventually took the Copernican view and pioneered the way to understand the Universe as the physics of astronomy. While Kepler studied the motion of astronomical objects, Galileo Galilei quantified the motion of objects on the Earth and pioneered the mathematical description of nature. Galileo's pioneering approach of applying mathematical descriptions to understand and predict natural phenomena marked a significant departure from qualitative to quantitative science. Sir Isaac Newton succeeded in unifying the natural phenomena in the Universe and on the Earth by describing them with a common language (mathematics), publishing *Philosophiæ Naturalis Principia Mathematica (1687)* and putting an end to the Scientific Revolution. Newton's formulation of the laws of motion and universal gravitation further revolutionized cosmology by providing a mathematical framework that described the motion of celestial bodies. These laws not only explained planetary orbits but also offered a universal description of motion that applied both on Earth and in the heavens, unifying the physics of the cosmos and Earth under the same principles.

The 20th century brought about multiple paradigm shifts in classical physics that Newton has established. Albert Einstein's theory of special and general relativity, published in 1905 and 1915, introduced a speed limit in nature and a new understanding of gravity as the curvature of space-time caused by mass and energy, laying the theoretical foundation for modern physics and cosmology. Observations by Edwin Hubble in 1929 showed that galaxies are moving away from each other and provided the first empirical evidence for the expansion of the Universe, leading to the development of the Big Bang theory as the leading explanation of the Universe's origin and evolution.

In the latter half of the 20th century and into the 21st century, cosmology has continued to evolve rapidly with the introduction of satellite-based observations, such as those from the Cosmic Background Explorer (COBE) and the Hubble Space Telescope among others.

These missions have provided detailed measurements of the cosmic microwave background radiation and the expansion rate of the Universe, offering a glimpse into the Universe's early moments and the late-time Universe. These measurements indicated indirect evidence of dark matter, which only interacts with ordinary matter through gravitational force and dark energy, which seems to cause the accelerated expansion of the Universe. These have further fine-tuned the Standard cosmological model, highlighting the fact that the majority of the Universe is made up of these mysterious components.

We are in an exciting era in the history of cosmology and physics, as there seems to be a discrepancy in the cosmological model between different probes, and the introduction of dark matter and dark energy in our cosmological model requires consistency with other fields in physics, such as with the Standard Model in particle physics. We have not found a consistent story to unify our understanding of nature. While the current imaging surveys provide more evidence of the existence of dark matter and dark energy, multiple next-generation telescopes have been built and launched to probe the nature of dark matter and dark energy and to understand the Universe's structure, composition, and evolution.

2

Fundamental Principles of Cosmology

This chapter delves into the core principles that form the backbone of modern cosmology, providing a comprehensive exploration of the theoretical frameworks and equations that have shaped our understanding of the Universe. We explore its geometry of space-time with the Friedmann–Lemaître–Robertson–Walker metric, its kinematics from Einstein's general relativity, and finally, its dynamics of the Universe to derive the Friedmann equations, which describe how each component in the Universe (radiation, dark matter, baryonic matter, and dark energy) behaves in our expanding Universe. But first, let's explore chronologically the significant events since the beginning of the Universe.

2.1 Cosmic History: From the Big Bang To Now

The idea that our Universe started from the Big Bang, which is an event of space expansion from the state that every point in space was infinitely hot and dense, came from the observation made by Edwin Hubble that the Universe is expanding (Hubble, 1929) – the Universe had to begin from somewhere hot and dense. We will not mention how or why the Big Bang happened. We will simply begin from the moment the Universe started.

After the Big Bang and in less than 10^{-32} seconds, the Universe is commonly thought to have experienced a period of what is called inflation – it doubled in size at least 80

times. This idea was proposed by Albrecht and Steinhardt, 1982; Guth, 1981; Linde, 1982 in order to resolve the homogeneity problem in cosmic microwave background (CMB) and the flatness problem in the late-time Universe. Inflation allows quantum fluctuations in vacuum space to expand and creates the initial primordial density fluctuations in the Universe. These Gaussian random fluctuations became the seed of the large-scale structure in the late-time Universe.

Just one second after the Big Bang, the temperature of the Universe was estimated to be about 10^{10} Kelvin. Within a trillionth of a second, all the elementary particles and antiparticles (e.g., quarks, leptons) described in The Standard Model (Particle Data Group et al., 2022) were equally abundant. As the Universe expanded and cooled down, reactions between particles and antiparticles (e.g., particle-antiparticle annihilation) started to happen, and quarks began to be held together to form protons and neutrons at about 10^{-5} seconds after the Big Bang. At this point, the Universe was still hot (10^9 K), yet many of the elementary particles had already been annihilated. At about a few minutes, within the pool of plasma of free electrons, protons, neutrons, and photons, atoms such as deuterium, helium, and lithium started to fuse (called Big Bang Nucleosynthesis). The Universe had not yet seen a stable hydrogen atom because protons could not capture electrons due to energetic photons.

After about $370,000$ years after the Big Bang, the Universe has cooled enough (~ 3000 K) for photons to begin decoupling from electrons (a state where a particle is able to free-stream without scattering) and hydrogen atoms to form, which we call recombination. These free-streaming photons still propagate through the expanding Universe, and we are able to observe them as a stretched light in a microwave range, which we call cosmic microwave background. These photons are from the surface of the last scattering, where they have been propagating freely since the moment of the last scattering with electrons.

As can be seen, the Universe has been through periods of annihilating, scattering off, and fusing particles. Nonetheless, the early Universe is expected to have been in thermal equilibrium, which means that the Universe itself should exhibit a blackbody spectrum, and
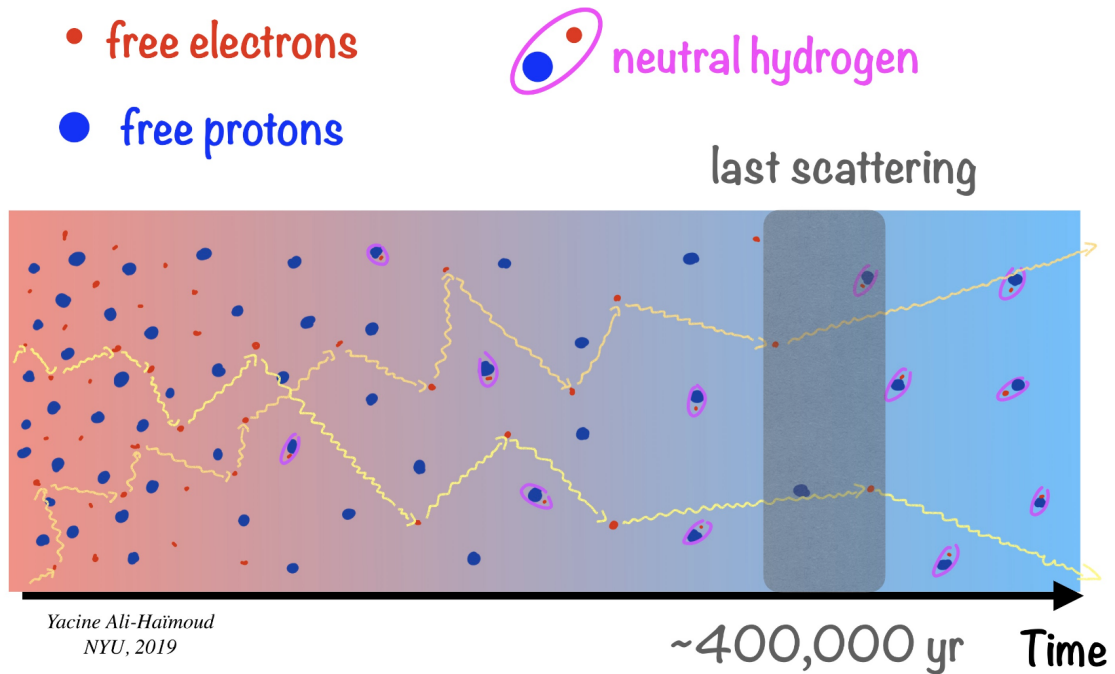
FIGURE 2.1: An illustration to describe how the cosmic microwave background radiation is able to begin free-streaming the Universe after scattering off of free electrons.

the CMB should have blackbody radiation at a particular temperature. This is exactly what has been observed very precisely (e.g., Bennett et al., 1996) with the average temperature of $T = 2.725$K. If we look closely at the observed CMB, however, there are small variations ($\sim 10^{-4}$K) in the temperature (i.e., hot and cold spots in the early Universe). These fluctuations come from the primordial density fluctuations in the earlier Universe that were quantum in nature but were expanded in the period of inflation. These variations became the seeds of the matter density fluctuations in the later Universe and grew into the structures (e.g., stars, galaxies, clusters) we see today. We are able to predict from theory what the spatial correlations of these temperature fluctuations would look like and that is what we observe. I will explore this quantitatively in § 2.3.

Since photons decoupled from matter, the Universe was transparent but dark. Clouds of hydrogen and helium atoms slowly accumulated together with their gravitational force and collapsed in their slightly over-dense gravitational potential. When the Universe was

6

about 100 million years old, the first stars were born. These stars played a few major roles in constructing our Universe today. Firstly, these stars were emitting ultraviolet energy and hence ionizing their surrounding gas, which led to the reionization of neutral hydrogen atoms ("epoch of reionization"). The reionization will later impact the formation of galaxies and play a major role in the scattering of the CMB photons. Secondly, these stars were massive, and their cores were able to fuse elements heavier than helium, such as carbon, oxygen, and iron, through their nucleosynthesis process – the first appearance of these elements in the Universe. Fusing up to iron atoms is an endothermic process (releasing more energy than absorbing due to nuclear binding energy – the energy required to break up a nucleus into its components – is the highest among other atoms), and fusing heavier atoms absorbs more energy than what comes out. Thus, the core of a star is not able to fuse more elements than irons and is no longer able to support its own mass by the pressure from nuclear fusion. This leads to the gravitational collapse and the violent explosion of a star (called a supernova) in the case of massive stars. During a supernova explosion, since it is such an energetic process, heavier elements such as uranium can be synthesized through the rapid neutron-capture process. Supernovae, hence, further enrich their surrounding environment and the Universe itself.

About 900 million years later, these stars became gravitationally bound, and the first galaxies formed. These galaxies ionized the neutral hydrogen gas further and further, and all of the Universe's hydrogen became ionized. Since then, more galaxies have formed and they have clumped together to form clusters and superclusters. While structures continue to grow in a gravitationally bound environment at present-day (the age of our Universe is estimated to be about 13.8 billion years old), it is slowing down as the Universe crossed the threshold where what is causing the Universe to expand started to dominate the Universe about 5 billion years ago.

This story is based on what we think happened in the past and what we can observe today. The goal of cosmologists is to build a model of how this Universe works (i.e., a cosmological model) and tell a consistent story that can be extrapolated from the model.

Our current cosmological model (Λ-CDM model), based on evidence from CMB, galaxies, and supernovae, suggests that the stuff we can see (ordinary atoms – cosmologists like to call it baryons) composes less than 5% of the Universe and the majority of what makes up the Universe is in what we cannot see and what we do not exactly understand – dark matter (~30%) and dark energy (~65%). What we know about them is that dark matter interacts with itself and other matter only through gravity, and dark energy is seemingly causing the accelerated expansion of the Universe. Throughout cosmic history, the Universe has experienced interactions of various scales, from particle collisions to galaxy mergers. Although the random Gaussian density fluctuations in the early Universe were the seed of early structures such as stars and galaxies, in order for these to be stable and grow, dark matter and dark energy are essential, and the interplay between dark matter and dark energy creates an even bigger structure in the Universe – the large-scale structure. Numerical simulations of the current cosmological model show that our Universe has a web-like structure (Figure 2.2). This structure exists because the proportion of what constitutes the Universe has been changing since the beginning. Dark matter has been exerting gravitational force on baryonic matter, making the overdense region denser, while dark energy has been causing the Universe to expand, making the underdense region more empty. I will discuss this more quantitatively in § 2.2.

All of the aspects mentioned here are active areas of research, and new observations with the latest telescopes and detectors confirm or change what we conceive as the law of nature. These new observations hold keys to unlock these fundamental mysteries in astronomy and physics.

2.2 Homogeneous Universe

This section introduces the Standard Model of Cosmology. Readers can refer to Baumann, 2022; Dodelson, 2003 (which I have found influential in understanding what is summarized in these chapters) for more details.
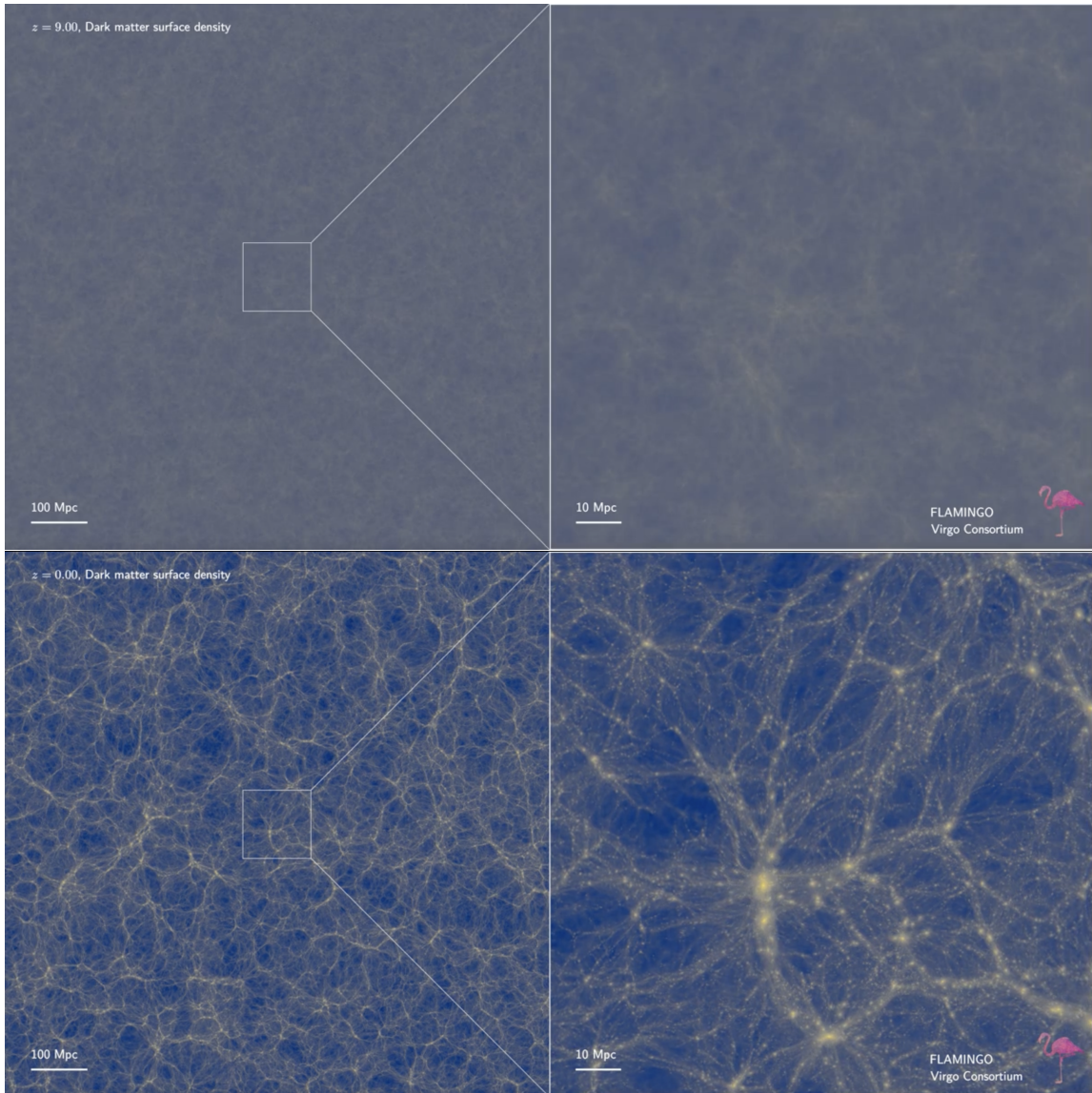
FIGURE 2.2: The evolution of dark matter surface density in *FLAMINGO* Hydrodynamical Simulations by Schaye et al., 2023. Each represents a 20Mpc slice (thickness) of the simulated Universe at redshifts 9.0 (top) and 0.0 (bottom). The right column is the zoomed-in images of the images on the left column.

2.2.1 Geometry – The Friedmann–Lemaître–Robertson–Walker metric

Every beginning of a cosmology class starts by stating, "There is no center in the Universe (we do not live at a special point), and it is homogeneous (looks the same everywhere, translational symmetry) and isotropic (looks the same in all directions, rotational symme-

try) on large scales." This is an assumption we make in order to build a cosmological model in which the spacetime geometry is simple. Fig. 2.2 shows that these assumptions are valid on large scales (> 100Mpc).

The Standard Model of Cosmology is constructed based on general relativity (GR), where spacetime curvature tells matter how to move, and matter tells spacetime how to curve. Therefore, it is essential for us to start by defining our spacetime geometry (i.e., coordinate system). We take our spacetime coordinates $x^\mu = (ct, x^i)$ and can define the physical distance between two points separated by the infinitesimal coordinate distances (which we call line element).

$$ds^2 \equiv g_{\mu\nu}dx^\mu dx^\nu, \tag{2.1}$$

where $g_{\mu\nu}$ is called metric, and it is an object that turns coordinate distances into physical distances. In our expanding Universe, which is filled with stuff, this metric has a dependence on time and space ($g_{\mu\nu}(t, \boldsymbol{x})$), since mass curves the geometry and the distribution of matter and energy varies over time and space. We incorporate all the time-dependence of the metric in terms of the scale factor $a(t)$, which describes the expansion of the Universe and is related to the matter content in the Universe. We define the scale factor at present-day to be $a(t_0) = 1$. The line element in our Universe can then be,

$$ds^2 = -c^2 dt^2 + a^2(t)\gamma_{ij}(x^k)dx^i dx^j, \tag{2.2}$$

where $\gamma_{ij}(x^k)$ is the spatial part of our metric and takes different forms depending on the intrinsic curvature of space. Possible intrinsic curvatures of space (parametrized as k) are "flat" ($k = 0$), "spherical" ($k = 1$), or "hyperbolic" ($k = -1$). If we incorporate the parametrized metric of the possible curvatures and introduce polar coordinates (r, θ, ϕ), we obtain the line element.

$$ds^2 = -c^2 dt^2 + a^2(t)\left[\frac{dr^2}{1 - kr^2/R_0^2} + r^2 d\Omega^2\right], \tag{2.3}$$

where $d\Omega^2 \equiv d\theta^2 + sin^2\theta d\phi^2$ and R_0 is the curvature scale which determines the radius

10

of the sphere or the curvature of the hyperboloid. Equation. 2.3 is called the Fried-mann–Lemaître–Robertson–Walker (FLRW) metric.

In the FLRW metric, we define our coordinate system to be *comoving coordinate* rather than *physical coordinate*. The relationship between the comoving and physical coordinates can be understood as, $d_{\text{physical}} = a(t)r$. Figure 2.3 describes the comoving distance, which is unchanged as a function of time, whereas the physical distance changes so that $d(t_2) > d(t_1)$. To further simplify Eqn. 2.3, we redefine $d\chi \equiv dr/\sqrt{1 - kr^2/R_0^2}$, and rewrite Eqn. 2.3 to achieve,

$$ds^2 = -c^2 dt^2 + a^2(t)\left[d\chi^2 + S_k^2(\chi)d\Omega^2\right],\tag{2.4}$$

where

$$S_k(\chi) \equiv R_0 \begin{cases} sinh(\chi/R_0) & k = -1 \\ \chi/R_0 & k = 0 \\ sin(\chi/R_0) & k = +1. \end{cases}\tag{2.5}$$
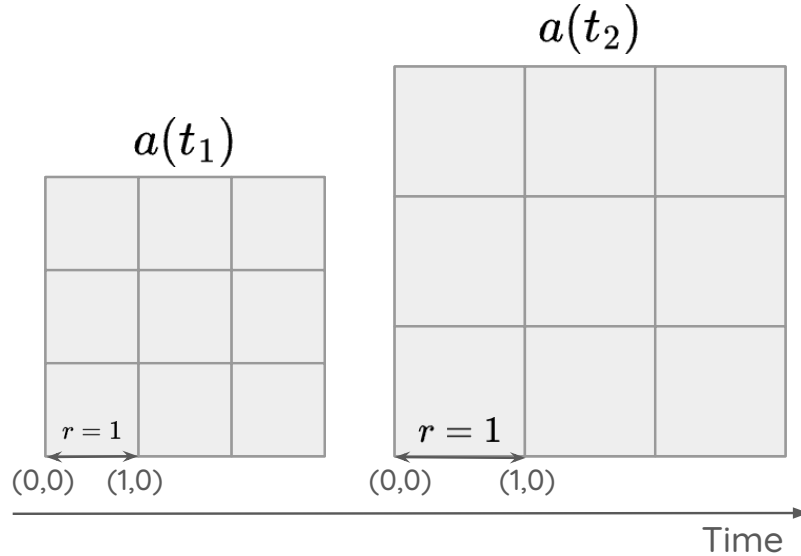
FIGURE 2.3: A diagram to explain the comoving coordinate with the scale factor (a) and comoving distance (r).

Our understanding of the Universe comes from photons from various sources that were emitted sometime in the past and took a finite amount of time to reach us. Given that the

Universe continues expanding while the photons travel, the wavelength of these photons gets stretched – the light appears to be "redder" than the original wavelength (λ_{emitted}). We call this redshift z ($z = 0$ at present-day), and the amount of redshift is practically a distance measure between the source and observer. The increase in the wavelength of light (i.e., decrease in energy) can be expressed as,

$$\lambda_{\text{observed}} = \frac{a(t_{\text{observed=now}})}{a(t_{\text{emitted}})}\lambda_{\text{emitted}}, \tag{2.6}$$

and we define $z \equiv (\lambda_{\text{observed}} - \lambda_{\text{emitted}})/\lambda_{\text{emitted}}$ to obtain

$$1 + z = \frac{1}{a(t_{\text{emitted}})}. \tag{2.7}$$

To an observer, the source of light is receding from the observer and we can practically define the recession speed as $v = cz$. If we derive the physical velocity of the source ($v_{\text{physical}} = dd_{\text{physical}}/dt$),

$$v = cz \sim \frac{da}{dt}r + a(t)\frac{dr}{dt} \equiv Hd_{\text{physical}} + a(t)\frac{dr}{dt}, \tag{2.8}$$

where we have introduced the Hubble parameter (expansion rate of the Universe),

$$H \equiv \frac{\dot{a}}{a}. \tag{2.9}$$

The first term is called the Hubble flow, which is the velocity of an object due to the expansion, and the second term is called the peculiar velocity, the motion of an object relative to cosmological rest frame (e.g., gravitational attraction). In the local Universe ($z < 1$), the expansion rate can be considered to be constant $H \sim H_0$ (Hubble constant – the expansion rate at present-day), and one can roughly estimate the current expansion rate of the Universe from the recession velocity and distance. Edwin Hubble made these observations in 1929 and discovered the expansion of the Universe (Hubble, 1929). To be more precise, the physical distance (d_{physical}) used above is not exactly accurate because d_{physical} is merely a distance at a fixed time (i.e., in each three-dimensional spatial slice). In

order to obtain a precise physical distance, one needs to integrate over time from when the light is emitted to when the light is observed. Since photons follow null geodesics, Eqn. 2.4 can be rewritten, and the comoving distance is,

$$\chi(z) = c \int_{t_{\text{emitted}}}^{t_{\text{observed}}} \frac{dt}{a(t)} = c \int_0^z \frac{dz}{H(z)}. \tag{2.10}$$

We can further exploit this to find a distance measure of two points in space. Imagine two points are separated on the sky by an angular separation θ and are physically separated by R. A simple trigonometry provides us the distance estimate: $D_A = R/\theta$, and rewriting R in comoving distance yields

$$D_A(\chi) = \frac{S_K(\chi)}{1+z}, \tag{2.11}$$

which we will refer to as angular diameter distance.

2.2.2 Kinematics & Dynamics – The Friedmann Equations

Now that we have obtained the FLRW metric, we can explore how particles evolve in this FLRW spacetime. We first introduce the geodesic equation (see Carroll, 2019 for more details on how to derive it), which is essentially Newton's equation of motion in GR. The geodesic equation shows how a particle moves along the geometry we have set up.

$$\frac{d^2 x^\mu}{dr^2} = -\Gamma^\mu_{\alpha\beta} \frac{dx^\alpha}{d\tau} \frac{dx^\beta}{d\tau}, \tag{2.12}$$

where the Christoffel symbol is

$$\Gamma^\mu_{\alpha\beta} \equiv \frac{1}{2} g^{\mu\lambda} \left[\frac{\partial g_{\beta\lambda}}{\partial x^\alpha} + \frac{\partial g_{\alpha\lambda}}{\partial x^\beta} - \frac{\partial g_{\alpha\beta}}{\partial x^\lambda} \right]. \tag{2.13}$$

For the FLRW metric ($g_{\mu\nu} = (-1, a^2(t)\gamma_{ij})$), we can compute the nonzero components of the Christoffel symbol as,

$$\begin{cases} \Gamma^0_{ij} = c^{-1} a\dot{a}\gamma_{ij} \\ \Gamma^i_{0j} = c^{-1} \frac{\dot{a}}{a}\delta^i_j \\ \Gamma^i_{jk} = \frac{1}{2}\gamma^{il}\left(\frac{\partial \gamma_{kl}}{\partial x^j} + \frac{\partial \gamma_{jl}}{\partial x^k} - \frac{\partial \gamma_{jk}}{\partial x^l}\right). \end{cases} \tag{2.14}$$

13

It is worthwhile to mention here that our equation of motion depends on the metric (i.e., the curvature of spacetime), and we have not yet discussed how the matter/energy content in the Universe curves the spacetime.

We start this discussion from the Einstein's field equation –

$$G_{\mu\nu} \equiv R_{\mu\nu} - \frac{1}{2}g_{\mu\nu}R = \frac{8\pi G}{c^4}T_{\mu\nu}, \tag{2.15}$$

where $R_{\mu\nu}$ is the Ricci tensor, R is the Ricci scalar ($R = g^{\mu\nu}R_{\mu\nu}$), and G is the Newton's gravitational constant ($G = 6.67 \times 10^{-11} m^3 kg^{-1} s^{-2}$). $G_{\mu\nu}$ is called the Einstein tensor and describes the measure of spacetime curvature. $T_{\mu\nu}$ is called the energy-momentum tensor and describes the matter/energy content of the Universe. We begin by describing how to determine the energy-momentum tensor in the frame of a comoving observer from our first principles – homogeneity and isotropy, which conserve the translational and rotational symmetry. Given that the energy-momentum tensor has components that explain the density and flux of energy and momentum (Figure 2.4), homogeneity requires the energy density to be position-independent (i.e., $T_{00} \propto \rho(t)$) and isotropy requires the momentum density and energy flux to be zero (i.e., $T_{i0} = T_{0j} = 0$). For the momentum flux, the diagonal part is called the normal stress (pressure), and the off-diagonal part is called the shear stress. Again, homogeneity and isotropy require $T_{ij} = P(t)g_{ij}(t)$, where $P(t)$ is the pressure. Hence, these cosmological principles create the energy-momentum tensor of a perfect fluid (Eqn. 2.16). This provides a great insight into what types of matter and energy *possibly* fill the Universe.

$$T^{\mu}_{\nu} = g^{\mu\lambda}T_{\lambda\nu} = \begin{pmatrix} -\rho(t)c^2 & 0 & 0 & 0 \\ 0 & P(t) & 0 & 0 \\ 0 & 0 & P(t) & 0 \\ 0 & 0 & 0 & P(t) \end{pmatrix} \tag{2.16}$$

Here if we impose the energy and momentum conservation condition (i.e., continuity equation – $\nabla_{\mu}T^{\mu}_{\nu} = 0$), we arrive at an important equation to explore the change in energy

14

$$T_{\mu\nu} = \begin{pmatrix} T_{00} & T_{01} & T_{02} & T_{03} \\ T_{10} & T_{11} & T_{12} & T_{13} \\ T_{20} & T_{21} & T_{22} & T_{23} \\ T_{30} & T_{31} & T_{32} & T_{33} \end{pmatrix}$$

Energy density   Momentum density

Energy flux   Momentum flux

FIGURE 2.4: A breakdown of each component of the energy-momentum tensor.

density over time in our expanding Universe.

$$\frac{\dot{\rho}}{\rho} + 3\frac{\dot{a}}{a}(1+w) = 0, \tag{2.17}$$

where we define an equation of state, $w = P/(\rho c^2)$. This shows that $\rho \propto a^{-3(1+w)}$ and the evolution of energy density in an expanding Universe depends on the types of fluids.

For a matter-like fluid ($|P| \ll \rho c^2$, meaning $w = 0$),

$$\rho \propto a^{-3}, \tag{2.18}$$

which has a nice physical interpretation that as the volume of the Universe expands ($V \propto a^3$), the density of normal matter decreases like an inverse of the volume ($\rho \propto V^{-1}$). From several observations, such as the rotation velocity of a galaxy (Rubin et al., 1980), scientists deduced that there needs to be more matter than what we can see, and we categorized them as baryons (ordinary matter, visible matter) and dark matter (c.f., microscopic nature of dark matter is still unknown). It turns out that including *cold* dark matter in our cosmological model works out quite well, and we can precisely infer the density of dark matter in the Universe from observations.

For a fluid of relativistic particles ($P = \frac{1}{3}\rho c^2$, meaning $w = 1/3$), which we generally call radiation,

$$\rho \propto a^{-4}. \tag{2.19}$$

15

The energy density of radiation (mostly in photons) decreases not only as the volume increases but also as the wavelength stretches due to redshift.

Lastly, there needs to be an explanation of why the Universe is accelerating in expansion, and a phenomenological fluid with negative pressure ($P = -\rho c^2$, meaning $w = -1$) fits this picture quite well. The energy of a fluid with negative pressure is created as the Universe expands (a time-independent constant energy density) rather being diluted –

$$\rho \propto a^0. \tag{2.20}$$

While there are many candidates for what this fluid is, we generally call it dark energy. Einstein introduced a term called a cosmological constant (Λ) to his field equation to keep the Universe from collapsing due to its own gravity. The dark energy equation-of-state of $w = -1$ is interpreted that dark energy *is* the cosmological constant. A recent discovery of the *accelerating* expansion of the Universe (Perlmutter and Riess, 1999; Riess et al., 1998) has further indicated that the Universe is filled with this unknown component with constant energy density. We will later discuss a model/parametrization that dark energy is not a cosmological constant ($w \neq -1$) and is time-dependent. Although the physical nature of the dark energy is still mysterious, there are some candidates. One physical candidate is "vacuum energy" – the background energy associated with empty/vacuum space. The value of the vacuum energy predicted by quantum field theory, however, is about 50-120 orders of magnitude larger than the energy density observed in cosmological observations.

Now that we have potential matter/energy contents of the Universe that curve the spacetime, we are able to utilize them to describe the evolution of the Universe using Einstein's field equation (Eqn. 2.15). We first compute the spacetime curvature ($G_{\mu\nu}$) for our FLRW metric. The non-zero components of the Ricci tensor are,

$$R_{00} = -\frac{3}{c^2}\frac{\ddot{a}}{a}, \; R_{ij} = \frac{1}{c^2}\left[\frac{\ddot{a}}{a} + 2\left(\frac{\dot{a}}{a}\right)^2 + 2\frac{kc^2}{a^2 R_0^2}\right]g_{ij}, \tag{2.21}$$

and the Ricci scalar is,

$$R = \frac{6}{c^2} \left[\frac{\ddot{a}}{a} + \left(\frac{\dot{a}}{a} \right)^2 + \frac{kc^2}{a^2 R_0^2} \right]. \tag{2.22}$$

Now the time-time component of the field equation, $G^\mu{}_\nu \equiv g^{\mu\lambda} G_{\lambda\nu} = \frac{8\pi G}{c^4} T^\mu{}_\nu$, is

$$\left(\frac{\dot{a}}{a} \right)^2 = \frac{8\pi G}{3} \rho - \frac{kc^2}{a^2 R_0}, \tag{2.23}$$

where ρ is the energy density of all the components in the Universe. Let's include matter, radiation, and dark energy as we discussed earlier and define $\rho = \rho_{\text{radiation}} + \rho_{\text{matter}} + \rho_{\text{dark energy}}$. The spatial part is then,

$$\frac{\ddot{a}}{a} = -\frac{4\pi G}{3} \left(\rho + \frac{3P}{c^2} \right). \tag{2.24}$$

Equations 2.23 and 2.24 are the two Friedmann equations. We rewrite the first Friedmann equation in terms of the Hubble parameter (Eqn. 2.9) and the density parameter of each component ($\Omega = \rho_0 / \rho_{\text{crit}}$), which is the density of each component at present-day with respect to the critical/total density for a flat Universe at present-day –

$$\frac{H^2}{H_0^2} = \Omega_{\text{radiation}} a^{-4} + \Omega_{\text{matter}} a^{-3} + \Omega_k a^{-2} + \Omega_\Lambda, \tag{2.25}$$

with $\rho_{\text{crit}} \equiv 3H_0^2 / 8\pi G$ evaluated at present-day ($a(t_0) = 1$):

$$1 = \Omega_{\text{radiation}} + \Omega_{\text{matter}} + \Omega_k + \Omega_\Lambda. \tag{2.26}$$

Here we defined the density of the intrinsic curvature to be $\Omega_k \equiv -kc^2 / (R_0 H_0)^2$. Figure 2.5 shows the evolutions of each component's energy density.

2.3 Inhomogeneous Universe

So far, we have discussed the large-scale behavior of our expanding Universe from its first principles – homogeneity and isotropy, and the Friedmann equations have provided us with tools to explore the evolution of its metric based on its matter and energy content.
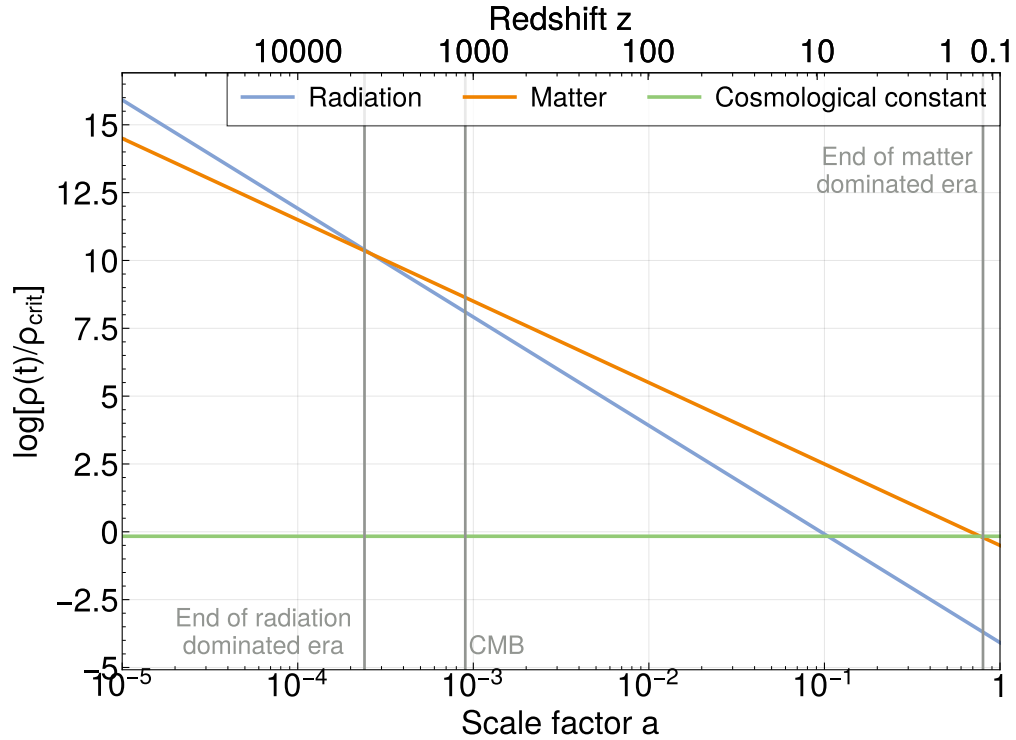
FIGURE 2.5: The energy density of radiation, matter, and dark energy (cosmological constant) components in the Universe as a function of scale factor (bottom axis) and redshift (top axis).

On large scales, the Universe does seem to be homogeneous and isotropic. However, the small density fluctuations in the early Universe have grown to become inhomogeneities in the present day. If we would like to understand our Universe better and more accurately, we need to understand how the structures formed, which are ultimately what we are able to observe to test against the cosmological model.

2.3.1 Structure Formation

In order to study the inhomogeneity, it is useful to consider it as a perturbation to the homogeneity. We will only explore the perturbations in a non-relativistic fluid with a Newtonian gravity. This is practical since most of the structure growth in the Universe has been induced by dark matter. Readers who are interested in the relativistic perturbation theory can refer to Chapter 6 of Baumann, 2022.

Consider a fluid with velocity $\boldsymbol{u}$, energy density ρ and pressure P. If we treat the fluid

in fluid dynamics, the continuity equation (i.e., matter conservation) and Euler equation (i.e., momentum conservation) can be written. In order to study the structure growth, we need to add the effect of the fluid's own gravitational potential and the expansion of the Universe. We can write three sets of equations –

$$\frac{\partial \rho}{\partial t} + 3H\rho + \frac{1}{a}\nabla(\rho \boldsymbol{v}), \tag{2.27}$$

where $\boldsymbol{u} = \dot{\boldsymbol{r}} = H\dot{\boldsymbol{r}} + \boldsymbol{v}_{\text{peculiar}}$.

$$\left(\frac{\partial}{\partial t} + \frac{\boldsymbol{v}}{a} \cdot \nabla\right)\boldsymbol{u} = -\frac{1}{a}\frac{\nabla P}{\rho} - \frac{1}{a}\nabla \phi, \tag{2.28}$$

where ϕ is the gravitational potential of the fluid. And finally,

$$\nabla^2 \phi = 4\pi G a^2 \rho, \tag{2.29}$$

which is the Poisson equation. Now if we introduce small perturbations at linear order to the density, pressure, and gravitational potential – $\rho = \bar{\rho}[1 + \delta]$, $P = \bar{P} + \delta P$, and $\phi = \bar{\phi} + \delta\phi$ (where we have introduced the density contrast, $\delta \equiv \delta\rho/\bar{\rho}$, and the over-bar denotes the mean value), we are able to linearize the above equations around small perturbations ($|\delta| \ll 1$) to achieve the equation of the linear growth of density contrast.

$$\ddot{\delta} + 2H\dot{\delta} - \left(\frac{c_s^2}{a^2}\nabla^2 + 4\pi G\bar{\rho}(t)\right)\delta = 0, \tag{2.30}$$

where the sound speed of the fluid (c_s) is defined as $c_s \equiv \partial P/\partial \rho$. It is useful to deconstruct the density contrast in a set of discrete Fourier modes (k) with a characteristic length scale (λ). In Fourier space, Eqn. 2.30 can be rewritten as,

$$\ddot{\delta}(\boldsymbol{k}, t) + 2H\dot{\delta}(\boldsymbol{k}, t) + c_s^2\left(\frac{k^2}{a^2} - \frac{4\pi G\bar{\rho}(t)}{c_s^2(t)}\right)\delta(\boldsymbol{k}, t) = 0. \tag{2.31}$$

On scales where the length scales of Fourier modes are well within the Hubble radius[1]

---

[1] In cosmology, "entering horizon" post-inflation means that the length scale of a given Fourier mode has become smaller than the Hubble radius ($d_h = (aH)^{-1}$). When the length scale is larger than d_h, we state that the mode is in super-horizon, and when it is smaller than d_h, we state that the mode is in sub-horizon.

$(k/a \ll \sqrt{4\pi G\bar{\rho}(t)}/c_s(t))$, we can ignore the contribution from pressure, and only gravitational instability becomes dominant. This can be written as,

$$\ddot{\delta}(\boldsymbol{k}, t) + 2H\dot{\delta}(\boldsymbol{k}, t) - 4\pi G\bar{\rho}(t)\delta(\boldsymbol{k}, t) = 0. \tag{2.32}$$

The solution to Eqn. 2.32, which is a second-order linear ordinary differential equation, can be written as,

$$\delta(\boldsymbol{k}, t) = \delta_+(\boldsymbol{k})D_+(t) + \delta_-(\boldsymbol{k})D_-(t), \tag{2.33}$$

where $\delta_\pm(\boldsymbol{k})$ are the Fourier transforms of the initial density field, which are fixed when they re-entered the horizon. Since the evolution of these sub-horizon modes is k-independent[2], the linear growth function $D_\pm(t)$ is only a function of time. While D_+ is a growing mode and D_- is a decaying mode, we will only consider the growing mode because the homogeneity and isotropy conditions require no decaying modes in the FLRW metric. We can then solve this equation at a radiation-, matter-, dark energy-dominated Universe to provide insights into how initial matter perturbations grow in these periods. Here, we will simply state the result, along with the growth of the perturbations for modes that are outside the Hubble radius (super-horizon modes), which results from the relativistic perturbation theory. We note that the initial density field is not fixed, and the growth function is not independent of k for super-horizon modes.

$$\text{Sub-horizon modes} \begin{cases} \delta \propto \ln a : \text{ radiation-dominated Universe} \\ \delta \propto a : \text{ matter-dominated Universe} \\ \delta \propto const : \text{ dark energy-dominated Universe} \end{cases} \tag{2.34}$$

$$\text{Super-horizon modes} \begin{cases} \delta \propto \frac{1}{(aH)^2} \propto a^2 : \text{ radiation-dominated Universe} \\ \delta \propto \frac{1}{aH} \propto a : \text{ matter-dominated Universe} \end{cases} \tag{2.35}$$

Figure 2.6 shows the evolution of the density contrast for different fluids. The evolution of cold dark matter corresponds to our example of the non-relativistic perturbation theory

---

[2] Any Fourier mode k that has entered the horizon is independent.
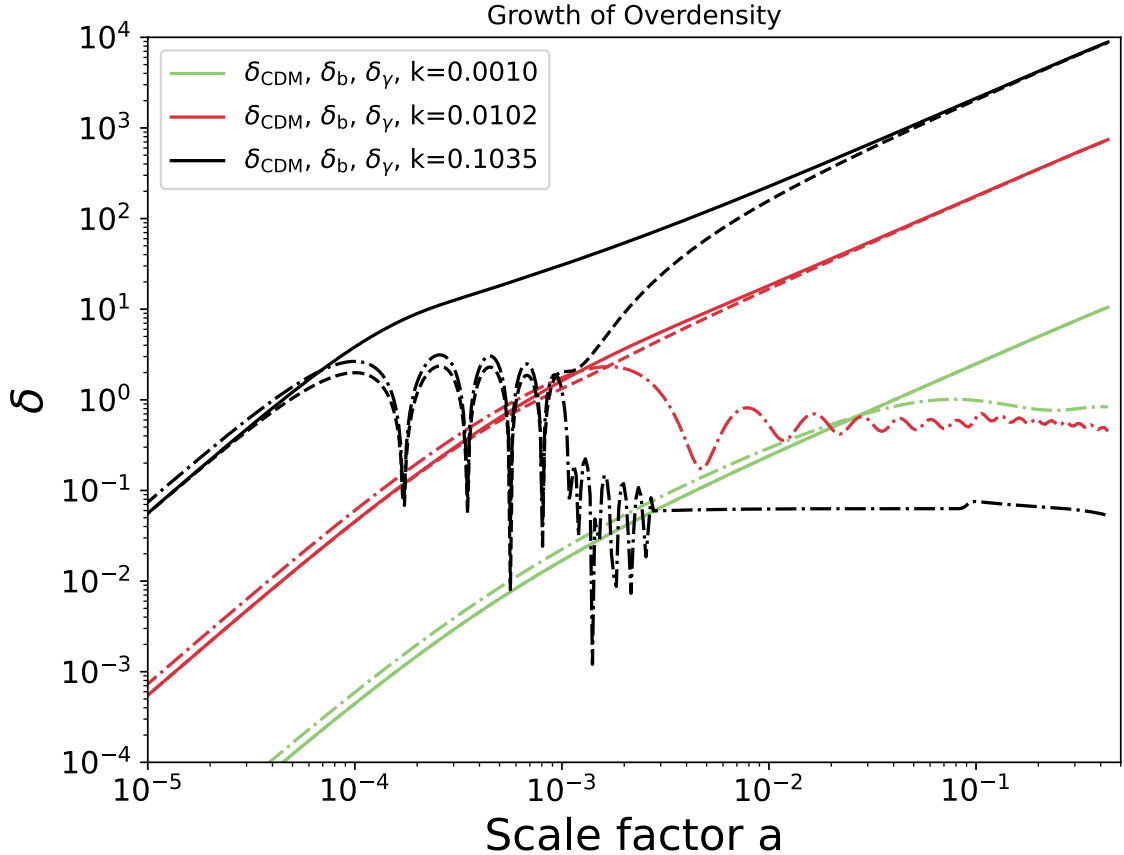
FIGURE 2.6: The growth of the density contrast of cold dark matter (δ_{CDM}), baryons (δ_{b}) and photons (δ_γ), as a function of the scale factor. Each color indicates different Fourier modes (k), and solid, dashed, dash-dot lines represent δ_{CDM}, δ_{b}, δ_γ respectively. Considering the black lines as an example, the baryon and photon densities oscillate until the photon-baryon fluid decouples and baryons follow the CDM density. This figure is produced using the numerical Boltzmann code: CAMB (Lewis et al., 2000).

of a simple fluid. It is important to note here that the growth of over-density in a matter-dominated Universe is dependent on a for all the modes and is hence independent of k. It is, however, not the case when the Universe was in a radiation-dominated Universe. In order to combine these results together to express the evolution of the initial density field $\delta(\boldsymbol{k}, t_i)$ for all the modes (sub- and super-horizon modes), it is convenient to write the equation of evolution with the transfer function $T(\boldsymbol{k})$:

$$\delta(\boldsymbol{k}, t) = \frac{D_+(t)}{D_+(t_i)} T(\boldsymbol{k}) \delta(\boldsymbol{k}, t_i), \tag{2.36}$$

where D_+ is the scale-independent growth function, and t_i denotes some time after inflation when all the modes were outside the horizon[3]. To explore $T(k)$ before and after the matter-radiation equality (a_{eq}), it is useful to separate modes that entered the horizon in the radiation-dominated era $(k > k_{eq} \equiv (aH)_{eq})$ and in the matter-dominated era $(k < k_{eq})$. For $k < k_{eq}$, since these modes were outside the horizon in the radiation era and inside the horizon in the matter era, we can write the evolution as:

$$\delta(\boldsymbol{k}, t) = \frac{a}{a_{eq}} \left(\frac{a_{eq}}{a_i} \right)^2 \delta(\boldsymbol{k}, t_i), \tag{2.37}$$

considering $\delta \propto a^2$ before a_{eq} and $\delta \propto a$ after a_{eq} for both sub- and super-horizon modes. For modes that are entering the horizon in a matter era, the transfer function is $T(k < k_{eq}) = 1$. For $k > k_{eq}$, as one can see in Figure 2.6, the time of horizon crossing (t_k) for these modes depends on the wavenumber of the mode $(k = (aH)_k)$ unlike any modes that cross the horizon in a matter era. The evolution should include the k-dependence and then

$$\delta(\boldsymbol{k}, t) = \frac{a}{a_{eq}} \ln \left(\frac{a_{eq}}{a_k} \right) \left(\frac{a_k}{a_i} \right)^2 \delta(\boldsymbol{k}, t_i) = \left(\frac{a_k}{a_{eq}} \right)^2 \ln \left(\frac{a_{eq}}{a_k} \right) \times \left[\left(\frac{a_{eq}}{a_i} \right)^2 \frac{a}{a_{eq}} \right] \delta(\boldsymbol{k}, t_i), \tag{2.38}$$

whose growth function is the same as the previous equation. Since $k = (aH)_k \propto 1/a_k$, $(a_k/a_{eq})^2 = (k_{eq}/k)^2$ and $\ln(a_{eq}/a_k) = \ln(k/k_{eq})$. Hence, $T(k > k_{eq}) = (k_{eq}/k)^2 \ln(k/k_{eq})$. These transfer functions will later be used to identify the pattern of matter power spectrum imprinted on galaxy distributions in the Universe.

With the non-relativistic perturbation theory, we have described how the density fluctuations evolve over time from an initial density field for fluids like cold dark matter (we have not treated baryons yet). We have learned that different Fourier modes evolve differently, depending on whether they are inside or outside the horizon and whether they cross the horizon before or after the matter-radiation equality. Next, we will predict what we are able to observe from the structure formation theory, given the homogeneity and isotropy.

---

[3] Before inflation, all the modes were inside the horizon and were causally connected. Inflation has made the modes to be outside the horizon.

2.3.2 Statistical Properties & Matter Power Spectrum

Given what we have learned so far, it is natural to assume the density perturbations in the Universe are correlated. This suggests that the large-scale structure of the Universe exhibits a pattern that can be studied and modeled. By analyzing the statistical properties of the density perturbations, cosmologists can gain insights into the physical processes that gave rise to the large-scale structure we observe today. We typically assume that the initial density field in the early Universe was a homogeneous and isotropic Gaussian random field due to inflation. It means that the field is *one* realization of many potential fields that can be generated by randomly sampling δ at N points from a Gaussian probability distribution with the mean $\langle\delta\rangle = 0$. The multivariate Gaussian probability density function of the density contrast at N positions is given by

$$P(\delta_1, \delta_2, ..., \delta_N) \;\; \propto \;\; \frac{1}{\sqrt{(2\pi)^N \det\{C_{ij}\}}} \exp\left\{\left(-\frac{1}{2}(\delta_i - \langle\delta\rangle)^T C_{ij}^{-1}(\delta_j - \langle\delta\rangle)\right)\right\}, \qquad (2.39)$$

where $\delta_i \equiv \delta(\boldsymbol{x}_i)$ and C_{ij} is the covariance matrix. It is important to note that $C_{ij} = \sigma^2 = \xi_{ij} \equiv \xi(|\boldsymbol{x}_i, \boldsymbol{x}_j|)$ for a Gaussian random field, where the variance of the field is σ^2 and ξ is the correlation function of the density at two points. No correlation of the density at N points means the generated field is random, and the correlated density means some structures appear in the Gaussian random field. A great feature of a Gaussian random field is that the mean and the two-point correlation function can completely describe the statistics of the field. A non-trivial statistical description of our cosmic density field would then be the two-point correlation function.

Given the homogeneity and isotropy conditions, the two-point correlation function of the density field can be written as an ensemble average of the correlation at different parts of the Universe (ergodicity).

$$\xi(r) \equiv \langle\delta(\boldsymbol{x})\delta(\boldsymbol{x}')\rangle, \qquad (2.40)$$

where $r \equiv |\boldsymbol{x} - \boldsymbol{x}'|$ and $\langle\rangle$ denotes the ensemble average. The two-point function in Fourier

space is then,

$$\langle \widetilde{\delta}(\boldsymbol{k})\widetilde{\delta}^*(\boldsymbol{k}')\rangle = \int d^3x d^3x' e^{-i\boldsymbol{k}\cdot\boldsymbol{x}} e^{i\boldsymbol{k}'\cdot\boldsymbol{x}'} \langle \delta(\boldsymbol{x})\delta(\boldsymbol{x}')\rangle$$

$$= (2\pi)^3 \delta_D(\boldsymbol{k} - \boldsymbol{k}') \int d^3 r e^{-i\boldsymbol{k}\cdot\boldsymbol{r}} \xi(r) \tag{2.41}$$

$$\equiv (2\pi)^3 \delta_D(\boldsymbol{k} - \boldsymbol{k}') P(k),$$

where $P(k)$ is the Fourier transform of the correlation function $\xi(r)$ and referred to as the power spectrum. As long as the evolution is linear (first-order approximation), the grown field is also Gaussian, and hence, the large-scale pattern of our late-time Universe with galaxies can be characterized by the power spectrum while the amplitude grows. From Eqn. 2.36, we can write the evolution of the power spectrum as,

$$P(k,t) = T^2(k)\frac{D_+^2(t)}{D_+^2(t_i)}P(k,t_i). \tag{2.42}$$

It is generally assumed that the primordial power spectrum is a power law and can be written as,

$$P(k,t_i) = A_s k^{n_s}, \tag{2.43}$$

where A_s is the amplitude of the spectrum and n_s is called the spectral index with $n_s \sim 1$. This primordial spectrum is called the Harrison-Zel'dovich spectrum.

If we recall the transfer function with Fourier modes k before and after $k_{\rm eq}$, we can predict the k-dependence of the matter power spectrum.

$$P(k,t) \quad \propto \quad \begin{cases} k^{n_s} & k < k_{\rm eq}, \\ k^{n_s-4}\ln{(k/k_{\rm eq})^2} & k > k_{\rm eq} \end{cases} \tag{2.44}$$

Figure 2.7 shows that the k-dependence of the primordial power spectrum is suppressed during the radiation era. The overall spectrum amplitude grows, which is parametrized by a normalization parameter (σ_8 – root-mean-square of overdensity fluctuations averaged in spheres of the comoving radius of 8 Mpc/h) defined with

$$\sigma_8^2 = \frac{1}{2\pi^2}\int W_s^2 k^2 P(k)dk, \tag{2.45}$$

where W_s is the tophat-filter function

$$W_s = \frac{3j_1(kR_8)}{kR_8}. \tag{2.46}$$

Although theory predicts the shape of $P(k)$ and does not predict σ_8 at present-day, it is an important parameter to learn about the large-scale galaxy clustering in the late-time Universe, and it can be included in our cosmological model. Additionally, while the two-point correlation function of the density field from luminous matter (e.g., galaxy clustering) is an obvious observable, this is not fully representative of the total matter density because we would be only looking at baryons. Some of these observables are called biased tracers of the total matter distribution – dark matter, and we must be careful not to produce biased results when analyzing these data. As we will discuss in § 2.4.6, we are able to infer dark matter distribution through weak gravitational lensing more directly.

In order to make an accurate theory prediction of $P(k)$ (not from our simplistic non-relativistic perturbation theory), it is necessary to compute an accurate transfer function and growth function. One needs to solve for the Boltzmann equation, which describes the joint evolution of the initial perturbations of the fluids (baryons, dark matter, photons, neutrinos) in the Universe at a particle species level for a given cosmology. This was first computed accurately by Bond and Szalay, 1983, and since then, the solutions have incorporated the effects such as the photon-baryon coupling and free-streaming neutrinos. For the recent cosmological observations, it is usually computed using the numerical Boltzmann codes such as CMBFAST (Seljak and Zaldarriaga, 1996), CAMB (Lewis et al., 2000) and CLASS (Lesgourgues, 2011). As we will explore more later, this photon-baryon coupling in the early Universe generated the oscillatory behavior in the density contrast (Fig. 2.6) and left an imprint in the galaxy distribution.

We have discussed the structure formation in the regime in which the density perturbations are small ($|\delta| \ll 1$) and the linear evolution with which the statistics are still Gaussian. On the smallest scales, however, gravitational effects become significant, and the structure formation process becomes highly nonlinear. Eventually, the density perturbation
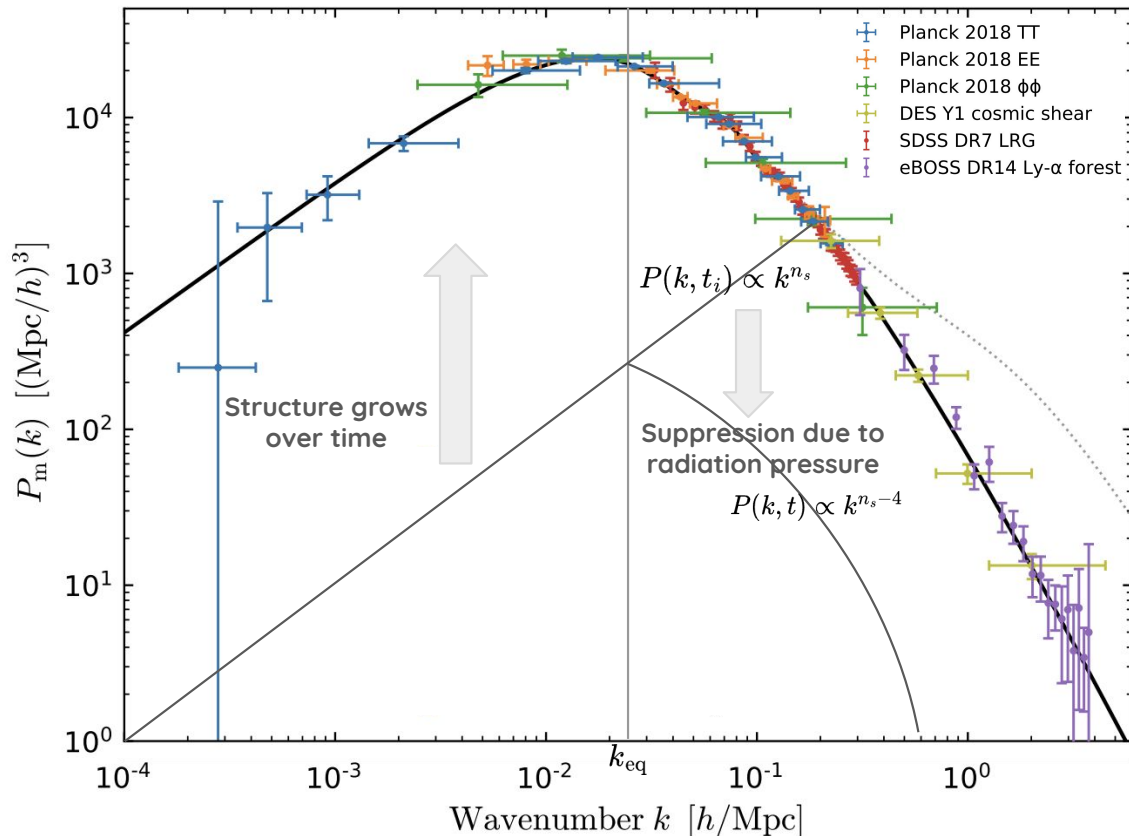
FIGURE 2.7: Schematic diagram of the evolution of the linear matter power spectrum overlaid with the observed matter power spectrum from various observations. While the dotted line represents a model with nonlinear effects, this is not an indication of data preferring linear evolution. Instead, the data are translated to fit the linear model, ignoring the nonlinear contribution. The diagram is adapted from Figure 15 in Peacock and Heymans, 2009, and the figure is adapted from Figure 1 in Chabanier et al., 2019.

amplitude grows to $\delta \sim 1$, and the matter distribution becomes non-Gaussian. While this non-Gaussianity has a significant impact on the predicted matter power spectrum, analytically computing the impact is challenging. The use of N-body simulations, which can characterize the nonlinear growth for varying cosmologies, is a common approach. Requiring the N-body simulations to account for gravity and other hydrodynamics, as well as generating a large volume of the result to be a representative of the real Universe, is computationally expensive. We will discuss this further in § 4.2.7.1 and § 5 with the example of how the Dark Energy Survey treats the nonlinear part of the matter power spectrum.

2.3.3 Λ-CDM Cosmological Model

Through various observational evidence (which we will discuss in § 2.4), we have a good but not complete description of our Universe. The current most-acknowledged model of the Universe includes cold dark matter and dark energy (cosmological constant) along with ordinary matter, neutrinos, and photons. This model is called Λ-CDM (Λ: cosmological constant, CDM: cold dark matter), and the evolution of the Universe in the model can fit our observations well.

2.4 Observational Cosmology

Up to this point, we have discussed the theory of the origin of the Universe, what components might be at play, and how the primordial density fluctuations might have evolved to generate the structure in the Universe. The theory of cosmological physics has been refined with observational evidence for more than 100 years, and it is not yet complete. New observations from powerful modern telescopes with state-of-the-art technologies can test the theory and provide evidence for new physics. In this section, we will first review a few principles of observational cosmology, including how to infer cosmological parameters and how to interpret results carefully. We will then briefly mention the kinds of "surveys" from which to extract cosmological information and finally explore several probes we observe to understand the history and the structure of growth in the Universe. A more complete discussion of observational probes of dark energy can be found in Weinberg et al., 2013.

Before we advance, let's briefly review what we call "cosmological parameters" that constrain the model of the Universe and that describe our current late-time Universe. We should note here that not all the parameters are required to fit a particular observation – only six parameters (the first group in Table 2.1) are necessary to describe the Λ-CDM model. Because some parameters are degenerate with others, depending on the observable, other parameters can be recast from the six parameters to better describe what each data set is able to constrain in the model. In order to learn what cosmological model describes observations well, we commonly use summary statistics (e.g., matter power spectrum) that

Table 2.1: A list of cosmological parameters that can describe the origin and the evolution of the Universe. The values are from Planck Collaboration, Aghanim, et al., 2020.

Parameter	Description	Value
A_s	scalar amplitude	$(2.098 \pm 0.023) \times 10^{-9}$
n_s	scalar spectral index	0.965 ± 0.004
Ω_{baryon}	amount of ordinary matter (baryons)	0.049 ± 0.001
Ω_{matter}	amount of total matter	0.315 ± 0.007
Ω_{Λ}	amount of dark energy	0.685 ± 0.007
τ	optical depth	0.054 ± 0.007
w	dark energy equation-of-state	-1.03 ± 0.03
σ_8	clustering amplitude	0.811 ± 0.006
H_0	Hubble constant	67.4 ± 0.5

encode cosmological information. For each set of cosmological parameters, there is a cosmological model and summary statistics we are interested in. We essentially compare the theoretical predictions of the summary statistics and the value from observations to determine what cosmological parameters fit the observations well. This is a very simplified description of how we measure cosmological parameters from cosmological observations. More details can be found in § 2.4.1.

2.4.1 Parameter Inference

2.4.1.1 Bayesian Analysis

In cosmology, the inference of parameters that describe the Universe's structure and evolution is crucial for understanding fundamental phenomena such as dark energy, dark matter, and the rate of cosmic expansion. Among the various statistical methods utilized in this field, Bayesian parameter inference and Markov Chain Monte Carlo (MCMC) techniques are quite useful for their robustness and efficacy in handling complex datasets and multi-dimensional parameter models. Full details can be found in Trotta, 2017.

Bayesian inference provides a powerful framework for the analysis of cosmological data. This approach updates the probabilities for a hypothesis as more evidence or information becomes available. It starts with a prior probability $P(\theta)$, which expresses what is known about the parameters before the data are examined. Here, θ represents the cosmological

parameters of interest. The likelihood function, $P(D|\theta)$, models how probable the observed data D are, given specific values of the parameters. Bayesian inference combines these elements through Bayes' theorem to produce the posterior distribution:

$$P(\theta|D) = \frac{P(D|\theta)P(\theta)}{P(D)}. \tag{2.47}$$

This equation shows that the posterior distribution $P(\theta|D)$ is proportional to the product of the likelihood and the prior, normalized by the evidence $P(D)$, which acts as a scaling factor ensuring that the posterior distribution sums to one. The likelihood is determined by comparing D against the theoretical prediction of the quantity from a cosmological model that is determined by a set of parameters θ. Assuming the measurement of the parameters is Gaussian-distributed, the likelihood function can take the form:

$$P(D|\theta) = \frac{1}{(2\pi)^{m/2}|C|^{1/2}} \exp\left\{-\frac{1}{2}(D - M(\theta))^T C^{-1} (D - M(\theta))\right\}, \tag{2.48}$$

where m is the number of parameters (determines the number of dimensions), C is the covariance matrix of data, and $M(\theta)$ is the model given a set of parameters. As long as C can be determined analytically or from numerical simulations (which will be the subject in § 4.2.7), one can construct and determine the confidence region of the multidimensional parameter space by repeating the computation of the likelihood function with different sets of parameters.

In modern cosmological analysis, the dimensionality of the parameter space can exceed 30 since we include not only the cosmological parameters of interest (less than 10) but also parameters related to calibrating measurement-related biases and modeling astrophysics, which results in the joint posterior distribution. We include them in our likelihood function because we could be over- and under-correcting the systematic biases depending on how well we know them. Since we are often only interested in the posterior distribution of the cosmological parameters, we compute it by integrating the joint distribution over the probability of the possible values of these so-called "nuisance" parameters. This process,

known as "marginalization," compresses the original multidimensional parameter space into the parameter space of interest.

2.4.1.2 Markov Chain Monte Carlo (MCMC)

Methods like Markov Chain Monte Carlo (MCMC) are useful and extensively employed to compute the Bayesian posterior distribution, especially when dealing with multiple parameters. Several packages such as EMCEE[4] (Foreman-Mackey et al., 2013) are helpful in implementing MCMC in one's analysis even outside cosmology. In short, in the MCMC process, multiple "samplers" (also referred to as "walkers")start from arbitrary points in multidimensional parameter space and move through the space in a way that mimics a random walk, typically using the Metropolis-Hastings algorithm. There are many literatures that have explored different sampling algorithms (i.e., how samplers advance to the next points efficiently and reach convergence) and we will only mention the commonly-used ones: MULTINEST (Feroz et al., 2009), POLYCHORD (Handley et al., 2015), and NAUTILUS (Lange, 2023).

The synergy of Bayesian inference and MCMC methods allows cosmologists to efficiently navigate the vast parameter spaces inherent in their models, dealing effectively with the uncertainties and complexities of observational data. As a result, these techniques have become foundational in unraveling the Universe, providing insights that are as profound as they are precise.

2.4.2 Statistical vs Systematic Uncertainties

The cosmological parameters we infer always have an associated error – no measurements are perfect. There are two primary types of uncertainties: statistical and systematic. Each plays a distinct role and must be carefully considered and managed to ensure robust results.

Statistical uncertainties arise from the inherent randomness in the observational data and are often referred to as "noise". These uncertainties are associated with the finite number of observations or the sampling variability that occurs when measuring observables.

---

[4] https://emcee.readthedocs.io/en/stable/

Statistical uncertainties can often be reduced by increasing the sample size—observing more galaxies or collecting more data over a larger area of the sky. The central limit theorem supports this approach, as it predicts that the mean of a sufficiently large number of independent random variables, regardless of distribution, will be approximately normally distributed. This makes the inference about the mean more precise.

Systematic uncertainties, on the other hand, stem from errors in the measurement process that can bias the results and are often referred to as "bias". These errors can be introduced through inaccuracies in instrument calibration, data processing algorithms, or modeling assumptions used in the analysis. Unlike statistical errors, systematic uncertainties do not decrease with larger data sets and require careful calibration, sophisticated modeling, and rigorous validation to identify and correct.

In cosmological parameter inference, achieving high precision (minimizing statistical uncertainty) and high accuracy (minimizing systematic uncertainty) is crucial. With the arrival of future telescopes such as the Rubin Observatory (Ivezić et al., 2018), systematic errors will likely be more significant than statistical errors. In order to understand the correct nature of the Universe, we must be able to control and correct for systematic errors. Moreover, quantifying both types of uncertainties is essential for the reliable interpretation of results. This involves using statistical methods to estimate the confidence intervals and performing robustness checks against various systematic issues. Only by thoroughly understanding and mitigating these uncertainties can cosmologists ensure that their inferences about the Universe are both accurate and reliable.

2.4.3 Spectroscopic and Photometric Surveys

Here, we briefly review the advantages and disadvantages of spectroscopic and photometric surveys in order to understand how the cosmological observations are carried out.

2.4.3.1 Spectroscopic Surveys

A spectroscopic survey measures the spectra of objects, such as stars and galaxies, across the sky. By analyzing the spectra, it reveals detailed information about an object's

color, distance, and motion. Cosmologically, we are interested in each object's redshift estimate to, for example, determine how far a supernova is or measure an accurate correlation function along the line-of-sight. These spectroscopic redshifts (spec-z) can also function as a calibration/training set for estimating redshifts from broad photometric bands. Despite these advantages, the number of objects that can be observed per night is a lot more limited than the objects that can be detected from astronomical images due to the available light being dispersed across a large range of wavelengths, requiring longer observing times to reach the same S/N.

2.4.3.2 Photometric Surveys

A photometric survey is probably more familiar to non-astronomers – essentially taking pictures with a camera. It measures the intensity of light from objects in multiple wavelength bands (Figure 2.8). Through the analysis of light distribution and color from images in each photometric band, photometric surveys are still able to estimate objects' redshifts (photo-z) over a few bandpasses, though not nearly as precisely as their spectroscopic counterparts in terms of spectral information. The main advantage of a photometric survey is its ability to cover vast areas of the sky efficiently. It is able to take multiple images every night on which we detect stars and galaxies and the number of objects ensures we are not limited by the cosmic variance and is appropriate to study the Universe's structure on a grand scale. A trade-off for a wide area coverage is the depth of the survey. As we increase the survey's depth by either extending the exposure time or stacking more images to reduce noise, we can detect fainter galaxies, resulting in a greater number of objects. The area will, however, be compromised. The choice of the number of bandpasses is also key in successfully reducing systematic biases such as the estimation of photo-z. Table 2.2 presents the current and future photometric surveys with their expected area coverage, depth, and photometric bandpasses.
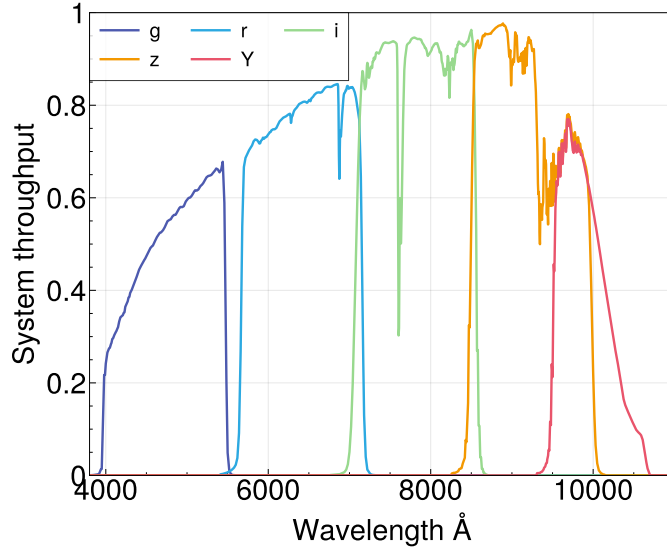
FIGURE 2.8: An example of Dark Energy Camera's photometric bandpasses and their throughputs as a function of incident ray wavelength.

2.4.4 The Cosmic Microwave Background

As discussed earlier, the cosmic microwave background (CMB) is the free-streaming photons that were able to escape without scattering as the Universe expanded and cooled down. Measuring the temperature and polarization of these background photons can provide us with very rich information about the early Universe. While the mean temperature

Table 2.2: A list of current and future photometric surveys, coverage area, depth, and bandpasses. Depth is written in terms of the 5σ point source depth in r-band AB magnitude for ground-based surveys and H-band for space-based surveys. KiDS: Kuijken et al., 2015, DES: DES Collaboration et al., 2021, HSC: Aihara et al., 2018, Euclid: Scaramella et al., 2022, LSST: Ivezić et al., 2018, Roman: Doré et al., 2018

Survey	Area (deg^2)	Bands	Num. of Galaxies ($\times 10^6$)	Depth
KiDS	1,500	*ugri*	100	25.0
DES	5,000	*grizY*	540	24.4
HSC	1,400	*grizY*	400	26.5
Euclid	14,700	*R+I+Z, Y, J, H*	1,500	24.0
LSST	20,000	*ugrizY*	4,000	27.5
Roman	2,000	*Y106, J129, H158, F184*	500	26.6
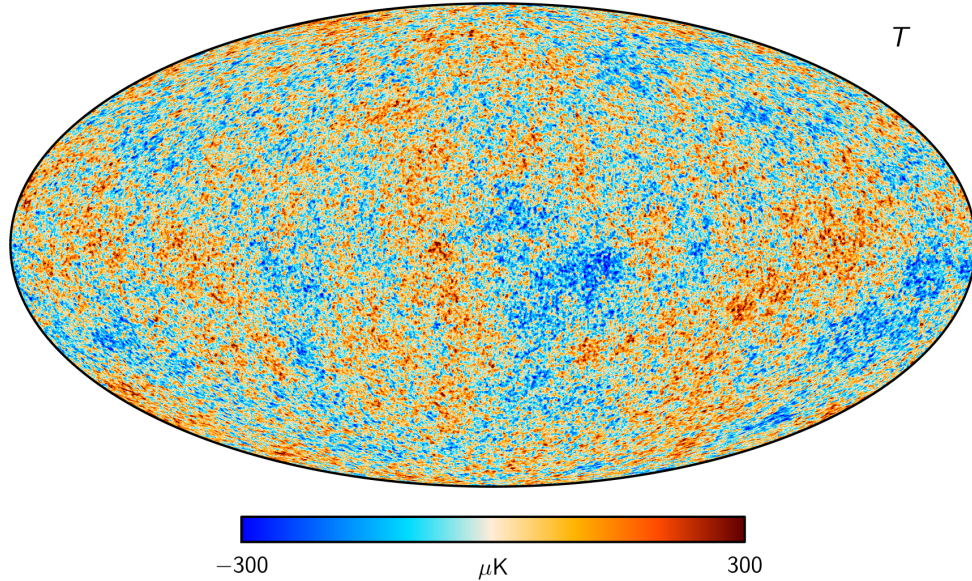
FIGURE 2.9: The map of the temperature fluctuations of the CMB ($T - \langle T \rangle$). Figure G.6 from Planck Collaboration, Akrami, et al., 2020.

of the CMB is $T = 2.73K$, observations show slight deviations from the mean (Figure 2.9), and this holds the key to understanding the primordial density fluctuations that originated from quantum fluctuations due to inflation.

2.4.4.1 Power Spectrum of the CMB Anisotropy

What we can measure from the temperature map is the two-point correlation of these temperature fluctuations (CMB temperature anisotropies). We can predict the power spectrum very well from the theory because the early Universe can be characterized by linear perturbation. Figure 2.10 shows the power spectrum with the best-fit theoretical prediction of the cosmological model. We now discuss how one can predict the power spectrum of the CMB anisotropies.

As usual, one can aim to compute the transfer function that captures the evolution of the primordial fluctuations before decoupling and the free-streaming photons after decoupling. We will only present the summary here, but curious readers who would like to follow the derivation should read §7.2 to §7.4 of Baumann, 2022. By considering the tightly-coupled photon-baryon fluid before decoupling as a single fluid, we can derive the second-order
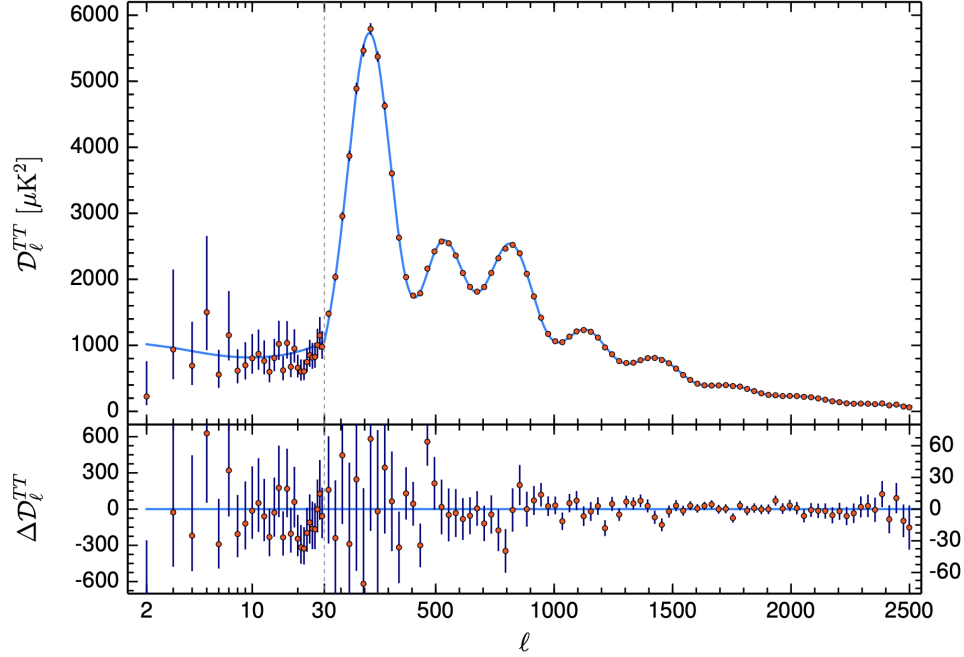
FIGURE 2.10: The temperature power spectrum from Figure 1 in Planck Collaboration, Akrami, et al., 2020. The best-fit Λ-CDM cosmology prediction is shown as a solid line. The bottom panel shows the residual of the data and model.

equation of the photon density contrast with hydrodynamics and write the solution for two ranges of Fourier modes ($k < k_{eq}$ and $k > k_{eq}$). After decoupling, the free-streaming photons encounter gravitational potential in the inhomogeneous Universe and gain or lose energy. The observed temperature anisotropies therefore depend on the photon density fluctuations and the baryon velocity at last-scattering, and the gravitational potentials along the line-of-sight. These fluctuations can be directly related to the transfer function in Fourier space. If we combine these two sources of the CMB temperature anisotropies before and after decoupling, we are able to predict the observed power spectrum. From the positions and amplitudes of the peaks in the power spectrum, we can estimate the distance to the surface of the last scattering and relative energy density associated with baryonic and dark matter, photons, curvature, and dark energy.

2.4.4.2 Major Challenges

In the late-time Universe, the structures can affect the measurement of the photon temperature as foregrounds. The origins of these foregrounds are miscellaneous – for example, interstellar dust, synchrotron radiation within our galaxy, and galaxy clusters in the line-of-sight. These foregrounds are typically measured with detectors at multiple frequencies. When the cosmological analysis is performed, these foregrounds are removed from the raw temperature map to produce the systematics-free temperature fluctuation map.

2.4.4.3 Other CMB Observables

Some of these foregrounds can, however, be taken advantage of to understand the late-time Universe. For example, through the Sunyaev-Zel'dovich effect (SZ effect (Sunyaev and Zeldovich, 1970): inverse Compton scattering of the CMB photons by high-energy electrons in galaxy clusters results in the increase/decrease of photon energy), galaxy clusters can be identified (Carlstrom et al., 2002).

Another main CMB observable that is frequently used together with the temperature map is the polarization of the CMB photons. We often call the temperature anisotropy the primary anisotropy and the polarization anisotropy the secondary anisotropy. Polarization describes the orientation of light perpendicular to the direction of the light propagation. Due to the Thomson scattering and density perturbations at the last-scattering, the CMB polarization is predicted to have a particular pattern called E-mode (Figure 2.11). The E-mode map of the polarization and temperature map are auto- and cross-correlated to produce a tighter constraint on cosmological parameters. We mention that there are many collaborative efforts that look for the B-mode signal in the polarization that is predicted to be produced from the primordial gravitational waves from the period of inflation.

Lastly, let's discuss the effect of gravitational lensing on the CMB photons (for a full review, please refer Lewis and Challinor, 2006). The idea is that as the CMB photons propagate through the Universe, they encounter gravitational potentials, and the paths of the photons are deflected and distorted as predicted by GR (called gravitational lensing). This
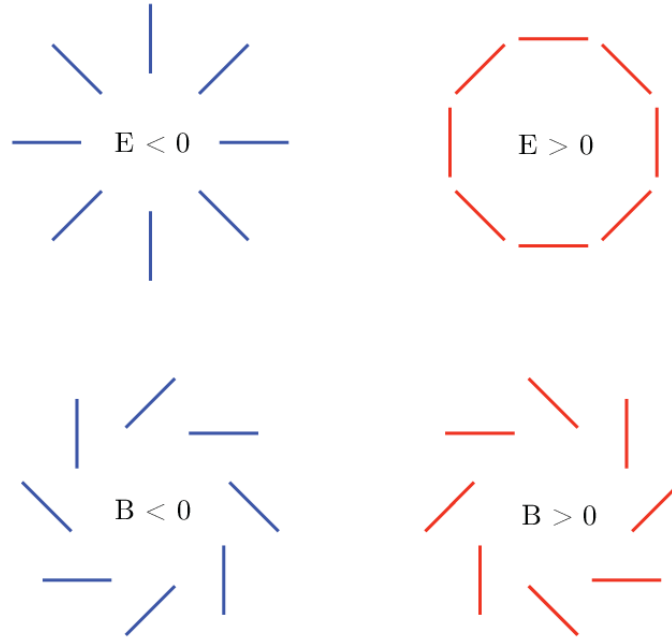
FIGURE 2.11: Example of E-mode and B-mode patterns. Figure 4 in Baumann et al., 2009

lensing effect leaves subtle imprints on the temperature and polarization signal and can be used to learn about the integrated distribution of the potentials (i.e., matter distribution). This lensing power spectrum provides complementary information to the power spectrum of the primary and secondary anisotropy and can break parameter degeneracy in a cosmological analysis. It is, however, worth noting that the B-mode polarization signal produced from CMB lensing can contaminate the primordial B-mode signal from early time.

2.4.4.4 The Frontiers of the CMB Cosmology

Since the first detection of CMB (Penzias and Wilson, 1965), space-based observation such as the Cosmic Background Explorer (COBE: Bennett et al., 1996) and the Wilkinson Anisotropy Probe (WMAP: D. N. Spergel et al., 2003), and the ground-based observations such as the South Pole Telescope (SPT) and Atacama Cosmology Telescope (ACT) have provided measurements of the temperature and polarization anisotropy at high resolution and precision. The most constraining result is currently the results from Planck 2020 (Planck Collaboration, Aghanim, et al., 2020), in which the scalar spectral index is measured

to be $n_s < 1$ at 8σ precision and the Universe is spatially flat to 1σ. Other parameters with Planck 2020 can be found in Table 2.1. One may notice that the errors on the parameters are very small.

As one of the next-generation CMB observatories, Simons Observatory (Ade et al., 2019) is expected to have ten times the sensitivity of the detectors and five times the angular resolution of the *Planck* satellite. Another main next-generation experiment, CMB-S4 (Abazajian et al., 2016), is planned to install over 500,000 detectors on 12 telescopes at the South Pole and in the Atacama desert in Chile. With these new experiments that have much-improved sensitivity and angular resolution, cosmologists will look to constrain things like the signature of inflation with the polarization and the neutrino mass scale.

2.4.5 Baryon Acoustic Oscillations (BAO)

As one can see in Fig. 2.6, the oscillatory behavior of the density contrast in the early Universe was caused by the tight coupling of photons and baryons. After baryons decouple from photons as the Universe cooled down, baryons began to follow the gravitational potential made by dark matter, which was able to evolve earlier because dark matter only interacts via gravity. This acoustic oscillation of the density contrast of the baryons left an imprint in the galaxy distribution. This can be seen as a sinusoidal wave in the power spectrum and a bump in the two-point correlation function (Figure 2.12). The angular position of the BAO peak (θ_d) is around 110 h^{-1}Mpc and is sensitive to the size of the sound horizon (r_d: also known as the acoustic scale at the surface of the last scattering) and angular distance ($D_A(z)$, similar to luminosity distance). The acoustic scale can be used as a standard ruler and is well-determined by CMB, and one is able to measure cosmological parameters such as the expansion rate of the Universe and the curvature of the Universe (e.g., Aubourg et al., 2015).

2.4.6 Weak Gravitational Lensing

As mentioned previously, GR predicts how masses curve the space-time geometry. If one is to observe a galaxy (source) far away and there is a large gravitational potential,
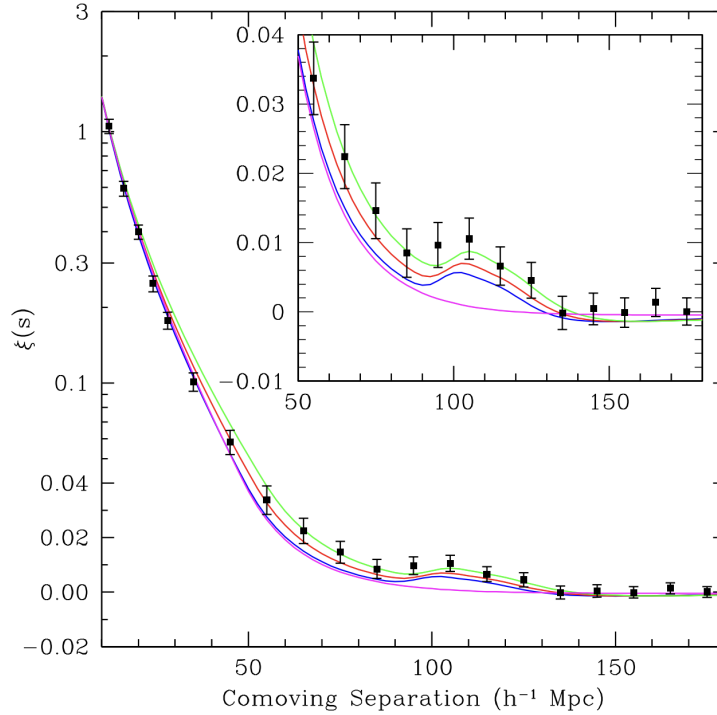
FIGURE 2.12: The correlation function of a sample of luminous red galaxies in the Sloan Digital Sky Survey (York et al., 2000). Different color lines show different cosmological models. Figure 2 in Eisenstein et al., 2005.

the path of the photons from the source is not straight anymore. The curved space-time acts like a lens, and the photons follow the null geodesics. Depending on the masses of the gravitational potential and the geometry of the observer-lens-source system, the following can happen to the image of the source due to deflection and distortion:

- The apparent position of the source changes
- The apparent size and brightness of the source changes (i.e., convergence and magnification)
- The apparent shape of the source changes (i.e., shear).

This is called the gravitational lensing. A simple illustration of the gravitationally-lensed system is shown in Figure 2.13. Using this phenomenon, we are able to study the geometry and structure of the Universe.

Depending on the magnitude of the apparent changes in the source property, we classify

39
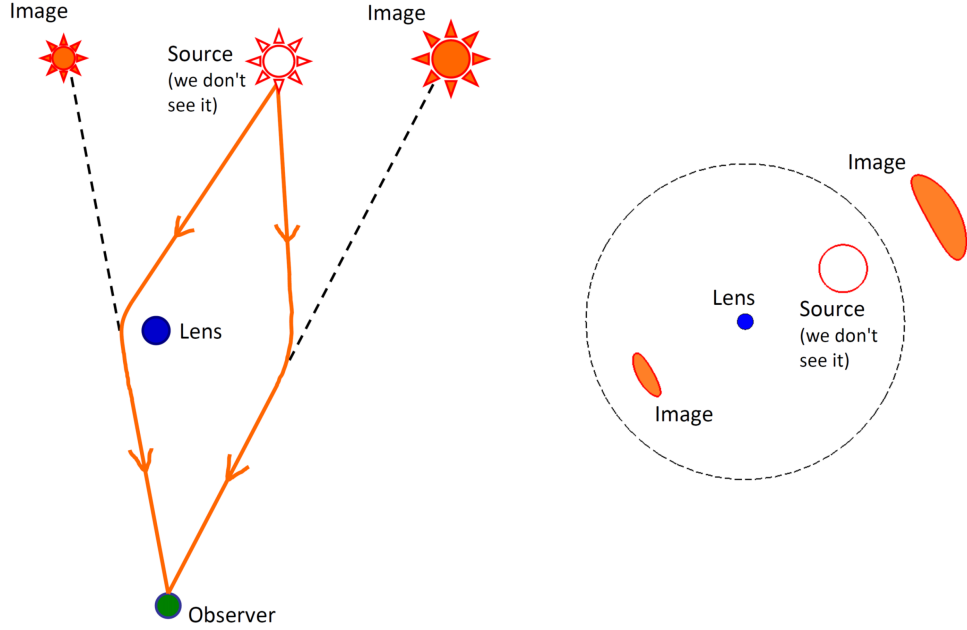
FIGURE 2.13: A schematic diagram of the gravitationally lensed system. Figure 2 in Bisnovatyi-Kogan and Tsupko, 2017. Reproduced under the terms and conditions of the Creative Commons Attribution (CC BY) license.

the gravitational lensing into weak gravitational lensing and strong gravitational lensing. In the limit of weak lensing (which will be discussed further in § 3), though the distortion of shapes and sizes is considered small, the dark matter overdensity field induces coherent distortions to the light rays of background galaxies, which can be statistically observed over many galaxies. The coherent distortion of galaxy shapes due to the matter density is called cosmic shear. The coherent distortion suggests that the correlation of galaxy shapes directly relates to the dark matter density field along the line-of-sight (Figure 2.14). As we will study further in § 3, the two-point correlation function of galaxy shapes is associated with the matter power spectrum and, hence, the direct measurement of the matter distribution in the Universe. Cosmic shear is such a powerful probe because it is a mostly unbiased tracer of dark matter distribution, unlike the correlation function of galaxy positions. While it is a probe of both the geometry of the Universe (e.g., H_0) due to the observer-lens-source system and the structure growth (e.g., Ω_m, σ_8), the projection of the galaxy shapes onto
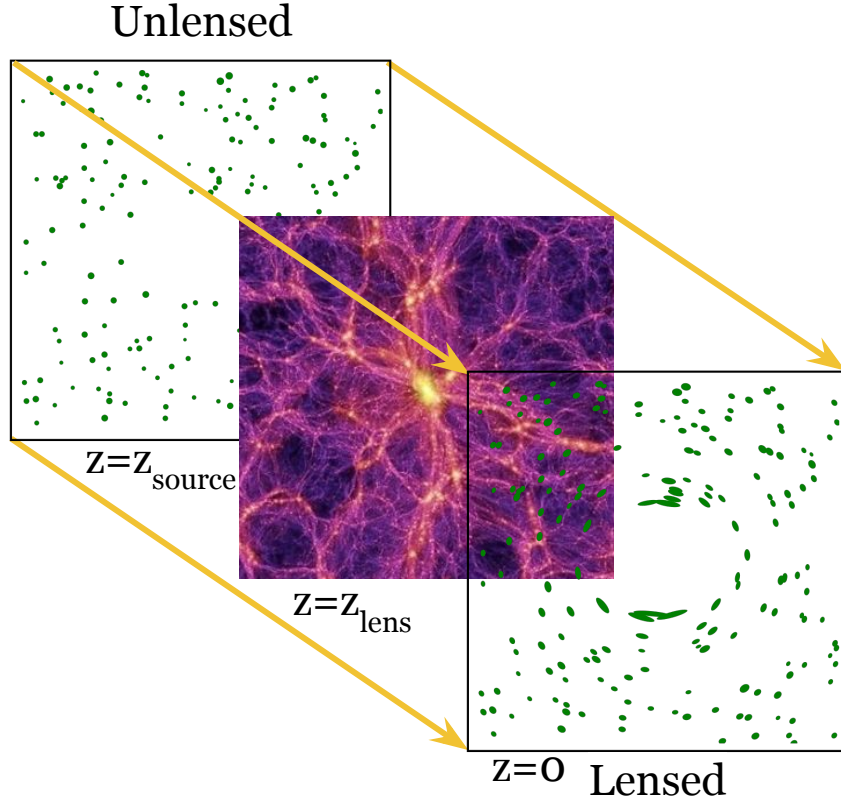
FIGURE 2.14: A schematic illustration of unlensed and gravitationally-lensed galaxy distribution and shapes (visualized by Jim Bosch) caused by the large-scale structure (Millenium simulation Springel et al., 2005). Gravitational lensing produces coherent distortions and hence leads to positive correlations between the shapes.

the sky plane reduces the sensitivity to the parameters regarding the geometry.

If the shapes of background galaxies are distorted by the dark matter distribution in which foreground galaxies are situated[5], one would expect that the shapes of background galaxies are correlated with foreground galaxy positions. This is known as galaxy-galaxy lensing (GGL). However, since galaxies (luminous matter) are the biased tracer of dark matter distribution, the observed matter power spectrum needs to account for the bias known as galaxy bias, which is shown below.

$$P_\delta = b_g^2 P_{\text{galaxy}} \tag{2.49}$$

b_g arises due to astrophysical processes in the late-time Universe such as baryonic feedback

[5] We believe that the galaxies are formed in the center of dark matter halos.

41
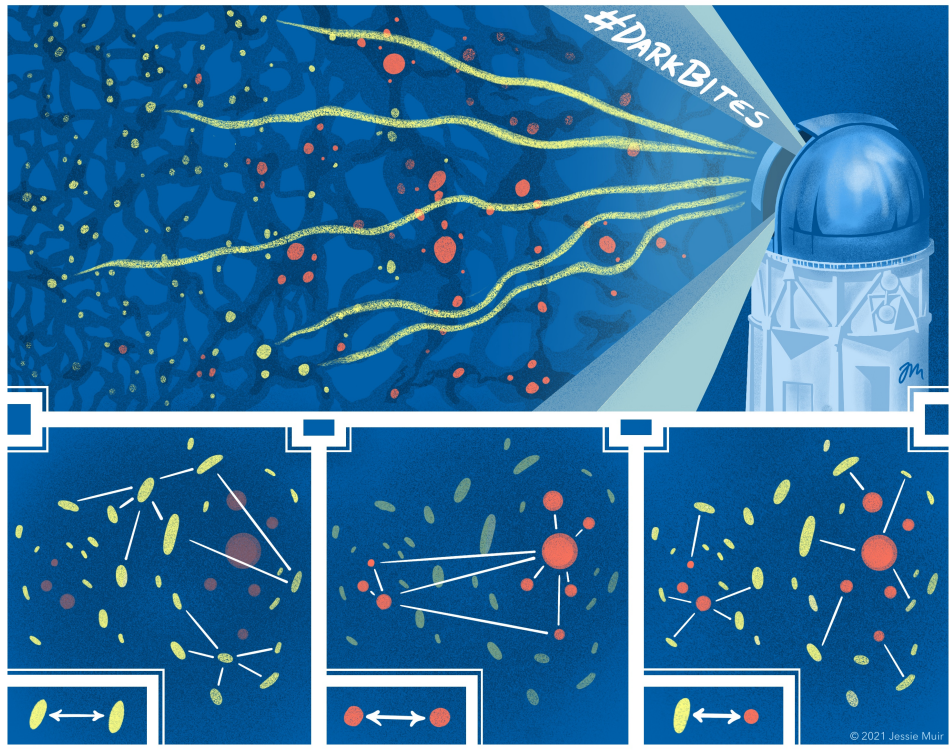
FIGURE 2.15: A schematic illustration of 3x2pt analysis – cosmic shear, galaxy-galaxy lensing, galaxy clustering. *Left*: cosmic shear, *Middle*: galaxy-galaxy lensing, *Right*: galaxy clustering. *Image credit: Jessie Muir*

process, which expels gas from galaxies by star formation, supernovae, and active galactic nuclei (AGN), and suppresses the formation of matter clustering. The theoretical modeling of these astrophysical processes is known to be difficult and we frequently fit and determine b_g using the combination of galaxy-galaxy lensing and the two-point correlation function of galaxy positions (galaxy clustering). The combined analysis of GGL and galaxy clustering is called the 2x2pt analysis, and one can add cosmic shear to perform the 3x2pt analysis, which further constrains cosmological parameters.

2.4.6.1 Major Challenges in Weak Lensing

While these probes are powerful in understanding the structure of the growth, the measurements are systematically dominated for various reasons. We can categorize the challenges in the weak lensing analysis to be – survey-limited, measurement-limited, and

theory-limited. One of the main assumptions in cosmic shear is that over a sufficiently large sample of galaxies, the intrinsic galaxy shapes (before shapes are distorted) average to zero. In practice, we have a finite number of galaxies in a survey, and they do not exactly average to zero (known as shape noise), and this increases the uncertainty of the inferred cosmological parameters. This is one of the survey-limited errors that should improve with future telescopes.

The observables of the cosmological analysis with weak lensing are the galaxy position, redshift, and ellipticity. The fact that our galaxies are noisy, faint, and pixellated and that our measurement methods are not perfect point to various measurement-related systematics. We will review these observational systematics in § 4

Even if one measures these galaxy properties perfectly, one is required to model the summary statistics (i.e., matter power spectrum) up to scales where nonlinear effects are relevant. As discussed before, this is a complicated subject requiring the treatment of baryons in hydrodynamics, and it requires an understanding of how galaxies are aligned themselves (intrinsic alignments) as well. We will further study the modeling systematics in § 4.

2.4.6.2 The Frontiers of the Weak Lensing Cosmology

Since the first detection of galaxy-galaxy lensing (Brainerd et al., 1996) and cosmic shear (Bacon et al., 2000; Kaiser et al., 2000; Van Waerbeke et al., 2001; Wittman et al., 2000) two decades ago, several early cosmological analyses have been performed in various surveys (VIRMOS-Descart: Van Waerbeke et al., 2005, CTIO: Jarvis et al., 2006, and COSMOS: Massey, Rhodes, et al., 2007; Schrabback et al., 2007). These surveys are defined as the Stage-I survey in the language of the Dark Energy Task Force (Albrecht et al., 2006). The Stage-II surveys are Science Verification (SV) results from the Dark Energy Survey (Abbott et al., 2016), the Deep Lens Survey (DLS: Jee et al., 2016), and the Candada-France-Hawaii Telescope Lensing Survey (CFHTLenS; Heymans et al., 2013; Kilbinger et al., 2013), which provided the first interesting cosmological constraints from weak lensing.

We are almost at the end of the Stage-III surveys with the Kilo-Degree Survey (KiDS: Kuijken et al., 2015), Hyper Suprime-Cam Subaru Strategic Program (HSC: Aihara et al., 2018) and the Dark Energy Survey (DES: Flaugher et al., 2015). The current state-of-the-art of these surveys is reported in Figure 2.16 with *KiDS-1000*: Heymans et al., 2021, *DES-Y3*: DES Collaboration et al., 2022, and *HSC-Y3*: Miyatake et al., 2023. One of the parameters (S_8) is defined in order to break the degeneracy between Ω_m and σ_8 –

$$S_8 \equiv \sigma_8 (\Omega_m/0.3)^{0.5}. \tag{2.50}$$

It is important to note here that the direction of degeneracy depends on the probes, and the exponent can be optimized for each probe.

These recent observations of the late-time Universe have hinted to us a lower value of S_8 compared to the observations of the early-time Universe, such as CMB. While this is often referred to as S_8 tension, the difference is, at most, a few sigma. Figure 2.17 shows the measurement of S_8 from a number of observations, and almost all of the late-time Universe probes show an indication of lower S_8 within their statistical uncertainties.

Future Stage-IV surveys such as Euclid (Laureijs et al., 2011), the Legacy Survey of Space and Time (LSST: LSST Dark Energy Science Collaboration, 2012), and the Nancy Grace Roman Space Telescope (Roman: D. Spergel et al., 2015) are expected to revolutionize our understanding by collecting a vast volume of data with unparalleled depth and accuracy across large areas of the sky. For example, LSST will produce 15 TB of data every night and can scan the whole sky every few nights, while Euclid will provide the space-based all-sky images, and Roman will provide higher-resolution images of the sky. This will allow for the testing of the Λ-CDM model with high precision and the exploration of alternative theories that could explain the observed S_8 tension.

2.4.7 Supernovae

Supernovae, particularly Type Ia supernovae (SNIa), serve as one of the pivotal cosmological probes, offering insights into the expansion history of the Universe. Type Ia Supernovae are the thermonuclear explosions of carbon-oxygen white dwarfs when they
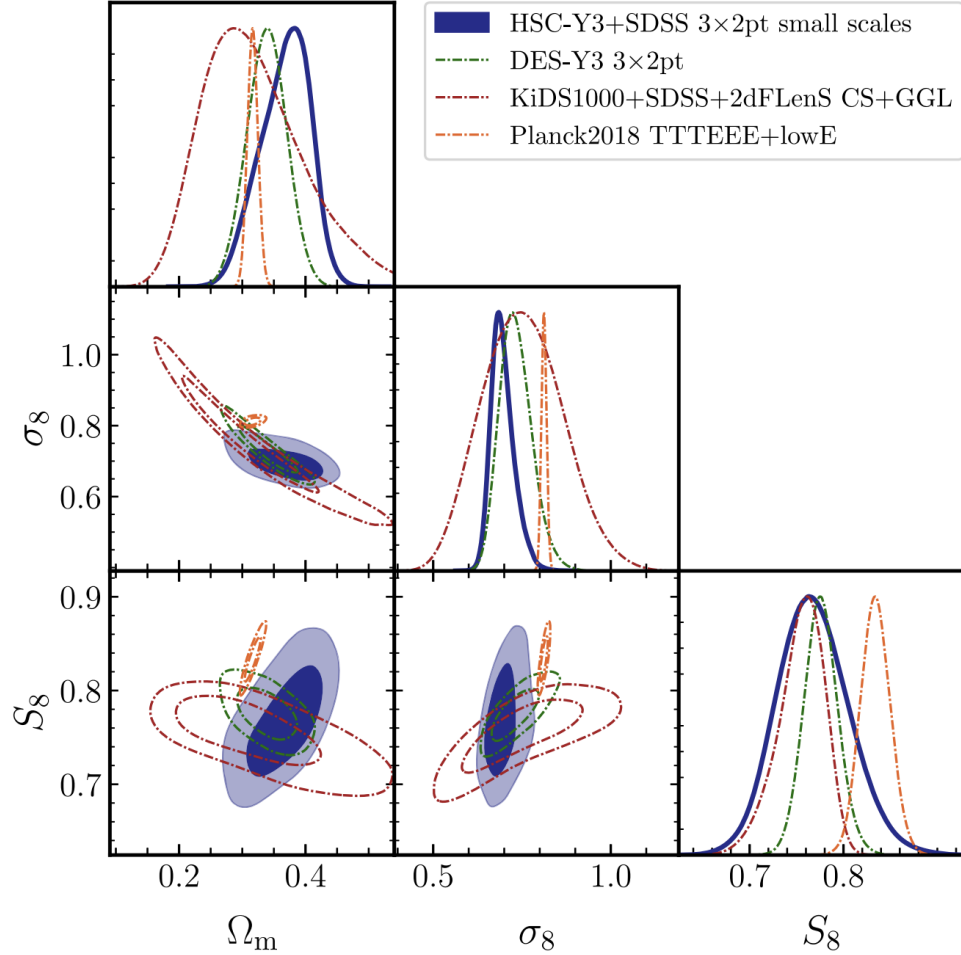
FIGURE 2.16: The 1D and 2D posterior distributions in the parameter space of (Ω_m, σ_8, S_8) for the flat Λ-CDM cosmology from the 3x2pt analysis in HSC Year-3 data. Figure 1 in Miyatake et al., 2023. Reprinted figure with permission from Miyatake et al., 2023. Copyright (2023) by the American Physical Society.

reach a critical mass of 1.44x solar mass (called Chandrasekhar limit). The exact progenitor of a Type Ia supernova is not known. However, since it explodes at a fixed mass, its peak brightness/luminosity and its characteristic light curve (luminosity vs time) are consistent. These stellar explosions act as "standard candles", allowing us to measure cosmic distances with remarkable precision. By comparing the observed brightness of a supernova with its known intrinsic brightness, we can determine its distance from an observer. The distance
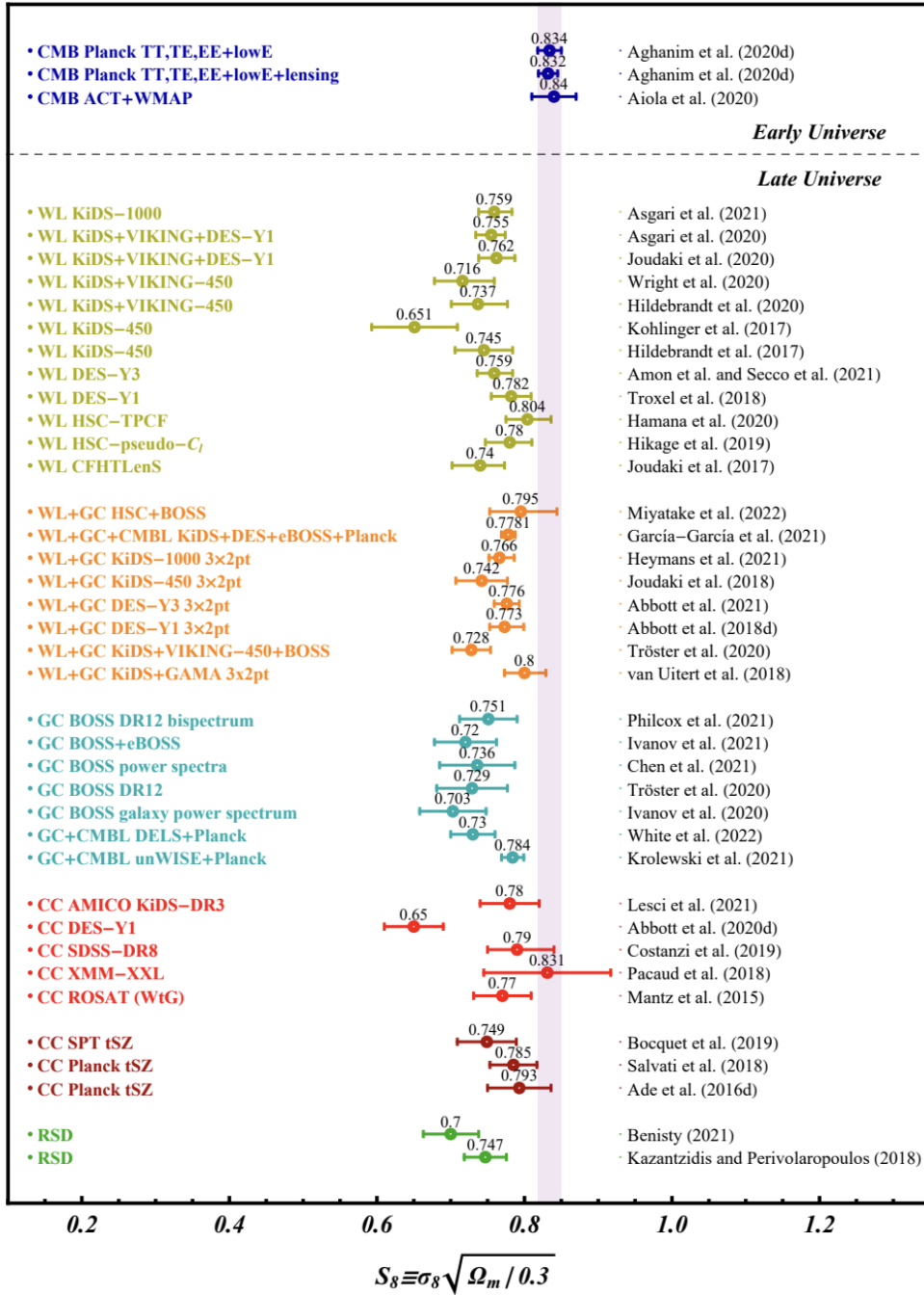
FIGURE 2.17: Constraints on S_8 and its corresponding 68% error from a variety of observations and probes of early-time and late-time Universe. Figure 4 in Abdalla et al., 2022.

can be measured through the distance modulus,

$$\mu = m_L - M_L = 5log_{10}\left(\frac{D_L}{10pc}\right), \tag{2.51}$$

where m_L and M_L are apparent magnitude and absolute magnitude, respectively, and D_L is the luminosity distance. For a flat Universe, the luminosity distance can be written as,

$$D_L(z) = (1+z)\int_0^z \frac{cdz'}{H(z')} = (1+z)\int_0^z \frac{cdz'}{H_0\sqrt{\Omega_{\text{radiation}}(1+z')^4 + \Omega_{\text{matter}}(1+z')^3 + \Omega_k a^{-2} + \Omega_\Lambda}}, \tag{2.52}$$

which encodes cosmological information. This methodology has been instrumental in the discovery of the accelerating expansion of the Universe (Perlmutter and Riess, 1999; Riess et al., 1998), providing evidence for the existence of dark energy. Through their role as distance indicators, supernovae contribute significantly to our understanding of the geometry of the Universe and the refinement of cosmological models.

2.4.7.1 Major Challenges in Type Ia Supernovae

While the Type Ia supernovae have a distinctive light curve, several observational systematics complicate the characterization of observed light curves. These are,

- SN classification – difficulty in identifying the type Ia features in spectral emission line from spectroscopy or photometry.
- Host galaxy identification – identifying the correct host galaxy becomes challenging as the distance to the supernova increases. Even if the host galaxy is identified, inferring the cosmological redshift of the host galaxy from photometry is known to be notoriously difficult.
- Peculiar velocities – the physical velocity of a supernova and its host galaxy within its local volume can impact the spectrum of the supernova and its redshift characterization.

Since there is a limit to the theoretical modeling of the light curve, any observational systematics must be carefully accounted for. For these reasons, the type Ia supernovae are

often called the "standardizable" candle rather than the standard candle.

2.4.7.2 The Frontiers of the Supernovae Cosmology

Since the first discovery of the expansion of the Universe (Hubble, 1929) and the recent discovery of dark energy, significant efforts have been dedicated to constrain the expansion rate of the Universe (H_0) and the dark energy equation-of-state (w) at high precision (e.g., Brout et al., 2022; Scolnic et al., 2022). The current state-of-the-art is the result from DES with more than 1500 supernovae (DES Collaboration et al., 2024). In which, with excellent control of systematics (Vincenzi et al., 2024), the dark energy equation-of-state is found to be constant within $\sim 2\sigma$. And, Riess et al., 2022 measured the Hubble constant to be $H_0 = 73.30 \pm 1.04$.

Local measurements of the Hubble constant from SN, however, are notably discrepant with H_0 derived from CMB. This is called the Hubble tension and is at about 5σ (much more significant than S_8 tension). The fact that both sides have extensively investigated systematic effects that could potentially alleviate the Hubble tension and have not found significant sources that can mitigate 5σ could indicate the physics in the early-time and late-time Universe is different and underscores a fundamental gap in our understanding of the Universe.

Supernovae from both spectroscopic surveys (DESI, 4MOST: de Jong et al., 2019) and photometric surveys (Euclid, LSST, and Roman) in the future will increase the number of supernovae by an order of 1000, discovering supernovae up to $z \sim 3$. These supernova samples are expected to deliver cosmological parameter constraints that differentiate the cosmological constant from time-varying dark energy and relatively high-z measurement of the Hubble constant.

3

Fundamental Principles of Weak Gravitational Lensing

In this chapter, we will explore the basic weak gravitational lensing formalism as predicted by GR and how weak lensing stands as one of the most powerful probes of both the expansion history and the structure growth of the Universe. For more detailed derivations and discussion, readers may refer to Bartelmann and Schneider, 2001; Dodelson, 2017. As introduced in § 2.4.6, weak lensing refers to a phenomenon where the paths of the photons from the background sources become deflected and distorted as they travel through gravitational potentials and reach an observer. In the limit of "weak" lensing, this produces a small amount of coherent magnification and shear of the sources when seen on images, and these distortions can help us learn about the gravitational potential (i.e., matter overdensity).

3.1 Gravitational Lensing Theory
3.1.1 Deflection and Distortion of Light

We first study the deflection of light and how the mass and density of the foreground objects (which we call lenses) relate to the amount of deflection. Imagine the geometric system of the background source, a point source with mass M as the foreground lens, and an observer, where the photons from the source travel through the lens and reach the observer (Figure 3.1). Here we assume the deflection is caused by a point mass and consider the
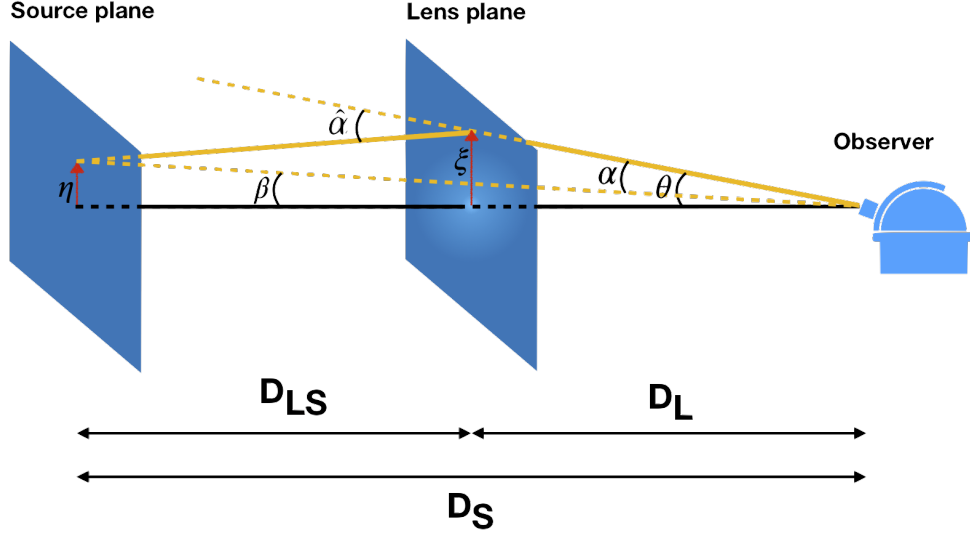
FIGURE 3.1: A schematic diagram of the source-lens-observer system where light is deflected by $\hat{\alpha}$ due to the gravitational potential of the lens. Image credit: Rémy Joseph

light ray does not pass through the gravitational field close to the horizon denoted by the Schwarzschild radius (R_s), and then GR provides the magnitude of the angle of deflection ($\hat{\alpha}(\xi)$) to be,

$$\hat{\alpha} = \frac{4MG^2}{\xi c^2}, \tag{3.1}$$

where $\xi \ll R_s$ condition provides $\hat{\alpha} \ll 1$. Our purpose is to obtain an expression for the magnitude and direction of the deflection angle $\boldsymbol{\alpha}$, which relates the true source position ($\boldsymbol{\beta}$) to the observed position ($\boldsymbol{\theta}$).

Considering the point mass deflection, the small angle approximation provides $\boldsymbol{\xi} = D_L \boldsymbol{\theta}$ and $D_{LS}\hat{\alpha} = D_S \boldsymbol{\alpha}$. Then, the deflection angle is,

$$\boldsymbol{\alpha} = \frac{4MG^2}{c^2} \frac{D_{LS}}{D_S D_L} \frac{\boldsymbol{\theta}}{|\boldsymbol{\theta}|^2} = \theta_E^2 \frac{\boldsymbol{\theta}}{|\boldsymbol{\theta}|^2}, \tag{3.2}$$

where θ_E is the Einstein radius that describes the ring of the light around the objects on the image when the source lines up perfectly with the lens along the line-of-sight –

$$\theta_E = \sqrt{\frac{4MG}{c^2} \frac{D_{LS}}{D_S D_L}}. \tag{3.3}$$

50

We can generalize the above for an ensemble of point masses to be the sum of the deflection angles due to individual masses because the gravitational field of our concern is weak (i.e., linearization of the field equations in GR). We still make an assumption here that the mass distribution is not thick (thin lens approximation), and the sum of the small deflection angles can be approximated to be the straight line (Born approximation). The impact vector (ξ') of the light ray due to a point mass (dm) is $\xi - \xi'$ and then the total deflection angle (2D vector) predicted by GR is,

$$\hat{\alpha}(\xi) = \frac{4G}{c^2} \sum dm(r) \frac{\xi - \xi'}{|\xi - \xi'|^2}, \tag{3.4}$$

where $r = (\xi'_x, \xi'_y, z)$ is the coordinates on the lens place of the mass element dm and the direction of the propagation of the incoming light ray. By defining the surface mass density,

$$\Sigma(\xi) \equiv \int dz \rho(\xi_x, \xi_y, z), \tag{3.5}$$

the general expression of the deflection angle becomes,

$$\hat{\alpha}(\xi) = \frac{4G}{c^2} \int d^2\xi' \Sigma(\xi') \frac{\xi - \xi'}{|\xi - \xi'|^2}. \tag{3.6}$$

3.1.2 The Lens Equation

Now that we have the expression of the deflection angle by a mass distribution rather than a point mass, we relate the position of the source on the source plane (η) to the position of the source on the lens plane (ξ) in order to obtain the expression of the observable deflection angle:

$$\eta = \frac{D_S}{D_L} \xi - D_{LS} \hat{\alpha}. \tag{3.7}$$

Utilizing the small angle approximation ($\eta = D_S \beta$, $\xi = D_L \theta$), the above expression becomes,

$$\beta = \theta - \frac{D_{LS}}{D_S} \hat{\alpha}(D_L \theta) \equiv \theta - \alpha(\theta), \tag{3.8}$$

where we defined the scaled deflection angle $\boldsymbol{\alpha}(\boldsymbol{\theta})$. We will refer to $\boldsymbol{\beta} = \boldsymbol{\theta} - \boldsymbol{\alpha}(\boldsymbol{\theta})$ as the lens equation

$$\boldsymbol{\alpha}(\boldsymbol{\theta}) \equiv \frac{D_{LS}}{D_S} \hat{\boldsymbol{\alpha}}(D_L \boldsymbol{\theta}). \tag{3.9}$$

Now if we parametrize the surface mass density $\Sigma(\boldsymbol{\xi}')$ with the critical surface mass density

$$\Sigma_{cr} \equiv \frac{c^2}{4\pi G} \frac{D_S}{D_{LS} D_L}, \tag{3.10}$$

then,

$$\Sigma(D_L \boldsymbol{\theta}) = \kappa(\boldsymbol{\theta}) \Sigma_{cr}, \tag{3.11}$$

where $\kappa(\boldsymbol{\theta})$ is a dimensionless parameter called convergence. The effect of gravitational lensing can be identified as "strong" when $\kappa > 1$ (i.e., $\Sigma > \Sigma_{cr}$) or "weak" when $\kappa < 1$. With this characteristic value of the surface density, Eqn. 3.9 can be rewritten as,

$$\boldsymbol{\alpha}(\boldsymbol{\theta}) = \frac{1}{\pi} \int d^2\theta' \kappa(\boldsymbol{\theta}') \frac{\boldsymbol{\theta} - \boldsymbol{\theta}'}{|\boldsymbol{\theta} - \boldsymbol{\theta}'|^2}. \tag{3.12}$$

With a bit of algebra, one can show the deflection angle is a gradient of the 2D gravitational potential ($\nabla\Phi(\boldsymbol{\theta}) = \boldsymbol{\alpha}(\boldsymbol{\theta})$) and hence we can define the lensing potential (deflection potential),

$$\Phi(\boldsymbol{\theta}) = \frac{1}{\pi} \int d^2\theta' \kappa(\boldsymbol{\theta}') \ln |\boldsymbol{\theta} - \boldsymbol{\theta}'|, \tag{3.13}$$

with the relationship of 2D and 3D potential

$$\Phi(\boldsymbol{\theta}) \equiv \frac{2}{D_S} \int_0^{D_S} dD_L \phi(x^i = D_L \theta^i, D_L; t = t_0 - D_L/c) \frac{D_{LS}}{D_L}, \tag{3.14}$$

which satisfies $\nabla^2 \Phi(\boldsymbol{\theta}) = 2\kappa(\boldsymbol{\theta})$ (Poisson equation).

3.1.3 Magnification and Shear

We have discussed how gravitational lensing with some gravitational potential causes a light ray to be deflected and changes the apparent position of the source. Let's now discuss how bundles of light rays undergo gravitational lensing and what we are able to observe.

While gravitational lensing changes the shape of the source seen in the image because each light bundle is deflected differently, the total surface brightness (intensity) is conserved. Consider the mapping of the distribution of the photons in the source plane ($I_{\text{source}}(\boldsymbol{\beta})$) to the lens plane ($I(\boldsymbol{\theta})$). As long as the source is much smaller than the scale where the mass distribution of the lens changes, one can write this mapping linearly around the source. This can usually be described by the 2x2 Jacobian matrix $A(\boldsymbol{\theta})$,

$$A(\boldsymbol{\theta}) = \frac{\partial \boldsymbol{\beta}}{\partial \boldsymbol{\theta}} = \frac{\partial}{\partial \boldsymbol{\theta}}(\boldsymbol{\theta} - \boldsymbol{\alpha}(\boldsymbol{\theta})) = \left(\delta_{ij} - \frac{\partial^2 \Phi(\boldsymbol{\theta})}{\partial \theta_i \partial \theta_j}\right). \tag{3.15}$$

The elements of the distortion tensor (Φ_{ij}) can be understood to be composed of the isotropic distortion (i.e., convergence – it leaves the shape and direction unchanged) and the anisotropic shape distortion (i.e., shear – it extends or compresses the line between two points in the lens plane, and adds rotation by 2ϕ). The Jacobian is then,

$$A(\boldsymbol{\theta}) = \begin{pmatrix} 1 - \kappa - \gamma_1 & -\gamma_2 \\ -\gamma_2 & 1 - \kappa + \gamma_1 \end{pmatrix}, \tag{3.16}$$

where we have defined the following –

$$\kappa = \frac{1}{2}\left(\frac{\partial^2}{\partial^2 \theta_x} + \frac{\partial^2}{\partial^2 \theta_y}\right)\Phi, \tag{3.17}$$

$$\gamma_1 = \frac{1}{2}\left(\frac{\partial^2}{\partial^2 \theta_x} - \frac{\partial^2}{\partial^2 \theta_y}\right)\Phi, \tag{3.18}$$

$$\gamma_2 = \frac{\partial^2 \Phi}{\partial \theta_x \partial \theta_y} \tag{3.19}$$

with $\gamma = \gamma_1 + i\gamma_2 = |\gamma| \exp\{(-2i\phi)\}$. Another observable quantity called magnification is also defined as the inverse determinant of the Jacobian matrix,

$$\mu = \frac{1}{(1 - \kappa)^2 - \gamma^2}. \tag{3.20}$$

Figure 3.2 shows the qualitative picture of the observable quantity in gravitational lensing on a circular source.

$$\kappa > 0, \gamma_{1,2} = 0 \qquad \kappa, \gamma_2 = 0, \gamma_1 > 0 \qquad \kappa, \gamma_1 = 0, \gamma_2 > 0$$

$$\kappa < 0, \gamma_{1,2} = 0 \qquad \kappa, \gamma_2 = 0, \gamma_1 < 0 \qquad \kappa, \gamma_1 = 0, \gamma_2 < 0$$
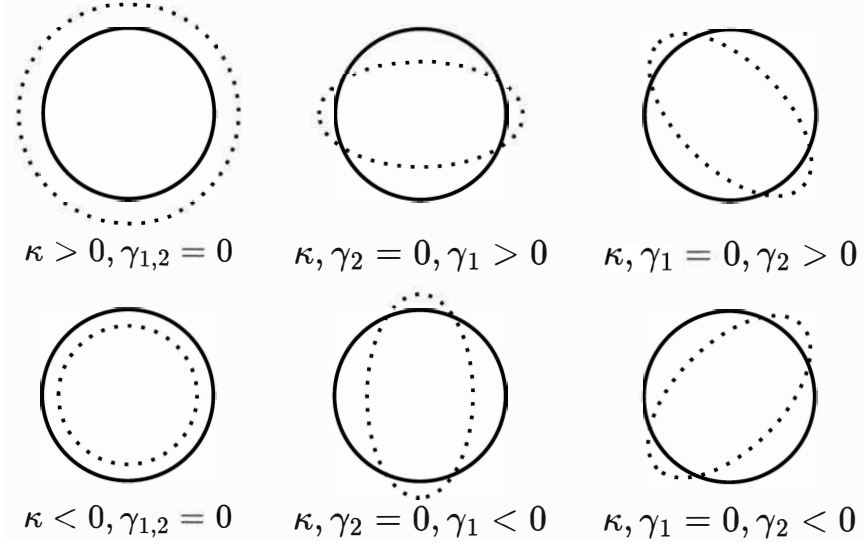
FIGURE 3.2: An illustration showing the lensed source (dashed black) under the effect of convergence and shear on the original unlensed source (solid black).

Utilizing Eqn. 3.13 and Eqn. 3.17, a general expression of γ can be derived as,

$$\gamma(\boldsymbol{\theta}) = \frac{1}{\pi} \int d^2\theta' D(\boldsymbol{\theta} - \boldsymbol{\theta}')\kappa(\boldsymbol{\theta}'), \qquad (3.21)$$

with

$$D(\boldsymbol{\theta}) \equiv \frac{\theta_y^2 - \theta_x^2 - 2i\theta_x\theta_y}{|\boldsymbol{\theta}|^4} = \frac{-1}{\left(\theta_x - i\theta_y\right)^2}. \qquad (3.22)$$

It is particularly important here to note that the shear is directly related to the projected gravitational potential along the line-of-sight. We will later use this expression of the shear to show that it encodes cosmological information which we can recover from observation of galaxy shapes.

3.2 Cosmological Weak Lensing Theory

Cosmic shear describes the distortions of the photon paths of background galaxies induced by the large-scale structure in the Universe. Since matter overdensity fluctuates along the line-of-sight, the shear can identify the cumulative projected gravitational potential that results in shearing background galaxies. In this section, we will explore ingredients needed

to make predictions about the matter distribution in the Universe from cosmic shear.

3.2.1 Effective Convergence to Projected Matter Overdensity

As we saw in Eqn. 3.17, the convergence is directly related to the 2D projected gravitational potential (Φ) of matter density. Our ultimate goal is to relate the convergence (κ) to the 3D matter overdensity (δ) in order to connect the lensing observable to matter distribution.

For cosmic shear, since the deflection angle represents a sum of cumulative deflections by all the density perturbations between the source and observer, it takes a different form from the previous case of a single thin lens. We refer readers to Chapter 6 in Bartelmann and Schneider, 2001 for a full derivation, and we will only state the result here. By studying how light from a source at comoving distance χ propagates in our homogeneous and isotropic FLRW Universe and how small density perturbations ($\phi \ll c^2$) affect the light propagation, we can obtain an expression for a deflection angle of a light ray relative to an arbitrarily chosen fiducial light ray.

$$\boldsymbol{\alpha}(\boldsymbol{\theta}, \chi) = \frac{S_K(\chi)\boldsymbol{\theta} - \boldsymbol{x}(\boldsymbol{\theta}, \chi)}{S_K(\chi)} \frac{2}{c^2} \int_0^\chi d\chi' \frac{S_K(\chi - \chi')}{S_K(\chi)} \nabla_\perp \phi[S_K(\chi')\boldsymbol{\theta}, \chi'], \qquad (3.23)$$

where $\boldsymbol{x}(\boldsymbol{\theta}, \chi)$ denotes the comoving separation between a light ray and the fiducial ray. In an analogy to our previous thin lens case, an effective convergence for a fixed redshift or comoving source distance (χ) can be defined as half the divergence of the deflection angle,

$$
\begin{aligned}
\kappa_{\text{eff}}(\boldsymbol{\theta}, \chi) &= \frac{1}{2} \nabla_\theta \cdot \boldsymbol{\alpha}(\boldsymbol{\theta}, \chi) \\
&= \frac{1}{c^2} \int_0^\chi d\chi' \frac{S_K(\chi - \chi')S_K(\chi')}{S_K(\chi)} \frac{\partial^2}{\partial x_i \partial x_i} \phi[S_K(\chi')\boldsymbol{\theta}, \chi'].
\end{aligned}
\qquad (3.24)
$$

Here we have replaced $\boldsymbol{x}(\boldsymbol{\theta}, \chi)$ by $S_K(\chi')\boldsymbol{\theta}$. The effective convergence here represents the projected mass density along the comoving coordinates weighted by the geometry of the source, lens, and observer system. The geometrical weight determines the efficiency of the lensing. Now we rewrite the Laplacian of the Newtonian potential in terms of the matter

overdensity (i.e., density contrast) using the Poisson equation (Eqn. 2.29) with critical density at a matter-dominated Universe

$$\nabla^2 \phi \;=\; \frac{3H_0^2 \Omega_m}{2a} \delta, \tag{3.25}$$

$$\kappa_{\text{eff}}(\boldsymbol{\theta}, \chi) \;=\; \frac{3H_0^2 \Omega_m}{2c^2} \int_0^\chi \frac{d\chi'}{a(\chi')} \frac{S_K(\chi - \chi') S_K(\chi')}{S_K(\chi)} \delta[S_K(\chi')\boldsymbol{\theta}, \chi']. \tag{3.26}$$

To obtain the effective convergence for a population of source galaxies (i.e., a projection of the matter overdensity), we need to weight the individual convergence at single χ by the observed galaxy distribution over redshift $p(z)$ (redshift distribution of galaxies) and integrate $\kappa_{\text{eff}}(\boldsymbol{\theta}, \chi)$ over $p(\chi)d\chi = p(z)dz$.

$$\kappa_{\text{eff}}(\boldsymbol{\theta}) \;=\; \int_0^{\chi_{\text{lim}}} d\chi\, p(\chi) \kappa_{\text{eff}}(\boldsymbol{\theta}, \chi)$$

$$\;=\; \int_0^{\chi_{\text{lim}}} W(\chi)\delta[S_K(\chi')\boldsymbol{\theta}, \chi'], \tag{3.27}$$

where the lens efficiency kernel $W(\chi)$ is defined as,

$$W(\chi) = \frac{3H_0^2 \Omega_m}{2c^2} \frac{S_K(\chi)}{a(\chi)} \int_\chi^{\chi_{\text{lim}}} d\chi'\, p(\chi') \frac{S_K(\chi' - \chi)}{S_K(\chi')}. \tag{3.28}$$

The upper boundary of the integration is the limiting comoving distance of the galaxy sample. The lens efficiency kernel describes the effectiveness of the lensing given a source redshift distribution, and it provides insight into the range of redshift that lensing is most sensitive to. For a flat Universe, the maximum lensing signal is produced when the lens is about halfway between the source and the observer (Figure 3.3).

3.2.2 The Lensing Power Spectrum

Finally, we will investigate the summary statistics of convergence and shear (i.e., power spectrum) and how this relates to the matter power spectrum we are able to predict from the perturbation theory.
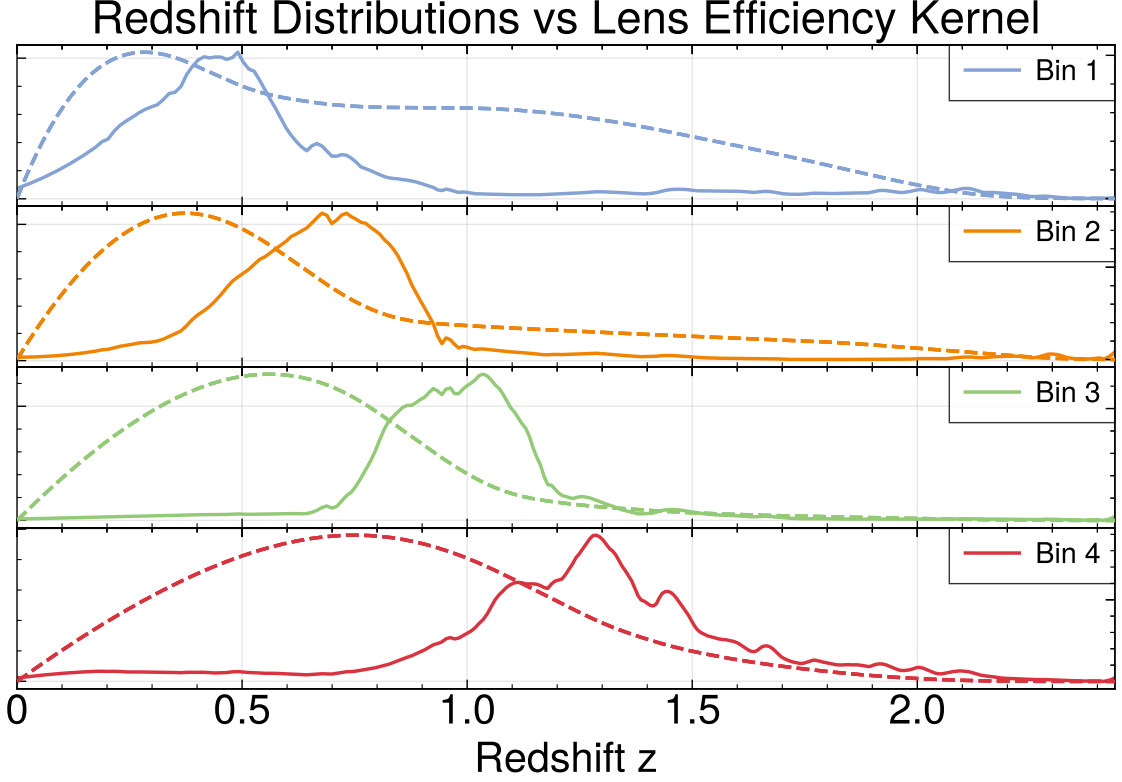
FIGURE 3.3: An example of redshift distributions (solid) and their corresponding lens efficiency kernel (dotted) at the Planck cosmology. The redshift distributions are estimated for the source galaxies observed in Dark Energy Survey Year-6 data (Yamamoto et al. in prep., Yin et al. in prep.) in four tomographic bins.

Similar to the case of 3D power spectrum in Eqn. 2.41, the 2D convergence angular power spectrum $(C_{\kappa\kappa}(\ell))$ can be computed with Eqn. 3.27 as,

$$
\begin{aligned}
\langle \widetilde{\kappa}(\ell)\widetilde{\kappa}^*(\ell') \rangle &= (2\pi)^2 \delta_D(\ell - \ell') C_{\kappa\kappa}(\ell) \qquad\qquad (3.29)\\[2mm]
&= (2\pi)^2 \delta_D(\ell - \ell') \frac{9H_0^4\Omega_m^2}{4c^4} \int_0^{\chi_{\text{lim}}} \frac{d\chi}{a^2(\chi)} q^2(\chi) S_K^2(\chi) \langle \widetilde{\delta}(\ell)\widetilde{\delta}^*(\ell') \rangle \\[2mm]
&= (2\pi)^2 \delta_D(\ell - \ell') \frac{9H_0^4\Omega_m^2}{4c^4} \int_0^{\chi_{\text{lim}}} \frac{d\chi}{a^2(\chi)} q^2(\chi) S_K^2(\chi) P_\delta\left(k = \frac{\ell}{S_K(\chi)}, \chi\right).
\end{aligned}
$$

Hence,

$$
C_{\kappa\kappa}(\ell) = \frac{9H_0^4\Omega_m^2}{4c^4} \int_0^{\chi_{\text{lim}}} \frac{d\chi}{a^2(\chi)} q^2(\chi) S_K^2(\chi) P_\delta\left(k = \frac{\ell}{S_K(\chi)}, \chi\right). \qquad (3.30)
$$

We will refer to this expression as the Limber equation. In the last step, we made a few approximations to replace the 2D with the 3D matter power spectrum. First, we used the Limber projection/approximation with which we ignore the modes in the line-of-sight and only use modes in the plane of the sky (e.g., Kaiser, 1992; Limber, 1953). Second, the flat-sky approximations, which replace the expansion in spherical harmonics with the expansion in Fourier modes, were applied (LoVerde and Afshordi, 2008). While Kilbinger, 2015 and Lemos et al., 2017 concluded that these approximations do not affect the inferred cosmological parameters for the surveys at that time, Fang, Krause, et al., 2020 showed that these could bias the future surveys such as LSST.

Now, if we rewrite the relationships between κ and γ from Eqn. 3.21 in Fourier space, we obtain

$$\widetilde{\gamma}(\boldsymbol{\ell}) = \frac{1}{\pi}\widetilde{\kappa}(\boldsymbol{\ell}) \times \widetilde{D}(\boldsymbol{\ell}), \tag{3.31}$$

where

$$\widetilde{D}(\boldsymbol{\ell}) = \frac{(\ell_1 + i\ell_2)^2}{\ell^2}. \tag{3.32}$$

The angular power spectrum of shear is then,

$$(2\pi)^2\delta_D(\boldsymbol{\ell} - \boldsymbol{\ell}')C_{\gamma\gamma}(\boldsymbol{\ell}) = \langle\widetilde{\kappa}(\boldsymbol{\ell})\widetilde{D}(\boldsymbol{\ell})\widetilde{\kappa}^*(\boldsymbol{\ell}')\widetilde{D}^*(\boldsymbol{\ell}')\rangle = \langle\widetilde{\kappa}(\boldsymbol{\ell})\widetilde{\kappa}^*(\boldsymbol{\ell}')\rangle. \tag{3.33}$$

Hence, we prove the equivalence of the convergence and shear power spectrum in the weak limit

$$C_{\gamma\gamma}(\ell) = C_{\kappa\kappa}(\ell) \tag{3.34}$$

$$= \frac{9H_0^4\Omega_m^2}{4c^4}\int_0^{\chi_{\text{lim}}}\frac{d\chi}{a^2(\chi)}q^2(\chi)S_K^2(\chi)P_\delta\left(k = \frac{\ell}{S_K(\chi)}, \chi\right). \tag{3.35}$$

3.2.3 Cosmic Shear As A Cosmological Probe

It is very useful and crucial to point out the wealth of cosmological information in the Limber equation (Eqn. 3.34), which can then be compared against the two-point correlation function of observed galaxy shear (left-hand side of the Limber equation). First, it is
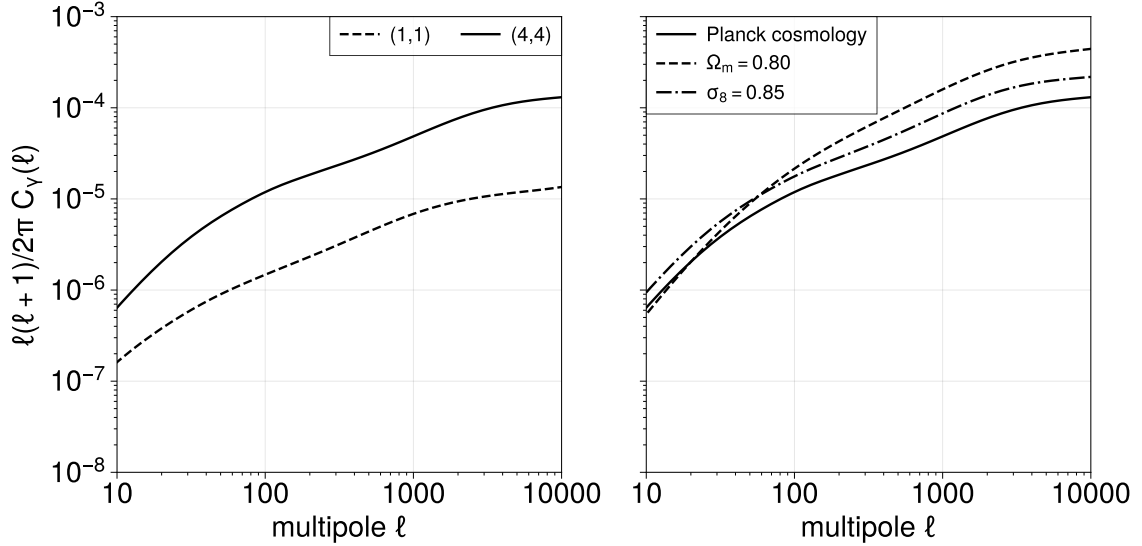
FIGURE 3.4: Numerical predictions of the shear angular power spectrum at Planck 2018 cosmology at four galaxy redshift distributions: bin1 – (0.0, 0.358), bin 2 – (0.358, 0.631), bin 3 – (0.631, 0.872), bin 4 – (0.872, 2.0). *Left*: auto-power spectrum for two redshift bin pairs (1,1) and (4,4). *Right*: auto-power spectrum for a bin pair (4,4) at different cosmologies.

apparent in the equation that it has dependencies on the Hubble constant, matter density, and curvature. The lens efficiency kernel then depends on the geometry of the source-lens-observer system, hence sensitive to the expansion history of the Universe. Lastly, as we discussed in § 2.3.2, the matter power spectrum encodes information about the initial conditions (i.e., primordial power spectrum) and the growth of structure in the Universe. Figure 3.4 compares the shear power spectrum of galaxies at different galaxy redshift distributions (*left*) and at different cosmologies (*right*), using numerical prediction code COSMOSIS (Zuntz et al., 2015).

3.3 Cosmic Shear in Practice

Up to this section, we have established the fact that cosmological weak gravitational lensing (cosmic shear) can produce visible impact on observed galaxies and how a statistical property of convergence and shear is related to that of the matter density field in the Universe. We now turn to learn what to look for and observe in the Universe to compute the observed power spectrum and compare against theory.

3.3.1 Relationship Between Shear and Galaxy Shapes

But how do we measure convergence and shear from galaxies? As it turns out, over a sufficient galaxy sample, galaxy shapes (i.e., ellipticity) can be a proxy to shear, and convergence can be reconstructed from a shear field inferred from galaxy ellipticity.

Let's first quantify a galaxy shape from the light distribution seen in an image. Let $I(x, y)$ be the pixel intensity of the light profile of an object at position (x, y). We can estimate the ellipticity about a centroid (μ_x, μ_y) using image moments as weighted averages of the image pixels' intensities. First, the centroid is defined by the raw moments normalized by the total intensity

$$\mu_x = \frac{\int dxdyxI(x, y)}{\int dxdyI(x, y)}, \quad \mu_y = \frac{\int dxdyyI(x, y)}{\int dxdyI(x, y)}, \tag{3.36}$$

and the higher moments around the centroid can be given by

$$M_{ij} = \frac{\int dxdy(x - \mu_x)^i(y - \mu_y)^j I(x, y)}{\int dxdyI(x, y)}. \tag{3.37}$$

Two definitions of frequently-used ellipticity (polarization: χ, distortion: ϵ) utilize the second moments (M_{11}, M_{20}, M_{02}) and they are,

$$\chi \equiv \frac{M_{20} - M_{02} + 2iM_{11}}{M_{20} + M_{02}} \tag{3.38}$$

$$\epsilon \equiv \frac{M_{20} - M_{02} + 2iM_{11}}{M_{20} + M_{02} + 2\sqrt{M_{20}M_{02} - M_{11}^2}}. \tag{3.39}$$

We will use the notion of ϵ as our quantity for a galaxy ellipticity for the rest of the discussion. As we have defined an ellipticity, we are interested in how shear affects an intrinsic source ellipticity (ϵ_s). We can factor the distortion matrix (Eqn. 3.16) into two components: one that only impacts the size and the other that impacts the shape of the object.

$$A = (1 - \kappa)\begin{pmatrix} 1 - g_1 & -g_2 \\ -g_2 & 1 + g_1 \end{pmatrix}, \tag{3.40}$$

where we have defined a new quantity $g \equiv \gamma/(1 - \kappa)$ called reduced shear. In the regime of weak lensing, since $\kappa \ll 1$, we are safely allowed to call g and γ equivalent. By following Seitz and Schneider, 1997, reduced shear distorts the second moments of the object light profile, and the observed ellipticity is,

$$\epsilon = \frac{\epsilon_s + g}{1 + g^* \epsilon_s} \sim \epsilon_s + g, \tag{3.41}$$

given the weak lensing limit ($|\gamma| \ll 1$ and $|g| \ll 1$). This indicates that over a large number of galaxy samples that experience the same coherent distortion, $\langle \epsilon \rangle \sim g$, with an assumption that the source galaxies are randomly oriented so that the average of intrinsic galaxy shapes is zero (i.e., $\langle \epsilon_s \rangle = 0$).

3.3.2 Shear Two-Point Correlation Function

In order to measure the shear power spectrum (Eqn. 3.34), we can compute the two-point correlation function of shear since the Fourier transform of the real-space correlation function is directly related to the power spectrum (Eqn. 2.41). We first denote the two components of shear – the tangential-component shear (γ_t) and cross-component shear ($\gamma_\times$). Given $\gamma = \gamma_1 + i\gamma_2$ and a separation vector between galaxies ($\boldsymbol{\theta}$) whose polar angle is ϕ, these can be defined as

$$(\gamma_t, \gamma_\times) = (-\gamma_1 cos2\phi - \gamma_2 sin2\phi, -\gamma_2 cos2\phi + \gamma_1 sin2\phi). \tag{3.42}$$

The tangential and cross-component shear are the orthogonal components of shear (γ_1 and γ_2) in a coordinate system that is rotated by ϕ and defined by the separation vector.

With this, the shear two-point correlation function as a function of angular separation between galaxies is,

$$\xi_\pm(\theta) = \langle \gamma_t \gamma_t \rangle(\theta) \pm \langle \gamma_\times \gamma_\times \rangle(\theta) \tag{3.43}$$

Miralda-Escude, 1991. Our practical estimator of the shear correlation function over pairs of galaxies (i, j) is,

$$\hat{\xi}_\pm(\theta) = \frac{\sum_{ij} w_i w_j (e_t^i e_t^j \pm e_\times^i e_\times^j)}{\sum ij w_i w_j}, \tag{3.44}$$

where e is the measured ellipticity and w is the weight of the galaxy Schneider, van Waer-beke, et al., 2002. While a two-point correlation function of a scalar field, such as con-vergence, can be converted to a power spectrum by taking the inverse Fourier transform, the shear two-point correlation function is two-dimensional and isotropic and, therefore, requires the Hankel transform to be related to the power spectrum. If we use the flat-sky limit $(\boldsymbol{k} \to \boldsymbol{\ell})$, we can establish a relationship between the two-point correlation function and the shear power spectrum (Eqn. 3.34) as

$$\xi_{\pm}(\theta) = \frac{1}{2\pi} \int d\ell \ell J_{0/4}(\ell\theta) C_{\gamma\gamma}(\ell), \tag{3.45}$$

where $J_{0/4}(\ell\theta)$ is the Bessel function of the first kind at $n = 0$ or 4.

3.3.3 E- and B-modes

In the recent cosmological analyses, it is often useful to measure two-point correla-tion function both in real space $(\xi_{\pm}(\theta))$ and Fourier space $(C(\ell))$ from galaxy shapes, and use both independently as summary statistics that are compared against a cosmological model prediction. In real space, convergence or shear angular power spectrum is computed (Eqn. 3.34), and the Hankel transform is taken to obtain $\xi_{\pm}$ prediction to match against the two-point correlation function of galaxy shapes (Eqn. 3.44). In Fourier space, there is no need to take the Hankel transform, but we need an estimator of the shear angular power spectrum $(\hat{C}(\ell))$ from galaxy shapes, which, as we will see, can be estimated from the two-point correlation function of the shear field.

With galaxy shapes, we are allowed to make a map of the shear field. Because it is a spin-2 field, the field can be decomposed into two scalar modes – E- and B-modes (Fig. 2.11) – on the basis of spherical harmonics (essentially a Fourier transform on a sphere) as

$$(\gamma_1 \pm i\gamma_2)(\boldsymbol{\theta}) = -\sum_{\ell m} [E_{\ell m} \pm iB_{\ell m}] \, _{\mp 2}Y_{\ell m}(\boldsymbol{\theta}), \tag{3.46}$$

where $_{\mp 2}Y_{\ell m}(\boldsymbol{\theta})$ is the spin-weighted spherical harmonics. It is important to note that the E-mode is the curl-free component and the B-mode is the divergence-free component of the

field. The shear angular power spectra are then defined as

$$\langle E_{\ell m} E_{\ell m}^* \rangle \;\; = \;\; C_\ell^{EE} \delta_{\ell \ell'} \delta_{mm'} \tag{3.47}$$

$$\langle E_{\ell m} B_{\ell m}^* \rangle \;\; = \;\; C_\ell^{EB} \delta_{\ell \ell'} \delta_{mm'} \tag{3.48}$$

$$\langle B_{\ell m} B_{\ell m}^* \rangle \;\; = \;\; C_\ell^{BB} \delta_{\ell \ell'} \delta_{mm'}, \tag{3.49}$$

and an optimal estimator of these angular power spectra are

$$\hat{C}_\ell^{EE} \;\; = \;\; \frac{1}{2\ell+1} \sum_m E_{\ell m} E_{\ell m}^*, \tag{3.50}$$

$$\hat{C}_\ell^{EB} \;\; = \;\; \frac{1}{2\ell+1} \sum_m E_{\ell m} B_{\ell m}^*, \tag{3.51}$$

$$\hat{C}_\ell^{BB} \;\; = \;\; \frac{1}{2\ell+1} \sum_m B_{\ell m} B_{\ell m}^*. \tag{3.52}$$

(Schneider, Van Waerbeke, and Mellier, 2002). Now that we found the decomposition, we can rewrite Equation 3.45 as

$$\xi_\pm(\theta) = \frac{1}{2\pi} \int d\ell \ell J_{0/4}(\ell\theta)(C_\ell^{EE} + C_\ell^{BB}). \tag{3.53}$$

If we assume that the deflection of light is only caused by the perturbation of spacetime due to the gravitational potential, gravitational lensing only produces the E-mode shear field and there should not be any B-mode signal. In real life, measured B-mode shear field signal is non-zero due to a few systematic biases such as PSF modeling and intrinsic alignment, and the higher-order terms in the light propagation equation (Eqn. 3.23) and other approximations we have made (e.g., reduced shear) can produce non-zero, but very small B-modes. This suggests that we can take advantage of the non-zero B-mode signal as the test of identifying the sources of systematic errors. We will explore this topic later.

4

Cosmic Shear: From Pixels to Cosmological Parameters

In Chapters 2 and 3, we have studied the theory of standard cosmological model and weak gravitational lensing as a technique to learn about our Universe. In this chapter, we will focus on the observation of weak lensing, the inference of cosmological parameters from the observation, and the challenges associated with weak lensing cosmology. We will first briefly explore the history of cosmology with cosmic shear as we mentioned in § 2.4.6 to establish the ground for describing the processes to obtain cosmological information from pixel data in modern cosmic shear observation in § 4.2.

4.1 History of Cosmic Shear Cosmology

The exploration of cosmic shear, a cornerstone of observational cosmology, traces its origins to the theoretical frameworks developed in the early 20th century. The concept fundamentally relies on the understanding that massive celestial bodies and structures can bend the path of light passing near them, an effect predicted by Albert Einstein's theory of general relativity. However, it was not until the late 20th century that technological advancements in telescopic imaging and data processing allowed cosmologists to observe and measure these distortions on a cosmic scale. This field has rapidly evolved from theoretical curiosity to a critical empirical tool used to test models of cosmic evolution and structure
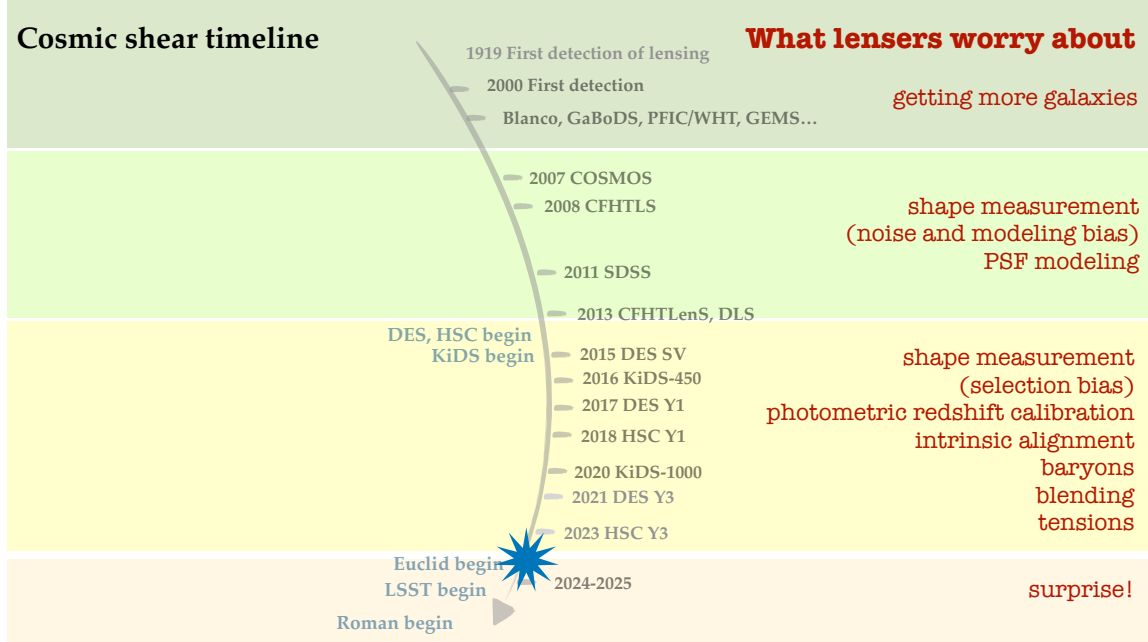
FIGURE 4.1: A timeline of cosmological surveys with cosmic shear. From top to bottom, each color represents Stage-I,II,III,IV surveys defined by the Dark Energy Task Force (Albrecht et al., 2006). *Image credit: Chihway Chang*

formation.

Figure 4.1 shows the timeline of the detection of cosmic shear and the cosmological analysis with cosmic shear with various telescopes and surveys, starting with the first observational evidence of gravitational lensing in 1919. On the right of the timeline, what cosmic shear cosmologists have been worried about at each Stage (i.e., statistical and systematic uncertainties) is listed. We will discuss these further in § 4.3. Figure 4.2 shows the measurement of S_8 for many surveys along the timeline in Fig. 4.1. Over the years, the uncertainty on the measurement has decreased dramatically, and there is an indication of "S_8 tension" from the results of recent Stage-III surveys where S_8 from galaxy surveys is consistently low compared to the S_8 measurement from CMB within $1 \sim 2\sigma$.

4.2 From Pixels to Cosmology

The process of extracting cosmological information from pixel data using weak gravitational lensing involves several intricate and critical steps. One can roughly categorize
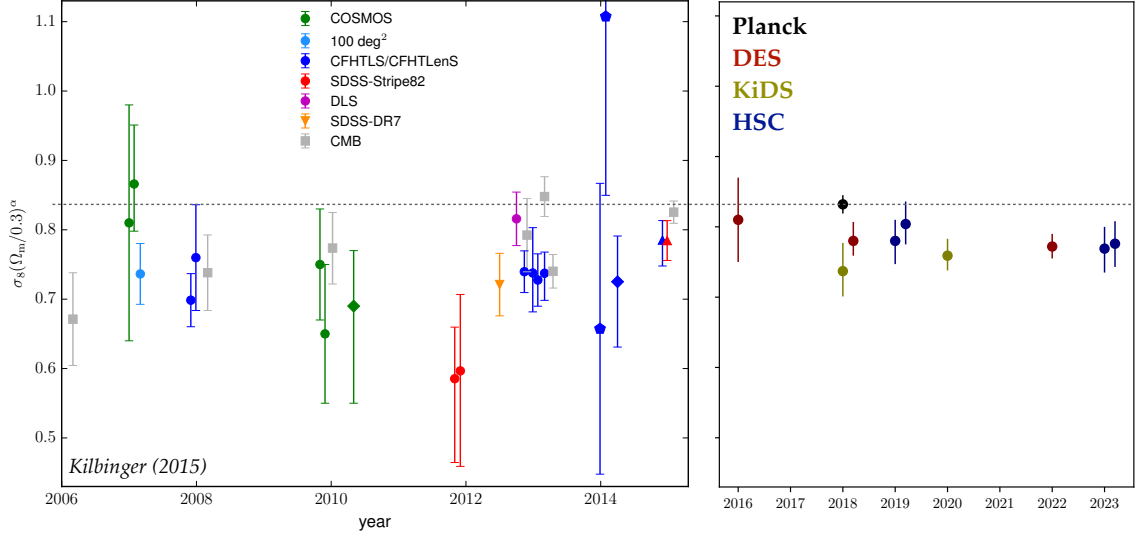
FIGURE 4.2: Measurement of S_8 as a function of publication year for numerous cosmological surveys. *Image credit: Chihway Chang*

them as "images to catalogs" and "catalogs to science" pipelines. The first step involves using observed images to identify astronomical objects and measure their properties. Initially, image calibration is performed to convert the raw pixel data from telescopes into usable scientific data, correcting for instrumental and atmospheric distortions. Following this, Point Spread Function (PSF) modeling is essential, as it corrects the images for the blurring effects caused by the telescope and atmosphere, which can significantly affect the next step. The following stage is galaxy identification, where galaxies are detected within the calibrated images, and shape measurement techniques are applied to estimate the shear caused by gravitational lensing. This shear measurement requires high precision, as the signal is typically very subtle. Parallel to shape measurement, photometric redshift inference is carried out to estimate the distances to these galaxies from their photometric data. This is because precise distance measurements are crucial for converting two-dimensional image data into three-dimensional maps of matter distribution. Producing catalogs of galaxy shapes and redshift is at the heart of the first, "images to catalogs" step.

In the second step, "catalogs to science," we first compute two-point statistics that quantify the spatial correlations of galaxy shapes across the sky from shape and redshift catalogs.

FIGURE 4.3: A flowchart describing the steps in modern cosmic shear cosmological analysis to extract cosmological information from pixel data. *Image credit: Alexandra Amon*

Then, in order to predict the power spectrum from a theoretical model, several analysis choices need to be made. These include how to handle intrinsic alignments (the tendency of galaxies to point towards each other in a non-random way) and baryonic modeling (accounting for the effects of ordinary matter on the dark matter distribution). Each step in this process influences the accuracy of the power spectrum predictions and, consequently, the inferred cosmological parameters. This makes the entire process from pixel data to cosmological information both complex and computationally intensive. These processes are summarized in a diagram in Figure 4.3, and we will explore some of the essential steps in more detail.

4.2.1 PSF Modeling

As photons from astronomical sources arrive at detectors on a telescope, they experience several detector effects, and raw image data show unwanted features and are not ready for scientific analysis. Readers may find Howell, 2006 useful for a general reference, Morganson et al., 2018 for the reference on raw image calibration on the Dark Energy Survey data, and

Bosch et al., 2018 for Hyper Suprime Cam data. We simply begin by assuming we have pre-processed data (referred to as "Wide Field Images" on Fig. 4.3). We briefly mention that astrometric solution (also known as the world coordinate system (WCS) solution), which maps the coordinates between pixels/CCD/focal plane (x, y or u, v) and sky (RA, Dec), is required to be estimated for all the exposures, and large astrometric errors could lead to a biased shear estimation (e.g., G. M. Bernstein et al., 2017). Common tools to compute the astrometric solution include SCAMP (Bertin, 2006) and PIXMAPPY[1].

The point spread function (PSF) is a function that describes how a bundle of light rays, which would be incident on a single point (e.g., a point source), spreads spatially over neighboring pixels around that point on a detector due to atmospheric distortions and/or telescope optics. It is essentially a blurring effect and can be considered as the convolution of a kernel on a true scene before these distortions. The observed image can be described as

$$I(x, y) = T(x, y) \otimes P(x, y), \tag{4.1}$$

where $T(x, y)$ is the surface brightness distribution of the true sky scene and $P(x, y)$ is the functional form of the effective PSF (a combination of optical PSF, atmospheric PSF, pixel response, and charge diffusion). This impacts the shape and size of a galaxy ($T(x, y)$), with which we would like to recover purely the distortion from gravitational lensing. If we find a way to know what the PSF is for each galaxy correctly, we will be able to remove this effect and recover the true scene by deconvolution on the observed image, as one can see in Figure 4.4. Thus, modeling the PSF effectively is crucial for accurately measuring galaxy shear.

The PSF modeling can be essentially separated into two components: 1) modeling the PSF using stars and 2) interpolating the PSF model at other positions, such as positions of galaxies. While the optical PSF can be considered to change very slowly as a function of time and be assumed to be unvarying over the extent of a single galaxy, the atmospheric

---

[1] https://github.com/gbernstein/pixmappy

Galaxies: Intrinsic galaxy shapes to measured image:

Intrinsic galaxy (shape unknown) → Gravitational lensing causes a *shear (g)* → Atmosphere and telescope cause a convolution → Detectors measure a pixelated image → Image also contains noise
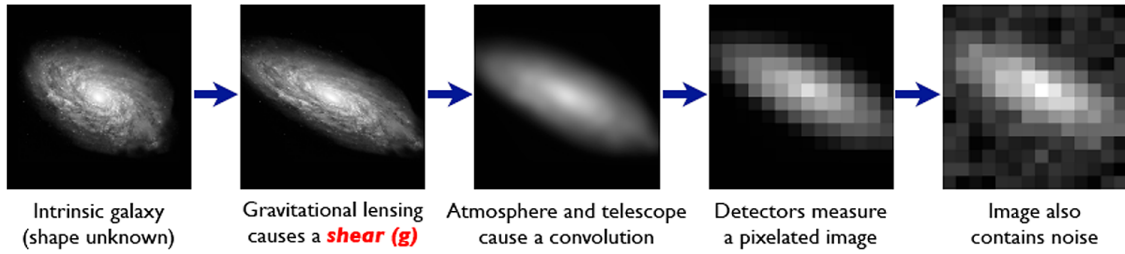
Stars: Point sources to star images:

Intrinsic star (point source) → Atmosphere and telescope cause a convolution → Detectors measure a pixelated image → Image also contains noise
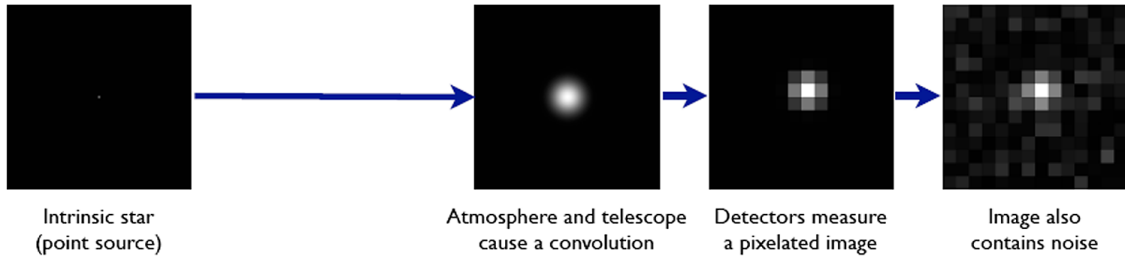
FIGURE 4.4: A schematic diagram describing the processes in which photons of a true sky scene (galaxy and star) go through and appear on an observed image. Figure 2 of Bridle et al., 2009

PSF shows a stochastic pattern. A common approach to empirically model the effective PSF is to sample bright stars in a single exposure image and describe the stars as a set of basis functions such as the Gaussian or Moffat profile. Once the PSFs are described at the positions of stars, they need to be spatially interpolated within a single CCD chip using, for example, polynomials. The more stars we are able to use in a CCD, the more accurate the interpolation is and the PSF model becomes. Methods such as PSFEx (Bertin, 2011) and PIFF[2] (Jarvis et al., 2020) are widely used in current surveys. While the stochastic behavior of the atmospheric PSF can be accounted for by some interpolation kernels such as Gaussian process regression (Figure 2 of Jarvis et al., 2020), it is challenging to model the optical PSF well with those kernels, and it is an active area of research.

Another approach is to forward-model the PSF based on the physics of optics. The idea is to calculate the PSF as a function of focal plane positions based on the physical effects such as diffraction, aberrations, obscurations, and other detector/optical effects.

[2] https://github.com/rmjarvis/Piff

While some baseline measurements of wavefront errors[3] from the telescope and detectors are required to implement the static component of the PSF model, per-exposure variation in the PSF (i.e., dynamic component) from optics and atmosphere can be fit from the pre-exposure measurement (e.g., donut exposures) and individual stars in the image. One example of this approach is the package called TINY TIM (Krist et al., 2011), which is the PSF modeling estimation software for the Hubble Space Telescope.

For ground-based observation, it is common to take an empirical approach because one needs to account for atmospheric disturbances. On the other hand, since there is no need to model the atmospheric PSF for space-based observations, space-based surveys often take the forward-modeling approach. As we will explore more in § 4.3, the reality of modeling the PSF is quite challenging, and there are many PSF systematics that can contaminate the shape measurement. Hence, several diagnostics on the PSF models have been developed, and showing that the model is robust is important. We will explore how the PSF modeling is implemented in the Dark Energy Survey in § 5.2.

4.2.2 Galaxy Identification & Measurement

Our ultimate goal is to assemble a catalog of galaxy properties (referred to as shape/shear catalog), such as magnitude, signal-to-noise (S/N), galaxy size, and shape, from images. This is normally carried out in multiple steps. Provided the calibrated single exposure images and PSF models for each exposure and CCD, the first step is to combine multiple images to create a "coadded" image (we will refer to it as a coadd or coadd image hereafter). Most of the surveys take multiple exposures of a given area in the sky in order to be able to recover areas that are spoiled by artifacts such as cosmic rays, fill in CCD chip gaps, and fully reconstruct a Nyquist-sampled image from multiple undersampled images[4], which is often the case for space-based images. By combining multiple images, one can increase the

---

[3] Wavefront errors refer to distortions in the light wavefront that deviate from the ideal or expected shape, typically caused by optical system imperfections, affecting the quality and focus of the final image.

[4] Undersampled images have a PSF that is small enough that there are Fourier modes in the image with wavenumber greater than 1/2 cycle per pixel. So then it is not possible to interpolate the images losslessly (e.g., polynomial, sinc or Lanczos interpolation does not converge as the number of points used to interpolate is increased).

signal-to-noise of a given object since the impact of some sources of noise, like electronic read noise, can be greatly reduced. This is helpful in achieving more depth for a particular survey. Averaging multiple ground-based images additionally results in better isotropy in the average atmospheric PSF in the coadded image.

For ground-based observations, a major approach is to resample all exposures in a region defined in the sky (referred to as a "tile") to a common output pixel grid (e.g., SWARP: Bertin, 2010). It essentially interpolates the input images and resamples at each output pixel grid, indicating that missing pixels due to cosmic rays or bad pixels can smoothly be handled. It requires the knowledge of WCS solution to find the projection from input to output pixels, and the choice of interpolation kernels is key to preventing artifacts in a coadd image such as the Moiré pattern. The PSFs on each exposure are also coadded similarly to form a coadd PSF. On the other hand, most space-based instruments are diffraction-limited due to the lack of atmosphere, producing images that are undersampled. Although each undersampled image is missing features/information of an object, a clever dithering strategy to take multiple exposures to reconstruct a Nyquist-sampled coadd image can losslessly recover full information. However, optimally combining information with an interpolation kernel in undersampled images is challenging because the interpolation on non-Nyquist sampled data can result in aliasing. AstroDrizzle (Fruchter and Hook, 2002) is a common software to perform a coaddition step for space-based imaging, but the method does not fully remove aliased Fourier modes, and the coadd PSF is ill-defined and may vary over the extent of a galaxy. Imcom (Rowe et al., 2011) is a linear image combination algorithm that optimizes the mapping from input to output pixels so that a well-defined PSF can be locally achieved and the correlated noise between output pixels is small. This method is currently advocated for the image coaddition algorithm for the Roman Space Telescope. We will explore this method further in § 6.3 as a part of my Ph.D. work.

Once the coadded image is obtained, galaxies need to be identified to measure their properties. Object detection is commonly performed by identifying the peaks of pixel in-

tensities above some threshold on an image. Once the peak is found, one can fit an aperture around the point to define a galaxy. If multiple peaks are found in a given region (about the size of a typical galaxy), objects are said to be "blended", and deblending (identifying which pixels/sub-pixels belong to which objects) needs to be performed. A common software is SExtractor[5] (Bertin, 2011) and it includes a simple deblending. In a real survey, a more complicated deblending needs to be performed using methods such as Shredder[6] and Scarlet (Melchior et al., 2018). "Recognized blends" may be separated into individual objects, but it is not possible to find "unrecognized blends" from a survey alone. One needs to estimate how the unrecognized blends bias our cosmology.

Once objects are detected, one can cut out individual object images from a coadd and measure their properties on the cutouts. There are roughly two classes of shear measurement techniques: moments-based and model-fitting methods. We are particularly interested in galaxy shear, which can be obtained by correcting galaxy shapes for the convolution by the PSF. Moments-based algorithms employ the concept of image moments similar to Eqn. 4.2. Although Eqn. 4.2 is the unweighted moments, in real surveys, it is always appropriate to weight the moments by some function, such as Gaussian, so that the integral can converge even in the presence of wings of the PSF. The weighted moments can be written as,

$$M_{ij} = 2\frac{\int dxdy(x - \mu_x)^i(y - \mu_y)^j w(x, y)I(x, y)}{\int dxdyw(x, y)I(x, y)}, \tag{4.2}$$

where $w(x, y)$ is the weight function. The idea is to correct the second moments of each galaxy image by the moments of the PSF (e.g., KSB: Kaiser et al., 1995, re-Gauss: C. Hirata and Seljak, 2003). Recent modifications to the original algorithm include "adaptive moments" (C. Hirata and Seljak, 2003; Mandelbaum et al., 2005), which iteratively estimate the best-fit elliptical Gaussian to the object. There are several modules to estimate shear from galaxy and PSF images such as `galsim.hsm` in GalSim (Rowe et al., 2015) and

---

[5] Useful reference on a guide to SExtractor can be found in http://star-www.dur.ac.uk/~pdraper/extractor/ Guide2source_extractor.pdf

[6] https://github.com/esheldon/shredder

`ngmix.admom` in NGMIX (E. Sheldon, 2015).

The model-fitting approach forward-models a galaxy model with model parameters (e.g., ellipticity, size, flux), convolves with the model PSF, and compares the "simulated" galaxy with the real galaxy image to find the likelihood of the model parameters. Several algorithms such as IM3SHAPE (Zuntz et al., 2013), LENSFIT (Miller et al., 2007), and NGMIX (E. Sheldon, 2015) were proposed during the Stage-II surveys under the Shear TEsting Programme (STEP; Heymans, Van Waerbeke, et al., 2006; Massey, Heymans, et al., 2007) and the GRavitational lEnsing Accuracy Testing challenges (GREAT; Bridle et al., 2009; Kitching et al., 2013; Mandelbaum et al., 2014) and developed for the Stage-III surveys (e.g., Fenech Conti et al., 2017; Jarvis et al., 2016; Miller et al., 2013; Zuntz et al., 2018). We will explore how the shape catalog is constructed in DES in § 5.3.

4.2.3 Photometric Redshift Inference

As we saw in § 3.2, Eqn. 3.27, in order to measure our effective convergence, we need to compute the redshift distribution of galaxy samples ($p(z)$) we are using to measure cosmic shear. If a redshift of each galaxy can be accurately measured, $p(z)$ can be easily calculable. As discussed in § 2.4.3, from spectroscopy, a redshift is easily identifiable given known emission lines, which we call "spectroscopic redshift" ("spec-z"). However, for lensing surveys in which we require millions of galaxies, it is not feasible to measure spectroscopy for each galaxy detected in a photometric survey. We, therefore, rely on photometry measured from multiple bandpasses to estimate the "photometric redshift" ("photo-z"). Since typical source samples used for weak lensing are deep, faint, and noisy, the accurate characterization of the redshift distribution from photometric bands is extremely difficult. It is noteworthy to mention here that weak lensing is not concerned with the point estimate of redshift for individual galaxies. We are rather interested in the redshift distribution of the ensemble of galaxies.

The depth of modern lensing surveys allows us to reconstruct the structure along the line-of-sight instead of the projected density distribution by dividing the source galaxies into

multiple redshift bins, measuring $p(z)$ for each redshift bin, and auto- and cross-correlating the galaxy shear between redshift bins (also known as "tomographic" bins). This analysis, referred to as "tomography," can drastically improve the constraints on the cosmological parameters with weak lensing (Hu, 1999).

A typical photo-z inference algorithm provides $p(z)$ as a conditional probability of a galaxy with some observable properties α being at redshift z –

$$p(z) = \sum_{j}^{all\,sample} p(z|\alpha_j) \sim \int p(z|\alpha)p(\alpha)d\alpha. \tag{4.3}$$

A relationship between the redshift and the color of a galaxy (color-redshift relation) has long been useful in providing a redshift estimate (e.g., Lima et al., 2008). Color-redshift relation from only optical-band photometry, for instance, cannot, however, break the degeneracy of color and redshift as one can see in Figure 4.5. To obtain a photo-z estimate from broad-band photometry, three relationships need to be established. The first relationship is between redshifts and galaxy spectra, which can be carried out from spectroscopic surveys or catalogs such as zCOSMOS (Lilly et al., 2009) and VIPERS (Scodeggio et al., 2018). The second is between spectra and photometry of those galaxies from a number of bands (typically more than 30 bands). For example, COSMOS15 (Laigle et al., 2016) is a 30-band photometric redshift catalog where the bandpasses span from UV to IR. The third is between multiple-band photometry and the photometry from usually a few bandpasses in a survey of interest. With these relationships, one can finally achieve photometric redshifts with high accuracy from broad-band photometry. SOMPZ (Buchs et al., 2019; Myles et al., 2021) is a recently developed algorithm, which groups galaxies into "phenotypes" based on their measured fluxes with self-organizing maps[7] and builds the color-redshift relation from a high-dimensional space with reliable spec-z, photo-z, and color relationships. Another common method is to fit the multi-band fluxes with spectral templates (e.g., BPZ:

---

[7] Self-organizing maps (SOMs) are a type of artificial neural network that uses unsupervised learning to produce a low-dimensional (typically two-dimensional), discretized representation of the input space of the training samples, organizing data into a grid that preserves the topological properties of the input space.
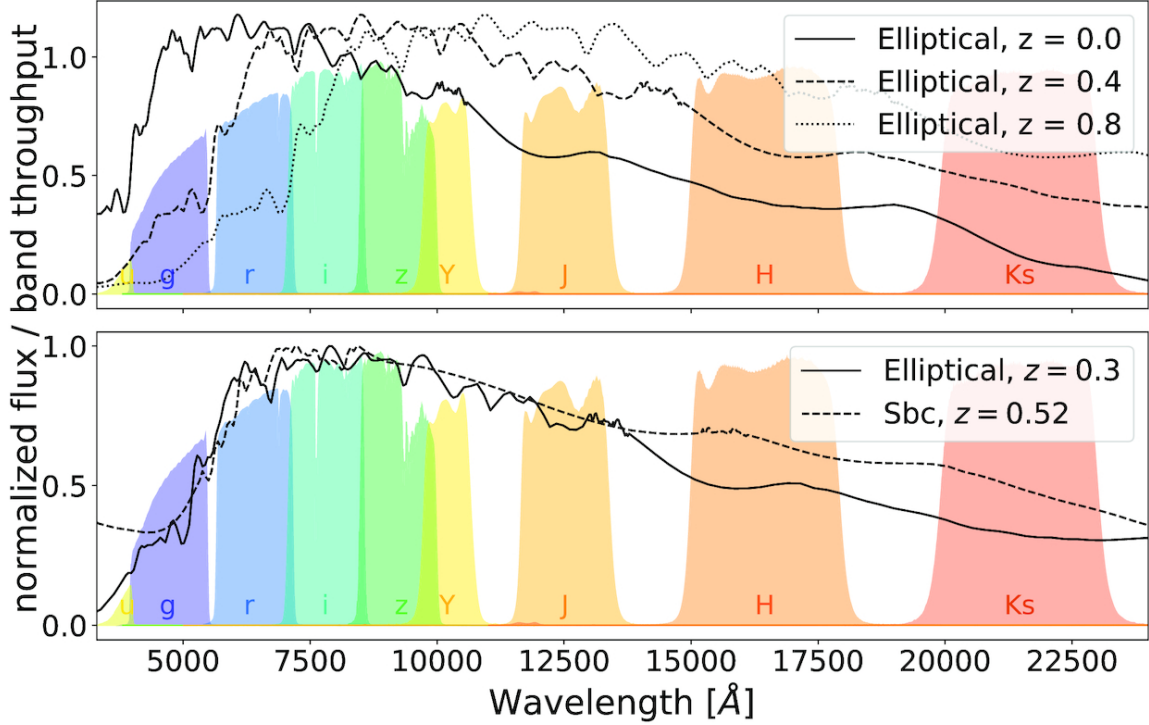
FIGURE 4.5: An illustration of the degeneracy between color/object type and redshift by showing the galaxy SEDs among several bands. If one would like to estimate the redshift of an object using optical band photometry ($griz$), the SED of an elliptical galaxy is distinguishable at different redshifts ($z = 0.0, 0.4, 0.8$) (*top*). However, two SEDs of an elliptical galaxy at $z = 0.3$ and a spiral galaxy at $z = 0.52$ are indistinguishable in optical bands, showing the degeneracy of color/type and redshift in $griz$. Figure 1 of Buchs et al., 2019

Benítez, 2000), which rely on galaxy's spectral energy distribution (SED) features such as Lyman break (at 912Å), in order to break the degeneracy between low-z and high-z galaxies (e.g., Graham et al., 2020). We will explore how the SOMPZ photo-z inference algorithm is implemented in DES in § 5.5.

4.2.4 Image Simulations

While we have introduced steps and specific techniques to produce catalogs from images, the lensing analysis on real data is known to be challenging (Mandelbaum et al., 2014), and none of these methods can yet perfectly model PSFs, recover shear, and obtain true redshift distributions in realistic data. Since these measurements are always subject to biases, the biases must be quantified in image simulations so that we can correct these biases in real

data and not infer biased cosmology. In terms of shear estimation, for decades, communities such as STEP and GREAT have dedicated efforts to estimate shear reliably. In the process, in order to test methods on a common setting, GalSim[8] (Rowe et al., 2015), an open-source image simulation software package, was developed. Once object properties (e.g., size, shape, surface brightness) and PSFs to convolve with the object are decided, GalSim can simulate images of stars and galaxies in numerous different ways.

Since image simulations can produce a realistic set of images that contain objects with known properties, such as shear at known positions, one can run the full pipeline in § 4.2.2 on simulated images to see if one can recover the true input shear. If one does not retrieve the true shear, that points to biases that likely exist in the shear catalog from real data as well.

The type of bias that we calibrate with image simulations is shear calibration bias which is associated with methods in § 4.2.1 and § 4.2.2. We quantify this bias as multiplicative (m) and additive bias (c) (Heymans, Van Waerbeke, et al., 2006) –

$$\gamma_i^{\text{obs}} = (1 + m_i)\gamma_i^{\text{true}} + c_i, \qquad (4.4)$$

where i is the i-th component of the observed and true input shear, which is a spin-2 quantity. There are multiple sources where non-zero m and c arise (e.g., noise bias, selection bias, PSF model bias). While it is possible to measure c from the data itself (ensemble average of galaxy shear estimate where expected mean shear is zero), quantifying the multiplicative bias requires a set of image simulations. Some of the shear estimation methods are able to correct for some of these biases but not all. Therefore, the calibration of the rest of the biases relies on realistic image simulations. We will explore these sources of biases in more detail in § 4.3 and how one builds realistic image simulations using an example in the Dark Energy Survey in § 5.4.

During the cosmological analysis (Markov Chain Monte Carlo analysis, read § 2.4.1 for full detail) to infer cosmological parameters that fit the observation well, multiplicative bias

---

[8] https://github.com/GalSim-developers/GalSim

is frequently used as a nuisance parameter to be marginalized over with a prior from the value from the simulations, indicating that all the expected possible shear bias scenarios are explored in the parameter space to ensure the systematic biases do not bias our cosmological parameters.

4.2.5 Measurement of two-point (2pt) Statistics

Once we produce the shear catalog and photometric redshift distributions ($p(z)$ in each tomographic bin in the case of tomography where each galaxy is assigned to a particular redshift bin), we are ready to advance to the next step "catalogs to science" by measuring the two-point correlation function of galaxy shear in the same redshift bins (known as auto-correlation) and in different redshift bins (known as cross-correlation).

The two-point correlation function can be estimated via Eqn. 3.44, but this requires computing the dot product of each galaxy pair in the bins of angular separation and averaging the product in each angular bin. This procedure however quickly becomes computationally unfeasible like $O(N^2)$, as the number of galaxy pairs increases. TREECORR[9] (Jarvis et al., 2004) handles this computation by using the ball tree algorithm. It uses tree-based data structures to organize data, allowing for rapid computation of correlations between large datasets. This algorithm partitions the data into hierarchical nodes, optimizing the process of querying distances between pairs. This method reduces the computational complexity compared to brute-force approaches, which directly calculate the distance between every pair of points. By structuring data in this way, TREECORR can average quantities of interest in each node and compute the correlation function of the averaged quantities among the nodes.

TREECORR supports various types of two-point and three-point correlations, including scalar and spin-N vector fields. In the "3x2pt" analysis mentioned in § 2.4.6, one can utilize TREECORR to compute the auto-correlation of galaxy number count (galaxy clustering), the cross-correlation of galaxy number count and spin-2 shear field (galaxy-galaxy lensing),

---

[9] https://github.com/rmjarvis/TreeCorr

and the auto-correlation of spin-2 shear field (cosmic shear), making TREECORR highly adaptable for different observational datasets. We often refer to the computed two-point correlation function as "data vector".

4.2.6 Covariance

Another component we need for the Bayesian parameter inference is the covariance matrix of the data as in Eqn. 2.48. Due to the fact that we can only observe a finite volume of the Universe and there is one realization of the Universe, known as "cosmic variance", one generally models the covariance matrix theoretically (e.g., Krause et al., 2017) or utilizes numerical simulations (e.g., Shirasaki et al., 2019). COSMOLIKE (Krause et al., 2017) is a widely utilized package to simulate data given cosmological parameters, observational and astrophysical systematics modeling, and survey conditions (e.g., survey area and geometry). COSMOCOV (Fang, Eifler, and Krause, 2020) is built on COSMOLIKE to generate a covariance matrix from the simulated data.

On the other hand, one can simulate multiple realizations of the Universe at fixed cosmology to extract the same cosmological information and measure the covariance of the simulated data. This approach is, however, computationally expensive, and one suffers from realism in terms of the simulation volume and resolution.

4.2.7 Analysis Choices & Modeling

Lastly, we must consider what cosmological and astrophysical models to use to calculate the theoretical prediction of summary statistics. Since the theoretical prediction of weak lensing observable is required to be accurate within ~1% over a wide range of scales and cosmologies to be able to achieve meaningful constraints (Huterer and Takada, 2005), one is required to have outstanding knowledge of how the matter power spectrum changes depending on cosmology and galaxy formation. We must choose a "fiducial" model with which we can carry out the likelihood analysis. In cosmic shear cosmology, the key model ingredients to consider are the linear and nonlinear evolution of the matter power spectrum due to only gravity, the impact of baryonic feedback on the matter power spectrum, and

the intrinsic alignment modeling.

4.2.7.1 Prediction of linear & nonlinear matter power spectrum

The linear evolution of the matter power spectrum is already discussed in § 2.3.2, which can be estimated using the numerical Boltzmann solver codes such as CAMB (Lewis et al., 2000). As we consider the scales where the structure formation process becomes highly nonlinear, even when gravity is the only considered force, we can no longer utilize the linear perturbation theory. There are a few approaches to tackle this. One common approach is to use N-body simulations at different cosmologies and interpolate the matter power spectrum between cosmological parameters. One achieves the matter power spectrum as a function of cosmology and can then emulate the values of the desired cosmology. A commonly used tool is BACCOEMU (Angulo et al., 2021; Aricò et al., 2021).

On the other hand, utilizing the halo model, which is an empirical galaxy-halo connection model, can be quite useful in modeling the nonlinear evolution of the structure formation. In a nutshell, the halo model views the cosmic structure as a sum of individual fields (dark matter, gas, and galaxies) and provides a prescription of how galaxies, as a tracer of matter distribution in the Universe, populate within a halo and how haloes cluster together (a review on the halo model can be found in Asgari et al., 2023). By identifying all haloes in the matter density field from N-body simulations and populating galaxies within those haloes given the model of the galaxy halo occupation distribution (Wechsler and Tinker, 2018 for a full review), one can predict the evolution of the matter power spectrum for these scales. A popular analysis tool for the halo model is, for example, HMCODE (Mead et al., 2015, 2021), which we will explore further in § 5.6 for the analysis of Dark Energy Survey data.

Another astrophysical process that can deviate the matter power spectrum from its linear prediction is baryonic feedback. The baryonic feedback is the process in which energetic feedback processes from star formation, supernovae, and supermassive black holes (i.e., AGN: active galactic nuclei) inflate the halo (Figure 4.6) and prevent matter from

An illustration of baryonic feedback
processes inflate the dark matter halos

Dark matter   Baryons
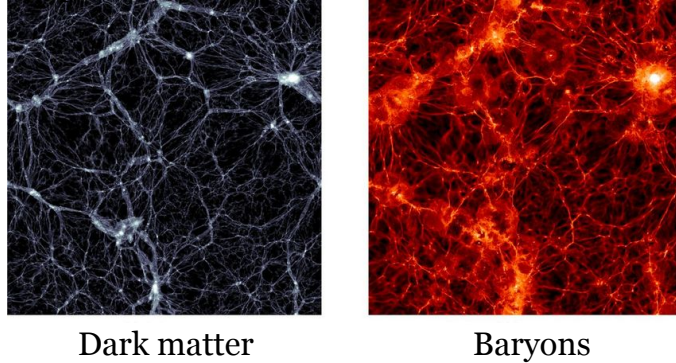
FIGURE 4.6: The distributions of dark matter and baryons in halos, simulated in the Illustris
hydrodynamical simulation (Vogelsberger et al., 2014)

falling in and collapsing is extremely difficult to model due to its complex gas dynamics, resulting in suppressing of the matter clustering over scales of $k > 0.1$ h/Mpc (e.g., Chisari et al., 2019; Semboloni et al., 2011). The left panel of Figure 4.7 shows the predicted power spectrum when considering only the linear evolution, the linear and nonlinear evolution but gravity-only, and the linear and nonlinear evolution with gravity and effect from baryons. Because we know baryons exist and have a non-negligible impact on weak lensing observable, especially the feedback from AGN, we must carefully account for the astrophysical effect.

Understanding the impact of baryonic feedback on galaxy formation has only become possible recently with the advent of high-resolution and large-volume (> 100 Mpc) hydrodynamical simulations with complex galaxy formation models (e.g., BACCO: Angulo et al., 2021, ILLUSTRIS: Vogelsberger et al., 2014, FLAMINGO: Schaye et al., 2023). The strength of baryonic feedback and the suppression of the matter power spectrum, however, vary significantly over simulations, as one can see in the right panel of Figure 4.7. Similar to the case of the nonlinear power spectrum due to gravity, we can predict the matter power spectrum by building emulators from hydrodynamical simulations (e.g., Salcido et al., 2023) that both depend on cosmologies and various feedback scenarios. This is an active area
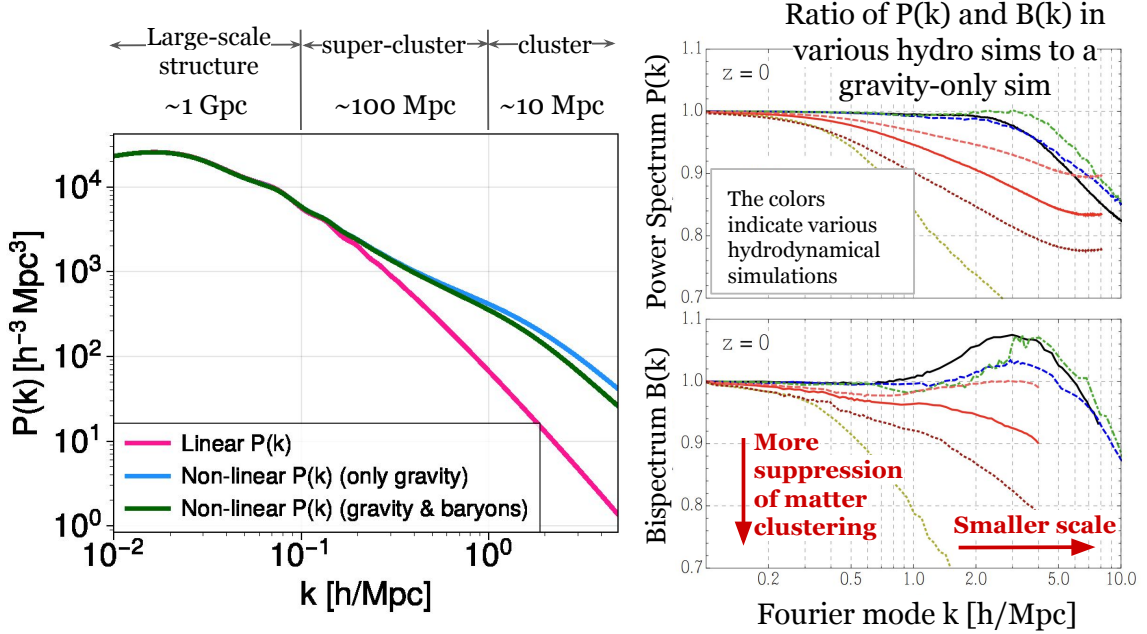
FIGURE 4.7: *Left*: Predicted power spectrum from theory (linear part) and simulations (gravity-only and with baryonic physics; nonlinear part) (Angulo et al., 2021). *Right*: A suppression of matter clustering measured in the matter power spectrum (*top*) and bispectrum (Fourier transform of three-point correlation function; *bottom*). It shows the measurements from various hydrodynamical simulations (Foreman et al., 2020).

of research. Another approach to accurately predict the power spectrum is to incorporate a model of baryon physics into the halo model. This requires parametrizing the feedback model and fitting the model with simulations or simultaneously fitting it with other cosmological parameters during the likelihood analysis. HMCODE2020 implemented a model with six parameters that include gas expulsion by AGN and star formation and a model with one feedback parameter $\log_{10}(T_{AGN}/K)$ related to feedback temperature. They achieved predicting the suppression of the power spectrum with accuracy $< 1\%$, compared with the suppression expected from BAHAMAS hydrodynamical simulations (McCarthy et al., 2017).

4.2.7.2 Intrinsic alignments

We have so far assumed that galaxies are randomly oriented (§ 3.3.1) so that the ensemble average of galaxy shapes is zero. Nonetheless, galaxies can be oriented in a particular way in their local gravitationally-bound environment and create a coherent correlation be-
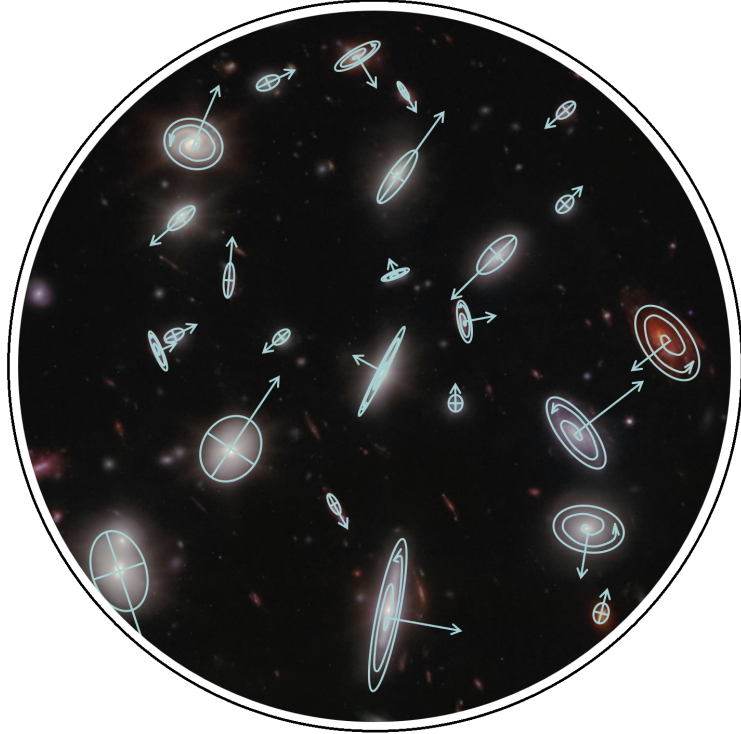
FIGURE 4.8: Galaxy shapes and orientations in a JWST's NIRCam image of Abell 2744. Figure 1 of Lamman et al., 2024. Reproduced under the terms and conditions of the Creative Commons Attribution-NonCommercial-No Derivatives License (CC BY NC ND)

tween galaxy shapes (Figure 4.8). We refer to this coherent physical alignment of galaxies as intrinsic alignments (IAs). Since intrinsic alignments produce correlations between galaxy shapes seen in images that are not caused by gravitational lensing, they are often treated as contaminants to the underlying matter distribution. For a full review on intrinsic alignments, read Joachimi et al., 2015; Kiessling et al., 2015; Kirk et al., 2015; Troxel and Ishak, 2015.

If one is able to parameterize and model how galaxies align themselves gravitationally, we can fit the IA parameters as the contamination to the observed shear power spectrum. Or, if one is able to calibrate the IA parameters with simulations, we can add the expected amount of contamination to the predicted shear power spectrum. In practice, although N-body simulations show that dark matter haloes intrinsically align, the way galaxies align themselves in dark matter haloes is not exactly known (Heymans, White, et al., 2006),

given the difficulty of limited observational constraints (e.g., Samuroff et al., 2023) and potential disagreement among large hydrodynamical simulations (e.g., Chisari et al., 2015; Tenneti et al., 2015).

Current cosmological analyses utilize a few IA models such as NLA (nonlinear alignment) model (Bridle and King, 2007; C. M. Hirata and Seljak, 2004) and TATT (Tidal Alignment and Tidal Torquing) model (Blazek et al., 2019) as a contaminant to the shear power spectrum predicted by gravitational lensing and simultaneously fit the IA parameters in the models with other cosmological parameters (e.g., Amon et al., 2022; Secco et al., 2022).

4.3 Challenges I: Observational Systematics

As discussed in § 2.4.2, in the era of precision cosmology with weak gravitational lensing, systematic biases pose significant challenges to infer unbiased and accurate cosmology that must be addressed carefully. Each survey prepares a science document that describes the mission requirements on systematic biases in order to achieve its science goals, given the statistical capability of the survey. We call this "error budget," and the requirements on various systematic biases, such as shear calibration bias, are quantified. Although we have studied the modern cosmological analysis pipeline that brings "images to catalogs" and "catalogs to science", the methods and techniques were developed with the motivation to mitigate intolerable systematic biases given the error budget. In this and the next section, we will dive into systematic biases that arise due to how we measure the cosmological observables (called "observational systematics") and how we model the Universe (called "astrophysical systematics"). Observational systematics are quantified in terms of the shear calibration bias (m, c), which results from anything from PSF modeling to shape measurement, and photo-z calibration bias (Δz – mean redshift offset in each tomographic bin and σ_z – the width of the redshift bin), which stems from photo-z estimation algorithms. Table 4.1 presents the requirements for these biases for the Dark Energy Survey (as a representative of the Stage-III surveys) and for the Stage-IV surveys. We will examine these sources of

Table 4.1: Measured systematics (DES Y3; MacCrann et al., 2021) and the requirements on observational systematics for different Stage-IV survey. Roman: Doré et al., 2018, LSST:The LSST Dark Energy Science Collaboration et al., 2021 Note that the mean shift in the Dark Energy Survey is shown for four tomographic bins.

Survey	m	c	$\Delta z_i/(1+z)$	σ_z
Dark Energy Survey	-2.1×10^{-2}	-1.1×10^{-4}	0.35,0.44,0.48,0.52	—
LSST	3.0×10^{-3}	—	0.001	0.003
Roman	3.2×10^{-4}	2.7×10^{-4}	0.002	—

the biases individually.

4.3.1 PSF Modeling

The PSF modeling plays an integral role in achieving a robust shear measurement. In order to obtain accurate PSF models, one needs to consider the factors below. We will investigate them in further detail.

- detector effects – Are detector effects corrected on the images to model the PSF from or taken into account during the modeling process?

- astrometric solution – Do the stars selected for modeling the PSF have an accurate astrometric solution?

- selection of stars – Is the sample of selected stars pure? Does it contain any galaxies?

- atmospheric PSF – How would one model the atmospheric part of the PSF?

- optical PSF – How would one model the optical part of the PSF?

- chromatic PSF – How would one treat the wavelength dependence of the PSF?

First of all, there are several detector effects that could undermine the PSF models. Luminosity-dependent effects such as the brighter-fatter effect (Antilogus et al., 2014; Guyonnet et al., 2015) can cause the overflow of the photons of objects to the neighboring pixels. Since the overflow only happens for bright objects such as stars we utilize to estimate the PSF and not for typical galaxies, the PSF models estimated utilizing these stars would be biased for galaxies, especially low S/N galaxies which are dominant in shear catalog (Jarvis et al., 2016; Melchior et al., 2015). Corrections at the image level are necessary and can be

carried out to show that the PSF residuals (the difference between the true PSF and PSF model) can be reduced under the requirement for the weak lensing survey (e.g., Coulton et al., 2018; Walter, 2015).

It is known that some detector effects such as "tree rings" impact the astrometric solution (Plazas et al., 2014), and astrometric distortions caused by optics and atmosphere can lead to significant bias in the PSF models (Jarvis et al., 2016). While the astrometric solution is calibrated well enough so that the errors do not impact cosmic shear measurement in the Stage-III surveys (e.g., G. M. Bernstein et al., 2017), the Stage-IV surveys need to address this carefully (e.g., Esteves et al., 2023). Tools like Pixmappy are able to correct for various astrometric distortions by fitting for the effect such as tree ring, telescope distortion, and edge distortion in the model. The WCS solution from Pixmappy has improved the residuals of the PSF shapes for Dark Energy Survey (Jarvis et al., 2020).

In order to begin modeling the PSF, one must identify and select stars in the images. The inclusion of non-stars or problematic stars in the sample can result in large PSF model residuals. One can identify stars in various ways: 1) apply object detection on an image and measure magnitude vs size, 2) utilize external catalogs such as Gaia (Gaia Collaboration, 2018) and VISTA-VIKING (Edge et al., 2013). Figure 4.9 shows the size-magnitude diagram (left) where a locus of points with a constant size are stars and the color-color diagram (right) with a near-infrared filter where the collection of bottom-right points are stars. Out of these "candidate" stars, one would exclude problematic objects such as saturated stars and low S/N stars. At this point, one can reject objects that are affected by detector effects and that do not have an accurate astrometric solution. We will see the current state-of-the-art with an example in Dark Energy Survey in § 5.2.

Modeling the atmospheric PSF has been a challenge for ground-based telescopes. Because the direction and magnitude of atmospheric disturbance can change over the scale of the focal plane, the PSFs evaluated at the positions of galaxies can show residuals if the stars with which the PSF models are estimated are far from the galaxies in the CCD. Left untreated, the stochastic behavior of the atmospheric PSF can impact the cosmic shear
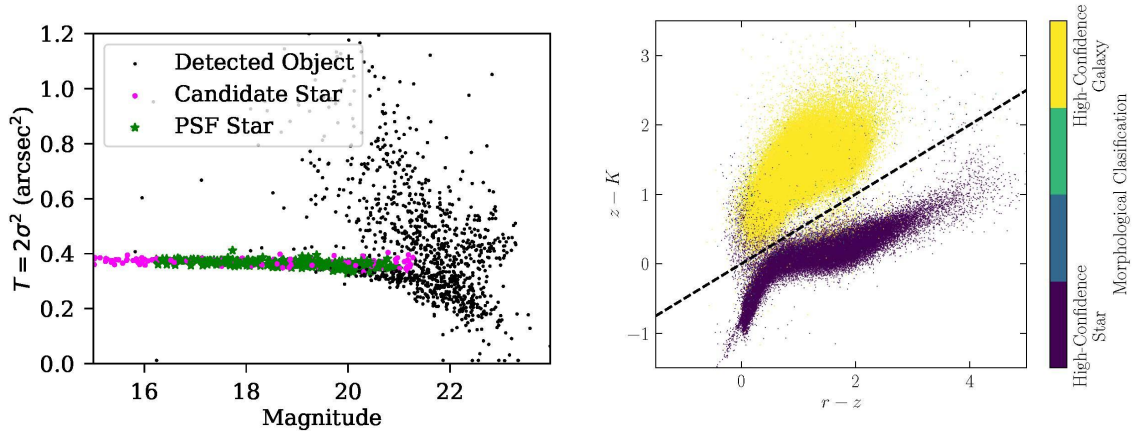
FIGURE 4.9: Methods to identify the PSF stars. *Left*: The size-magnitude diagram can identify the stellar locus within the survey. *Right*: utilizing the photometry of stars from near-infrared surveys can be useful in increasing the purity of the stellar sample. Figure 3 and 6 of Jarvis et al., 2020

measurement for Rubin (Léget et al., 2021). Although utilizing a Gaussian process interpolation algorithm can mitigate the residuals on the atmospheric part of the effective PSF (Jarvis et al., 2020; Léget et al., 2021), it does not yet work well with the optical component of the PSF. Rubin Observatory plans to construct the effective PSF by separately modeling the atmospheric and optical parts and convolving them. With the real-time and historical weather data, Hébert et al., 2024 has provided a tool to model the atmospheric component of the PSF. For the optical component, the static part (e.g., PSF discontinuity, wavefront error) can be identified by averaging over previous images, and the dynamic part (e.g., telescope and optics disturbance) can be iteratively fit during the PSF modeling process for each new image.

Lastly, there are several optical and atmospheric effects that induce the PSF to be wavelength-dependent (Meyers and Burchat, 2015; Plazas and Bernstein, 2012). When the PSF is wavelength-dependent, the PSF model that is estimated with stars' SEDs needs to be wavelength-dependent, and the model needs to be evaluated with a galaxy's SED when the galaxy shape is measured. We will call the impact of wavelength-dependent PSF on both steps chromatic effects. Particularly, the differential chromatic refraction (DCR) and the wavelength dependence of seeing are dominant chromatic effects that can bias the

Effect #1: DCR

Zenith

$R_{450\text{nm}} - R_{650\text{nm}} \approx 0.9"$

λ_{blue}

λ_{red}

Atmosphere

Earth

Effect #2: λ-dependent seeing

g r i z

1"
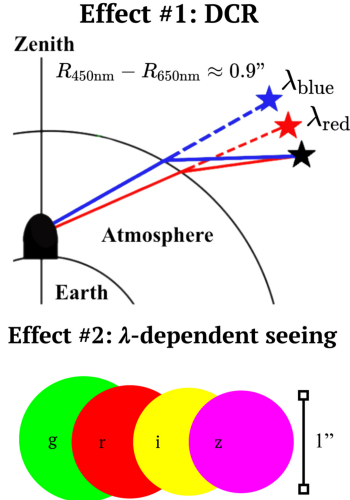
FIGURE 4.10: A schematic diagram of the differential chromatic refraction (DCR) effect (*top*) and the chromatic seeing effect (*bottom*) for *griz* bandpasses. If a blue and red star are in the same position in the sky (black), the apparent position of the blue star becomes slightly higher up towards the zenith than the red star since the bluer photons are refracted more by the atmosphere. The relative difference in the amount of refraction for photons with 450nm and 650nm at the airmass of 1.4 is 0.9 arcseconds. On the other hand, atmospheric disturbances cause the PSF size to increase as the wavelength of the filter decreases. Figure 1 of Lee, Acevedo et al. 2023 ©reproduced by permission of the AAS.

future cosmic shear measurement (Meyers and Burchat, 2015). Figure 4.10 illustrates the schematic diagram of both the DCR and chromatic seeing effects. In the DCR, bluer photons are refracted more by the atmosphere than red photons, and their apparent positions in the sky tend to be more toward the zenith. On the other hand, atmospheric disturbances smear out bluer photons, causing the PSF size to be dependent on color. Figure 4.11 illustrates the more quantitative picture of the DCR and chromatic seeing. The DCR is shown with the left y-axis, indicating the amount of refraction as a function of wavelength at each zenith angle. The chromatic seeing is shown with the right y-axis, indicating that the relative PSF size (r_{PSF}) increases as the wavelength of the filter decreases following the power law, $\lambda^{-0.2}$.

Most of the current analyses model the PSF without color dependence. The shear bias arising from not modeling the chromatic effects is relatively small compared to other sources of shear bias and the overall error budget for the current analyses. However, the chromatic
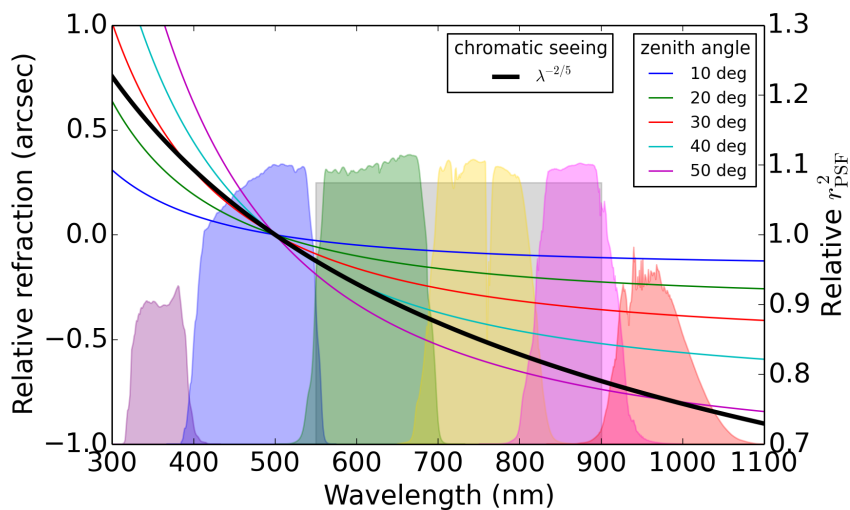
FIGURE 4.11: Wavelength dependence of the differential chromatic refraction (colored line and left y-axis) and the chromatic seeing (black line and right y-axis). Figure 1 of Meyers and Burchat, 2015 ©reproduced by permission of the AAS.

effects will become significant sources of shear bias for the Stage-IV surveys, and hence, mitigation strategies are needed. This is an active area of research, and we will explore the first example of modeling the color dependence in the Dark Energy Survey and show the improvement in the PSF models in § 5.2.

4.3.2 Shear Estimation

As is the case with the selection bias, shear estimation algorithms are subject to multiple biases – one of which is "noise bias". In the presence of pixel noise and PSF, the noise bias is incurred with any shape estimator since ellipticity is not a linear function of pixel intensities, and the bias is dependent on the S/N of the object (e.g., C. Hirata and Seljak, 2003; Kacprzak et al., 2012; Melchior and Viola, 2012; Refregier et al., 2012).

Another bias, which started arising as shape measurement algorithms evolved from moments-based algorithms, is "model bias." When a parametric galaxy model is fit to the real observed galaxy, the model cannot always capture the complexity of the light profile of the galaxy. By simplifying the real profile and limiting the flexibility of the model, one can incur a model bias on the estimated galaxy shapes (e.g., Kacprzak et al., 2014; Melchior

et al., 2010; Voigt and Bridle, 2010).

These biases were identified to cause a few percent of shear calibration bias during the Stage-II surveys, and the lensing community has dedicated efforts to develop new unbiased shear estimation algorithms and mitigate/self-calibrate these biases for the Stage-III surveys. During the STEP and GREAT challenges, the METACALIBRATION (E. Huff and Mandelbaum, 2017; E. S. Sheldon and Huff, 2017) method has been developed and shown to calibrate these biases sufficiently for the Stage-III surveys. METACALIBRATION essentially estimates a calibration factor called the shear response (i.e., the relationship between the observed and true shear) without the need to use simulations of the data (we will discuss in full detail in § 5.3 and § 6.2). Nonetheless, with the advent of GALSIM (Rowe et al., 2015), it has become conventional to develop realistic image simulations during the shear analysis and calibrate the biases in the end because there might be other biases we are not aware of. Indeed, the shear-dependent detection bias (C. Hirata and Seljak, 2003; Kannawadi et al., 2019) was identified to cause the majority of the shear bias in the Dark Energy Survey Year-3 analysis. They have found it because the shear bias determined from the image simulations was above the expected level of shear bias from METACALIBRATION. As a rule of thumb, it is best to keep the known biases in the shear catalog smaller by utilizing a self-calibrating shape measurement algorithm and best to use the image simulation suite to calibrate other unknown and residual biases that are not calibrated by the measurement algorithm.

4.3.3 Galaxy Selection

In order to extract cosmological information from galaxies, one needs to be sure that the shear and photometry measurements for each galaxy can be trusted. One way to avoid problematic objects is to mask bright stars and foreground objects, including nearby galaxies. Diffraction spikes and bleed trails of bright stars can lead to fake detections of objects and can mess up the photometry of objects whose light is blended with the light of stars. Extended light from bright foreground objects can also contribute to false detections,

which we can remove via masking around these foreground objects. These masks can be constructed from external catalogs such as Gaia (Gaia Collaboration, 2018) and Hyperleda (Paturel et al., 2003). We will explore the example of masks and the impact on shear calibration in DES in § 5.3.

An additional way to select a pure galaxy sample and perform quality assurance on the sample is to select objects based on the measured properties. These include signal-to-noise ratio (S/N), size, magnitude, and color. For example, a ratio of PSF size and object size (size ratio) can be utilized to identify stars because the size ratio of stars should be close to zero. We often refer to this selection as star-galaxy separation. When we select galaxies, however, one must be aware of "selection bias". Selection bias occurs when the sample used in a study or analysis is not representative of the population intended to be analyzed, leading to skewed or biased results. In cosmic shear analysis, the population of interest is the galaxy sample where the average intrinsic ellipticity is zero. If we select galaxies based on their shapes, this leads to a selection bias. Even if the selection is not explicitly based on the shapes, other quantities can happen to depend on the shapes through the complex image analysis pipeline. Shape measurement algorithms can additionally produce galaxy shapes that are preferred in one direction or another due to detector effects and imperfect PSF correction.

As for the case of noise and model bias, METACALIBRATION can also self-calibrate the selection bias by measuring the shear response for selected samples (which we call selection response). For full detail, readers may refer to § 3 of E. S. Sheldon and Huff, 2017.

4.3.4 Photo-z Calibration

We briefly cover the challenges associated with photometric redshift calibration and mention how these can be addressed. In order to provide unbiased cosmological parameters, we rely on the accurate estimation of the redshift distributions of source galaxies. The raw $p(z)$ is often systematically biased, and so the calibration of $p(z)$ or the mitigation of the bias needs to be addressed. For weak lensing, the shift in mean redshift for each tomographic

bin and the scatter/width of the bin greatly impact the inferred cosmology (Hildebrandt et al., 2012; Hoyle et al., 2018).

As described well in Myles et al., 2021, the main sources of uncertainties are not in the redshift calibration method itself but in the completeness and calibration of various galaxy samples utilized in the methods (Hildebrandt et al., 2017). The primary ones are

- the incompleteness and sample variance of spectroscopic/redshift, the many-band photometric sample (e.g., COSMOS2015), and the multi-band deep-field sample. These samples are often observed in a small area of the sky and the redshift sample is particularly more incomplete in high redshift.
- the photometric calibration of the many-band and multi-band deep-field galaxies.
- the degeneracy in the color-redshift relation of the wide-field galaxies.

While mitigating the incompleteness and sample variance cannot be done so easily and requires new observations, methodological improvements can improve the photometric calibration (e.g., BALROG) and lessen the degeneracy (e.g., better photometry of wide-field galaxies, measurement of more photometric bands, and the inclusion of near-infrared data). Additionally, blending can impact the normalization and the shape of the redshift distributions. We will explore this further in § 4.3.5.

In addition to these methods, the $p(z)$ can be robustly validated using other methods such as clustering redshifts (e.g., Gatti, Giannini, et al., 2021), and we can characterize the uncertainties using image simulations as is the case with shear calibration (e.g., MacCrann et al., 2021).

4.3.5 Blending

While METACALIBRATION can self-calibrate multiple biases that occur due to the fact that the galaxy sample for weak lensing is noisy, pixellated, and poorly resolved due to PSFs, biases related to blending has recently been found to be unable to calibrate with METACALIBRATION during the Dark Energy Survey Year-3 analysis (MacCrann et al., 2021; E. S. Sheldon et al., 2020). While the level of multiplicative shear bias due to blending

is 1-2%, which satisfies the requirement for the current surveys, this will exceed the error budget for future surveys like LSST and need to be well characterized as the rate of blending increases with survey depth (Dawson et al., 2016).

There are different kinds of biases and mitigation strategies for blending. For isolated objects, detection is not in and of itself a source of bias, and METACALIBRATION is unbiased at high precision for this case. For mildly blended objects that are recognizable, one can build multiple deblended objects using model fits from tools like SHREDDER and SCARLET. If objects are at the same redshift and the shear estimation from deblended objects is unbiased, the shear can be calibrated as an ensemble object since the lensing contribution is the same. Approaches to help properly deblend objects and mitigate the bias are in active areas of research, especially utilizing the complementarity between ground-based and space-based observation. However, for recognized blends where the components in the ensemble system are at different redshifts, the estimated shear and photo-z can be problematic without care. Fundamentally, the calibrated shear of the object in a blend has mixed calibrations from different redshifts and a method like METACALIBRATION becomes a biased estimator in the presence of blending. One way to avoid this is to remove objects that are blended, but this quickly becomes unfeasible as the rate of recognized and unrecognized blends for future surveys like LSST exceeds 60% (Sanchez et al., 2021).

There are multiple ways that the blending impacts the estimated shear. As explored briefly in § 4.3.3, neighboring fluxes and certain shear-dependent masking of foreground objects can contaminate the signal of interest and lead to a bias in the shape measurement step. If one tries to measure the shear response for one object in the two-component blend, it will be biased because it contains information about shear from another redshift. Another bias stems from the detection step when a detection algorithm detects objects depending on shear, or the combination of detection and deblending assigns the peaks of multiple objects depending on shear. This is called the shear-dependent detection bias, and it is fully described in E. S. Sheldon et al., 2020. The redshift distributions of source galaxies, on the other hand, can be biased when the contaminated photometry of blended objects biases

the assignment of photo-z to individual objects and skews the total redshift distribution. The miscalibration of shear additionally affects the calibration of $p(z)$ through the shear response. Blending hence couples the relationship between γ and $p(z)$. MacCrann et al., 2021 is the first analysis that has explored the effect of blending on the combination of shear and photo-z calibration.

While the shear-dependent detection bias can be mitigated on the data using the method called METADETECTION described in E. S. Sheldon et al., 2020, the residual bias from cross-redshift blends needs to be fully characterized in the image simulations. In a tomographic cosmic shear measurement, the mean observed shear $\gamma^{\text{obs}}(\boldsymbol{\theta})$ at angular position $\boldsymbol{\theta}$ can be written as an integral of the true shear field as a function of redshift $\gamma^{\text{true}}(\boldsymbol{\theta}, z)$ weighted by a redshift distribution $p(z)$;

$$\gamma^{\text{obs}}(\boldsymbol{\theta}) = \int dz p_\gamma(z) \gamma^{\text{true}}(\boldsymbol{\theta}, z) + c, \tag{4.5}$$

where c is the additive bias and $p_\gamma(z)$ has now absorbed the multiplicative bias, referred to as effective redshift distribution. In the case of isolated galaxies, $p_\gamma(z) = (1 + m(z))p(z) = R(z)p(z)$ with the multiplicative shear bias (m) and the shear response (R). Since META-CALIBRATION can estimate unbiased R for isolated galaxies, $p_\gamma(z)$ can also be calibrated accordingly. For the case of blended galaxies, we cannot decouple $p_\gamma(z)$ into the bias from shear and photo-z calibration, and the shear response attributed from blending cannot be estimated from METACALIBRATION alone because one requires rebuilding individual components of a blend at high precision to disentangle fluxes and shear at different redshifts. Yet, one can write the effective redshift distribution as a functional derivative of observed and true shear from Eqn. 4.5,

$$p_\gamma(z) = \frac{d\gamma^{\text{obs}}}{d\gamma^{\text{true}}(z)}, \tag{4.6}$$

which can be estimated from image simulations. This can be measured with sets of simulations where the applied shear depends on the redshift of the input galaxy, unlike the traditional simulations with constant shear for all redshifts. As long as the rate of blending

is rare or mild, the difference between $R(z)p(z)$ and $p_\gamma(z)$ should be small. In DES Y3 analysis, a non-negligible difference was found, and the correction to the multiplicative bias and the mean redshift for each tomographic bin was derived and applied in the end. We will discuss this in detail with an ongoing effort in DES Y6.

4.4 Challenges II: Astrophysical Systematics

As we have described earlier in § 4.2.7, our theoretical prediction of the lensing statistics depends a lot on which astrophysical model we use to describe the Universe. Our inferred cosmological parameters would be biased if we used the wrong astrophysical description. These biases attributed to astrophysical modeling are referred to as astrophysical systematics. Unlike observational systematics, this is an opportunity to be able to test and discover different models of non-standard dark matter (e.g., axions) and astrophysical processes on a cosmological scale, given the statistical power of the observational data. In this section, we will revisit the sources of astrophysical systematics – nonlinear matter power spectrum, baryonic feedback, and intrinsic alignment, and discuss the current limitations and mitigation strategies.

4.4.1 Nonlinear Matter Power Spectrum

First of all, we must understand how the nonlinear evolution of structure on small scales modifies the matter power spectrum that is described by the linear perturbation theory. In this section, we only consider the nonlinear evolution of dark matter fluctuations. The evolution of total matter (dark matter and baryons) fluctuations will be covered in the next section. The analytical calculation of the nonlinear perturbation theory becomes intractable at some point, and one needs a different approach. While the emulator-based approach such as BACCOEMU or the halo model approach are often employed in the analyses of the current surveys, the model space, resolution, and box size of the current cosmological N-body simulations (with collisionless dark matter) to emulate from and to be fit with the model prevent one from building a robust model and fitting the parameters at high precision.

Despite the current limitations, we can test the robustness of the model choice to the observation in various ways. By "robustness", we mean that the fiducial analysis choice of the model should not shift cosmological parameters in the presence of different observational and astrophysical systematics for a particular dataset. The model needs to be flexible enough but still constraining. In order to validate that, the use of synthetic/simulated data vectors is useful. CosmoSIS (Zuntz et al., 2015) is a publicly available and widely utilized software framework designed to facilitate the inference of cosmological parameters from observational data. The tool is built with flexibility in mind, allowing users to easily combine different cosmological and astrophysical models and datasets through a configuration-driven approach. CosmoSIS operates by linking together a series of modules, each responsible for a specific aspect of the cosmological analysis pipeline. This modular structure enables one to customize their analysis workflows, easily swapping in new models or data without altering the overall infrastructure. The modules can range from different structure evolution models to MCMC samplers. With this in hand, one can build a theoretical model framework and produce lensing observables by selecting a model for each step (e.g., initial power spectrum, linear perturbation theory, nonlinear power spectrum, and baryonic feedback) and including a redshift distribution. Utilizing a few more modules, one is also able to add observational systematics to the synthetic data vector that matches a survey. One can generate a synthetic data vector with a model and test the robustness of the model by contaminating the data vector with different models and running a parameter inference. We will see the examples of these validations for the Dark Energy Survey in § 5.6.

4.4.2 Baryonic Feedback

While the computational power is the bottleneck for the nonlinear evolution of dark matter-only clustering, the evolution and suppression of matter clustering due to baryonic feedback involve complex baryonic physics, which cannot be simulated without a prescription of the feedback process (e.g., how far the feedback pushes baryons in the dark matter halo). It is an active area of research that explores the feedback process in hydrodynamical

simulations based on X-ray observation (e.g., Schaye et al., 2023).

A commonly employed strategy to avoid having to model the impact of baryonic feedback on the matter power spectrum is not to use the data that might be impacted by the feedback process. These scales are usually $k > 0.1$ h/Mpc, which can range from $2 - 100$ arcmin in angular scales depending on the combination of tomographic bins and ξ_+ or ξ_-, indicating that considerable amount of data points are discarded from the fiducial analysis. In the case of DES Y3, $\xi_\pm$ was measured from 2.5 to 250 arcmin with 20 logarithmic bins for four tomographic bins (a total of 400 data points), and the fiducial scale cuts cut this down to 167 (ξ_+) and 60 (ξ_-) data points (Amon et al., 2022). This led to a decrease of the signal-to-noise of the DES cosmic shear measurement of 30% compared to the data vector without scale cuts. This is necessary until we have a better understanding of the baryonic effects. However, as future experiments will observe billions of galaxies, we must not waste this small-scale correlation that has a wealth of cosmological information.

There have been multiple studies to simultaneously constrain baryonic feedback parameters along with cosmological parameters without scale cuts (e.g., Aricò et al., 2023; García-García et al., 2024). They have shown that the constraining power of cosmological parameters slightly increases, and utilizing small scales provides hints at constraining a few feedback process parameters on a cosmological scale. Some of these studies (e.g., McCarthy et al., 2023) have additionally attempted to resolve the "S_8 tension" by changing the feedback model and modifying the power spectrum, but it is still uncertain whether correctly modeling the baryonic feedback can resolve the "S_8 tension" or if there is new physics behind it.

While these results are well-motivated and meaningful, they do not provide a new perspective on the interplay of cosmology and astrophysics because our astrophysical models are "conservative" and not robust enough. For future surveys to provide more insights, a better understanding of the feedback model within the framework of theory, simulations, and multi-wavelength observations (e.g., X-ray, CMB) must be pursued.

4.4.3 Intrinsic Alignments

Intrinsic alignments have been a notoriously difficult problem that contaminates the true lensing signal by producing galaxy shape correlations that are not due to gravitational lensing by large-scale structure in the Universe. The effort to mitigate this can broadly be categorized into 1) direct constraints on real data, 2) simultaneous constraints on real data, and 3) simulation-based constraints.

One is able to measure the IA signal directly from real data with precise redshifts and galaxy shapes if they can differentiate physically close galaxies. Luminous red galaxies (LRGs) from spectroscopic surveys (e.g., SDSS) and photometric surveys (e.g., DES and KiDS) have also been used to measure the IA signal (e.g., Fortuna et al., 2021; Samuroff et al., 2023; Singh et al., 2015). Admittedly, these measurements were carried out with a limited galaxy sample (a part of color-luminosity-redshift space) to ensure the precise redshifts and galaxy shapes, so they are not representative of the typical galaxies utilized for lensing analysis. This essentially limits the use of these results in the current cosmological analysis. For a complete galaxy sample, a new spectroscopic survey like DESI will play a significant role and obtaining accurate photo-z from photometric surveys should be highly prioritized.

Secondly, recent cosmological analyses with weak lensing have used an IA model to simultaneously constrain the IA parameters as well as the cosmological parameters (e.g., Secco et al., 2022). While the IA constraints from various surveys agree fairly well with each other, the constraining power is still limited with current data.

Lastly, numerous studies have explored the intrinsic alignments in both dark matter-only simulations (e.g., Harnois-Déraps et al., 2021) and hydrodynamical simulations (e.g., Horizon-AGN: Chisari et al., 2015, MassiveBlack-II: Tenneti et al., 2015, MilleniunTNG: Delgado et al., 2023). All of these measurements show a clear signal of intrinsic alignments for elliptical galaxies and a weaker signal for spiral galaxies that are consistent with measurements from observation (e.g., Samuroff et al., 2023). These are then fit with the IA

model to determine the IA parameters. With the use of simulations, they are also able to show the dependency of the IA signal on redshift, galaxy, and its environment. Although the uncertainty of the results has significantly improved with the high resolution and large simulation volume, the realism of the simulations (e.g., realistic galaxy sample) could hinder us from utilizing the measured IA parameters in the simulations as priors for cosmological analysis. Because of the uncertainty in the baryonic feedback process and the still unknown relationship between IA and baryonic feedback (which depends on sub-grid assumptions), one needs to take a conservative approach of widening the IA parameter prior range during the cosmological parameter inference. Given these uncertainties, another approach attempts to populate dark matter halos in DM-only N-body simulations with galaxies with a "semi-analytic" IA model (Joachimi, Semboloni, Bett, et al., 2013; Joachimi, Semboloni, Hilbert, et al., 2013) that is calibrated with real observation (e.g., Hoffmann et al., 2022; Van Alfen et al., 2023). By assigning intrinsic galaxy shapes to galaxies given the relationship between the properties of dark matter halos and the photometric properties of galaxies in the IA model, one is able to generate shape catalogs of galaxies with IAs and realistic photometry matched with a real survey since one can choose the photometry of galaxies to populate the halos. This approach is computationally much less expensive and depends less on sub-grid assumptions, yet is shown to produce consistent results with hydrodynamical simulations.

For future surveys, with better constraints on IA parameters from direct IA measurement from spectroscopic surveys like DESI and the calibration from simulations, we should be able to have better IA priors so that our cosmological constraints are less limited by IA systematics.

5

Applications to the Dark Energy Survey Year-6 Data

In Chapter 2, 3, and 4, we explored the fundamental principles of cosmology, weak gravitational lensing and the observation and standard pixel-to-cosmology pipeline of cosmic shear, as well as the challenges we have faced and must be addressed for future surveys. In this section, we will explore the observation of cosmic shear in the Dark Energy Survey Year-6 data, which will be the legacy analysis of all the DES data. During my PhD, I have contributed to several parts of the pixels-to-cosmology pipeline of the final cosmological analysis with DES data. Since 2021, I have co-led the shear and image simulations analysis team with Theo Schutt and have contributed to the "images to catalogs" process – the production and validation of the coadd images and weak lensing shape catalog (Yamamoto et al. in prep.) and the development of image simulations (Becker, Mau et al. in prep.). Additionally, since 2023, I have co-led the cosmic shear analysis team with Simon Samuroff and have contributed to the "catalogs to science" process – the production and validation of shear two-point correlation functions and the modeling of cosmic shear signal (DES Collaboration et al. in prep.). The following sections will look into the collaborative effort to take the DES images and produce cosmological parameter constraints. This includes my own work and those of others within the Dark Energy Survey and the Year-6 Key Project

(Y6KP), and I will acknowledge each collaborator's contribution in each section.

5.1 Dark Energy Camera and 6 Years of Images

Initiated in August 2013 and concluding its observations in January 2019, DES employed the 570-megapixel Dark Energy Camera mounted on the Blanco 4-meter telescope at Cerro Tololo Inter-American Observatory in Chile (Figure 5.1). DES leverages the advanced Dark Energy Camera (DECam; Flaugher et al., 2015) to observe hundreds of millions of galaxies, aiming to understand dark energy and the Universe's expansion. The camera's design was driven by DES's scientific requirements, necessitating sensitivity to light from distant galaxies while covering large sky areas. Its field-of-view (FoV) is 3 $\deg^2$, and the camera is equipped with 62 CCD sensors where each CCD contains 2048 x 4096 pixels with a pixel scale of 0.263 arcsecond/pixel. The images were taken with five filters ($grizY$), which span 400 nm to 1080 nm to capture a wide spectrum of colors. DES started with its official survey/observation in 2013 following the Science Verification (SV) and finished the six-year survey in 2019. This survey covered approximately 5,000 square degrees of the southern sky, capturing detailed optical and near-infrared images of over 500 million galaxies and thousands of supernovae (e.g., DES Collaboration et al., 2021, Bechtol et al. in prep.). A series of data releases and analyses have been carried out by the DES collaboration. The cosmological analysis with the first year of data is referred to as the Year-1 (Y1) analysis (DES Collaboration et al., 2018), the one with the three years of data is referred to as Year-3 (Y3) analysis (DES Collaboration et al., 2022), and lastly, the analysis with six years of data is referred to as Year-6 (Y6) analysis – Y6 will be the legacy analysis using all the DES data.

Bechtol et al. in prep. describes the photometric data set with six years of DES science operations that are derived from the images from Data Release 2 (DR2: DES Collaboration et al., 2021), but have improved image processing, photometric calibration, and object classification. We refer to this photometric data set as the *Gold* catalog.

FIGURE 5.1: *Top row*: Images of Blanco-4m telescope at the Cerro Tololo Inter-American Observatory (CTIO) in Chile. *Bottom-left*: An image of the telescope and the equatorial mount. *Bottom-right*: An image of other telescopes at the CTIO complex.

5.2 PSF modeling

The summary presented in this section is from the current collaboration work in DES.

Most of the work has been done by the DES Data Management and shear analysis team

that I co-lead, especially Theo Schutt and Mike Jarvis. Most of the work will be described in Schutt et al. in prep., and I will summarize our work on Y6 PSF models below.

For the PSF modeling in Y6, we utilize the software package PIFF similarly to Y3 following the discussions in Jarvis et al., 2020. We have however made major improvements to PIFF and how we select the stars used to model the PSF. Details can be found in the DES Y6 PSF modeling paper (Schutt et al. in prep.). We briefly summarize these improvements below.

First of all, we increased the purity of the stellar samples to be used in our PSF modeling by

- matching the stars in the DES single-exposure images with *Gaia* Data Release 2 (DR2) stellar catalog (Gaia Collaboration, 2018) within 0.5 arcseconds.
- identifying a stellar locus in optical-NIR color-color space with external NIR imaging data from the VISTA Kilo-degree Infrared Galaxy Public Survey (VIKING) data release 4 (DR4) (Kuijken et al., 2019) and VISTA Hemisphere Survey (VHS) data release 5 (Edge et al., 2013) and removing objects that are not in the locus.
- removing any objects with measured $0 < g - i < 3.5$ or $0 < i - z < 0.7$ in the GOLD catalog.
- adding objects according to the star-galaxy separation algorithm (SIZEMAG) based on the objects' size and magnitude.

Secondly, for the first time in DES weak lensing analysis, we have incorporated the color information of stars in our PSF models in order to decrease the impact of chromatic effects on inferred shear (Meyers and Burchat, 2015). As described in § 4.2.1 and 4.3.1, we use a polynomial model to interpolate between star positions and additionally star colors with 1st order polynomial. For full details of the implementation, please refer to Schutt et al. in prep. 2024. These improvements resulted in being able to model PSFs for all the *griz* photometric bands and reducing the PSF modeling errors for each band compared to Y3.

5.3 Cell-based Coadds and Metadetection Weak Lensing Shape Catalog

The results presented in this section are from the current collaboration work in DES. Most of the work has been done by the DES Data Management and shear analysis team that I co-lead, and it will be described in Yamamoto et al. in prep. The text presents my own work, and the contributions of other authors are presented as such:

- *Matt Becker: Implementation of the cell-based coadd and* METADETECTION.
- *Erin Sheldon: Implementation of* METADETECTION *and the production of pixel and object masks.*

As the Stage-III surveys continue observing deeper and more areas that are comparable to what is projected in the early stage of the Stage-IV surveys (Euclid[1] (Laureijs et al. 2011), the Vera C. Rubin Observatory Legacy Survey of Space and Time[2] (*LSST*: Ivezić et al. 2018; LSST Science Collaboration 2009), and the *Nancy Grace Roman* Space Telescope[3] (*Roman*: D. Spergel et al. 2015), we must start addressing certain observational systematics that were not significant in previous analyses. One is the issue of the discontinuity in the coadd PSF. The coadd PSF needs to be well-defined in order to assure that the PSF deconvolution does not bias the shear measurement (Mandelbaum et al., 2023). As the number of single-exposure images increases for a given region in the sky, there are more overlapping detector chip gaps in a coadd image, which results in a discontinuity in the coadded PSF. Another issue is that as the number density of galaxies increases, the fraction of blended galaxies increases. Object detection is a form of selection that depends on shear, and this causes the shear-dependent object detection bias (E. S. Sheldon et al. 2020; hereafter S20). S20 proposed a new algorithm to address this problem, and E. S. Sheldon et al. 2023 has shown that in the LSST simulations (which contain a realistic level of blending), the algorithm can calibrate shear at a sub-percent level. This shows that the new method will be less biased

---

[1] http://sci.esa.int/euclid

[2] http://www.lsst.org

[3] https://roman.gsfc.nasa.gov

at the level of DES Y6 blending compared to the method in Y3. The residual shear bias (both multiplicative and additive bias) can be calibrated with image simulations (Hoekstra et al. 2021; MacCrann et al. 2021) and with the null tests in the catalog itself.

Given the above motivations, Pizza-Cutter (Becker, Sheldon, and Jarvis in prep.) for image coaddition and Metadetection (E. S. Sheldon et al. 2020) for shape calibration have been developed. We apply these techniques for the first time on real observation to the DES Year Six (Y6) image data to enable high-accuracy weak lensing shape measurement. This work presents the weak lensing shape catalog measured with the new image processing and measurement pipeline in DES Y6 imaging data, along with the catalog validation tests. These empirical tests are performed in the form of "null tests" to ensure that the catalog does not contain any induced systematic biases in the image processing pipeline and that it is reliable to extract cosmological information.

This work is accompanied by another paper (Schutt et al. in prep), which describes the PSF modeling with Piff (PSFs in the Full FOV; Jarvis et al. 2020) upgraded to include color-dependent modeling and reports several diagnostic tests on the models created for Y6 data. This addition of color-dependent PSF modeling allows us to use all of the *griz*-band images in weak lensing analysis, which increases the signal-to-noise compared to *riz*-bands. We note that as a complementary shape calibration method, we plan to produce a second shape catalog measured with the Bayesian Fourier Domain (Bfd; G. M. Bernstein et al., 2016) method that estimates shear completely independently from Metadetection.

5.3.1 Data

In the previous series of analyses (Y1 and Y3), the weak lensing catalogs were produced by measuring various galaxy quantities at object locations from Gold on individual galaxy stamps cut out from the coadd images. For Y6, the processing steps are slightly different. As described below, for the Year 6 Metadetection catalog, we constructed cell-based coadds directly from the calibrated single-epoch images and ran Metadetection on the cell-based coadds.

104

The calibrated single-epoch images use the calibration products from the DES processing pipeline. First, we use the PIXMAPPY astrometric solutions. These are important because they include the effects of tree rings in the astrometry (Plazas et al., 2014). Second, we use the PIFF PSF models, updated to account for chromatic effects for the DES Y6 analysis (Schutt et al. in prep). Below, we describe how we incorporate the chromatic dependence of the PSF model into METADETECTION. Third, we use the FGCM Burke et al., 2018 photometric zero points from the DES GOLD catalog. Finally, we use the background, bad pixel masks, and weight maps produced by DESDM for each single-epoch image. These data were generated during the standard DES processing described in DES Collaboration et al., 2021.

5.3.1.1 Mock catalogs

In some validations of our shear catalog, the covariances can be better estimated with mock catalogs due to sample variance. We made several measurements, such as correlations of shear with survey systematics maps and estimated variances from mock catalogs. We explain the details of our simulated shear catalog below.

Mock shape catalogs were generated from the shear maps in gravity-only N-body simulations. We make use of COSMOGRIDV1 (Fluri et al., 2022). The dataset is described in Kacprzak et al., 2023. We use 200 independent realisations at the fixed cosmology ($\Omega_m = 0.26$, $\sigma_8 = 0.84$, $\Omega_b = 0.0493$, $n_s = 0.9649$, $h = 0.673$). The simulations provide 69 full-sky lens planes between redshift 0 and redshift 3.5 with HEALPix[4] (Górski et al., 2005) `nside`=2048; the lens planes are converted into convergence planes under the Born approximation (e.g., Eq. 2 from Fosalba et al. 2015), and shear planes are obtained from the convergence maps using a full-sky generalization of the Kaiser and Squires, 1993 algorithm (Jeffrey et al., 2021). Mock DES Y6 shear fields are obtained by integrating the shear planes assuming the preliminary DES Y6 redshift distributions; last, we create mock shear catalogs by sampling the simulated shear fields at the DES Y6 METADETECTION galaxy

---

[4] http://healpix.sourceforge.net

positions and adding DES Y6 shape noise. This last step is performed by randomly rotating the DES Y6 galaxy ellipticities and adding them to the simulated shear field sampled at each galaxy position. Since we can cut four DES Y6 footprints out of each simulation, this procedure provides us with 800 independent shear catalogs that can be used to infer uncertainties.

5.3.1.2 Catalog blinding

In order to prevent accidental unblinding of cosmological information during testing, we applied a random scaling factor to the catalog. We followed Gatti, Sheldon, et al. 2021; Zuntz et al. 2018 to blind the catalog by first transforming ellipticity e into $|\eta| \equiv$ 2arctanh($|e|$) and multiplying $|\eta|$ by a blinding factor f ($0.9 < f < 1.1$). This random factor was removed once we completed the initial validation of our catalog using the null tests detailed below.

5.3.2 Cell-based coadding algorithms

The DES Y6 METADETECTION catalog is generated in two large steps. We first make cell-based coadds as described in this section. The second step is running METADETECTION and is described in § 5.3.3. Our cell-based coadding code is the precursor of the code developed for the Vera C. Rubin Observatory Legacy Survey of Space and Time described in E. S. Sheldon et al. (2023). We describe the relevant aspects of the algorithms and code here.

In this work, we define a cell-based coadd as a coadd made in a small, fixed region of the sky made with single-epoch images with no CCD edges intersecting the coadd region. We use regions defined through the DES coadd tile WCS. A DES coadd tile is 10,000 x 10,000 pixels. We layout the cells so that they start 50 pixels inside the border of the coadd tile and are 100 pixels on each side with a border. Each cell overlaps its adjacent cells by 50 pixels. When running algorithms on the cells, like object detection, we run the algorithm on the full 200 x 200 cell. For cells not on the edge of the coadd tile, we cut objects whose centers fall outside the inner 100 x 100 pixels. For cells on the edge of a coadd tile, we use the boundary of the unique region of each coadd tile for the edge of the cell near the

boundary. This procedure ends up defining each cell using the coadd tile WCS for some specific range of pixel locations.

The actual coadd is constructed as follows. We first find all of the SE CCDs that do not have an edge in the cell. We cut a border of 50 pixels from the edges of the CCDs due to larger astrometric residuals and tape bumps (Derylo et al., 2006). Second, we use the bad pixel masks to find all of the pixels that we could not observe due to bleeds, cosmic rays, bad columns, hot spots, etc. We apply the 2D Clough-Tocher interpolation from scipy to these pixels using their surrounding data. Third, we use the PIXMAPPY WCS solutions to map the single-epoch pixels to the cell-coadd pixels using a Lanzos-3 interpolant. Finally, all of the single-epoch image contributions to the cell-coadd are averaged together with inverse-variance weighting determined by the median of the weight map. These same steps are applied to a pure noise image generated from the weight map to form a Monte Carlo noise realization for use in METADETECTION later.

In the coadd process above, we generate two other specialized data products. First, we generate a masked fraction image (`mfrac` image), which measures the fraction of the input images in each pixel which were masked and then interpolated. To make this image, we construct an image of zeros (no interpolation) and ones (interpolated) for each input single-epoch image according to which pixels were interpolated. We then coadd these images using an interpolation with the same weights as the image and noise coadds above. Second, we generate a PSF image for each cell-coadd. The algorithms for handling the PSF coadding are critical to not generating multiplicative shear biases. In particular, the procedure adopted in this work is to pick a single pixel center in the cell-coadd as the location about which we will compute the PSF. This pixel location is mapped back to the SE image location for each input SE image. We then draw the SE image PSF models at the SE image location and coadd them with the same weights and interpolation as the image and noise coadds above. This procedure slightly broadens the PSFs due to the smearing in the coadding process. See Armstrong et al., 2024 for more details.

Finally, the DES Y6 PSF and astrometric models have chromatic dependence. Namely,

107

FIGURE 5.2: An example of the mosaic (10,000 x 10,000) of 200 x 200 cell-based images.

the PSF and astrometric solution vary as a function of the color of the input object. In this work, we take a simplified approach of using the median galaxy color for the PSF models. We used the median galaxy color for the PIXMAPPY astrometric solutions as well. However, this is a small effect relative to the PSF models. We estimate the effects of these approximations using the image simulations as described in § 5.4. An example of the 10,000 x 10,000 coadd image can be found in Figure 5.2.

5.3.3 The METADETECTION shape catalog

In this section, we overview the basic concepts of METADETECTION algorithm and describe our object measurement method. We then discuss the masking of objects and object selections performed on the shape catalog to enable the unbiased detection of cosmic shear

and present summary statistics relevant to the weak lensing analysis.

5.3.3.1 Shear calibration formalism

A cosmological analysis with weak lensing requires the knowledge of shear, which is how much a true scene of a galaxy is distorted due to an intervening mass between the galaxy and the observer. It is, however, impossible to know apriori what the original/intrinsic galaxy shape is. Nevertheless, we can estimate the shear by measuring galaxy ellipticities over a large enough sample of galaxies and computing the two-point correlation function of galaxy shapes. To provide an unbiased estimate of the shear, the measured galaxy shapes must be calibrated to be free of systematics.

Consider a measurement of galaxy ellipticity (e). In the limit of small gravitational shear and convergence ($\gamma \ll 1$, $\kappa \ll 1$), one way to estimate shear from galaxy ellipticity is to Taylor-expand e around shear $\gamma = 0$, and one is able to obtain an expression of the ellipticity in terms of the intrinsic galaxy shape and shear,

$$e = e|_{\gamma=0} + \left.\frac{\partial e}{\partial \gamma}\right|_{\gamma=0} \gamma + \dots, \tag{5.1}$$

where the first derivative (which we call shear response R) can quantitatively be considered as how the observed shapes of galaxies respond to an applied gravitational shear.

From this expression, we define the full shear response matrix (derivative of spin-2 objects) as

$$R \equiv \left.\frac{\partial e}{\partial \gamma}\right|_{\gamma=0} = \begin{pmatrix} \partial e_1/\partial \gamma_1 & \partial e_2/\partial \gamma_1 \\ \partial e_1/\partial \gamma_2 & \partial e_2/\partial \gamma_2 \end{pmatrix}. \tag{5.2}$$

The ensemble mean of measured ellipticities $\langle e \rangle$ can then be computed, and we have the estimate of the true shear,

$$\langle \gamma \rangle \approx \langle e \rangle / \langle R \rangle, \tag{5.3}$$

assuming that galaxies are intrinsically randomly oriented such that $\langle e \rangle|_{\gamma=0} = 0$. It shows that measuring the shear response allows for obtaining unbiased statistics of shear from the ensemble average of galaxy ellipticity, and this holds true in our two-point statistics.

109

In practice, we can measure galaxy shapes quite well, but measuring shear response can be challenging due to image complications such as PSF modeling. In order to compute the full shear response, we can use techniques such as METACALIBRATION (E. Huff and Mandelbaum 2017; E. S. Sheldon and Huff 2017), where we deconvolve an image of an astronomical object by its PSF, artificially shear the image by a small amount in all spin axes and reconvolve it with a slightly large and isotropic PSF[5]. We then measure the shapes of sheared images of the object and calculate the shear response for an individual object with the numerical finite difference method.

$$R_{ij} = \frac{e_i^+ - e_i^-}{\Delta \gamma_j},$$ (5.4)

where the subscript i denotes one of the two shear components, and the superscript $+/-$ denotes the sign of the applied shear. In total, we essentially need to create five images (unsheared, sheared in $+\gamma_1$, $-\gamma_1$, $+\gamma_2$ and $-\gamma_2$ directions) to compute the response.

In previous years of DES shear analysis, METACALIBRATION was applied on the individual galaxy cutout images. S20 has, however, found that object detection depends on gravitational shear, and the use of METACALIBRATION in the presence of blending causes shear-dependent object detection bias. S20 provides a prescription which we call METADE-TECTION[6] to mitigate this bias by artificially shearing the images before the object detection happens and computing the shear response over the catalogs of detected objects, implying that the number of objects detected in each sheared image will be different. The shear response for METADETECTION can, therefore, be computed by taking an ensemble average of ellipticities in the finite difference.

$$\langle R_{ij} \rangle = \frac{\langle e_i^+ \rangle - \langle e_i^- \rangle}{\Delta \gamma_j}.$$ (5.5)

Note the difference in how the response is computed compared to METACALIBRATION. METADE-TECTION does not measure an individual object's response and becomes a noisy quantity

---

[5] The deconvolution, artificial shearing, and the reconvolution steps can be done using the GALSIM package (Rowe et al., 2015). https://github.com/GalSim-developers/GalSim

[6] https://github.com/esheldon/metadetect

when the number of objects is small. In addition, the selection effects (e.g., tomographic bins) in the response (see Sec 3.1.1 of E. S. Sheldon and Huff, 2017) are implicitly included in our computation of shear response for METADETECTION.

5.3.3.2 Masking

There are two levels at which we want to remove data from our processing: Problem areas in individual images, which we interpolate before image combination, and problem areas on the sky, where we remove objects from the catalog. In §5.3.3.2.1 we describe the pixel masks, and in §5.3.3.2.2 we describe the object masks.

5.3.3.2.1 Pixel masks

Before image combination, we mask and interpolate artifacts in the single epoch images, such as bad columns, cosmic rays, and saturated regions, as described above. During the METADETECTION processing, we further mask bright stars to avoid FFT artifacts during the deconvolution, shear, and the reconvolution processes. We assemble a bright star catalog using a combination of Gaia data release 2 and high-confidence stars found in GOLD.

Each Gaia star was masked using a circle with a magnitude-dependent radius in arcseconds given by

$$\log_{10}(R_{\text{Gaia}}) = 0.004432G^2 - 0.2257G + 2.996, \tag{5.6}$$

where G is the magnitude in the Gaia band. We further place a lower bound on the radius of 5 arcseconds.

The image was set to zero inside the circular masked area, with the edges "apodized" to transition smoothly between unity on the outside to zero on the inside of the mask. This smooth transition was parameterized using the cumulative integral of a triweight kernel, which is a function of two parameters, m and h, and is defined for a point x with quantity $y = (x - m)/h$ as

$$K(x, m, h) = \begin{cases} 0 & y < -3 \\ (-5y^7/69984 + 7y^5/2592 - 35y^3/864 + 35y/96 + 1/2) & -3 \le y \le 3 \\ 1 & y > 3 \end{cases} \tag{5.7}$$

This kernel smoothly transitions from zero to unity over a range of $6h$, centered on the location m. We chose h to be 1.5 pixels, which should vary more slowly than the PSF profile without significant additional expansion of the mask. We also set $m + 3h$ to the radius of the star mask hole so that the mask reaches unity at its nominal size.

We applied the same masking and apodization to the `mfrac` image. We use this `mfrac` image during object measurement in order to flag objects with potentially bad measurements (see §5.3.3.3).

5.3.3.2.2 Object level masks

After the production of the full catalog of measurements, we additionally cut objects based on measurement flags and `mfrac` (see §5.3.3.3). We also apply a spatial mask in order to remove problematic regions of the sky. This mask, which is created in the HEALSPARSE format[7], incorporates all the above pixel level masks (which can be somewhat larger area after HEALPIX pixelization) and the following additional sources. All masking is done at nside=131072 except where noted.

1. Gold footprint mask: the mask was produced following these conditions: 1) at least 50% of the effective area in a HEALPIX pixel in each band (*griz*), 2) at least 50% of the effective area in a HEALPIX pixel combined *griz* coverage area, 3) at least two exposures in each band *griz*. The map was generated with the resolution of nside=4096.

2. Foreground mask: The foreground mask contains regions and objects that are close to bright and extended sources. These foreground objects include very bright Gaia stars (G < 11.5, with a different radius relation from that used for our pixel level Gaia masking (Bechtol et al. in prep.), Yale bright stars, 2MASS stars (5<J<12), Globular clusters and a region near the LMC.

3. Gaia mask: We masked all stars in the Gaia catalog using the parametric radius-magnitude relationship (see §5.3.3.2.1. This mask matches what was done in the pixel-level masking but at a lower resolution (nside=131072).

---

[7] https://github.com/LSSTDESC/healsparse
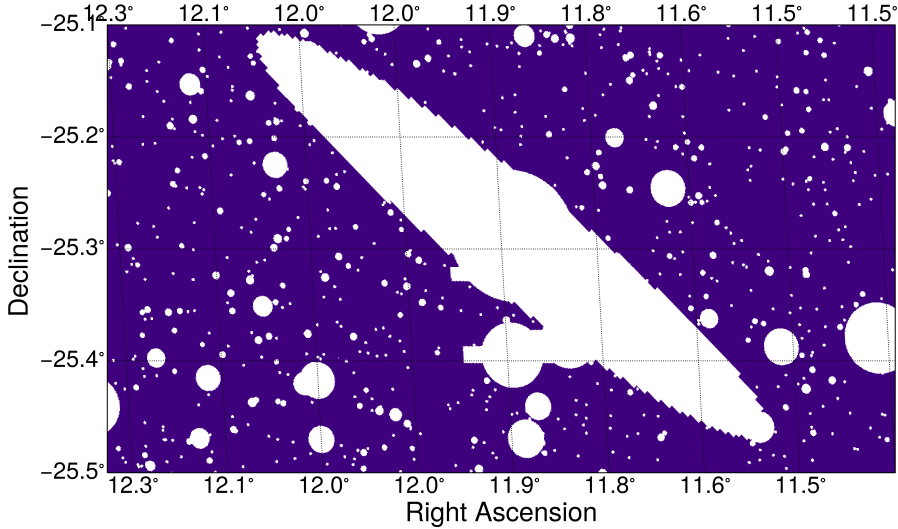
FIGURE 5.3: A region in our footprint with the fiducial mask of all the individual masks combined.

4. DES stars: We augmented the Gaia star catalog with high-confidence DES stars, defined as `MASH== 0` and $r < 21$ (Bechtol et al. in prep.). These objects were masked with a fixed circular radius of 5 arcseconds. Many of these stars are also in Gaia, and thus may already have a larger mask applied.

5. Hyperleda mask: After application of the foreground mask, we visually found additional unmasked regions near bright and extended objects at low-z that caused spurious detections and contaminated the light profile of neighboring objects. We found that masking objects from the HYPERLEDA (Paturel et al. 2003) significantly reduced spurious detections and poor measurements. Each object was masked with a circular, B magnitude dependent circular mask with a radius in degrees $0.147 - 0.00824 * B$.

5.3.3.3 Object identification & measurement

We have previously discussed the need to calibrate galaxy ellipticity to obtain a proxy to the gravitational shear field and derived how we obtain the shear response with METADETECTION. Here, we dive into the details of how we identify objects and measure their properties (e.g., flux, shape, size).

Given the coadd images for each band, we form the multi-band coadd image (riz[8]) and apply object detection (SExtractor: Bertin and Arnouts 1996) on the unsheared and sheared versions of the coadd image that are generated from METADETECTION. We use these detections in each version and perform forced photometry on the unsheared and sheared coadds for each band.

In order to measure the properties of each detected object, we use an image processing package NGMIX[9], from which we choose *PrePSFMom* and *Fitter* classes. *PrePSFMom* class (*pgauss* hereafter) calculates weighted real-space moments on the PSF-deconvolved image in Fourier space. Another measurement is performed with a Gaussian fitting in *Fitter* class (*gauss* hereafter). Here, a mixture of galaxy models with a Gaussian profile is fitted with a PSF-deconvolved galaxy image and the best fit is computed using multivariate least-squares. While we measure all the essential quantities (e.g., fluxes, shapes) with both methods, the tests and validations of the quantities led to selecting the quantities with one of the methods (size quantity is an exception). We describe how some of the chosen quantities are measured.

First, the object fluxes and sizes were computed with *pgauss*. Each detected galaxy image is deconvolved with the isotropic PSF from the METADETECTION process (reconstructed PSF hereafter), and the real-space moments are estimated in the PSF-deconvolved image in Fourier space (Becker et al. in prep.). If we define $I(x)$ to be an image of a galaxy and $S(k)$ to be the image deconvolved with PSF $P(x)$ in Fourier space, the following real-space quantities are estimated with Fourier-space moments;

$$M_f = \int dk^2 S(k) W(k)$$

$$T^{\text{pgauss}} = (\int dk^2 S(k) \frac{d^2 W(k)}{dk_x dk_x} + \int dk^2 S(k) \frac{d^2 W(k)}{dk_y dk_y})/M_f, \quad (5.8)$$

where $W(k)$ is the weight function, which is chosen to be a circular Gaussian with FWHM

---

[8] mention why we did not use griz coadds

[9] https://github.com/esheldon/ngmix

$= 2.0$ arcseconds. This choice is made so that the weight function can suppress Fast Fourier Transform (FFT) artifacts. We note that T^{pgauss} has a unit of arcsec^2.

For object sizes, shapes, and signal-to-noise ratio (S/N), we use *gauss* measurement. If we define the best-fit amplitude/flux, centroid, and the 2$^{\mathrm{nd}}$ moments of a Gaussian model to be (F, x, y, **M**),

$$T^{\mathrm{gauss}} = M_{xx} + M_{yy}$$

$$(g_1, g_2) = \frac{(M_{xx} - M_{yy}, 2M_{xy})}{M_{xx} + M_{yy} + 2\sqrt{M_{xx}M_{yy} - M_{xy}^2}}$$

$$S/N = F/\sigma_F$$

Other quantities to make an effective galaxy selection and test systematics include the size of the reconstructed PSF (T_{PSF}^{gauss}). This can also be used in the measure of how well an object is resolved, called size ratio (T/T_{PSF}).

5.3.3.4 Object selections

Here we discuss the standard weak lensing object selections applied on the METADETECTION shape catalog, where the masks described in § 5.3.3.2 are applied. It is important to note here that we need to apply the selections on the objects that are detected not only in the unsheared images but also in the sheared images to ensure our selections do not introduce the shear-dependent detection bias. As explained in § 5.3.3.3, we have implemented a few estimators (PSF-deconvolved: *pgauss* and convolved: *gauss* measurements), so we hereafter denote which measurement algorithm was used in our selections and analyses as a superscript on each property.

(i) **star/galaxy separation**

- $T^{\mathrm{gauss}}/T_{\mathrm{PSF}}^{\mathrm{gauss}} > 0.5$ – we employ a star-galaxy separation using per-object size ratio ($T^{\mathrm{gauss}}/T_{\mathrm{PSF}}^{\mathrm{gauss}}$) and measurement error on the object size ($\sigma_T^{\mathrm{gauss}}$). While high S/N stars populate at $T^{\mathrm{gauss}}/T_{\mathrm{PSF}}^{\mathrm{gauss}}=0.0$, low S/N stars have larger error bars and hence their measurement deviates from $T^{\mathrm{gauss}}/T_{\mathrm{PSF}}^{\mathrm{gauss}}=0.0$. Thus, we select objects whose size ratio is larger than 0.5. Figure 5.4 shows the impact of
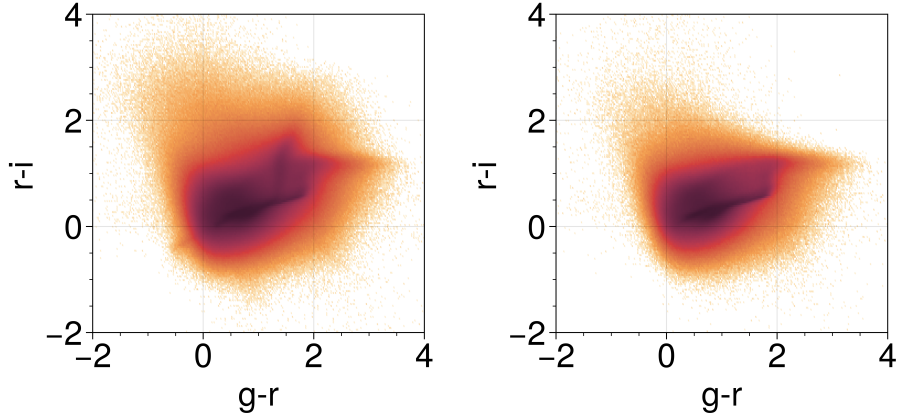
FIGURE 5.4: **Left**: Log density of objects from randomly chosen 500 tiles in object color space (g-r vs r-i) We should note that the rest of the selections have already been applied here. **Right**: Log density of selected galaxies with the s/g cut.

this star-galaxy separation cut on the population. Table 5.1 shows the fraction of our estimated rate of stellar contamination in our catalog.

(ii) **S/N and size selection**

- $10 < S/N^{\mathrm{gauss}}$ – low S/N cut ensures signals not to be noise dominated.
- $T^{\mathrm{gauss}} < 20$ – we visually inspected the large-size objects and found them to be image artifacts and small galaxies whose measurement is impacted by the fluxes from neighbor galaxies.

(iii) **flux/color, heavily interpolated objects selection**

- In order to obtain reliable photometric redshifts of the sources, we make magnitude cuts on each bandpass. $g < 26.5$, $r < 26.5$, $i < 24.7$, $z < 25.6$.
- In order to reject objects that have outlier colors, we make cuts on measured galaxy color. $|g - r| < 5$, $|r - i| < 5$, $|i - z| < 5$.
- `mfrac`< 0.1 – the fraction of the stamp that was masked/interpolated as described in § 5.3.3.3. This quantity is measured using a Gaussian weighted aperture centered on the object. The purpose here is to avoid measuring objects that have a large fraction masked. Tests in our image simulations suggested that utilizing `mfrac`< 0.1 is sufficient not to introduce shear calibration biases.
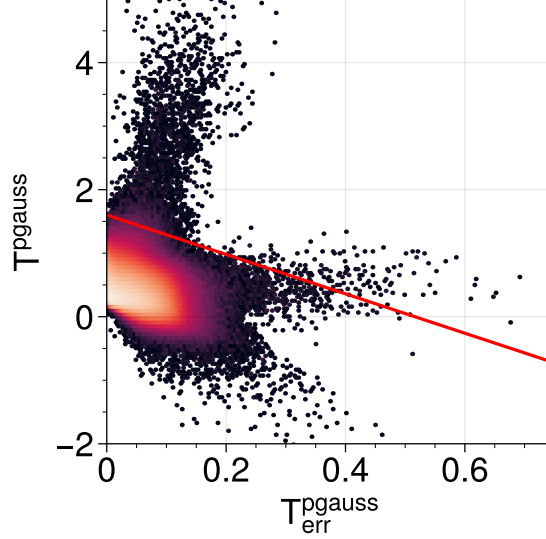
FIGURE 5.5: A density of objects in (T^{pgauss}, $T^{\mathrm{pgauss}}_{\mathrm{err}}$) space. We remove objects above the red line from the catalog.

(iv) **Junk detections**

- $T^{\mathrm{pgauss}} < 1.6 - 3.1 \times T^{\mathrm{pgauss}}_{\mathrm{err}}$ – we have identified a population of objects in (T^{pgauss}, $T^{\mathrm{pgauss}}_{\mathrm{err}}$) space (above the red line in Fig. 5.5) which are falsefully detected as real objects. We verified visually that this cut removes those objects that happened to be around bright stars and blended systems. This does not change the population in T^{gauss}.

- $T^{\mathrm{gauss}} \times T^{\mathrm{gauss}}_{\mathrm{err}} < 1$ or $T^{\mathrm{gauss}}/T^{\mathrm{gauss}}_{\mathrm{err}} > 10$ – This cut was based on the similar cut in GOLD (Bechtol et al. in prep.) to avoid junks in the cluster field (i.e., super-spreader objects). We visualized them and confirmed that most of these objects were false detections.

Table. 5.1 presents the fraction of objects being removed from the *noshear* catalog at each selection step. After these selections are applied to our METADETECTION catalog, the total number of objects for DES Y6 cosmological analysis with weak lensing is 151,922,791.

Table 5.1: We present the number of objects after each selection, the fraction of objects in *noshear* METADETECT catalog that are matched with GOLD sample within 0.263 arcseconds. The last column shows the fraction of stars within matched samples that are identified in GOLD sample (MASH= 0, 1).

Selection	Fraction of removed objects	Fraction of stars
Basic	–	7.06%
Mask	14.3%	7.06%
Star-galaxy separation	60.2%	0.16%
S/N and size	33.8%	0.037%
Flux/color, mfrac	3.81%	0.032%
Junks	0.30%	0.032%
All	78.3%	0.032%
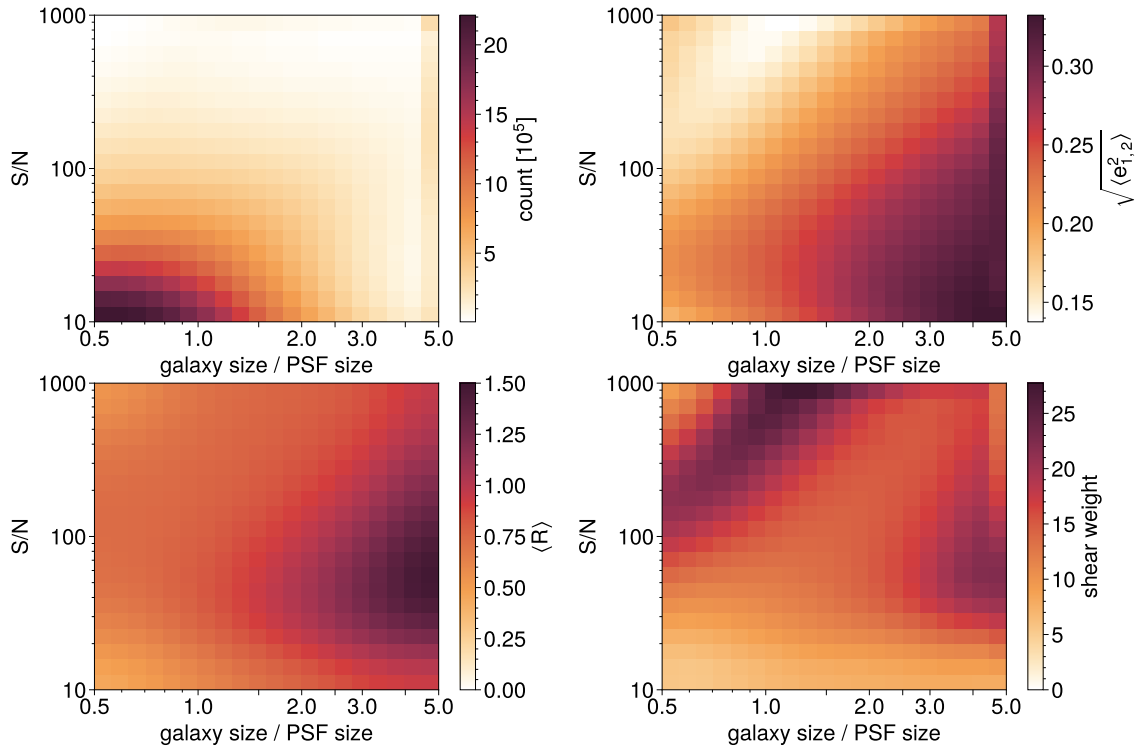
FIGURE 5.6: Various statistics (number count, a root-mean-square of measured shape, shear response, shear weight) as a function of object S/N and size ratio (galaxy size/PSF size) are presented. S/N and size ratio are divided in the log-space of 20 steps with a limit of 10<S/N<1000 and 0.5<galaxy size/PSF size<5.0. The objects whose S/N is larger than 1000 are allocated in the last bin, and the same goes for the objects whose size ratio is larger than 5.0. The measured shapes for each sheared image are averaged to compute the shear response in each bin. This grid of shear response is smoothed by a Gaussian kernel of σ=2.0 to lower the noise in each bin. The shear weight is then computed from this smoothed response grid using Eqn. 5.9.

5.3.3.5 Weighting

As shown in GS20, determining galaxy weights from measured properties and applying shear weight for each galaxy increase the statistical power of the weak lensing shape catalog defined by the shape noise divided by the square-root of effective sample size ($\sigma_e/\sqrt{N_{\text{eff}}}$). For our Y6 METADETECTION shape catalog, we follow the same weighting scheme in GS20, where shear weight is determined in the space of object S/N and size ratio shown in Figure 5.6. Galaxies are allocated to 20 x 20 logarithmically scaled bins of S/N=10...1000 and T/T_{PSF}=0.5...5.0. Objects that have S/N $>$ 1000 or $T/T_{\text{PSF}} >$ 5.0 are assigned to the last bins.

The weighting here is essentially an inverse variance weighting.

$$w_i(T/T_{\text{PSF}}, S/N) = \sigma_{i,\gamma}^{-2}(T/T_{\text{PSF}}, S/N) = \sigma_{i,e}^{-2}\langle R_{i,\gamma}\rangle^2, \tag{5.9}$$

where the subscript i denotes the index of each bin in the S/N and size ratio grid. This suggests that we need to calculate the shape variance ($\sigma_{i,e}^{-2}$) and shear response ($R_{i,\gamma}$) in each bin.

The variance of measured ellipticities (intrinsic and measurement-related shape noise) can be computed with,

$$\sigma_{i,e}^2(T/T_{\text{PSF}}, S/N) = \frac{1}{2}\left[\frac{\Sigma(e_{i,1})^2}{n_{i,\text{gal}}} + \frac{\Sigma(e_{i,2})^2}{n_{i,\text{gal}}}\right], \tag{5.10}$$

where the index i represents a value in each bin and $n_{i,\text{gal}}$ is the number of galaxy in each bin.

The distribution of number count, shape variance averaged in two components, shear response and shear weight is shown in Figure 5.6. We note here that the grid of shear response is smoothed with a Gaussian kernel of σ = 2.0 to reduce the impact of shot noise of the response itself. The distribution of the shear weight is similar to that of the METACALIBRATION shape catalog in Y3.
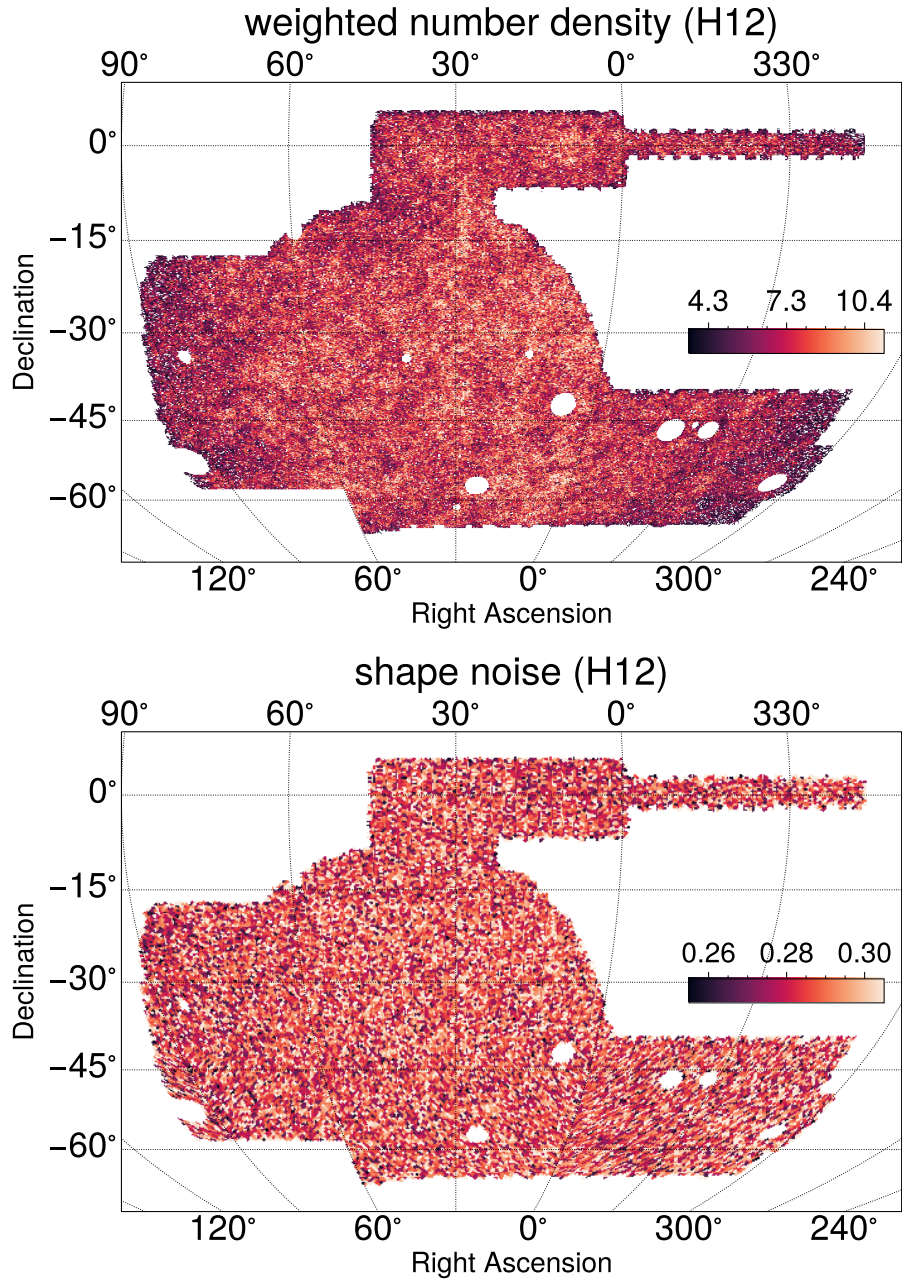
FIGURE 5.7: **Left**: weighted galaxy number density in units of gal/arcmin^2 using Eq. 5.14. The number density is computed in a HEALPix (Górski et al. (2005)) of resolution 10 (`nside = 2^{10} = 1024`). **Right**: object shape noise computed with Eq. 5.13 in a HEALPix grid of resolution 7 (`nside = 2^7 = 128`).

5.3.3.6 Summary statistics of the catalog

We summarize a few summary statistics of the catalog after the selections described in § 5.3.3.4.

As we have described before, we compute the shear response over the catalog rather than each object using Eqn. 5.5 to obtain our estimate of shear. Our shear response over the catalog is $\langle R \rangle = 0.817$. When we validate our catalog with a whole galaxy sample, we divide the measured ellipticity in the catalog by $\langle R \rangle$ to obtain a noisy per-object estimate of shear.

The statistical power of the catalog can be determined by the effective sample size and the shape noise. The overall statistical power is quantified as the variance of the estimated shear, $\sigma_{fl} = \sigma_e/\sqrt{N_{eff}}$.

Following the definitions of Heymans et al. 2012 (H12) and Chang et al. 2013 (C13), the shape noise (σ_e) and the effective number density (n_{eff}) are computed in the following ways.

$$\sigma^2_{e,C13} = \frac{1}{2}\frac{\Sigma w_i^2 (e_{i,1}^2 + e_{i,2}^2 - \sigma^2_{m,i})}{\Sigma w_i^2 R^2} \tag{5.11}$$

$$n_{eff,C13} = \frac{1}{A}\frac{\sigma^2_{e,C13}(\Sigma w_i R_i)^2}{\Sigma w_i^2 (R^2 \sigma^2_{e,C13} + \sigma^2_{m,i}/2)}, \tag{5.12}$$

where w_i is the shear weight computed in § 5.3.3.5, R is the global shear response, $e_{i,j}$ is the per-object ellipticity (uncorrected for R), and $\sigma^2_{m,i}$ is the variance of the per-object ellipticity. A is the effective area of our footprint.

$$\sigma^2_{e,H12} = \frac{1}{2}\frac{\Sigma w_i^2 (e_{i,1} - \langle e_1 \rangle)^2}{(\Sigma w_i R)^2} + \frac{\Sigma w_i^2 (e_{i,2} - \langle e_2 \rangle)^2}{(\Sigma w_i R)^2}]\frac{(\Sigma w_i)^2}{\Sigma w_i^2} \tag{5.13}$$

$$n_{eff,H12} = \frac{1}{A}\frac{(\Sigma w_i)^2}{\Sigma w_i^2} \tag{5.14}$$

121

Table 5.2: Effective number density, shape noise computed using two definitions Eqn. 5.11 and Eqn. 5.13, and weighted residual mean shear in the catalog. The bottom row presents the same statistics from GS20, which used the H12 definition for the final shape catalog.

Definition	n_{eff}	σ_{e}	c_1	c_2
Chang+13	7.97	0.270	1.94×10^{-4}	-3.14×10^{-5}
Heymans+12	8.22	0.289	1.94×10^{-4}	-3.14×10^{-5}
GS20 (H12)	5.59	0.261	3.5×10^{-4}	0.6×10^{-4}

We report the effective galaxy number density and the variance of the estimated shear of the objects in our METADETECTION shape catalog in Table 5.2. The statistical power of the Y6 shape catalog has increased by 11.6% for the H12 definition and 10.0% for the C13 definition, compared to that of the Y3 weak lensing shape catalog. There is a loss in the statistical power compared to BFD catalog (Gatti et al. in prep.), and we believe that this is likely the result of employing the cell-based coadd method (i.e., loss of low S/N objects). Figure 4 of Armstrong et al. in prep. shows the loss of fractional loss of exposures using the cell-based coaddition method for LSST simulations.

5.3.4 Correlations with PSF properties

In this section, we present tests to validate that the measured shear signal is not systematically biased due to PSF modeling. The PSF quantities are measured in the catalog of reserved stars, which constitute 20% of all the stars observed in our footprint. In particular, we explore the following items:

- dependencies of the mean galaxy shear on PSF modeling (§ 5.3.4.1);
- additive biases due to the PSF leakage and modeling errors (§ 5.3.4.2);
- tangential and cross-component galaxy shear around PSF candidate stars (§ 5.3.4.3).

5.3.4.1 Mean shear as a function of PSF properties

A simple but effective test to ensure the quality of measured shear is to check the dependency of mean shear on the sizes and shapes of PSF models. Figure 5.8 shows the effect of PSF modeling errors on galaxy shapes. Here, the shear response is re-computed in each bin of the PSF property, and the mean shear is divided by the response. In an ideal

Table 5.3: Comparison of mean shear (e_1 and e_2) of the objects in Y3 and Y6 shape catalog. We split the objects by three colors ($g-i$) ranges (blue: [-2.00, 0.76], mid: [0.76, 1.49], red: [1.49, 4.00]). For Y3, we used shapes from the Y3 catalog, and the shear and selection response are re-computed for each color sample for Y3. For the Y6 color sample, we compute the shear response of the objects that are selected to be in each color range from the whole catalog.

	Color sample	N	$\langle R \rangle$	$\langle e_1 \rangle$	$\langle e_2 \rangle$
	Blue	16,043,877	0.71	$(9.75 \pm 0.75) \times 10^{-4}$	$(3.34 \pm 0.75) \times 10^{-4}$
Y3	Middle	48,602,072	0.74	$(5.79 \pm 0.39) \times 10^{-4}$	$(2.02 \pm 0.39) \times 10^{-4}$
	Red	34,980,219	0.69	$(2.84 \pm 0.48) \times 10^{-4}$	$(-1.80 \pm 0.48) \times 10^{-4}$
	Blue	36,633,208	0.73	$(2.92 \pm 0.55) \times 10^{-4}$	$(2.30 \pm 0.55) \times 10^{-4}$
Y6	Middle	71,910,867	0.84	$(1.74 \pm 0.33) \times 10^{-4}$	$(0.22 \pm 0.33) \times 10^{-4}$
	Red	43,326,212	0.83	$(1.52 \pm 0.43) \times 10^{-4}$	$(-2.73 \pm 0.43) \times 10^{-4}$

world, one would hope to demonstrate a null signal (i.e., zero slope and offset).

In our catalog, however, as one can see in Fig. 5.8, $\partial e_1 / \partial e_{1,\mathrm{PSF}}$ = -0.0057±0.0018 and $\partial e_2 / \partial e_{2,\mathrm{PSF}}$ = -0.0034±0.0017. These are about 2σ larger for the slope in e_1 and statistically consistent in e_2 compared to the same test in GS20. This non-zero slope in e_1 can be explained by the PSF modeling errors associated with chromatic effects. When galaxy samples are split into three $g-i$ color bins (red/mid/blue), the slopes in each color sample are about the same or smaller compared to the samples in the Y3 catalog (Figure 5.10). The overall slope, however, is larger for Y6 because of the accidental cancellation due to the signs of the slopes in Y3, as one can see in the red dotted lines in Fig. 5.10. We also expect there to be non-zero slopes for blue and red sample bins in Y6. Because we evaluate the PSF at the center of cell-coadd at a median galaxy color ($g-i$ = 1.1) (§ 5.3.2), the PSF for each galaxy is slightly wrong relative to the true galaxy color. This PSF modeling error due to the chromatic effect should be better in Y6 since PSF models in the Y3 shape catalog did not have color dependence, which can be seen in the mid row of Figure 5.9.

This systematic effect associated with PSF modeling errors can further be generalized by its effect in the 2pt statistics as the PSF contamination model in § 5.3.4.2.

5.3.4.2 Additive biases due to PSF leakage and modeling errors

In this section, we explore the additive biases induced by the PSF misestimation. We ignore the contribution of the PSF misestimation to the multiplicative bias, which can be

123
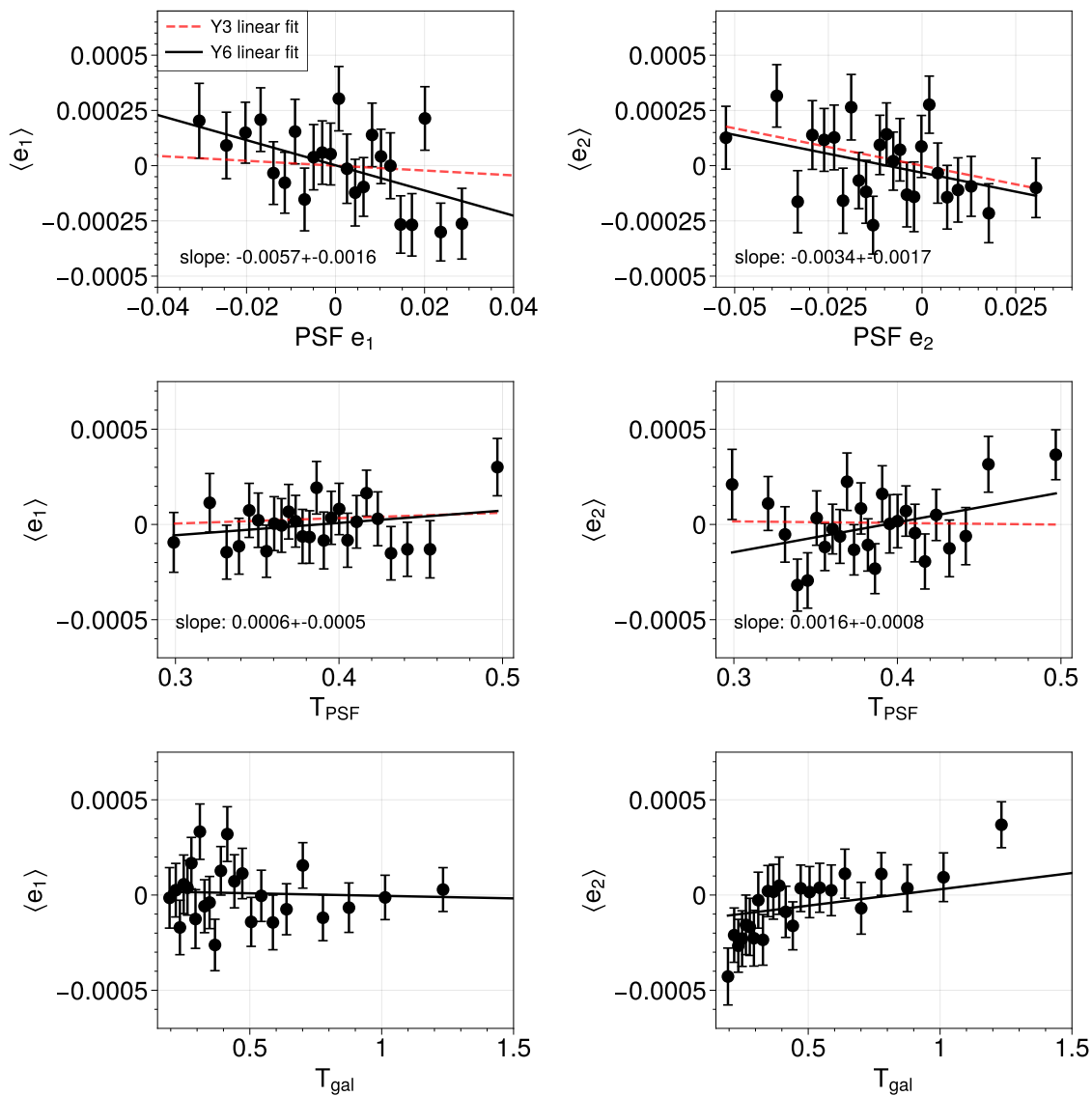
FIGURE 5.8: Mean shear (e_1, e_2) as a function of several PSF and galaxy properties as a null test on one-point statistics. The mean shear is corrected by the shear response, and the global mean shear in the catalog is subtracted from each data point. The linear fit (slope and offset) to the data points was computed with ordinary least-squares. The error bars were estimated by dividing the sample into 200 patches in the sky and computed via jackknife covariance estimation. ***Top***: as a function of PSF shape. ***Middle***: as a function of PSF size. ***Bottom***: as a function of galaxy size.
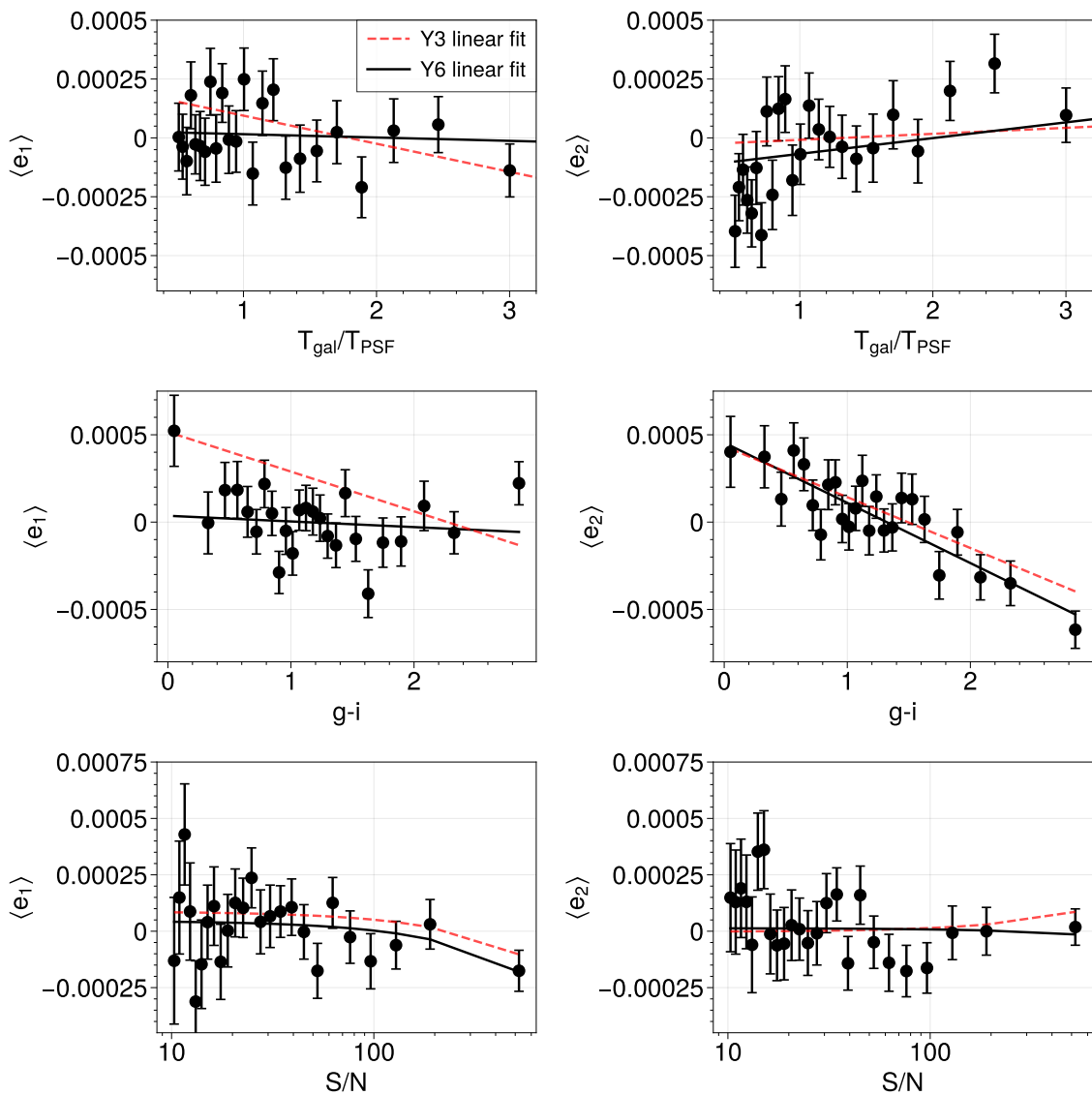
FIGURE 5.9: Mean shear (e_1, e_2) as a function of several PSF and galaxy properties as a null test on one-point statistics. The mean shear is corrected by the shear response, and the global mean shear in the catalog is subtracted from each data point. The linear fit (slope and offset) to the data points was computed with ordinary least-squares. The error bars were estimated by dividing the sample into 200 patches in the sky and computed via jackknife covariance estimation. **Top**: as a function of galaxy and PSF size ratio. **Middle**: as a function of galaxy $g - i$ color. **Bottom**: as a function of galaxy signal-to-noise (S/N).
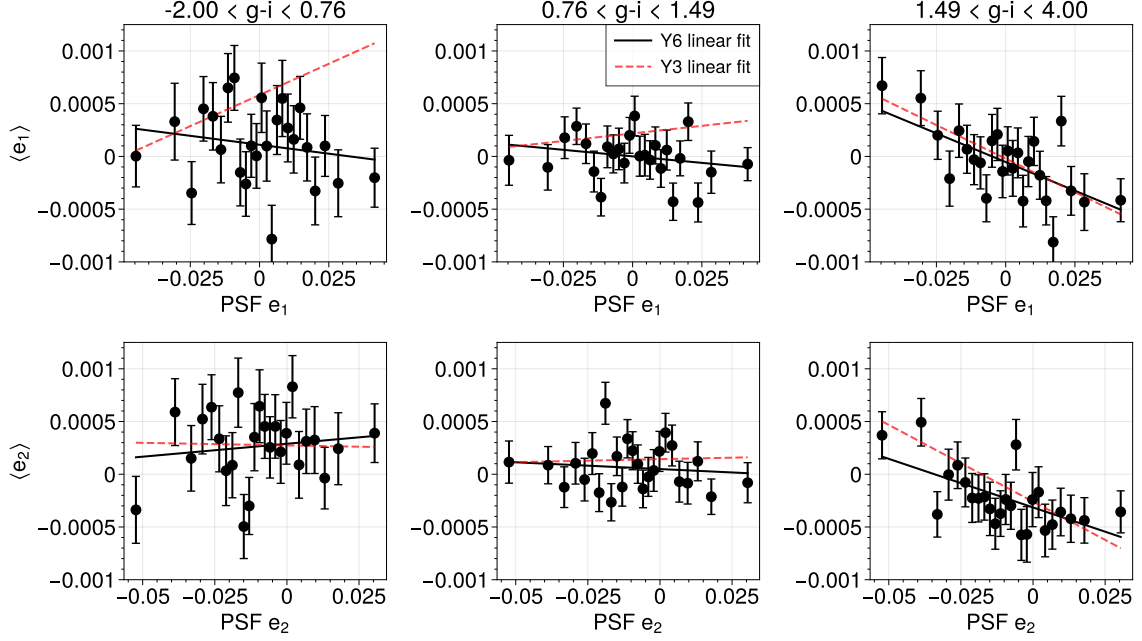
FIGURE 5.10: Mean shear (*top* row: e_1 and *bottom* row: e_2) as a function of PSF shapes where the catalog is split in 3 ($g - i$) color bins. **Left** column: color range is set between $-2.00 < g - i < 0.76$. **Middle** column: color range is set between $0.76 < g - i < 1.49$. **Right** column: color range is set between $1.49 < g - i < 4.00$. Ordinary least-square fits are performed on the data points to produce the black line and red dotted line for the linear fit performed on the Y3 shape catalog.

directly calibrated using the image simulations (e.g., MacCrann et al. 2021). Consider an observed shape of a galaxy that can be decomposed into the intrinsic shape, the real shear signal, and the systematic contribution from the PSF modeling errors and noise.

$$g^{\text{obs}} = g^{\text{int}} + g + \delta e^{\text{sys}}_{\text{PSF}} + \delta e^{\text{noise}} \tag{5.15}$$

Since $\langle \delta e^{\text{noise}} \rangle = 0$ when taking an ensemble of observed shear, $\langle \delta e^{\text{sys}}_{\text{PSF}} \rangle$ would persist and we must estimate the impact of $\langle \delta e^{\text{sys}}_{\text{PSF}} \rangle$ in the final $\xi_\pm$. We follow Jarvis et al. 2016; Paulin-Henriksson et al. 2009; Rowe 2010 for how the 2nd-order PSF modeling residuals ($\delta e^{\text{sys}}_{\text{PSF}}$) propagate to the cosmological signal $\xi_\pm$.

In addition, it is also essential to quantify the contributions of higher-order moments of PSF as T. Zhang, Li, et al., 2023 described its impact on two-point correlations of galaxy shapes for the HSC Y3 shape catalog (Li, Miyatake, et al., 2022). In our analysis, following

T. Zhang, Almoubayyed, et al., 2023, we only consider the impact of spin-0 and spin-2 quantity of 4th-order moments

$$e_{\text{PSF}}^{(4)} = \frac{M_{31} + iM_{13}}{T^2} - 3e_{\text{PSF}}^{(2)}, T_{\text{PSF}}^{(4)} = \frac{M_{22}}{M_{11}}. \tag{5.16}$$

With the contributions from 4th-order moments, we are able to expand the PSF contamination model as follows.

$$\delta e_{\text{PSF}}^{\text{sys}} = \alpha e_{\text{PSF}} + \beta \Delta e_{\text{PSF}} + \eta(e_* \Delta T_{\text{PSF}}/T_*)$$

$$+\alpha^{(4)} e_{\text{model}}^{(4)} + \beta^{(4)} \Delta e_{\text{PSF}}^{(4)} + \eta^{(4)}(e_*^{(4)} \Delta T_{\text{PSF}}^{(4)}/T_*^{(4)})$$

$$+\eta^{(24)}(e_* \Delta T_{\text{PSF}}^{(4)}/T_*^{(4)}) + \eta^{(42)}(e_*^{(4)} \Delta T_{\text{PSF}}/T_*) \tag{5.17}$$

$\Delta e_{\text{PSF}} = e_* - e_{\text{PSF}}$, where e_{PSF} and e_* are the ellipticity of the PSF model and of the PSF directly measured from stars. $\Delta T_{\text{PSF}} = T_* - T_{\text{PSF}}$, where T_{PSF} and T_* are the size of the PSF model and of the PSF measured from stars. The superscript (4) on the ellipticity and size means the ellipticity and size measured with the 4th-order moments of the PSF models and stars. If the galaxy shape measurement recovers the shapes perfectly and produces no PSF leakage, we expect the α and $\alpha^{(4)}$ to be zero. On the other hand, in the absence of PSF modeling errors, we would expect $\beta, \beta^{(4)}, \eta, \eta^{(4)}, \eta^{(24)}, \eta^{(42)}$ to be an order of unity. Our goal here is to fit for these coefficients from the measurements of auto- and cross-correlations of galaxy and PSF shapes, with which we are able to estimate the systematic bias ($\delta e_{\text{PSF}}^{\text{sys}}$) associated with PSF leakage and modeling.

To proceed, we evaluate the PSF models at the locations of the reserve stars that are found in single-exposure images and utilized in the PSF modeling process at the median galaxy color, producing the reserve star catalog. We then correlate the observed shapes in the METADETECTION catalog with $p_2 = e_{\text{PSF}}$, $q_2 = \Delta e_{\text{PSF}}$, $w_2 = e_{\text{PSF}} \Delta T_{\text{PSF}}/T_{\text{PSF}}$, $p_4 = e_{\text{PSF}}^{(4)}$, $q_4 = \Delta e_{\text{PSF}}^{(4)}$, $w_4 = e_*^{(4)} \Delta T_{\text{PSF}}^{(4)}/T_*^{(4)}$, $w_{24} = e_* \Delta T_{\text{PSF}}^{(4)}/T_*^{(4)}$, $w_{42} = e_*^{(4)} \Delta T_{\text{PSF}}/T_*$ in the PSF catalog, in 16 angular bins ranging between 2.5-250 arcmin. Each correlation is written out in Eqn. 5.18–5.25.

$$\langle g^{\mathrm{obs}} p_2 \rangle = \alpha \langle p_2 p_2 \rangle + \beta \langle q_2 p_2 \rangle + \eta \langle w_2 p_2 \rangle + \alpha^{(4)} \langle p_4 p_2 \rangle + \beta^{(4)} \langle q_4 p_2 \rangle + \eta^{(4)} \langle w_4 p_2 \rangle$$
$$+ \eta^{(24)} \langle w_{24} p_2 \rangle + \eta^{(42)} \langle w_{42} p_2 \rangle \tag{5.18}$$

$$\langle g^{\mathrm{obs}} q_2 \rangle = \alpha \langle p_2 q_2 \rangle + \beta \langle q_2 q_2 \rangle + \eta \langle w_2 q_2 \rangle + \alpha^{(4)} \langle p_4 q_2 \rangle + \beta^{(4)} \langle q_4 q_2 \rangle + \eta^{(4)} \langle w_4 q_2 \rangle$$
$$+ \eta^{(24)} \langle w_{24} q_2 \rangle + \eta^{(42)} \langle w_{42} q_2 \rangle \tag{5.19}$$

$$\langle g^{\mathrm{obs}} w_2 \rangle = \alpha \langle p_2 w_2 \rangle + \beta \langle q_2 w_2 \rangle + \eta \langle w_2 w_2 \rangle + \alpha^{(4)} \langle p_4 w_2 \rangle + \beta^{(4)} \langle q_4 w_2 \rangle + \eta^{(4)} \langle w_4 w_2 \rangle$$
$$+ \eta^{(24)} \langle w_{24} w_2 \rangle + \eta^{(42)} \langle w_{42} w_2 \rangle \tag{5.20}$$

$$\langle g^{\mathrm{obs}} p_4 \rangle = \alpha \langle p_2 p_4 \rangle + \beta \langle q_2 p_4 \rangle + \eta \langle w_2 p_4 \rangle + \alpha^{(4)} \langle p_4 p_4 \rangle + \beta^{(4)} \langle q_4 p_4 \rangle + \eta^{(4)} \langle w_4 p_4 \rangle$$
$$+ \eta^{(24)} \langle w_{24} p_4 \rangle + \eta^{(42)} \langle w_{42} p_4 \rangle \tag{5.21}$$

$$\langle g^{\mathrm{obs}} q_4 \rangle = \alpha \langle p_2 q_4 \rangle + \beta \langle q_2 q_4 \rangle + \eta \langle w_2 q_4 \rangle + \alpha^{(4)} \langle p_4 q_4 \rangle + \beta^{(4)} \langle q_4 q_4 \rangle + \eta^{(4)} \langle w_4 q_4 \rangle$$
$$+ \eta^{(24)} \langle w_{24} q_4 \rangle + \eta^{(42)} \langle w_{42} q_4 \rangle \tag{5.22}$$

$$\langle g^{\mathrm{obs}} w_4 \rangle = \alpha \langle p_2 w_4 \rangle + \beta \langle q_2 w_4 \rangle + \eta \langle w_2 w_4 \rangle + \alpha^{(4)} \langle p_4 w_4 \rangle + \beta^{(4)} \langle q_4 w_4 \rangle + \eta^{(4)} \langle w_4 w_4 \rangle$$
$$+ \eta^{(24)} \langle w_{24} w_4 \rangle + \eta^{(42)} \langle w_{42} w_4 \rangle \tag{5.23}$$

$$\langle g^{\mathrm{obs}} w_{24} \rangle = \alpha \langle p_2 w_{24} \rangle + \beta \langle q_2 w_{24} \rangle + \eta \langle w_2 w_{24} \rangle + \alpha^{(4)} \langle p_4 w_{24} \rangle + \beta^{(4)} \langle q_4 w_{24} \rangle$$
$$+ \eta^{(4)} \langle w_4 w_{24} \rangle + \eta^{(24)} \langle w_{24} w_{24} \rangle + \eta^{(42)} \langle w_{42} w_{24} \rangle \tag{5.24}$$

$$\langle g^{\mathrm{obs}} w_{42} \rangle = \alpha \langle p_2 w_{42} \rangle + \beta \langle q_2 w_{42} \rangle + \eta \langle w_2 w_{42} \rangle + \alpha^{(4)} \langle p_4 w_{42} \rangle + \beta^{(4)} \langle q_4 w_{42} \rangle$$
$$+ \eta^{(4)} \langle w_4 w_{42} \rangle + \eta^{(24)} \langle w_{24} w_{42} \rangle + \eta^{(42)} \langle w_{42} w_{42} \rangle \tag{5.25}$$

We call the correlations between galaxy shapes and PSF quantities on the left-hand side of Eqn. 5.18–5.25 the τ-statistics and the correlations of PSF quantities on the right-hand side the ρ-statistics. The ρ-statistics have been used as the metrics for the quality of the PSF models.

Given these measurements, we find the best-fit parameters to the contamination model (Eqn. 5.17) by minimizing the χ^2 with the Nelder-Mead algorithm (Nelder and Mead, 1965), where the covariance matrix is computed by repeating the measurement on our 800 mock catalogs (see § 5.3.1.1) with the Hartlap factor applied (Percival et al., 2022). With the

Table 5.4: The coefficients of the system of equations that represent the two-point correlations of galaxy shapes and PSF modeling errors.

parameter	2.5' < θ < 250'	0.25' < θ < 1000'
α	$0.017^{+0.009}_{-0.009}$	$0.007^{+0.008}_{-0.008}$
β	$0.851^{+0.624}_{-0.624}$	$1.192^{+0.232}_{-0.232}$
η	$7.402^{+6.796}_{-7.414}$	$-1.453^{+1.366}_{-1.367}$
$\alpha^{(4)}$	$0.006^{+0.028}_{-0.028}$	$-0.007^{+0.025}_{-0.025}$
$\beta^{(4)}$	$2.256^{+0.265}_{-0.261}$	$2.142^{+0.216}_{-0.215}$
$\eta^{(4)}$	$3.303^{+3.205}_{-3.223}$	$0.462^{+0.703}_{-0.701}$
$\eta^{(24)}$	$-1.910^{+1.416}_{-1.410}$	$-0.103^{+0.100}_{-0.100}$
$\eta^{(42)}$	$3.260^{+23.759}_{-23.797}$	$-0.638^{+1.761}_{-1.758}$
χ^2	124.37	176.17
χ^2_{reduced}	1.04	0.71

best-fit parameters, we additionally sample the parameter space using Markov Chain Monte Carlo (MCMC) in EMCEE package (Foreman-Mackey et al., 2013).

The 1D and 2D marginal posterior contours of the parameters are shown in Figure 5.11, and the mean of the 1D marginalized posterior is calculated to obtain the best-fit parameters that are shown in Table 5.4. We obtain χ^2/n=124.37/120=1.04 (n: degrees of freedom) with p-value=0.374. The best fit to our τ-statistics measurement is shown as a violet solid line in Figure 5.12, which is in good agreement with the data presented as the cross sign with the shaded region showing the 1σ error in the diagonal part of the data covariance matrix.

We find that we see no evidence of PSF leakage in our galaxy sample, meaning α and $\alpha^{(4)}$ are consistent with zero (within 2σ region of posterior contour). We, however, find a non-negligible impact of PSF modeling errors in our galaxy sample, which needs to be further investigated as contamination in our cosmic shear data, which we will cover in § 5.6.1.

5.3.4.3 Tangential and cross-component shear around stars

In this test, we explore the tangential and cross-component of shear around the positions of faint and bright stars as a test of spurious signal around the PSF candidate stars observed
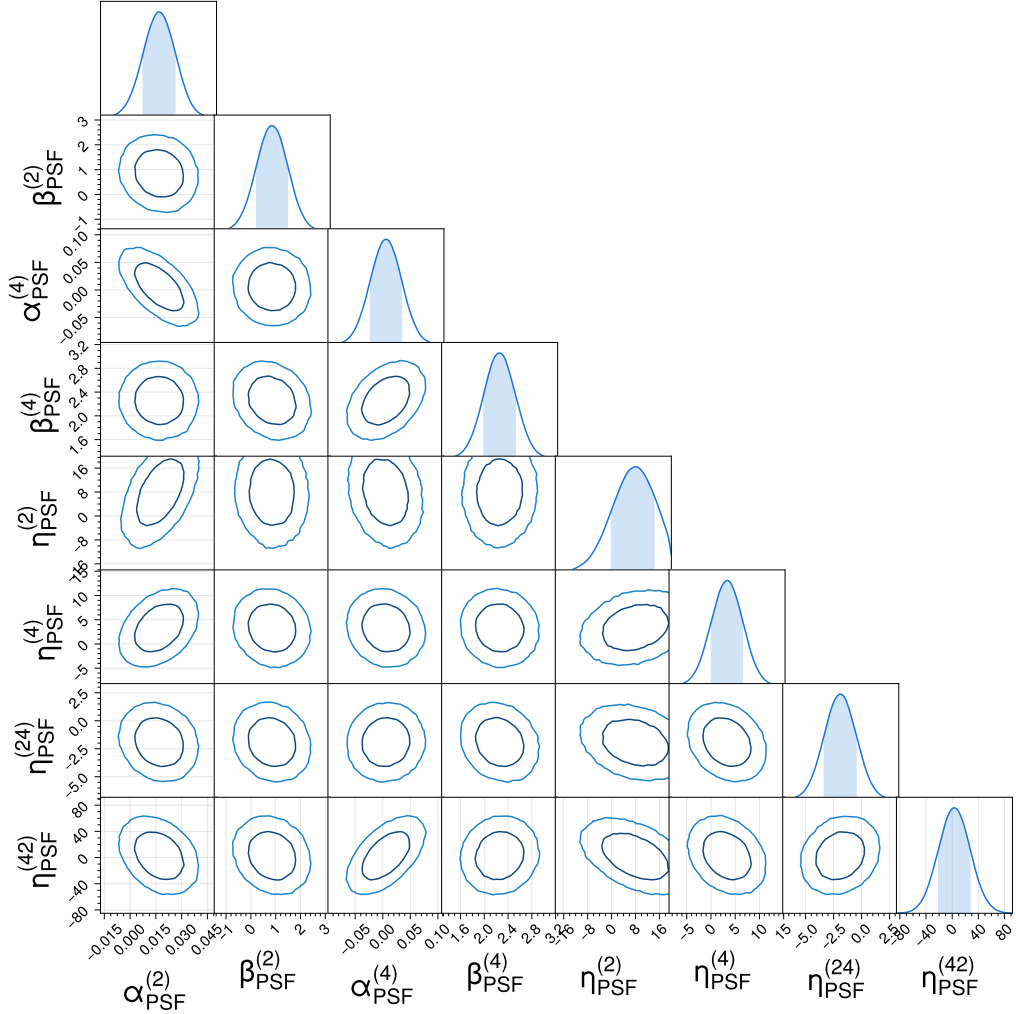
FIGURE 5.11: Posterior contours of our PSF contamination model parameter space for the fiducial angular scales and binning.

in the field. Since we do not expect any correlation between the location of stars and galaxy shear, any residual correlation of the tangential and cross-component galaxy shear around faint stars can reveal an additional additive bias due to the PSF modeling errors (which is not detected in ρ−statistics). On the other hand, the tangential and cross-component shear around bright stars can reveal the effect of pixel saturation and light halos of those stars on the observed galaxy shear.

Among the stars in our reserved star catalog, we first select a unique set of stars that made it to the coadd images. We then divide the stars into bright ($m_r < 16.5$) and faint
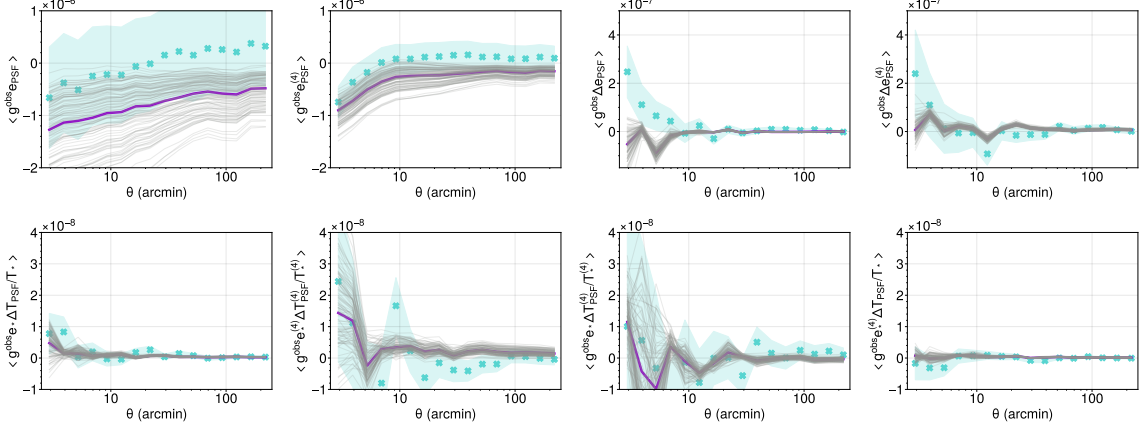
FIGURE 5.12: The measurement of τ-statistics (the correlations of galaxy shapes and PSF quantities) for the fiducial angular scales and binning is presented as cross data points. The 1σ error on the data (a diagonal part of our simulated covariance matrix) is shown as a shaded region. The best-fit τ-statistics model (measured from the best-fit parameters) is shown as a violet line in each panel, and grey lines show the measurements by sampling 100 sets of the model parameters from the posterior parameter space.

(m_r>16.5) samples. Figure 5.13 shows the result of this test. The signal around random points within our masked footprint is subtracted. For the shear around the bright star sample, reduced χ^2 statistics with respect to a null signal is $\chi^2_{\mathrm{reduced}}$=20.6/20 for γ_t and $\chi^2_{\mathrm{reduced}}$=14.7/20 for γ_x. We see no evidence of the impact around bright stars. For the shear around faint star sample, reduced χ^2 statistics with respect to a null signal is $\chi^2_{\mathrm{reduced}}$=25.3/20 for γ_t and $\chi^2_{\mathrm{reduced}}$=18.5/20 for γ_x. Again, we see no significant deviation from the null signal for the faint sample. We note that in order to guarantee the uniform distribution of galaxies and stars in our footprint, we apply weights to the star sample, which is the ratio of the number of galaxies and stars in each HEALPix grid.

5.3.5 Shape catalog systematics tests

We have examined how the Y6 PSF modeling impacts the observed shear in the form of additive bias. Now we turn to the empirical tests (null tests) within the catalog that might arise due to the configurations of the observations. It is important to mention here that we cannot know a priori how the observed shear is diverged from true shear (i.e., multiplicative bias) with these tests. Rather, they are suitable for detecting trends as a function of galaxy
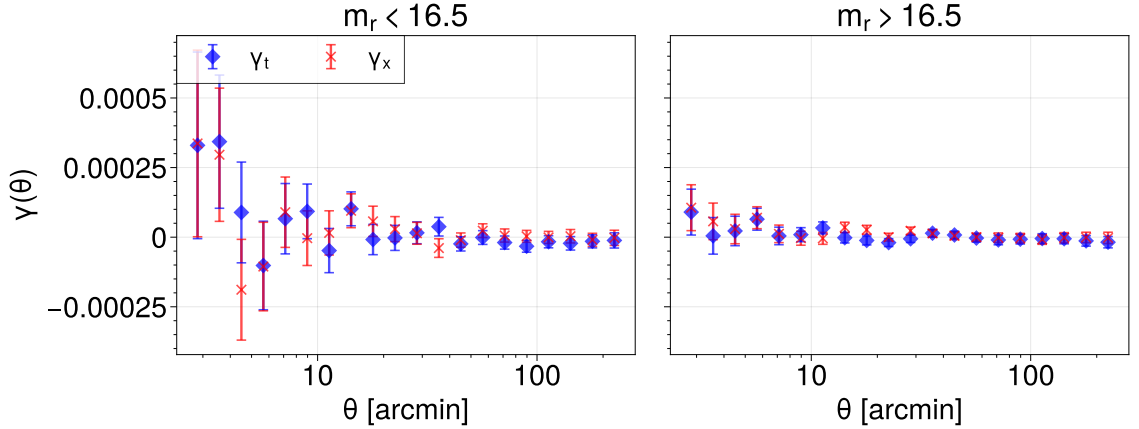
FIGURE 5.13: Tangential and cross-component shear around bright and faint stars. **Left**: tangential and cross-component shear around bright stars with r-band magnitude < 16.5. Reduced χ^2 statistics computed using the full covariance matrix for each γ_t and γ_x is χ^2_{reduced}=12.2/20 and χ^2_{reduced}=16.7/20, respectively. **Right**: tangential and cross-component shear around faint stars with r-band magnitude > 16.5. Reduced χ^2 statistics computed using the diagonal components of the covariance matrix for each γ_t and γ_x is χ^2_{reduced}=21.3/20 and χ^2_{reduced}=17.3/20, respectively.

and survey properties and signals larger than shape noise (i.e., additive bias).

In this section, we performed the following tests,

- shear variations in the focal plane, cell-coadd, coadd coordinates (§ 5.3.5.1);

- tangential and cross-component shear around the field, cell-coadd, coadd centers (§ 5.3.5.2);

- dependencies of mean shear on survey properties (§ 5.3.5.3).

5.3.5.1 Mean shear variations in the focal plane, cell-coadd, coadd coordinates

In this test, we explore the mean shear variations across different coordinate systems. Shear variations in focal plane coordinates (across CCD chips) can point to the problematic regions in CCDs where there is the masking of bad pixels or the effect of charge transfer inefficiency Zuntz et al., 2018. Shear variations in cell-coadd (200 x 200 pixels) and coadd (10,000 x 10,000 pixels) coordinates can reveal any correlations associated with our new coadding technique.

This is performed by first defining the grid to assign galaxies. In our case, we define each bin to be 128 x 128 pixels grid for focal plane coordinates, 15 x 15 pixels grid for cell-coadd

coordinates, and 250 x 250 pixels grid for coadd coordinates. We can then bin the galaxies from the five METADETECT catalogs according to the positions in each coordinate system. The shear in these bins is then averaged to compute the shear response and response-corrected shear in each bin. Figure 5.14 shows the mean shear variations where all CCDs are stacked together so that the signal in each CCD can be enhanced if it exists. In the bottom panel, the rows and columns of the grid are summed together to calculate the average to check the correlations. In both cases, we do not see a significant trend of measured shear as a function of focal plane coordinates. We also present the mean shear variations in all CCDs in Figure 5.15, but there is nothing suspicious here other than the noisy patch in CCD 2 due to the chip only taking half of the total observations and the white strip in the CCD fourth column from the left for e_1 which corresponds to the columns of bad pixels. Reduced χ^2 with respect to null detection is $\chi^2/\mathrm{dof} = 26621/25200$ for e_1 and $\chi^2/\mathrm{dof} = 25844/25200$ for e_2.

Another interesting test here is to look for the correlation of observed shear with PSF residuals in focal plane coordinates. Figure 5.16 shows the pattern of PSF shape and size residuals in the focal plane with individual whiskers showing the observed shear in each bin for the *coarse* grid. Visual investigation of this correlation does not find anything suspicious. This means that our observed shear is robust against the PSF residuals regardless of the patterns one sees in Figure 5.16.

As for shear variations in cell-coadd and coadd coordinates, Figure 5.17 shows no significant pattern appearing in both coordinate systems. The reported χ^2 with respect to zero mean shear is, $\chi^2_{\mathrm{reduced}}$=96.1/64 in e_1 and $\chi^2_{\mathrm{reduced}}$=66.8/64 in e_2 for cell-coadd coordinates and $\chi^2_{\mathrm{reduced}}$=1501/1444 in e_1 and $\chi^2_{\mathrm{reduced}}$=1388/1444 in e_2 for coadd coordinates.

5.3.5.2 Tangential shear around cell-coadd, coadd and field centres

In order to validate that there is no spurious radial pattern around the different coordinate systems, we measure tangential and cross-component shear around the center of cell-coadd, coadd, and field centers. The center of each cell-coadd image in sky coordinates
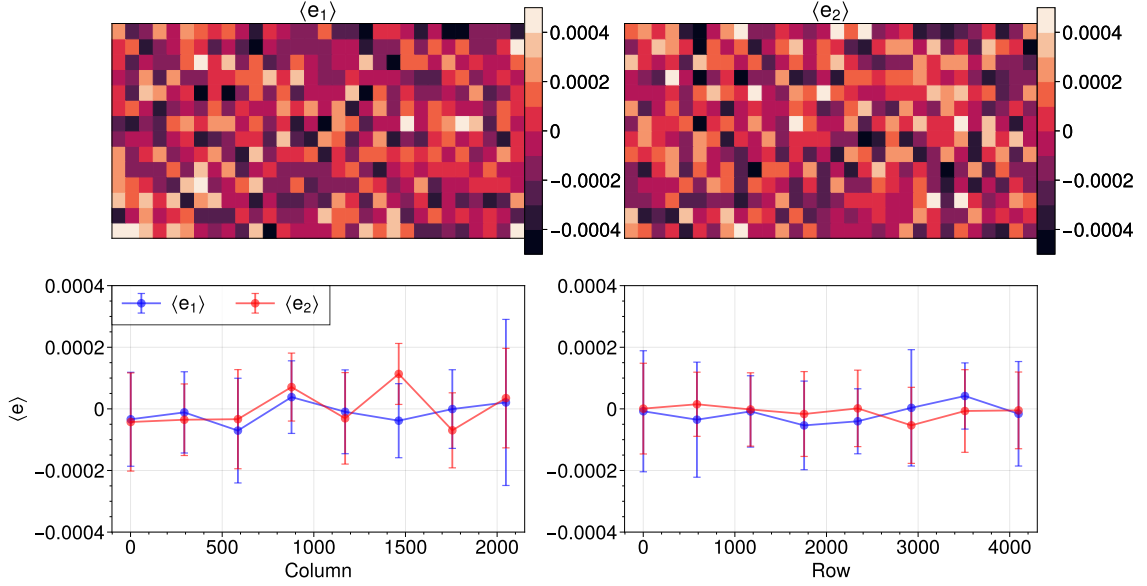
FIGURE 5.14: ***Top Row***: mean shear (e_1 and e_2) averaged in a cell (CCD coordinates 2048 x 4096 are divided into 16 x 32 cells of 128 x 128 pixels) where all CCDs from all exposures are stacked on top. For each object detected in a coadded image, the CCD coordinates of where it is located in single-exposure images are identified, and the galaxy shape measured on a coadd image is collected. After all galaxy shapes are collected, the shear response is computed in each cell, and the ensemble average of shear in each cell is corrected by the response. ***Bottom Left***: The accumulated shapes are summed over 2 rows, and the response corrected shear is plotted. ***Bottom Right***: The accumulated shapes are summed over 4 columns. Note that global mean shear residuals in the catalog are subtracted in all panels.

can be obtained by converting cell-coadd coordinates to a coadd coordinate system and by applying the WCS of the coadd tile. The center of each coadd image can be obtained easily since a DES coadd tile is defined in sky coordinates. As for a field center, each exposure has a pointing, and the field center is the position of the pointing center (RA, Dec). The number of field centers used in this test is 47610. We present the result in Figure 5.18. From the left to right panels, it shows both the tangential and cross-component shear around cell-coadd, coadd, and field centers. The reduced χ^2 with respect to a null signal is $\chi^2_{\text{reduced}}=6.37/15$ for γ_t and $\chi^2_{\text{reduced}}=16.6/15$ for γ_x around cell-coadd centres. $\chi^2_{\text{reduced}}=12.9/15$ for γ_t and $\chi^2_{\text{reduced}}=19.4/15$ for γ_x around coadd centres. $\chi^2_{\text{reduced}}=61.1/20$ for γ_t and $\chi^2_{\text{reduced}}=19.4/20$ for γ_x around field centres. These χ^2 are measured with full covariance matrices associated with each measurement. We also note that signals around random points are subtracted
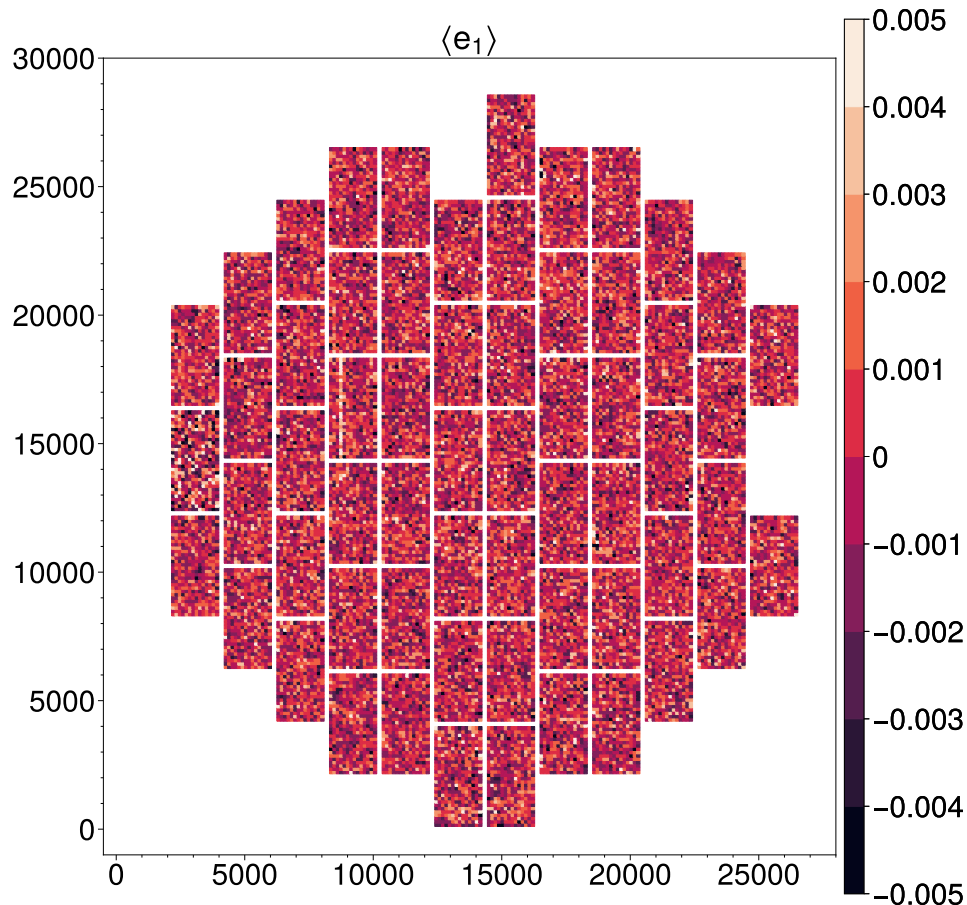
FIGURE 5.15: Mean shear (e_1) in focal plane coordinates. Galaxy ellipticity is averaged in a cell (CCD coordinates 2048 x 4096 are divided into 16 x 32 cells of 128 x 128 pixels) where the contributions from all exposures in r-band are averaged. The variations in e_2 look similar, and we report $\chi^2/\mathrm{dof} = 26387/25200$ for e_1 and $\chi^2/\mathrm{dof} = 25802/25200$ for e_2.

for each measurement.

As seen in GS20, we see a non-null tangential shear signal around field centers. In order to verify that we are not dominated by cosmic variance, we run the same test on 800 mock catalogs (see § 5.3.1.1) and re-estimate the covariance matrix. Nonetheless, we do not see any improvement in our measurement and report $\chi^2_{\mathrm{reduced}}=67.7/20$ for γ_t.

In order to understand where the signal stems from, we split our galaxy sample by their $g - i$ color. Figure 5.19 shows the same measurement of tangential shear around different coordinate systems. We again find no trend around cell-coadd and coadd centers, but one can find a significant deviation from the null signal around 7-8 arcmin, 10-20 arcmin, and
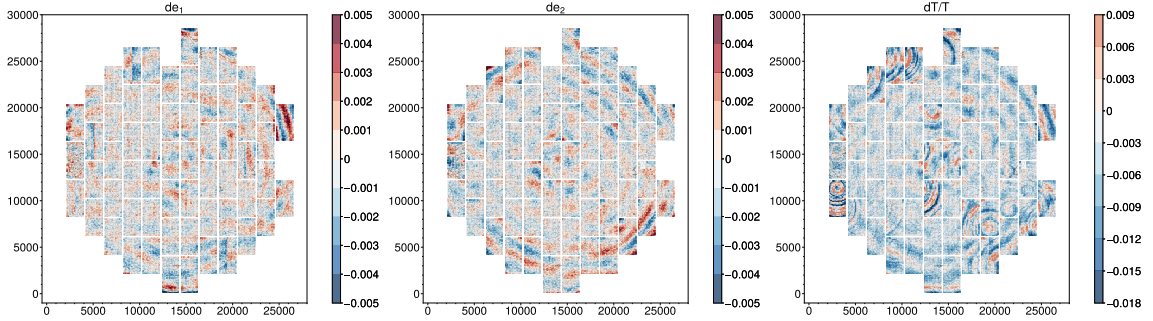
FIGURE 5.16: A spatial map of the galaxy shapes (whisker) and PSF shape (**left** and **middle** column) and size (**right** column) residuals shown in color. Galaxy ellipticity and PSF quantities are averaged in a cell of 128 x 128 pixels. The whiskers are scaled so that the length of one grid cell corresponds to $e = 4x10^{-5}$.

40-60 arcmin scale, which corresponds to the deviations seen in the right panel of Fig 5.18. Some of these effects can be understood as PSF modeling errors due to color that can be seen in the left panel of Figure 5.20 when PSFs are evaluated at median star color. Even when the PSFs are evaluated at their actual star color, the right panel of the figure suggests the non-zero patterns at scales around 10-20 arcmin, which corresponds to the scales of each CCD.

One could estimate the impact of this signal in a cosmologically relevant signal by interpolating γ_t as a function of distance from the focal plane center and measuring $\xi_\pm$. Our measurement, however, indicates that the signal amplitude is smaller than that of GS20, and they concluded that the level of contamination on $\xi_\pm$ is 0.01%. Given this, we also conclude that the signal observed here is cosmologically irrelevant, and we pass this test.

5.3.5.3 Survey property maps

Another important test to identify the observational systematics on the recovered shear is the correlation of galaxy shapes with observing conditions. Verifying the shear is not dependent on any survey condition is particularly important since it cannot be characterized through simulations. A survey property such as airmass is recorded during each observation, and the data is averaged or summed over each HEALPix grid of resolution 14 for 6 years of
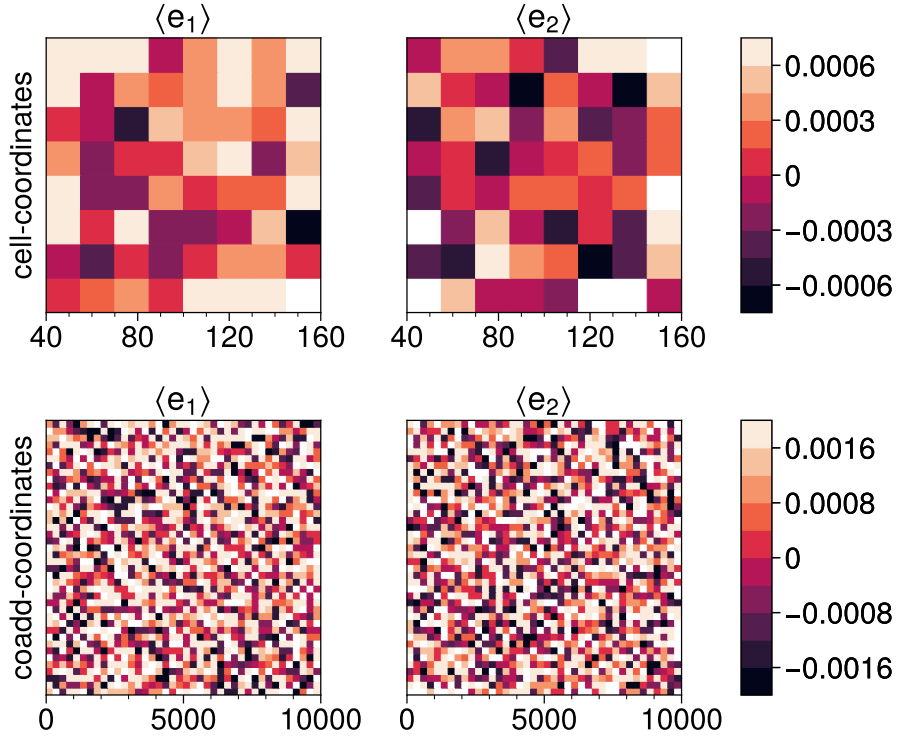
FIGURE 5.17: *Top Row*: mean shear (e_1 and e_2) in coadd slice coordinates, which consists of 200 x 200 pixels. Due to a buffer region around each slice where objects are not detected, the figure covers the central region of a slice. χ^2 with respect to zero mean shear is, $\chi^2_{reduced}$=96.1/64 for e_1 and $\chi^2_{reduced}$=66.8/64 for e_2. The definition of a coadd slice can be found in § 5.3.2. *Bottom Row*: mean shear (e_1 and e_2) in coadd coordinates. A coadd that is 10,000 x 10,000 pixels consists of 9800 coadd slices. χ^2 with respect to zero mean shear is, $\chi^2_{reduced}$=1501/1444 for e_1 and $\chi^2_{reduced}$=1388/1444 for e_2. In both coordinate systems, objects are allocated to each grid cell, and then the shear response for each cell is computed to measure the calibrated mean shear. Here, the global mean shear from the catalog is subtracted.

observations as a survey property map (Bechtol et al. in prep.). For each galaxy position, there is a survey property value, and we take an average of shear (e_1 and e_2) in the bins of the survey property.

The survey property maps with the number of HEALPix values we consider are,

- airmass (weighted mean) – secant of the zenith angle for the observations. (`nside`=16384)

- exposure time (sum) – the total time in seconds for exposures. (`nside`=16384)

- FWHM (weighted mean) – the full-width half maximum (in arcseconds) of the PSF (seeing). (`nside`=16384)

137
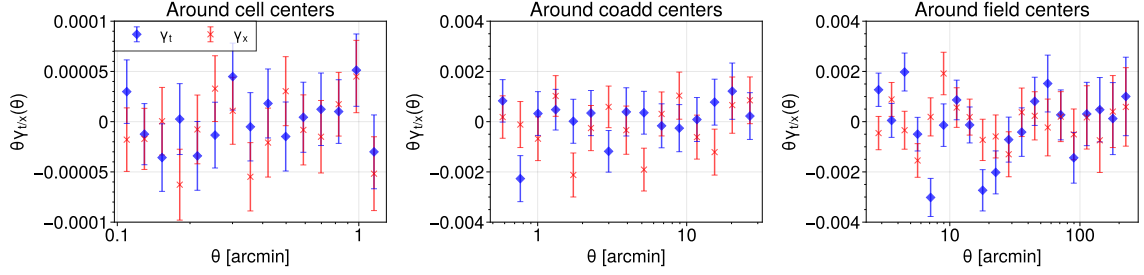
FIGURE 5.18: **Left**: tangential and cross-component shear around cell-coadd coordinates, which has a dimension of 200 x 200 pixels. Reduced χ^2 statistics computed using the full covariance matrix for each γ_t and γ_x is χ^2_{reduced}=6.37/15 and χ^2_{reduced}=16.6/15, respectively. **Middle**: tangential and cross-component shear around cell-coadd coordinates, which has a dimension of 10,000 x 10,000 pixels. Reduced χ^2 statistics computed using the full covariance matrix for each γ_t and γ_x is χ^2_{reduced}=12.9/15 and χ^2_{reduced}=19.4/15, respectively. **Right**: tangential and cross-component shear around field centers. Reduced χ^2 statistics computed using the full covariance matrix for each γ_t and γ_x is χ^2_{reduced}=61.1/20 and χ^2_{reduced}=19.4/20, respectively. The number of field centers used for this test was 47610.
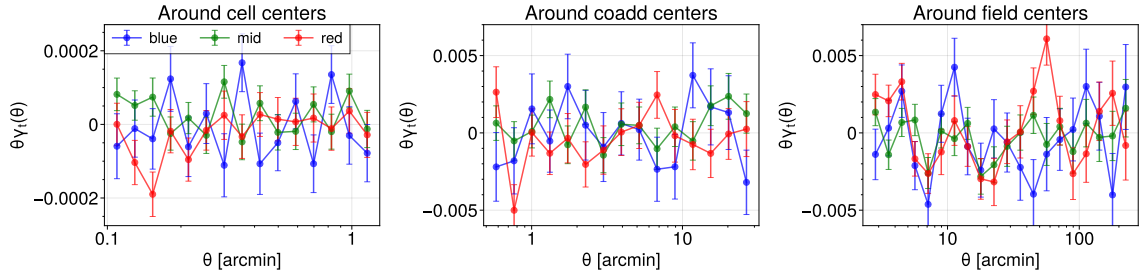
FIGURE 5.19: Tangential shear around cell-coadd, coadd, and field centers where the galaxy sample is split by their measured $g - i$ color (blue: [-2.00, 0.76], mid: [0.76, 1.49], red: [1.49, 4.00]).

- sky brightness (weighted mean) – contributions from airglow, zodiacal light, and scattered starlight are measured and weighted. (**nside**=16384)

- Differential Chromatic Refraction (DCR; weighted mean) – the effect of DCR on PSF shape e_1 and e_2 and on the sky coordinates (RA, DEC) (**nside**=16384)

- Background Offset – background offset estimated from stellar photometry. (**nside**=64)

- Stellar Density – the density of *Gaia* stars found in our footprint. (**nside**=16384)

Bechtol et al., in prep, provide a more detailed description of how each survey property is measured.

The measurement is conducted as follows. We first divide the range of a survey property
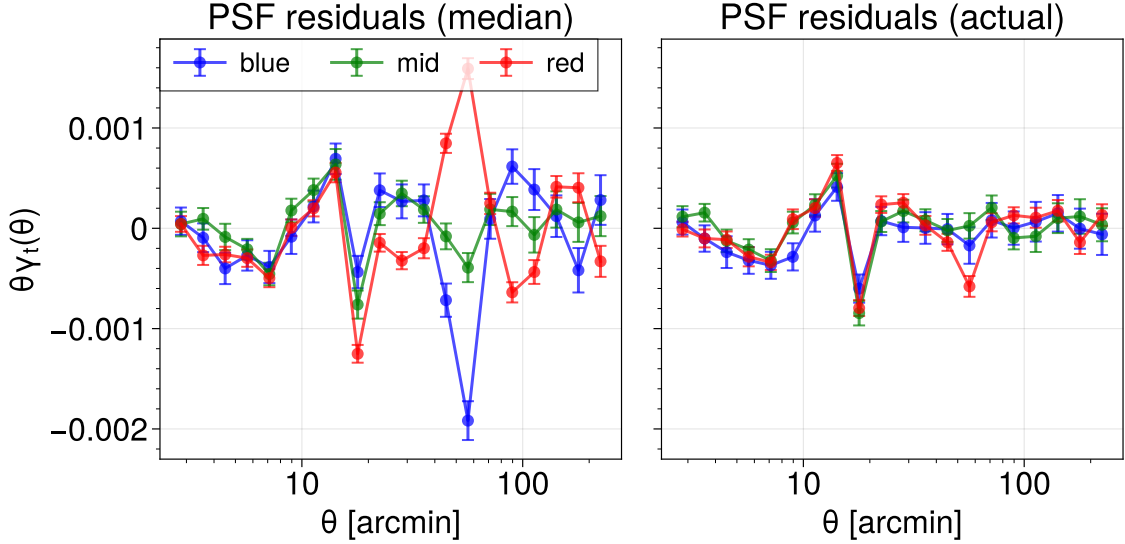
FIGURE 5.20: Tangential projection of PSF shapes around field centers where the star sample is split by their measured $g - i$ color (blue: [-2.00, 0.76], mid: [0.76, 1.49], red: [1.49, 4.00]). ***Left*** panel shows the case when the PSFs were drawn at their median color, which is the case in our METADETECTION shape catalog. ***Right*** panel shows the case when the PSFs were drawn at their actual star colors, which is the case in our BFD shape catalog.

signal into several bins and assign galaxy shear to each bin based on their positions in the sky. We then calculate the mean shear for the five METADETECT catalogs, compute the shear response in each signal bin, and correct the raw mean shear by the response. This results in a relation of shear with a survey property signal, which can then be fit linearly with slope and offset in an ordinary least-squares manner. We note that the survey property signals are normalized to $\subseteq [0,1]$ prior to the fitting.

Uncertainties on the fit parameters are, however, estimated using mock shear catalogs. This allows us to estimate uncertainties in the absence of observational systematics. Using the 800 realizations, slope, and offset parameters are calculated, and the uncertainties on m, σ_m, are estimated as the standard deviation of 800 slope parameters. Figure 5.21 shows the m/σ_m, which is the statistical significance of the non-zero slope. In all survey properties, we find that slopes are statistically consistent with zero, meaning observed shear is not correlated with survey conditions. We report reduced χ^2 statistics in Table 5.5.
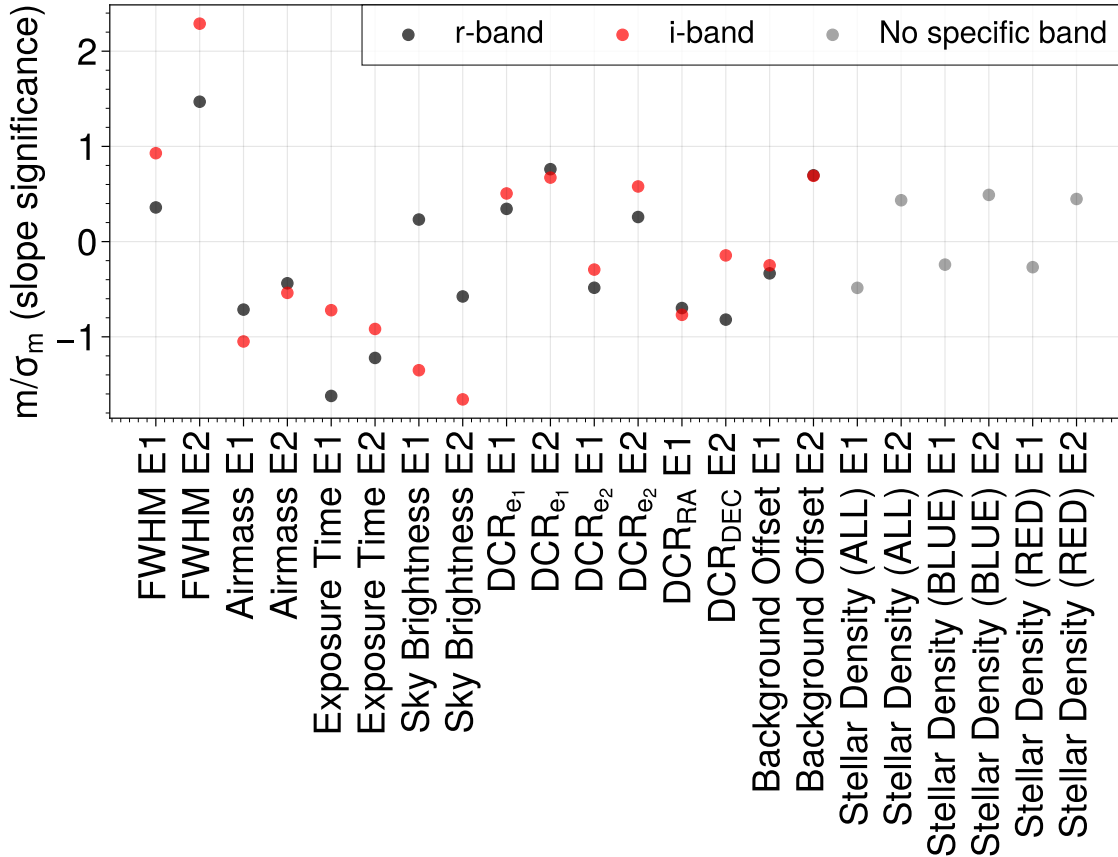
FIGURE 5.21: Statistical significance of the slope of the best-fit (ordinary least-square) line on the mean shear signal in the bins of several survey properties is presented. $E1/E2$ in the x-axis denotes e_1/e_2 component of the mean shear correlated with the survey property. In order to beat cosmic variance, we use simulated shape catalogs from 800 realizations of COSMOGRID simulations to estimate the uncertainties of mean shear in each bin.

5.4 Image Simulations

The summary presented in this section is from the current collaboration work in DES. Most of the work has been done by the shear analysis team that I co-lead, especially Matt Becker and Sid Mau. Most of the work will be described in Yamamoto et al. in prep. and Mau et al. in prep. and I will summarize our work on Y6 image simulations below.

So far, we have discussed the catalog-level systematics tests and mostly examined the sources of additive bias, which we can calibrate from data. The calibration of multiplicative bias, however, needs to be characterized and carried out in realistic image simulations, as

Table 5.5: The reduced χ^2 with respect to the null detection for each correlation of observed shear with survey property map.

survey property	χ^2/dof (r-band; e_1, e_2)	χ^2/dof (i-band)
Airmass	0.47, 0.75	0.96, 0.38
Exposure Time	0.57, 0.51	0.71, 1.12
FWHM	0.53, 0.69	0.50, 0.64
Sky Brightness	0.56, 0.92	0.53, 0.61
DCR (RA)	0.86, 0.44	0.63, 0.81
DCR (DEC)	0.63, 0.50	0.61, 0.52
DCR (PSF e_1)	0.76, 1.32	0.50, 1.14
DCR (PSF e_2)	0.67, 0.33	0.67, 0.69
Background Offset	0.95, 1.31	1.25, 1.01
Stellar Density (ALL)	0.79, 1.38	
Stellar Density (BLUE)	0.40, 0.99	
Stellar Density (RED)	0.43, 1.26	

discussed in § 4.2.4 and § 4.3. Our Y6 image simulation suite is built and developed further on top of the Y3 image simulations described in MacCrann et al. 2021. The full details of the Y6 image simulations and the shear and photo-z calibration will be presented in Mau, Becker et al. in prep.. In this section, we will briefly summarize the image generation and processing steps of the simulations and present the multiplicative and additive bias results for our Y6 image processing pipeline in simple simulation setups and the Y6 simulation suite setups without blending-related measurement described in § 4.3.5.

In the simple simulation setups, we test the shear recovery of objects placed on a hexagonal grid with four types of input shear, (g_1, g_2)=[(+0.02, 0), (-0.02, 0), (0, +0.02), (0, -0.02)]. These objects were drawn at the center of each grid point with an exponential radial profile at a half-light radius of 0.5 convolved with either a Gaussian profile or PIFF PSF model produced for our real data. We have then tested the shear recovery of objects at both high (r=18) and low S/N (r=23.5). The results will be provided later.

After checking the shear calibration biases are under control for simple grid configurations, we increase the complexity of the simulations by placing realistic galaxies at random positions in the image. The realistic galaxies are simulated using the parameters (e.g., bulge-to-disk fraction) that are fit to the deep-field galaxies in the COSMOS field (Hartley

et al., 2022). These galaxies are then sheared with the same input shear as the simple configurations, and they are rendered and placed in the image with the Y6 WCS solutions and PSF models. With the simulations of 400 tiles, we obtain the following preliminary results: $m = (-0.4 \pm 0.7) \times 10^{-2}$ and $c = (-0.01 \pm 0.02) \times 10^{-2}$ with 3σ uncertainty. The multiplicative bias has decreased about 5× with the new image processing pipeline compared to the bias measured in Y3 image simulations (MacCrann et al., 2021) and is almost competitive with the requirement for LSST.

5.5 Photo-z Estimation

The summary presented in this section is from the current collaboration work in DES. Most of the work has been done by the photo-z analysis team, especially Boyan Yin, Andresa Campos, and Alex Alarcon. Most of the work will be described in Yin et al. in prep. and I will summarize their work on implementing the method to infer the photo-z and generate the redshift distribution of the DES Y6 galaxies from the shape catalog below.

In Y6, the basic methodology is the same as Y3 (SOMPZ: Myles et al., 2021) and utilizes the Self-Organizing Map to establish the color-redshift relationship. We summarize the concepts and specific implementation below. Firstly, four samples from which we draw the color-redshift relation are,

- Wide-field galaxy sample – the weak lensing source galaxies from the shear catalog.
- Deep-field galaxy sample – the deep field galaxies, which have measured fluxes in additional bands *ugrizJHK* (Hartley et al., 2022).
- BALROG galaxy sample (deep and wide) – the synthetic galaxies injected on wide-field images based on the photometry of the deep-field galaxies (BALROG: Everett et al., 2022; Suchyta et al., 2016). These galaxies contain both wide and deep photometric information. Figure 1 of Everett et al., 2022 summarizes the process of generating the BALROG sample.
- Redshift sample – a subset of the deep field galaxies have accurate redshifts obtained from the spectroscopic sample (e.g., zCOSMOS) and many-band photometric sample
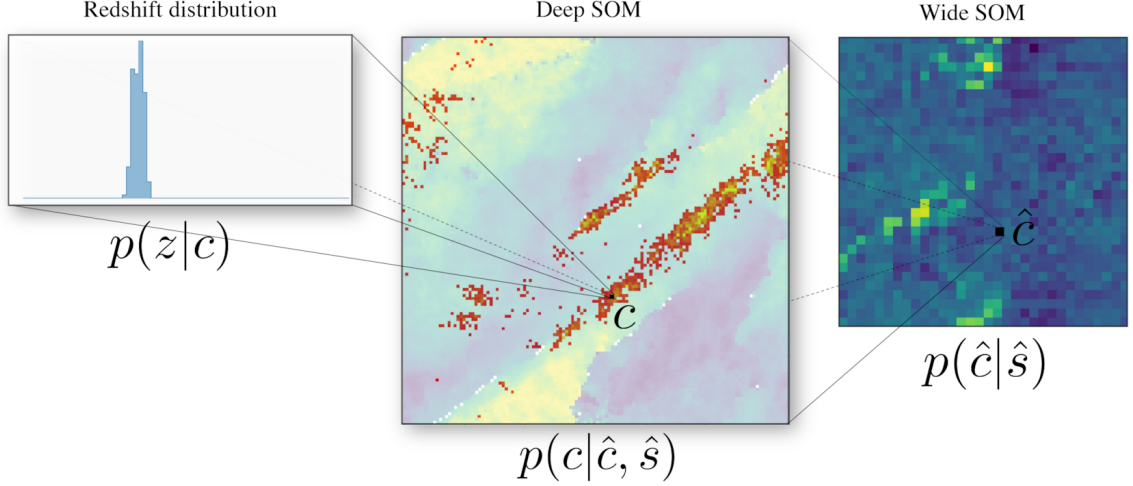
FIGURE 5.22: An illustration of the correspondence between the redshift distribution and deep and wide self-organizing map. Figure 3 from Buchs et al., 2019

(e.g., COSMOS+PAUS 66 band photometric redshift catalog).

From the photometric color of deep-field and wide-field samples, we can construct two SOMs, deep and wide SOM, as shown in Figure 5.22. We can then assign the galaxies in the deep-BALROG sample and redshift sample to the cells in the deep SOM (c) and the galaxies in the wide-BALROG and wide sample to the cells in the wide SOM ($\hat{c}$). The redshift distribution of galaxies given a tomographic bin ($\hat{b}$) and selection function ($\hat{s}$) can be estimated as,

$$n(z) \equiv p(z|\hat{b}, \hat{s}) = \sum_{\hat{c} \in \hat{b}} \sum_{c} p(z|c, \hat{s}) p(c|\hat{c}, \hat{s}) p(\hat{c}|\hat{s}, \hat{b}). \qquad (5.26)$$

$p(z|c, \hat{s})$ describes the probability of a galaxy in a deep cell belonging to a redshift and can be computed from the assignment of the redshift sample to the deep SOM. $p(c|\hat{c}, \hat{s})$ describes the probability of a galaxy being in a deep cell given that a galaxy is in a wide cell and its selection (i.e., color), and this is called as the transfer function connecting the deep and wide cells. Since the BALROG sample contains both wide-field and deep-field galaxies (though wide-field galaxies are simulated and deep-field galaxies are injected), it is possible to estimate the probability of a wide cell belonging to a deep cell. Finally, $p(\hat{c}|\hat{s}, \hat{b})$ describes the probability of a galaxy of a given color belonging to a wide cell and can be

computed from the assignment of wide-field galaxies. When estimating redshift, galaxies are assigned to cells in a self-organizing map (SOM) based on their similarity in redshift. Galaxies with similar redshifts are grouped in the same or nearby cells. This allows for a fairly accurate determination of the redshift distribution for those galaxies.

Now we briefly summarize several updates compared to Y3 below.

- SOMPZ algorithmic update – a new algorithm takes account of the fact that the training data of SOMs includes faint galaxies, which have large measurement uncertainties (Sánchez et al., 2020).

- redshift sample – The COSMOS2020 sample (Weaver et al., 2022) will be employed for the redshift sample. Compared to COSMOS2015, COSMOS2020 has increased the photometric redshift precision with the new data and achieved a reliable photo-z at fainter magnitude ($i>26$).

- BALROG sample – Y6 BALROG sample makes use of the Y6 image simulations and generates images for all the DES coadd tiles (about 10,000 tiles), which is about 6 times more tiles than what was run in Y3. This work is described in Tabbutt et al. in prep.

- inclusion of g-band – for Y6, we will be able to include the g-band photometric information in the photo-z inference thanks to the color-dependent PSF modeling that improved the PSF models in g-band.

The algorithmic update and the impact of adding g-band information are well described in Campos et al. in prep., and it shows that the new algorithm can reduce the standard deviation in the redshift distribution in each cell and greatly reduce the bin overlaps. The effort to apply these updates on Y6 data is in progress, and Figure 5.23 shows the preliminary redshift distribution compared to Y3. The results will be described in Yin et al. in prep.
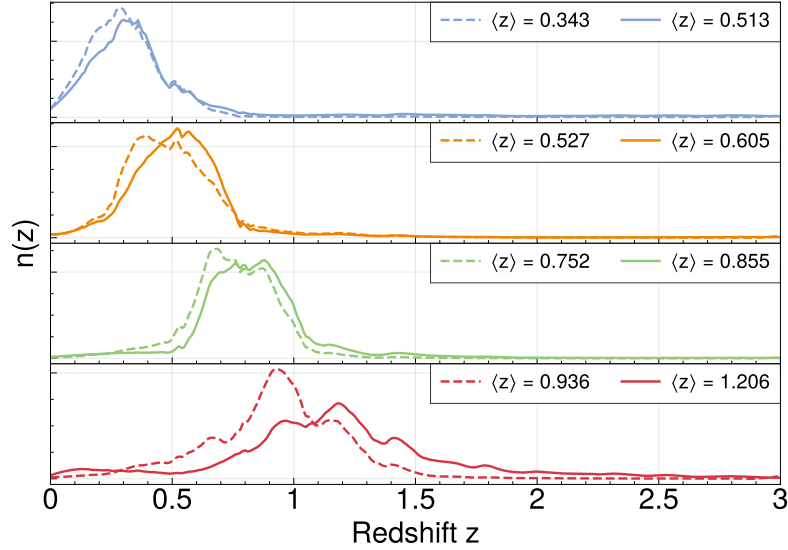
FIGURE 5.23: Redshift distributions $n(z)$ produced with the Y6 SOMPZ pipeline from source galaxies in DES Y6 shear catalog, compared with $n(z)$ from Y3 analysis.

5.6 Cosmic Shear Cosmology

The summary presented in this section is from the current collaboration work in DES. Most of the work has been done by the cosmic shear team that I co-lead and the modeling team, and it will be described in DES Collaboration et al. in prep. The text presents my own work, and the contributions of other authors are presented as such:

- *Giulia Giannini & Jessie Muir: Implementation of the scheme for blinding data vectors.*

- *Simon Samuroff, David S. Cid, & Modeling team: Several works related to the theoretical computation of the cosmic shear data vector, especially scale cuts and the validation of the nonlinear matter power spectrum and the impact of the baryonic feedback model.*

Given the galaxy shear and their redshift distribution, we are able to perform the cosmological analysis with the DES Y6 data. This section is divided into the **data** (which will talk about the measurement of the two-point correlation function of galaxy shapes and various validation tests on the 2pt data) and **theory** part (which will explore the analysis

145

choices we make in DES Y6).

5.6.1 Data

Following § 4.2.5, we are able to compute the two-point correlation function (2PCF) of galaxy shapes that are divided into four tomographic bins according to the redshift catalog produced in § 5.5. Our fiducial data vector is computed with TREECORR for an angular range of 2.5 to 250 arcmin in 20 logarithmic bins. Figure 5.24 shows the correlation in the same redshift bin (indicated in each panel) and across different redshift bins. In order to avoid observer bias (one visually compares $\xi_\pm$ signal from theory or previous analyses, extrapolates the cosmological parameters of interest, and attempts to make informed decisions on the analyses, whether it is intentional or unintentional), we are required to produce blinded data vectors and conduct a blind analysis. One first chooses a reference cosmology (one used during modeling tests) and applies a random shift in cosmological parameters (the seed is saved). This indicates that $\xi_\pm(\Theta_{ref})$ is transformed to be $\xi_\pm(\Theta_{ref} + \Delta\Theta)$. One can then add the shift $\Delta\xi_\pm$ to the raw data vector, and the blind data vector is produced. Once we are allowed to unblind, the blinding seed is used to recover the original data vector.

Our Y6KP Analysis Plan suggests that we can unblind our real data vectors once appropriate null tests show no significant systematics in our blinded data vectors for individual probes. We conduct the following null tests for cosmic shear data vector and define our requirements to pass them (note some of the tests are still in progress). The requirements can be quantitative or qualitative, as some tests require validating the impact of individual systematics on cosmological parameters, and requiring a quantitative threshold can be challenging for other tests.

- PSF systematics
- B-mode
- Additive bias correction
- Correlations with survey properties or measured quantities
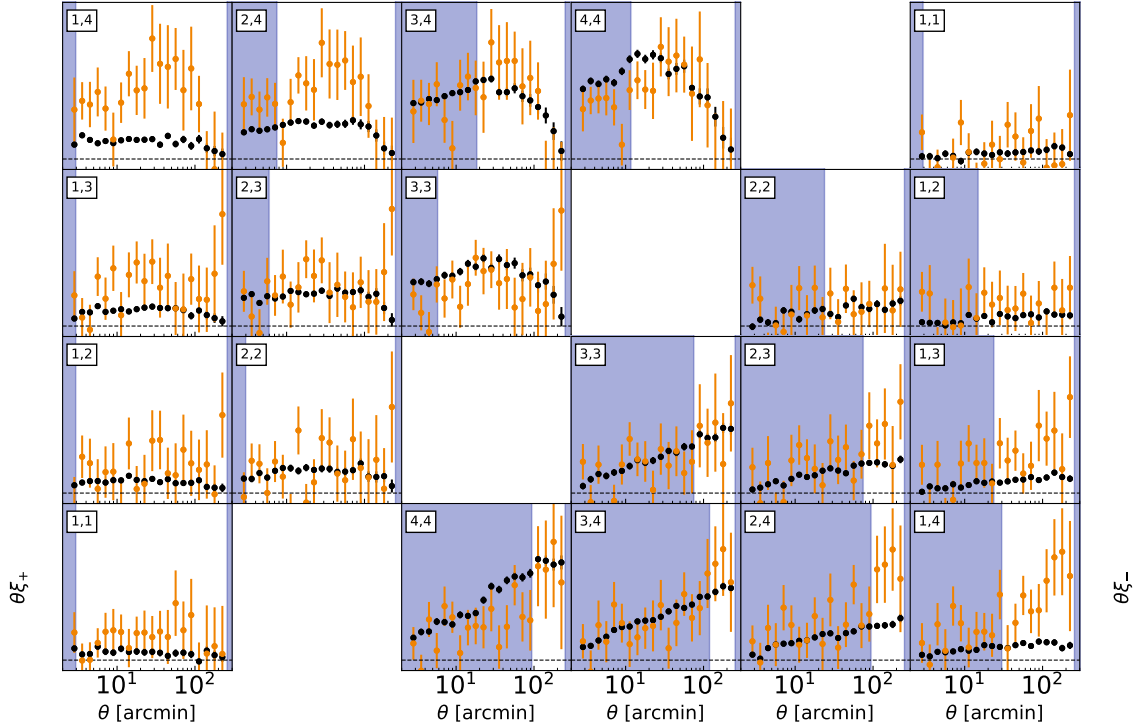
FIGURE 5.24: The tomographic measurement of the DES Y6 cosmic shear two-point correlation function, overlaid with DES Science Verification (SV) cosmic shear signal (orange; Becker et al., 2016) measured in the Y6 tomographic binning. In the cosmological analysis, the data points in the blue-shaded region (which defines the scale cuts) will not be used. The y-axis is not shown because the data vector is still blinded.

5.6.1.1 PSF systematics

Our PSF models are not perfect, and galaxy ellipticity recovered from images can possibly have dependencies on PSF shapes/sizes. We usually model the impact of PSFs on galaxy ellipticity as an additive signal, meaning that we can estimate the impact on cosmic shear data vector and cosmological parameters. The catalog-level test of the PSF contamination can be found in § 5.3, and here we will describe the data vector-level and cosmological parameter-level tests.

For the data vector-level test, we measure correlations of galaxy ellipticity from a shear catalog and PSF shapes for each tomographic bin, similar to what we did in § 5.3. We repeat the measurement with 800 mock catalogs in each tomographic bin. We then fit the

147
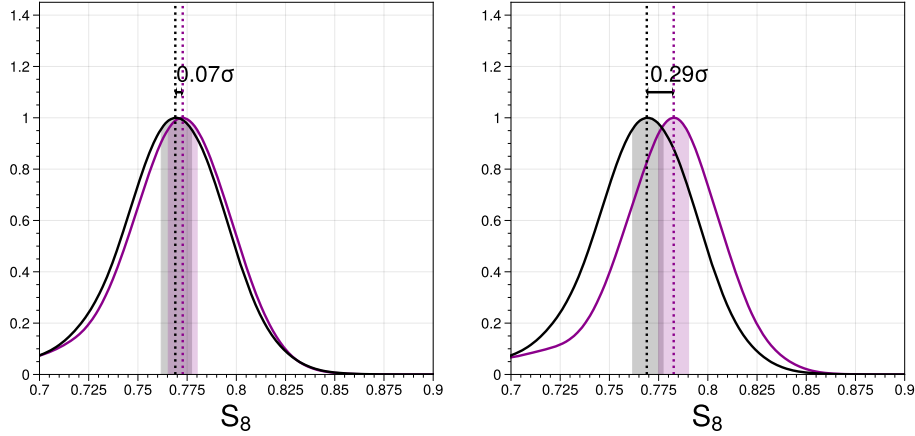
FIGURE 5.25: *Left*: the shift in S_8 from the mean PSF contamination compared with the S_8 value measured with the fiducial theory data vector. *Right*: the shift in S_8 from the maximum PSF contamination scenario, where the contamination is 3σ larger than the mean contamination. Both cases satisfy the requirement of the shift being smaller than 0.3σ.

coefficients/parameters (α, β etc.) of the PSF contamination model with the covariance matrix computed from mocks. We sample the parameters from the posterior chain of the fit, measure the contamination as $\delta\xi_{\pm,i}$, repeat 800 times, and calculate the mean contamination $\langle\delta\xi_{\pm}\rangle$.

For the parameter-level test, we explore two cases of contamination. One is to add the mean PSF contamination estimated in the previous test to the fiducial theory data vector as a contaminated data vector. The other is to add the 3σ errors on the mean to the mean contamination to generate a maximum PSF contamination signal and add it to the fiducial theory data vector (maximum contamination). We run cosmological parameter inference chains with these contaminated data vectors at the baseline model and compare the inferred S_8 with the fiducial theory data vector with the same baseline model. Our preliminary test shows that both mean and maximum contamination scenarios do not lead to a significant shift in S_8, and both cases satisfy the requirement of the shift being smaller than 0.3σ, as shown in Figure 5.25.

5.6.1.2 B-mode

As described in § 3.3.3, the detection of a B-mode signal can point towards observational or astrophysical systematics for the current sensitivity of the data since we expect that lensing produces only E-mode at first order. Therefore, the null detection of the B-mode signal in our cosmic shear data vector is one of the most important validations in cosmic shear analysis.

While there are a few ways to estimate B-mode from $\xi_\pm$ (real-space correlation function), such as COSEBIs (Schneider et al., 2010) and Pseudo-C_ℓ (Alonso et al., 2019; Hikage et al., 2011), which require producing a shear map and/or interpolating $\xi_\pm$ to compute C_ℓ, these methods are sensitive to the E- and B-mode mixing from masking, binning/interpolation and pixelization (e.g., Becker, 2013). We utilize the Fourier Band-Power E/B-mode estimator (Becker and Rozo, 2016) to estimate the B-mode from the linear combinations of our real-space correlation function. This method takes the advantage of directly utilizing the binned-statistics without interpolation while accounting for survey mask in real space, showing that it can separate E/B-mode competitively or more compared with Pseudo-C_ℓ method. Our preliminary test suggests that the B-mode for the non-tomographic case shows a null detection with p-value = 0.2986 (Figure 5.26).

5.6.1.3 Additive bias correction

As we saw in § 5.3, we find the mean residual additive shear at the level of 10^{-5} to 10^{-4} in our shear catalog. During the analysis, we subtract the correlation of mean shear in each tomographic bin from the measured 2PCF in the data. One must however check whether the mean residual shear has any impact on our inferred cosmology. We measure mean shear in each tomographic bin and compute the contamination on $\xi_\pm$ as $\langle e_1^i \rangle \langle e_1^j \rangle \pm \langle e_2^i \rangle \langle e_2^j \rangle$. We will add this contamination to the fiducial theory data vector to investigate if the impact of our correction strategy is large.
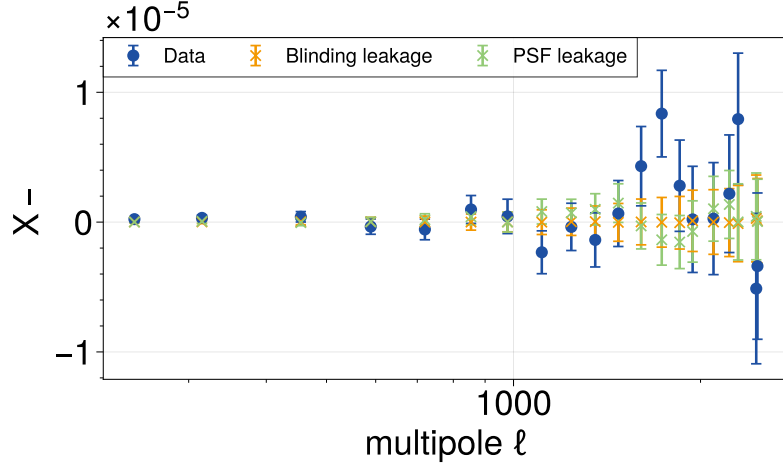
FIGURE 5.26: B-mode estimated from $\xi_{\pm}$ computed from all the samples (no tomographic bins) in our Y6 shear catalog. χ_2/dof = 22.8/20 with p-value = 0.2986.

5.6.1.4 Correlations with survey properties or measured quantities

In order to ensure that our data is not systematics-dominated, a useful test is to examine the 2PCF as a function of survey conditions (e.g., airmass) and measured quantities (e.g., S/N). For each survey property/measured quantity, we define two samples with low and high signals. For each object in a shear catalog, we assign the survey property value according to its HEALPix location (no need for this for measured quantity), and we split the catalog into two halves. We measure $\xi_{\pm}$ in these bins and take the difference to study that the residual signal is consistent with zero. It is important to note here that we need to correct any differences in the redshift distributions in each bin for two samples. We will likely utilize the survey property maps and measured quantities we have tested the shear catalog within § 5.3.

5.6.2 Theory

For an accurate modeling of the statistical uncertainties in the measurement of $\xi_{\pm}$ with an assumption that our likelihood is multi-variate Gaussian, we utilize CosmoCov (Fang, Eifler, and Krause, 2020) which allows one to analytically compute the covariance matrix as a function of both cosmological parameters and nuisance parameters. The relevant "data"

150

parameters to input in CosmoCov are the area of our footprint, the number density in each tomographic bin, the shape noise, and the redshift distributions. The details of the choice of input parameters and the validation of the covariance matrix are described in Sanchez et al. 2024 in prep.

Next, we must decide on our modeling choices described in § 4.2.7 that are optimized for our Y6 data analysis. For cosmic shear cosmology, these have been determined, and the validations using synthetic data vectors computed from CosmoSIS have been partially completed. The following is our cosmic shear modeling strategy:

- Matter power spectrum (nonlinear evolution) – the baseline choice is the Hmcode2020 (HM20), where the robustness of the model is tested by contaminating the synthetic data vector made with HM20 with the mismodeling of the nonlinear structure evolution in Euclid Emulator v2.0 (EE2).

- Matter power spectrum (baryonic feedback) – the baseline choice is the feedback model with $\log T_{\mathrm{AGN}} = 7.7$, which is tested against two scenarios. Data vectors with dark matter-only and with extreme feedback scenario described by BAHAMAS 8.0 are simulated, and the model is tested to produce less than 0.5σ shift in the recovered 1D S_8 posterior and 2D (Ω_m, S_8) posterior.

- Intrinsic alignment (IA) – Cosmic shear poorly constrains IA model parameters on its own, and the constraining power is degraded substantially as the IA model complexity increases. Thus, one could take an empirical approach to select a fiducial model for intrinsic alignment following Campos et al., 2023. In this approach, one generates synthetic data vectors with several IA parameter sets and calibrates the relation between model insufficiency bias and the bias threshold. This provides a model choice optimized for a particular data set, balancing model bias and constraining power.

The above strategy was determined and tested where the scale cuts have already been applied. The scale cuts are determined by first generating data vectors with three feedback scenarios: with a baseline model, minimum baryon scenario (i.e., DM only), and maximum baryon feedback scenario. We then remove data points from the smallest scales and compare
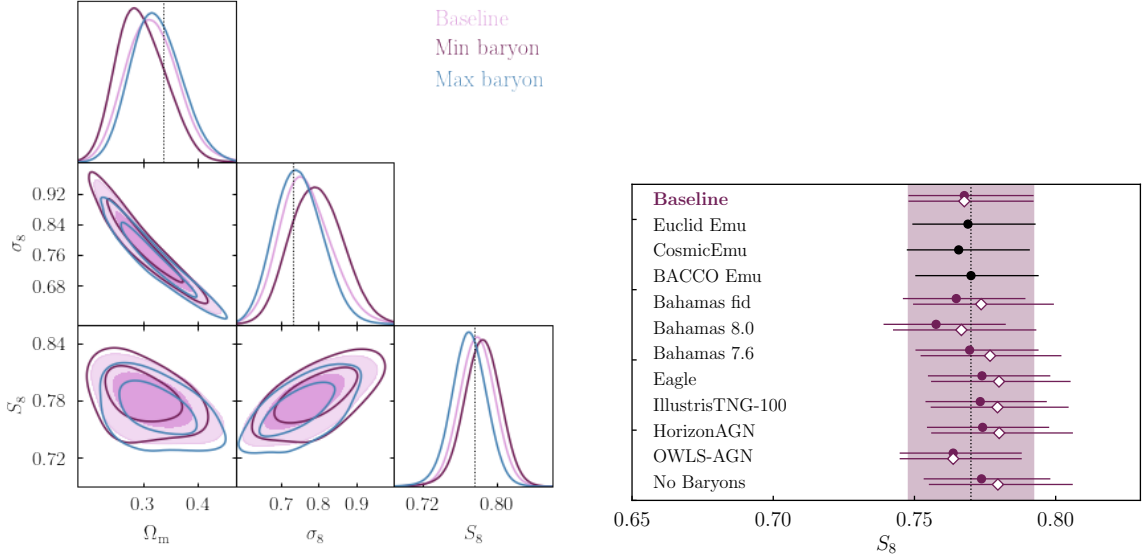
FIGURE 5.27: *Left*: 1D and 2D posterior contour of $(\Omega_m, \sigma_8, S_8)$ for the baseline data vector and the data vector contaminated with minimum and maximum baryon feedback scenarios. *Right*: the validation of the scale cuts against several baryon feedback models from emulators and hydrodynamical simulations. *Figure credit: Simon Samuroff*

these data vectors. We continue increasing the scales to remove until the mean of the 1D posterior of S_8 between the baseline model and min/max baryon model is within some threshold (0.5σ in Y6). This can be quantitatively defined as

$$(\xi_{\pm,\text{baryon}}^{ij} - \xi_{\pm,\text{baseline}}^{ij})^T C^{-1} (\xi_{\pm,\text{baryon}}^{ij} - \xi_{\pm,\text{baseline}}^{ij}) < \frac{\Delta\chi^2_{\text{threshold}}}{N}, \qquad (5.27)$$

where N is the number of data points. In Y6, our minimum baryon scenario is produced with HM20 DMO (dark matter only), and the maximum scenario is produced with BAHAMAS 8.0 + EE2. Our preliminary work suggests that the cuts with $\Delta\chi^2 = 3.25$ satisfy our requirement (left panel of Figure 5.27). Once the scale cuts are decided, one can test the cuts against the baseline data vector contaminated with various baryon feedback scenarios from various hydrodynamical simulations as shown in the right panel of Fig. 5.27.

5.6.3 Results

With the Y6 data and theory with updated modeling, the cosmological parameter inference with MCMC will be carried out soon. The forecasted constraining power of S_8 and
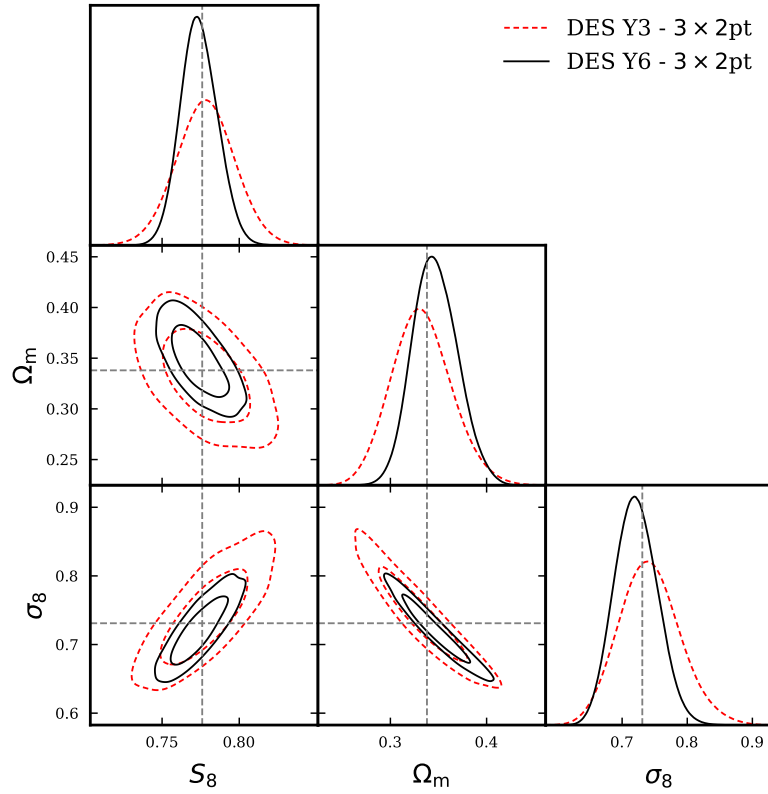
FIGURE 5.28: Forecast of $(S_8, \Omega_m, \sigma_8)$ from the mock Y6 3x2pt data vector analyzed with the preliminary Y6 modeling choices. This is compared with the published results of the DES Y3 3x2pt analysis (DES Collaboration et al., 2022). *Figure credit: David S. Cid*

Ω_m with cosmic shear along with galaxy-galaxy lensing and galaxy clustering (i.e., 3x2pt analysis) can be found in Fig. 5.28.

6

Towards Cosmological Analysis with Weak Lensing from the Nancy Grace Roman Space Telescope

While the Stage-III surveys like the Dark Energy Survey finish off their final analyses and the community moves on preparing for the next ground-based surveys like Rubin Observatory's Legacy Survey of Space and Time, the community has also been laying the groundwork for the successful experiments with the next space-based surveys such as Euclid and Nancy Grace Roman Space Telescope (Roman). In terms of weak lensing, Euclid and Roman will be the first space-based observations to cover more than 2000 deg^2. The last space-based weak lensing survey was carried out with Hubble Space Telescope (HST) in Massey, Rhodes, et al., 2007, which covered only 1 deg^2 in the COSMOS region. NASA's next flagship mission, Roman, is different from its predecessors in that it is designed to efficiently survey large regions of the sky and will produce high-resolution deep imaging over a wide area comparable to ground-based surveys covering multiple photometric bands. While the data quality of space-based imaging is generally much better than ground-based imaging, science requirements are much more stringent, and these space-based observations pose new challenges that need to be addressed differently from ground-based observations (Figure 6.1).

One of the main challenges for weak lensing in Roman is that individual images will be undersampled. Current weak lensing analysis tools (§ 4) rely on the fact that images are properly sampled. Another research project during my PhD focused on mitigating Roman's observational systematics by developing and utilizing image simulations (Troxel et al., 2021). This chapter covers the project that has applied METACALIBRATION on simulated Roman images and demonstrated that the shear calibration bias cannot be mitigated without properly treating the undersampled images (Yamamoto et al., 2023) and the project that has attempted to reconstruct well-sampled images with IMCOM (Rowe et al., 2011) and showed the feasibility of the methodology and succeeded in achieving well-characterized PSF which is essential in accomplishing precision cosmology with Roman (C. M. Hirata et al., 2024, Yamamoto et al., 2024).

6.1 Ground- vs Space-based Telescopes

We first reiterate the advantages, disadvantages, differences, and limitations of various aspects between ground-based and space-based telescopes and discuss the impact on weak lensing science. The following factors are frequently taken into account when designing a survey and deciding on a survey strategy to maximize the scientific return.

- Resolution – While the image resolution of the ground-based telescopes is limited by the atmosphere (seeing-limited), the resolution for the space-based telescopes is only diffraction-limited and can achieve the theoretical limit defined by the optics. Quantitatively, the expected size of the PSF for Roman will be about 3x smaller than that of the Rubin observatory. This indicates that there will be more blended objects for the ground telescopes than the space telescopes, and hence, we expect more observational systematics for weak lensing for ground-based surveys.

- Image sampling – According to the Nyquist-Shannon Sampling Theorem, in order to reconstruct an unbiased continuous band-limited function without a loss of information, the sufficient sample rate is twice the band-limiting frequency per second. In the context of image sampling, the criterion that the sample pixel spacing needs to
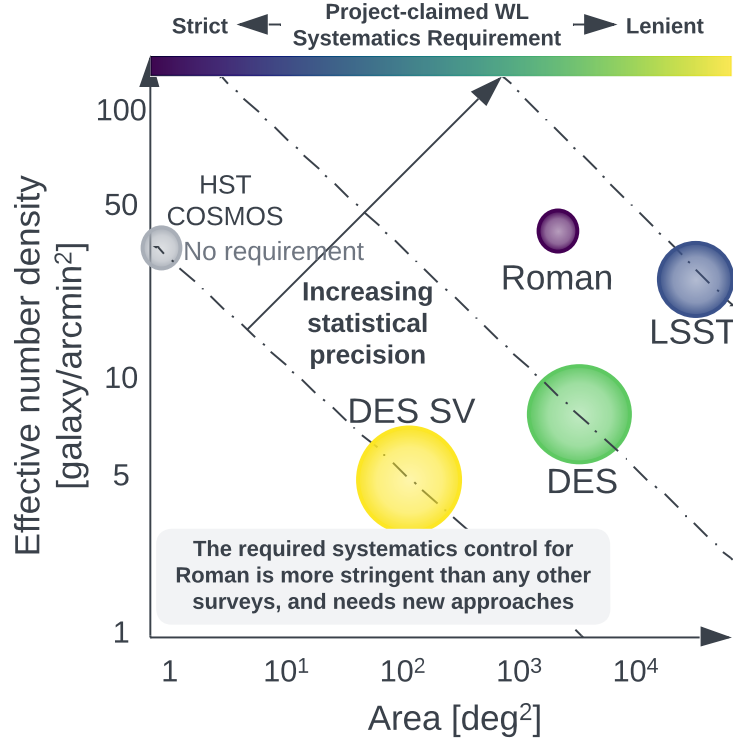
FIGURE 6.1: The expected coverage area and weak lensing effective number density of past, current, and upcoming surveys. The color of the circle represents how strict the science requirements are, and the size of the circle is the approximate PSF FWHM. A dotted line indicates the line of roughly the same number of objects.

satisfy is $p < \frac{1}{2u_{\max}}$ ($u_{\max}$ is the maximum spatial band-limiting frequency). Since the spatial band-limiting frequency in an astronomical image is defined as

$$u_{max} = \frac{1}{\lambda_{\min} N_f},$$ (6.1)

the sampling factor for a space telescope is defined as

$$Q = \frac{\lambda_{\min} N_f}{p},$$ (6.2)

where $\lambda_{\min}$ is the shortest wavelength of the incident light in each filter, N_f is the focal ratio of the telescope ($N_f = 7.8$ for Roman) and p is the pixel spacing of the sensor ($p = 10\,\mu m$ for Roman). An image with sampling factor $Q \geq 2$ is considered

Nyquist-sampled (or well-sampled) and an image with sampling factor $Q < 2$ is undersampled, indicating that Roman images with the reference bandpasses ($YJHF$) will all be undersampled. For the ground-based images, on the other hand, the maximum frequency will be limited by the seeing and they are typically well-sampled even at the best seeing condition. Because undersampled images are missing information compared to the full signal, science derived from undersampled images will be biased. In addition, even if one wants to reconstruct a Nyquist-sampled image or recover a true sky scene from undersampled images, the reconstructed images will be *aliased*, which is an effect where high-frequency signals appear to be low-frequency signals (e.g., Moiré pattern). Until recently, the impact of undersampling and aliasing on weak lensing has not exactly been characterized. But, these works (e.g., Kannawadi et al., 2021, Yamamoto et al., 2023) have demonstrated that aliasing can cause shear calibration bias. This will be discussed further in § 6.2.

- Survey area – The Field-of-View (FoV) (i.e., size of the camera) and survey duration limit the survey area. It is generally challenging for space-based observations to cover a wide area while maintaining depth because what can be sent into space is limited, and the radiation/cosmic rays can degrade the detectors much faster in space (about 5 years of operation).

- Depth – Although a larger mirror has the ability to capture deeper images, background light will degrade the depth greatly for ground-based telescopes, and the capability to launch a large mirror into space limits the depth in space. To achieve a desirable depth, ground-based telescopes avoid a long exposure time due to atmospheric disturbances and skyglow, revisit the same region of the sky multiple times, and reconstruct coadd images to perform object detection. For space-based observation, one is able to take a long exposure time and acquire a deeper single-exposure image. However, in order for the images to be science-ready, *dithering* is needed to reconstruct a Nyquist-sampled image. Dithering refers to the overlapping, random, or regular pattern the telescope is pointed at for each observation. In both cases, the dithering strategy is

Table 6.1: Key numbers of the lensing surveys for Stage-III & IV observatories. Note that Euclid is observing each region once, while others will have repeated observations overlapping each point in the sky in multiple filters.

Observatory	FoV	Primary Mirror	Pixel Size & Counts	Exposure Time
Blanco (DECam)	3 deg^2	4m	0.263", 520M	90sec
Rubin	9.6 deg^2	8.4m	0.2", 3.2G	15sec
Euclid (VIS)	0.56 deg^2	1.2m	0.101", 600M	$4 \times 566 + 2 \times 95$ sec
Roman (HLIS)	0.28 deg^2	2.4m	0.11", 288M	140sec

key to achieving science images that are deep and well-sampled, and this obviously impacts the consideration of the survey area as well.

- Noise – The images from ground-based telescopes will always contain more noise from various sources (e.g., background light) besides noise from instruments and detectors. While the same detectors experience the same detector effects on the ground and in space (optical and near-infrared detectors behave differently), the images from space telescopes contain more artifacts from cosmic rays.

- Wavelength coverage – As described in § 5.5, having multiple photometric bands is useful in determining the redshift distribution of galaxies. Given the limited survey time and FoV, however, one must choose a set of bandpasses to observe with. The use of near-infrared (NIR) filters in space is often useful and complementary to optical imaging surveys on the ground because the NIR imaging on the ground is disturbed by the glow in the atmosphere. As the wavelength of the filter decreases, the images become more undersampled, and the number of ditherings increases to reconstruct the well-sampled image. Therefore, one must choose a set of bandpasses carefully for space-based observations to be able to satisfy the scientific requirements and still look towards the joint effort between ground- and space-based surveys.

Table 6.1 presents key numbers of different kinds of observatories on the ground and in space.

6.2 Challenges Towards Cosmic Shear with Roman

The results presented in this chapter are from Yamamoto et al., 2023. The text represents my own work, and the contributions of other authors are presented as such:

- *Michael Troxel: Development of the image simulations in Troxel et al., 2021 used for some measurements.*

Given the differences between ground- and space-based images and the challenges to satisfy tighter systematics requirements, Roman's weak lensing analysis strategies[1] can differ from those of ground-based surveys such as LSST. One of the most important questions we face for the successful weak lensing experiment is whether we are able to utilize the existing shear estimation techniques and incur a small enough shear calibration bias on the recovered shear with undersampled images. In order to understand the systematic uncertainties we face, we must develop realistic image simulations, apply existing shape measurement methods to the simulated images, determine any potential residual systematic effects, and build a strategy for modifying the calibration methodology to mitigate them.

6.2.1 Weak gravitational lensing shear estimation with METACALIBRATION for the Roman High-Latitude Imaging Survey

While the major advantage of METACALIBRATION or METADETECTION is that they can be directly applied to real galaxy images without needing to rely on an ensemble calibration from image simulations, limitations for future surveys are not well-known. One possible limitation might lie in the effect of undersampled images in space-based surveys like Euclid and Roman, which will operate at their respective diffraction limits. The Point Spread Function (PSF) needs to be interpolated and estimated from well-sampled images to accurately deconvolve and measure shapes because the Roman PSF has a complex structure that cannot be captured in the original undersampled images. It is, therefore, necessary to build a robust strategy to reconstruct well-sampled images to estimate the PSF to allow unbiased shape measurement. Recently, Kannawadi et al., 2021 (hereafter K21) addressed

---

[1] The High-Latitude Imaging Survey (HLIS) is the name of the weak lensing survey for Roman Space Telescope.

this potential issue of the limitations of Metacalibration on undersampled images in Euclid image simulations. They found that for the Euclid mission, the shear estimate with Metacalibration is biased by about 1%. It is mentioned that their result could be extended to the Roman mission due to similarities in the instruments, and for Roman, they predicted the multiplicative bias was more than 1%. They show that these effects can be mitigated using additional weighting kernels in the measurement.

In this work, we explore how Metacalibration performs using coadd images at a higher resolution than the native resolution of the instrument, taking advantage of the dithering of images in the reference HLIS. We use an updated suite of image simulations specifically made for the Roman reference HLIS mission. Our work is based on the image simulation suite for the Roman Space Telescope developed by Troxel et al., 2021 (hereafter T21), where we render star and galaxy images using GalSim[2] (Rowe et al., 2015). We describe several important updates to the simulation capabilities and realism following T21. We also implement for the first time Metacalibration using the simulated imaging within the T21 simulation suite so that we can start to explore if the shear calibration goals of the HLIS for Roman ($m = 3.2 \times 10^{-4}$) (Doré et al., 2018) can be achieved with current Metacalibration implementations,[3] or will require substantial additional development.

6.2.1.1 Simulations

The base of our image simulations of the Roman Space Telescope is the Roman simulation suite[4] developed by T21, which renders realistic galaxy and star images on 18 Sensor-Chip Assemblies (SCAs) of a 2.5×2.5 $\deg^2$ patch of the sky following the observing strategy for the 5-year reference mission and Cycle 7 instrument specifications.[5] We begin by creating a truth catalog using the simulated galaxy distribution from the Buzzard simulation (DeRose et al., 2019), a photometric galaxy catalog sampled from the Cosmic Assembly

---

[2] Version 2.3.1 was used. https://github.com/GalSim-developers/GalSim

[3] We limit the study to Metacalibration for now, since we can extract unblended cutouts of objects in our simulations.

[4] https://github.com/matroxel/roman_imsim

[5] https://roman.gsfc.nasa.gov/science/Roman_Reference_Information.html

Near-infrared Deep Extragalactic Legacy Survey (CANDELS; Grogin et al., 2011; Hemmati et al., 2019; Koekemoer et al., 2011), and a Milky Way simulation (Galaxia; Sharma et al., 2011) for star positions and magnitudes. Then, the following properties are assigned to each galaxy:

- positions (RA, Dec),
- flux within each Roman filter (F184/H158/J129/Y106),
- intrinsic galaxy shapes and random orientations,
- flux ratios of de Vaucouleurs bulge, exponential disk, and star-forming knots, and
- artificial gravitational lensing shears.

Positions are drawn from the galaxy density in the Buzzard simulation, while other properties are drawn randomly from realistic distributions, with intrinsic object properties following a distribution based on CANDELS data. Within four identical realizations of the simulation, we use four sets of gravitational shears $(g_1, g_2)=\{(+0.02, 0.00), (-0.02, 0.00), (0.00, +0.02), (0.00, -0.02)\}$. This approach helps us to reduce shape and measurement noise when taking the difference in recovered shapes to compute the multiplicative bias (Pujol et al., 2019).

The next step of the process is to create postage stamps and SCA images using GAL-SIM. In this stage, the point-spread function (PSF) is convolved with the intrinsic galaxy light profile. Here, the Roman PSF is rendered using the `galsim.roman` module, which has implemented Roman-specific instrument properties such as the PSF and World Coordinate System (WCS) for a given telescope pointing, rotation angle, and SCA. The simulated detector effects were then added to the images in the following order: reciprocity failure, quantization, dark current, persistence, non-linearity, interpixel capacitance, read noise, and electron-to-ADU conversion (Mosby et al., 2020). These simulations have an achromatic PSF implementation due to it being computationally infeasible to do a large chromatic simulation when the work began. For this analysis, we use isolated object cutouts for each object so that effects related to blending can be ignored in this first study of METACALI-BRATION for *Roman*.
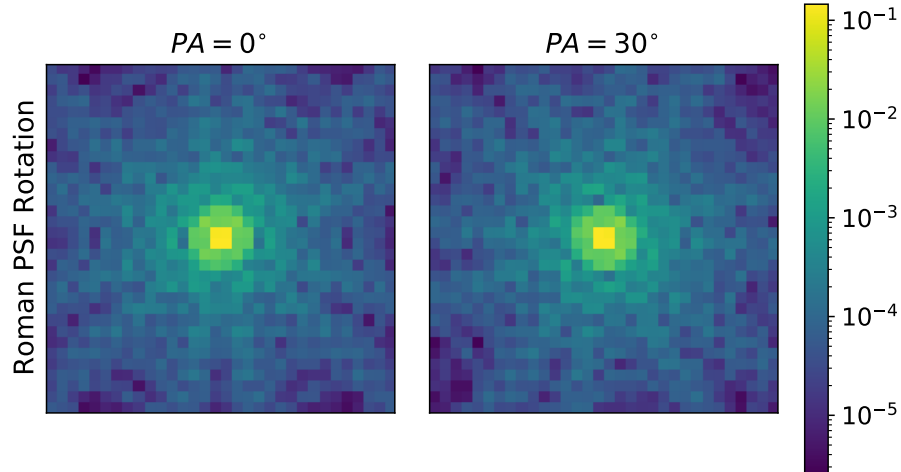
FIGURE 6.2: The rotation of the Roman PSF produced by the `galsim.roman` module. The position angle (PA) which determines the rotation of the focal plane is 0° (*left*) and 30° (*right*) clockwise. These are drawn for SCA=1 and H158 bandpass at a native pixel scale. The rotation of the PSF is particularly important when an object has multiple exposures. As more exposures are rotated relative to one another on the sky, the average impact of the PSF will be rounder. This will translate to a substantially less-elliptical coadd PSF.

After we generate the object stamps across all the SCAs and pointings, we create Multi-Epoch Data Structure (MEDS[6]; e.g., Jarvis et al., 2016) files in which each unique object dictionary contains information of all the exposures in which it appears in. These MEDS files are partitioned in a given Hierarchical Equal Area isoLatitude Pixelisation (HEALPIX) of n_{side} = 512. They contain all objects that are located in that region of the sky partitioned according HEALPIXEL[7] (Górski et al., 2005; Zonca et al., 2019).

Once the objects are sorted in MEDS files, we pass these multiple exposures with the corresponding PSFs to NGMIX[8] to fit the galaxy shapes with the Gaussian mixture fitting method (E. Sheldon, 2015). This shape measurement process produces shape catalogs from which the shear response is calculated with METACALIBRATION, and shear calibration bias can finally be computed.

---

[6] Version 0.9.8 was used. https://github.com/esheldon/meds

[7] https://healpix.jpl.nasa.gov/

[8] Version 1.3.6 was used. https://github.com/esheldon/ngmix
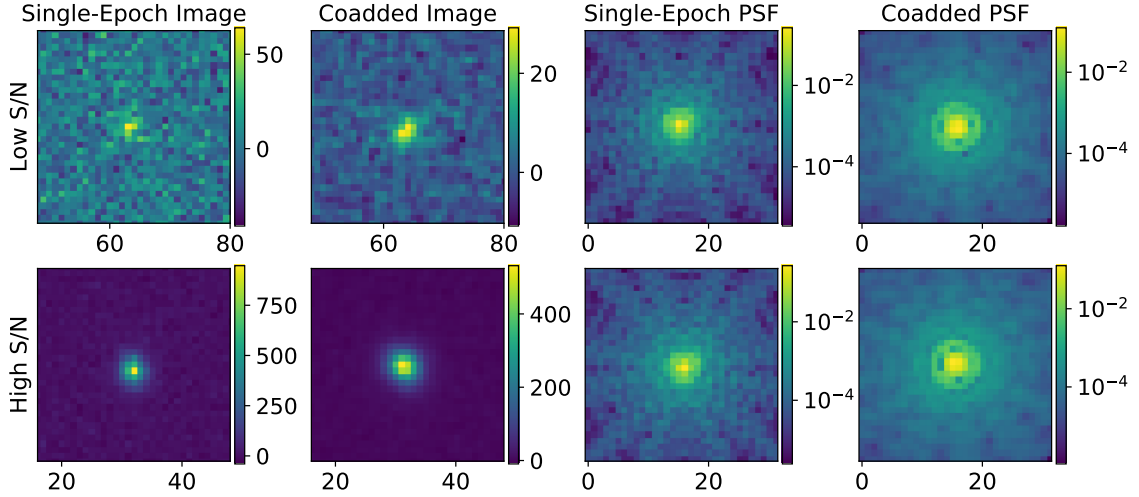
FIGURE 6.3: *Top Row*: the first observation of the single-epoch images and its coadded image, and the corresponding single-epoch and coadded oversampled PSF images for a galaxy with low signal-to-noise ratio (S/N=20 in a single-epoch image). *Bottom Row*: the same as above for a galaxy with high signal-to-noise ratio (S/N=390 in a single-epoch image). The H158 bandpass was used to represent images here. The single-epoch PSFs are almost identical, since there is no visually different feature for modeling them in different dithers and SCAs. There are two features to note here. One is how coaddition helps for low S/N objects, and the other feature is that the coadded PSFs look more isotropic than the single-epoch PSF due to different numbers of exposures.

6.2.1.1.1 Updates to simulation capabilities

In order to accomplish the science goals, and build and test weak lensing calibration pipelines for Roman, we have continued to update the realism of our image simulations. We have implemented and made updates to the following parts of the simulation framework to be able to better test shear calibration using METACALIBRATION.

- **Saturation Cuts**: We have implemented a pixel saturation limit of 100,000 electrons. This value is an expected pixel saturation level for Roman detectors, but in the next generation of the simulations we will use a more accurate pixel saturation limit measured directly from the flight detectors.

- **Rotation of the Roman PSF on the sky**: In the study by T21, the rotations of the Roman PSF with respect to the telescope rotation were not properly applied by the `galsim.roman` module. Since a non-rotating PSF produces an artificial preferred di-

rection, which can translate to galaxy shapes through errors in the process of deconvolution, properly accounting for the averaging of the PSF orientation across exposures due to the survey dithering strategy is essential for a realistic shear calibration estimate. There has been an update in the `galsim.roman` module to correctly rotate the PSF given the WCS of the SCA in a given telescope pointing. Figure 6.2 shows an example of how the PSF for one SCA changes with the rotation angle of the telescope.

- **Single-band and multi-band Coadds**: We have used the postage stamp coadds (PSC) algorithm[9] to create coadditions of single-epoch postage stamps of individual objects. Coadds are usually performed to enhance the signal-to-noise ratio (S/N) of an image and mitigate the impact of measurement noise, while allowing for better sampling of the image if the overlapping images are dithered. However, it is challenging to create a robust, continuous coadd PSF model over an entire image. This is mitigated if we instead construct small, local coadds (at the size of an object postage stamp cutout in this work), which is a method also utilized in METADETECTION. If we take advantage of fitting an object in the coadd instead of fitting multiple images of each object in each filter, we can save a factor of approximately six in computing time, since there are on average six exposures at any point on the sky in the reference survey. Additionally, coadding is one way to reduce the effect of the undersampling of the images since the coadd can be better sampled due to dithering. For these reasons, we explore utilizing this coadding scheme for the Roman galaxies. In future work, a coaddition algorithm could be used such as IMCOM[10] (ROWE ET AL., 2011) that explicitly addresses the undersampling in a way that PSC does not. The examples of the low and high S/N galaxy and PSF images for single-epoch and coadd are shown in Figure 6.3. The detailed overview of the coadd process in PSC is described in in § 6.2.1.2.1.

---

[9] https://github.com/esheldon/psc

[10] https://github.com/barnabytprowe/imcom

- **Metacalibration in Ngmix**: We implemented the METACALIBRATION[II] bootstrapper method, which is a wrapper class to run measurements in the NGMIX package and was used to produce the weak lensing shape catalog in the DES Y3 analysis (Gatti, Sheldon, et al. 2021). The METACALIBRATION process can be performed on single-epoch or coadd images in each bandpass. With this calibration method, we hope to significantly reduce some of the shear calibration bias T21 measured in order to make comparisons of effects contributing to the bias more realistic and meaningful as we explore future Roman pipeline development. The detailed overview of the METACALIBRATION method can be found in § 5.3.3.1.

6.2.1.1.2 Simulated weak lensing sample

The way galaxies are simulated in this paper resembles the one in T21. We briefly overview how the galaxy properties are assigned from the CANDELS catalog and the galaxy distributions are provided using the Buzzard simulation.

Among several galaxy properties, the morphological distributions are uniformly random (e.g., bulge/disk ratio), but the random intrinsic ellipticity distribution is appropriate to that expected from the data (e.g., the right ellipticity variance). The photometric, size, and redshift properties are all drawn consistently from the Roman weak lensing sample predictions based on the CANDELS measurements (Hemmati et al., 2019). Since this CANDELS-based catalog was designed to be the representative of the ultimate Roman weak lensing source sample, both the association of magnitude, size, and redshift for each individual object and the total distribution overall for our galaxies is consistent with what is expected for the Roman measurements. It is also worth mentioning that our input catalog is actually the distribution of a noisy selection that has cuts in size and signal-to-noise (S/N>18) representative of the nominal selection of the Roman weak lensing sample (Doré et al., 2018).

As mentioned in the beginning of this section, we use the Buzzard simulation to distribute the galaxies. In our simulations, only the projected distribution is selected randomly

---

[II] Version 1.3.6 was used. https://github.com/esheldon/ngmix/wiki/Metacalibration

Table 6.2: The runtime for a single CPU and disk size of the shape catalogs for different simulation runs. The runtime for multi-band measurements is slower due to having to copy, uncompress, and read from the three MEDS files (each 1GB compressed) for each bandpass. Runtime for coadd measurements also includes the postage-stamp coadding, which dominates the runtime over the METACALIBRATION process. For comparison, the image generation of one SCA takes 1.8 CPU hours.

Measurement type	CPU runtime (hours)	Catalog disk size
single-band multi-epoch	3.7	3.9 GB
single-band coadd	2.9	3.8 GB
multi-band multi-epoch	4.8	3.8 GB
multi-band coadd	5.0	3.8 GB

to enable a realistic projected clustering signal. The Buzzard has an upper redshift limit of 2.5. While we simulate the full Buzzard images, we isolate object stamps and only the isolated object stamps are added to the full image which are eventually used in the shape measurement for this work. This pre-selection of the galaxies ends up with the distribution that is close to the nominal weak lensing sample that we did not need to do a selection post-simulation.

6.2.1.1.3 Simulation runtime, data products, and data access

The simulations here match those produced in T21, but with different true shear values and the updates mentioned in §6.2.1.1.1, and so information about processing and data volume prior to the processing additions described in this paper match that provided in App. D of T21. The runtime of the shape measurement per MEDS region in the simulations and data volume on disk of the full shape catalogs (5 METACALIBRATION catalogs for one of four shear sets) is summarized in Table. 6.2 for each of the different simulation runs. The simulations are run on the Duke Compute Cluster[12], with solid-state disks for the simulation I/O. The time it takes to process one MEDS file is shown in the table. The simulation is composed of a total of 480 MEDS files, for a total run time of about 2381 CPU hours for the multi-band coadd measurement.

[12] https://oit-rc.pages.oit.duke.edu/rcsupportdocs/dcc/

6.2.1.1.4 Validations with simple simulations

In addition to the main, realistic simulation of the Roman reference HLIS survey, we also produce several sets of much faster, simple simulations to verify that there are no obvious fundamental sources of systematic biases using the METACALIBRATION method on undersampled space-based images. These simple simulations thus play a role in ruling out the sources of systematic biases that may a priori potentially be a problem in the use of METACALIBRATION with space-based images.

The fixed parameters for the simulations are listed in Table 6.3. We fix the original pixel scale of the Roman, bandpass and input galaxy size. With these parameters, we simulated images with varying galaxy model profile, PSF model profile, artificial shear, and background noise level, without any complications in the images and pipelines such as detector effects and coaddition. We first chose simple light profiles for galaxies and PSF to be Gaussian (with PSF half-light radius of 0.089 arcsec, which matches the expected average PSF size for H158 of 0.178 arcsec from T21), and verified with *Basic-0.02* simulation that our input gravitational shear ($|g|$=0.02) is unbiased in the METACALIBRATION framework and achieves the required multiplicative bias for Roman. We also tested the same setup with different input shears (*Basic-0.05* and *Basic-0.1*) to test where the weak shear approximation breaks down. The values of inferred bias are shown in Table 6.4.

Next, we tested the shape measurement pipeline by doubling the background noise with *Doublesky-0.02*. This test should validate that the METACALIBRATION process can tolerate the induced correlation of Poisson noise in the object profiles during the METACALIBRATION shearing process, since it is not currently symmetrized in the process as the background noise field is (E. S. Sheldon and Huff, 2017). We find that this result is also consistent with zero, so we can confirm that the treatment of correlated Poisson noise does not trigger any bias at the level we can probe with the current simulations.

In the final row in Table 6.4 (*RomanPSF-0.02*), we finally validate that the use of the complex Roman PSF instead of a Gaussian PSF does not bias the shape recovery even

Table 6.3: List of the parameter choices for the simple simulations. For all the simple simulation runs, we used a Gaussian galaxy profile and the magnitude for each object is drawn randomly from the CANDELS catalog. For the stamp size, the multiplying factor was chosen so that 99.5% of the flux is in the stamp.

Parameter	Value
Pixel scale	0.11 arcsec/pixel
Bandpass	H158
Galaxy half-light radius	1.0 arcsec
Stamp size	Multiples of 32 pixels each side

Table 6.4: This table compares the shear calibration bias, both multiplicative and additive bias for different simple simulation runs where the galaxy profile is Gaussian. In each simulation except the first and last row, 5 million objects were simulated. We simulated 15 million objects for the first and last row to obtain sufficiently small uncertainties. Background noise is nominally 5714.36 e-/arcsec^2, but doubled for the "Doublesky-0.02" configuration. Note that the Roman PSF used in "RomanPSF-0.02" is not rotated according to the paintings.

simulation variants	PSF profile	shear	$m_1 \times 10^2$	$m_2 \times 10^2$	$c_1 \times 10^4$	$c_2 \times 10^4$
Basic-0.02	Gaussian	0.02	0.01±0.10	-0.02±0.10	-0.02±0.14	1.06±0.14
Basic-0.05	Gaussian	0.05	0.23±0.07	0.22±0.07	0.05±0.33	1.08±0.33
Basic-0.1	Gaussian	0.1	0.99±0.03	0.99±0.03	0.13±0.33	0.88±0.33
Doublesky-0.02	Gaussian	0.02	-0.12±0.18	0.01±0.18	0.06±0.36	1.04±0.36
RomanPSF-0.02	Roman	0.02	0.13±0.10	0.18±0.10	-0.02±0.19	5.33±0.19

though it is undersampled. We note that these tests were performed before updating the PSF rotation, and so they do not benefit from rotationally-induced isotropy of the effective PSF. Since none of these obvious potential issues using simple Gaussian galaxy profiles will cause bias in m at the level we can probe in the more complex simulation, we can more easily interpret results of the more complicated simulation and analysis pipelines described in the following sections. However, there remains a potentially concerning non-zero additive bias in c_2, particularly when using the Roman PSF model that will need to be studied further.

6.2.1.2 Coadd and shear calibration pipelines

Our goal is to test whether the recovered shear with METACALIBRATION is non-biased for Roman and to understand the factors that might contribute to any non-negligible bias. In order to do so, we need to build measurement pipelines within the current simulation framework that produce a final calibrated shear measurement. In this section, we present

in detail how coadd images are produced with PSC from the undersampled single-epoch images and how METACALIBRATION is implemented to calibrate the measured shear.

6.2.1.2.1 Postage stamp coadds

Coaddition is the process of summing information from multiple overlapping images. If the single-epoch images are dithered, a Nyquist-sampled image can be constructed out of multiple undersampled exposures of an object. While this process can also be beneficial in increasing the S/N value of an object and reducing the impact of pixel noise, several challenges need to be addressed for images taken with telescopes that can rotate. When rotation is introduced, this coadding process becomes more complex to interpolate the image to stack a pixel grid. While coaddition can introduce new challenges and potential biases due to the complexity of coadding the original PSF and its interpolation scheme, potential bias due to the undersampling of the original images can be mitigated by appropriately coadding dithered images.

Among imaging surveys, coadding a small region of the sky is common, for example SWARP (Bertin, 2010) or DRIZZLE (Fruchter and Hook, 2002). However, we decided to coadd the postage-stamp cutouts to simplify the treatment of the coadd PSF. It is also beneficial to use this method because we need coadds which can be directly injected into the shape measurement pipeline in memory rather than written as images to disk due to the number of cutouts we have to process. We specifically use the simple interpolation-based coadding method using GALSIM, PSC (postage stamp coadds), as our coadding process. While this method does not explicitly account for undersampling of the images and will produce aliasing at some level, we find that this is not an important factor at our current precision of tests in this work. Future work will explore more principled methods like IMCOM (Rowe et al., 2011) that explicitly account for the undersampling of space-based imaging like our Roman image simulations.

We reconstruct a better-sampled coadd image from multiple exposures in MEDS files. For each exposure of the object we render the Roman PSF with a stamp size of 32 pixels at the galaxy centroid. This choice of stamp size ends up losing about 2-4% of the total flux

of the PSF. However, we have no evidence that this impacts the shape measurement. We modified the original PSC code to improve performance for this Roman study, and these modifications are explained below with the general coadding process in PSC.

The algorithm:

1. Finds the WCS of the first exposure of the object.

2. Translates the original WCS to a flat WCS (locally diagonal Jacobian representation), because it produces more stable results with NGMIX.

3. Creates the coadd stamp with $0.8 \times$ original pixel scale. We scale the original pixel scale of the final coadd stamp to increase the image sampling. This final pixel scale was chosen to prevent the presence of visual artifacts in the structure of the coadd PSF image.

4. Creates an interpolated image with GALSIM using a `lanczos3` interpolant and sums them.

5. Creates a coadded noise image from the weight of the original images.

Figure 6.3 shows an example of the simulated single-epoch and coadded images and PSFs for objects with low and high S/N. Note that the shape and struts pattern in the original PSF can be isotropized by coadding the rotationally dithered PSFs. Figure 6.4 shows the coadd products in different bandpasses for a relatively high S/N object.

6.2.1.2.2 Shape calibration & measurement with NGMIX

Once we construct the individual galaxy stamp coadds from the MEDS files, we recover the calibrated shear signal using the METACALIBRATION process (E. Huff and Mandelbaum, 2017; E. S. Sheldon and Huff, 2017). In this work, the default interpolation kernel (`lanczos15`) was used to create the Metacalibrated images, and the numerical tolerances used are also the default GALSIM settings. The bootstrapper method used in NGMIX wraps the METACALIBRATION and the shape fit processes. The priors used for the fit are listed in Table 6.5.

| Coadded J129 | Coadded H158 | Coadded F184 | Multiband Coadd | RGB Coadd | Multiband Coadd PSF |
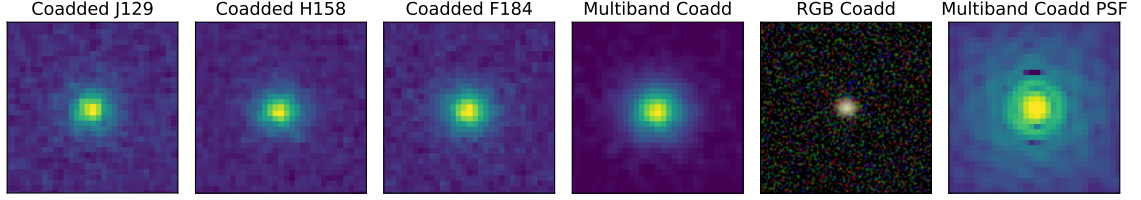
FIGURE 6.4: The left 3 panels show an example of the coadded galaxy images for each filter. The S/N for each filter is S/N=90, 68, 108, respectively. The 4th and 5th panels show the multi-band coadd images of the same object; each with linear scale and RGB scale. The S/N of the coadd image is S/N=110. Finally, the right-most panel shows the coadded multi-band PSF in a log scale. Some pixels with negative values were produced in the process of making the multi-band coadd PSF due to limitations in the fast interpolant functions used, but this has no impact on the results.

Table 6.5: List of prior values and distributions used for the Gaussian mixture fit.

Parameter		Prior
Pixel centroid offset	Flat	$0 < p_{x,y} < 0.11$
Shear	Gaussian	$\langle g \rangle = 0.0, \sigma_{|g|} = 0.3$
Galaxy size	Flat	$10^{-5} < \mathrm{T\ (arcsec^2)} < 10^4$
Flux fraction of the bulge	Gaussian	$\langle f \rangle = 0.5, \sigma_f = 0.1$
Total flux	Flat	$0 < \mathrm{F\ (ADU)} < 10^6$

The deconvolution process in METACALIBRATION was performed using the coadded PSF that is still undersampled. Since having a matching pixel scale in the galaxy and PSF image is a requirement for the version of the NGMIX pipeline we implemented, we were not able to oversample the simulated Roman PSF to utilize a more accurate PSF model. Future versions of these measurements should include the ability to provide a better-sampled PSF image for the deconvolution in the measurement. We also note that for the reconvolution process in METACALIBRATION we have attempted the measurement with the `fitgauss`[13] and `gauss` PSF model to reconvolve the sheared galaxy images, and the measurement with `fitgauss` model was numerically unstable resulting in the inconsistency between m_1 and m_2. We, therefore, use the `gauss` model for the rest of the simulations.

The covariances are computed using the bootstrap estimate of standard error. From the observed ellipticity catalogs, we randomly choose n samples with replacement, where n is the length of the data set, and compute the distributions of multiplicative (f_i^m) and additive

---

[13] An isotropic Gaussian PSF model fitted to the original PSF.

(f_i^c) bias for $i = 1, 2, 3, ..., N$ (N is the number of times the resampling is carried out) in the same way as above. The distributions are then used to compute the error estimate,

$$\sigma_{N,f} = \sqrt{\frac{1}{N-1} \sum_{i=1}^{N} (f_i - \bar{f}_i)^2},$$ (6.3)

where we use sample N=200.

6.2.1.3 Results

In this section, we present the properties of the simulated data products and the shape measurement results from various simulation variants. We divide our shape measurement into two categories; single-band and multi-band. For single-band measurements, in each filter, we measured the shapes from the original single exposures by jointly fitting them: we call this single-band multi-epoch measurement. We also measured shapes with the single-band coadd in each filter: we call this single-band coadd measurement. For the mutli-band multi-epoch measurement, we matched the objects between each filter and measured the shapes with the joint-fit of single exposures across all the filters. The multi-band coadd measurement was jointly fit across the three coadds from each filter to recover the shapes.

6.2.1.3.1 Statistics of the shape catalog

Galaxies that are simulated are pre-selected to meet the Roman Weak Lensing selection used for the mission requirements (Doré et al., 2018; Troxel et al., 2021). In total, the galaxy photometry catalog contains 907,170 galaxies and from this catalog we simulated galaxies on 18 SCAs across 198 pointings for F184, 227 pointings for H158, and 238 pointings for J129 bandpass. We did not make any selection cuts on the simulated catalogs based on measured properties, since all input objects are selected to pass requirements for weak lensing selection. In our samples, no de-blending was necessary since the shape measurement was performed on object stamps without neighboring objects. Blending issues related to the object detection is mentioned later in §6.2.1.4.

In the end, we were able to measure the shapes of about 95% of all the objects in the

photometry catalog in each filter. This 5% loss is mostly due to the fact that some objects are not saved in stamps due to being too large (i.e., require a stamp size of greater than 256 pixels). This selection is on the true size only, and so is not correlated with the shear. Some additional object shapes were not measured due to the Gaussian mixture fit in Ngmix failing to converge. This also includes a very small number of objects that are rejected due to all cutouts being too near the SCA edges. The total number of the recovered objects for single-band measurements was, 861,407 for F184, 863,146 for H158, and 859,193 for J129. For the multi-band (H158+J129+F184) coadd measurements, we used objects that are measured successfully in all of the filters and the total number of the recovered objects is 851,821. Figure 6.5 shows the true magnitude and size, the measured signal-to-noise and size of galaxies in the Metacalibration shape catalogs. There is a significant boost in signal-to-noise in the multi-band catalog vs the single-band catalogs. While the measured size (T) does not agree well with the input size derived from the half-light radius, this is a known issue due to fitting a Gaussian model to a galaxy with size defined as part of a much more complex profile.

6.2.1.3.2 Shear calibration bias

We estimate the levels of shear calibration bias associated with calibrating shapes with Metacalibration in Roman images as described in §6.2.1.2.2. The multiplicative and additive bias values listed in the text are the average of m_1 and m_2, and c_1 and c_2. The comprehensive results can be found in Table 6.6 and Fig. 6.6 shows the single-band single exposures and coadd results compared. These multiple simulation variants were run to achieve three milestones. One is to characterize how much the shear bias exists if we were to use the original, undersampled images, by recovering shears from the single exposures in each bandpass. Second is to verify if coadding can mitigate the effect of undersampling. Lastly, as the final assessment we investigate how combining the three bandpasses can result in better constraining the recovered shear.

For the single-band measurements, we can use the sampling factor defined in Equation 6.2 per bandpass to show the relationship between the shear bias and image sampling.
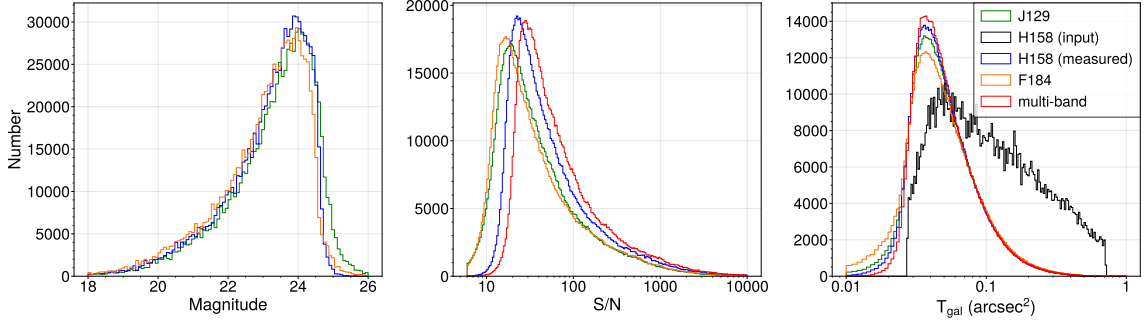
FIGURE 6.5: The histograms of input and measured galaxy properties in NGMIX for single-band coadd and multi-band coadd measurements. *Left*: the input magnitudes of galaxies for all three filters we have used to measure shapes. The mean magnitude for J129, H158, F184 are respectively 23.3, 23.1, 23.0. *Middle*: the signal-to-noise ratio of the single-band and multi-band coadds. The median S/N for JHF and multi-band are respectively 29, 39, 27, and 50. *Right*: the input galaxy size for H158 approximated using a Gaussian profile with the half-light radius in the input H158 catalog, and the measured galaxy size T for the single-band and the multi-band coadd in units of arcsec^2. The mean size for input and measured galaxies are 0.15 and 0.09 arcsec^2 for H158. The measured size is the size of the best fit Gaussian (maximum likelihood in this case) and it is not expected to match with the true size based on the half-light radius of the nominal (non-Gaussian) profiles.

The sampling factor is an indication of how undersampled the image is in each bandpass. The sampling factor for each single-band measurement can be found in Table 6.6. This relationship between sampling factor and shear bias was previously explored in K21 using Euclid simulation with different shape measurement algorithms, where they found that the estimated multiplicative bias has a relatively large dependence on the sampling factor. Their result can be extrapolated to our single-band multi-epoch results. The multiplicative bias of single-band multi-epoch measurements is consistent with zero within 2σ in each filter, with mean uncertainty $\sigma_m = 0.72\%$, except for $m_2 = (-1.61 \pm 0.66)\%$ in H158, which is slightly larger. This level of bias is consistent with the finding from K21.

When the coadded images for each filter are used, the recovered multiplicative shear bias is about half the multi-epoch cases, and is consistent with zero at the ~1σ level. The additive bias remains at a similar level within uncertainties.

Finally, we discuss the results with multi-band measurements. We performed multi-band measurements with the three filters used in the previous measurements. One multi-band

174

Table 6.6: A comparison of the shear calibration bias, both multiplicative and additive bias, for different simulation runs.

Simulation variants	Q	$m_1 \times 10^2$	$m_2 \times 10^2$	$c_1 \times 10^4$	$c_2 \times 10^4$
single-band multi-epoch (J129)	0.88	1.17±0.68	0.44±0.75	4.46±1.32	0.64±1.31
single-band multi-epoch (H158)	1.08	-1.07±0.62	-1.61±0.66	2.83±1.35	2.33±1.22
single-band multi-epoch (F184)	1.31	-0.86±0.72	-0.69±0.83	2.62±1.56	0.23±1.53
single-band coadd (J129)	1.10	-0.59±0.68	-0.94±0.64	4.91±1.46	1.78±1.17
single-band coadd (H158)	1.35	-0.69±0.63	-0.83±0.61	2.16±1.31	0.77±1.19
single-band coadd (F184)	1.64	0.37±0.83	0.10±0.75	2.22±1.46	0.08±1.58
multi-band multi-epoch	N/A	-0.68±0.59	-0.85±0.58	3.09±1.21	2.04±1.11
multi-band coadd	N/A	-1.02±0.62	-1.24±0.57	2.37±1.26	2.38±1.22

measurement used all of the single epoch images from all the filters and jointly fit the shape of the galaxy. The multiplicative and additive bias is, respectively, $m = (-0.76 \pm 0.43)\%$ and $c = (2.56 \pm 0.79) \times 10^{-4}$. This result generally agrees with the single-band multi-epoch measurements, and is consistent with zero bias at the $\sim 2\sigma$ level. The other measurement is performed as a joint-fit across the coadd images for each filter. The multiplicative and additive bias is, respectively, $m = (-1.13 \pm 0.60)\%$ and $c = (2.38 \pm 1.24) \times 10^{-4}$. These results are again consistent with zero at the 2σ level, but have a large uncertainty relative to the Roman mission requirements. Scaling simply by volume, assuming a Gaussian error distribution, we would need a significantly larger simulation volume of about 2000 deg^2 in this complex simulation mode to draw firm conclusion about the performance of multiband measurements. This is comparable to the area of the reference Roman survey.

To further explore the shape catalogs, we performed a set of basic null tests and show representative results for e_1 for the H158 multi-epoch and coadd catalogs, and multi-band coadd catalog. The null tests should show that the mean shear residual ($\langle \Delta e_1 \rangle$) is zero (flat as a function of galaxy properties) in the absence of any systematic biases. Figure 6.7 shows the relationship between the mean shear and several input and measured properties of galaxies for all the measurement cases. We find no significant trends in mean shear vs. galaxy properties or vs PSF properties, which are not included in the figure.
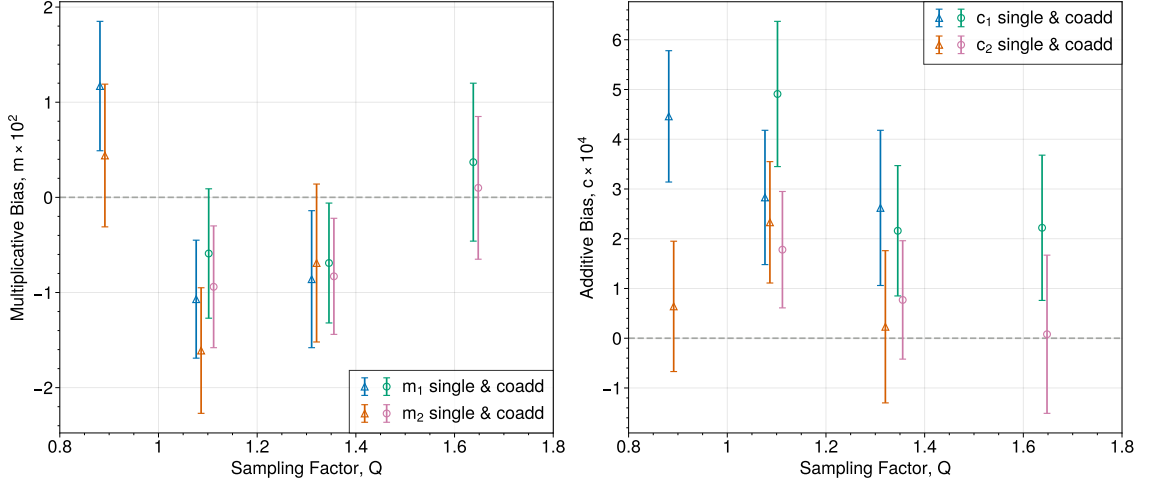
FIGURE 6.6: The multiplicative ($m \times 10^2$) (*left*) and additive ($c \times 10^4$) (*right*) bias of the single-band multi-epoch and coadd measurements. From the left to the right data points, they represent the data for each of the J129 multi-epoch, H158 multi-epoch, J129 coadd, F184 multi-epoch, H158 coadd and F184 coadd measurements. The data points for the m_2 and c_2 measurements are shifted by +0.01 for visual clarity. The non-calibrated results from the first-generation of the simulations by T21 were $m_1 = (-7.56 \pm 0.19)\%$, $m_2 = (-9.49 \pm 0.19)\%$ and $c_1 = (1.20 \pm 0.17) \times 10^{-3}$, $c_2 = (-1.57 \pm 0.16) \times 10^{-3}$. We can conclude that our calibration bias is an order of magnitude smaller than the previous versions of the simulations, and comparable or smaller than the bias-level seen in the Stage-III surveys.
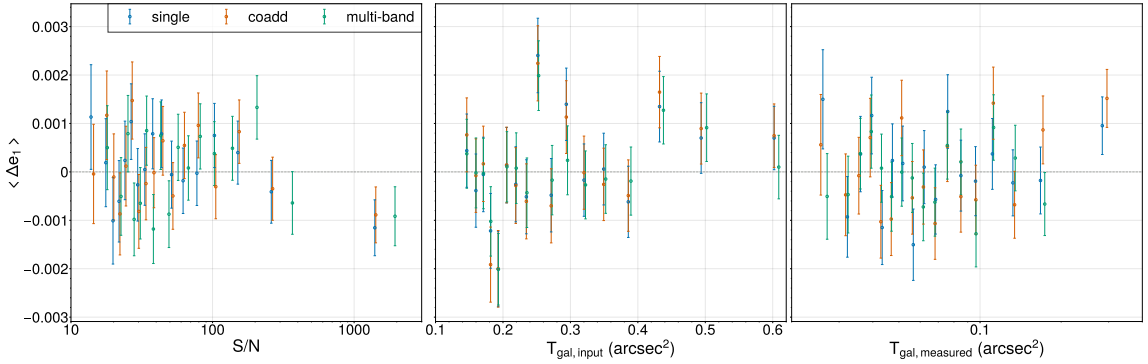
FIGURE 6.7: The mean shear residual ($\langle \Delta e_1 \rangle$; $\langle e_{1,\text{measured}} \rangle - \langle e_{1,\text{expected}} \rangle$) as a function of various properties of galaxies for H158 single-band multi-epochs, coadds, and multi-band measurements. We are only showing the e_1 residual because e_2 showed similar behaviors in each test. We find results that are consistent with a null signal for signal-to-noise (*left*), true galaxy size (*middle*), and measured galaxy size (*right*). The mean shear is computed with the shear response and selection response in each bin to account for the selection bias. To make the figure more visible, blue points are shifted by -1.0 in S/N, -0.005 in $T_{\text{gal,input}}$, -0.001 in $T_{\text{gal,measured}}$, and yellow points are shifted by +1.0 in S/N, +0.005 in $T_{\text{gal,input}}$, +0.001 in $T_{\text{gal,measured}}$.

6.2.1.4 Future simulation needs and plan

We have investigated how Metacalibration handles the complex Roman PSF and undersampled images without accounting for the effect of blending. However, it has been found that galaxy blending at different redshifts could introduce a significant shear-dependent detection bias when calibrated with Metacalibration (e.g., MacCrann et al., 2021; E. S. Sheldon et al., 2020). In future studies, we will investigate the impact of blending in Roman image simulations and implement an extended pipeline to correct shear-dependent blending/detection biases (e.g., Metadetection) to explore more realistic shear calibration for the real survey.

Our team continues to increase the realism of the image simulations for future weak lensing calibration analyses. In the next generation of these simulations, we expect to include the following updates or upgrade these parts of the simulation.

- **Simulation Volume**: Expand the simulated area by a factor of four to 20 $\deg^2$, in order to obtain smaller error bars on the resulting shear calibration biases. Increasing the simulation volume has additional benefits beyond a more precise bias estimate, such as the ability to calibrate spatial dependence of shear and to measure two-point correlation function and propagate the biases into a cosmological analysis.

- **Pixel Masks**: Future versions of the simulations will take into account complex pixel masking of detector non-idealities, such as hot or dead pixels. This masking will be propagated through the analysis to provide realistic masking challenges.

- **Near-Infrared Detector Effects**: Incorporate more realistic detector effects as measured in tests on the flight detectors (Mosby et al., 2020) and produce two versions of the simulation with and without them to determine the impact on the final cosmology result. The detector effects that are not simulated in this paper but will be incorporated are relative quantum efficiency, quantum yield, charge diffusion, brighter-fatter effect, burn-in, count rate non-linearity, classical non-linearity, vertical trailing pixel

177

effect, bad pixels, gain, and the bias frame.

- **Image Coaddition**: As one of the scene coadd algorithms, we will implement a new coaddition strategy that coadds the whole scene instead of individual stamp cutouts using `AstroDrizzle`[14]: A Python implementation of MultiDrizzle which was used for *Hubble* Space Telescope (Brammer et al., 2003). With `AstroDrizzle`, we are able to further mitigate the effect of undersampling in the Roman images with smaller coadd pixel scales. We expect this to further reduce the measured shear bias based on its trend with sampling factor. As a more mathematically-principled method that directly accounts for the undersampling of the images, we can also evaluate the use of the IMCOM) algorithm in the future.

- **Source Detection**: Implement a source detection and deblending methodology to allow more realistic tests of shear recovery.

- **Selection Cuts**: Simulate objects to below the detection threshold of the survey and incorporate standard quality assurance cuts (e.g., S/N) on the shape catalog.

6.2.1.5 Conclusions

In this paper, we explored the performance of the METACALIBRATION shape measurement calibration algorithm and presented the first shear calibration result without the effect of blending on a realistic simulated version of the reference Roman HLIS. Accurately characterizing how much shear estimates are biased using realistic simulated survey images is a requirement to successfully complete the weak lensing program of the Roman HLIS. This early work allows us to develop such simulation resources and to benchmark current weak lensing methods to explore where effort is still needed in development for the Roman mission.

In a larger suite of simple simulations, where the galaxy and PSF profiles are Gaussian, we find that the shear calibration bias using METACALIBRATION is consistent with zero

---

[14] https://github.com/spacetelescope/drizzlepac

at the 0.1% level, even though the images are undersampled. This finding persists even when using an accurate, complex Roman PSF model. When exploring the performance of METACALIBRATION in the current simulation framework where realistic complexities are incorporated, the runtime cost is significantly increased, and we can only constrain the shear calibration bias at the 0.6% level. In these simulations we include coadding the single-epoch cutout images and fitting the shapes from multiple bandpasses, and we find that shear estimates with METACALIBRATION are unbiased at the $\sim 2\sigma$ level, which is similar to current-survey constraints. At the original image sampling level, the trend in bias vs sampling factor Q is similar to what was previously found for METACALIBRATION bias on undersampled images in the study by K21 using image simulations built for Euclid, but at lower levels of bias. By coadding the cutout images and increasing the image sampling factor, we find that the residual bias is reduced by about a factor of two, but this is similar to the uncertainty. However, this is a promising result for using coadd-level shape measurement for Roman, and we plan to further investigate the use of METACALIBRATION with image coadds that can reconstruct Nyquist-sampled images in all bandpasses in future work.

These results are currently limited by the available simulation volume in the realistic simulated survey. To further constrain the shear calibration bias and validate that the Roman mission will be able to achieve the weak lensing calibration required for the survey, we have outlined in §6.2.1.4 a variety of simulation improvements being planned in future versions of the Roman simulations that are currently being developed, including an exploration of the impact of blending and object detection on the calibration. We will also need to simulate much larger volumes of data, which is a significant challenge in terms of computing resources and storage space. The next version of the realistic simulation will cover about a factor of four more of the sky. These first results with METACALIBRATION in realistic simulated Roman HLIS imaging demonstrate that the METACALIBRATION shear calibration approach is a feasible strategy for the Roman mission and undersampled imaging more generally. However, significant additional work to study shear calibration in the

presence of blending and at significantly larger survey volumes is essential for reaching the precise requirements for the Roman weak lensing mission.

This is the Accepted Manuscript version of an article for publication in Monthly Notices of the Royal Astronomical Society. IOP Publishing Ltd is not responsible for any errors or omissions in this version of the manuscript or any version derived from it. The version of Record is available online at the following doi: 10.1093/mnras/stac2644.

6.3 Reconstruction of Nyquist-Sampled Images from Undersampled Roman Images

The results presented in this chapter are from Hirata, Yamamoto, et al., 2024 ("Paper I") and Yamamoto et al., 2024 ("Paper II"). The contributions of other authors are presented as such:

- *Chris Hirata: Implementation of IMCOM algorithm and the production of the coadd images in some filters. General advice and guidance for the project.*
- *Katherine Laliotis & Emily MacBeth: Analysis of noise images and the measurement of 1D and 2D noise power spectrum.*
- *Tianqing Zhang: Measurement of 4th-order moments of injected stars in the coadd image.*
- *Michael Troxel: Development of the image simulations used from Troxel et al., 2023.*

Although space is in many ways an ideal location for a weak lensing experiment, the high angular resolution brings some challenges related to the pixel scale. A diffraction-limited telescope produces a point spread function (PSF) with a characteristic angular width of λ/D, where λ is the wavelength of observation and D is the diameter of the entrance pupil. If the pixel scale P is larger than $\lambda/(2D)$, then the image is *undersampled* in the Nyquist sense: there are Fourier modes present in the image with more than $\frac{1}{2}$ cycle per sample, with the consequence that the images cannot be unambiguously interpolated, and thus the image intensity $I(r)$ cannot be treated as a continuous field. It also produces biases in the moments of images, including the first moment (centroid, relevant to astrometry) and the

180

second moments (sizes and shapes, relevant to weak lensing), which have been studied in many contexts (e.g. Anderson & King, 2000; High et al., 2007; Lauer, 1999; Samsing & Kim, 2011). One possible solution to the undersampling problem is to simply use small pixels – but if one has a fixed pixel count in the focal plane (often limited by available resources or technical considerations), then shrinking the pixels leads to a smaller field of view and a slower survey if we fix the survey depth and hence the required exposure time per pointing. An alternative, adopted for Euclid and Roman, is to accept undersampling, and use multiple dithered exposures of each field. This increases survey speed, but requires the development of algorithms for each application that take multiple undersampled images as input.

Undersampling can affect several stages of a weak lensing analysis (e.g. Finner et al., 2023; Kannawadi et al., 2021). One particular step is calibration of the shear estimator – that is, determining how the measured ellipticity of a galaxy e_i in a catalog responds to an applied shear γ_j.[15] While one might hope for an ellipticity measurement algorithm that has unit shear response $\partial \langle e_i \rangle / \partial \gamma_j = \delta_{ij}$, any stable ellipticity estimator has a response that depends on the galaxy population Massey, Rhodes, et al., 2007; J. Zhang and Komatsu, 2011, and so modern lensing analyses contain a "shear calibration" step that determines this response given the ensemble of galaxy morphologies present in that survey (at that depth, resolution, and observed wavelength). Whether the data are well-sampled or not, shear calibration must work with the fact that Fourier modes in the image are only well-measured up through some $k_{\max}$, and the shear operation moves modes across the $k = k_{\max}$ boundary (e.g. G. M. Bernstein, 2010), so one cannot take an observed image and infer what the sheared image would look like at the same resolution. In the past decade, several principled shear calibration approaches have been introduced that apply some re-smoothing (or in Fourier space, a cut $k_{\mathrm{cut}} < k_{\max}$) before measuring galaxy shapes (or moments) and have been successful at mitigating the galaxy population-dependent shear calibration biases in simulations. These include METACALIBRATION, which numerically applies a shear to each

---

[15] We include an index since e and γ are 2-component quantities.

object to compute the ensemble response (E. Huff & Mandelbaum, 2017; E. S. Sheldon & Huff, 2017; Z. Zhang et al., 2023); the Bayesian Fourier Domain technique, which builds the probability distribution of Fourier-space moments (G. M. Bernstein & Armstrong, 2014; G. M. Bernstein et al., 2016); and approaches that analytically build shear responses (Li & Mandelbaum, 2023). Further development of these methods is anticipated in support of final analyses of the Stage III ground-based survey data and the upcoming Vera Rubin Observatory. However, all of these techniques rely fundamentally on operations such as cuts in Fourier space that cannot be performed on undersampled data. Indeed, the first attempts to simulate METACALIBRATION for undersampled images resulted in percent-level biases (Kannawadi et al., 2021; Yamamoto et al., 2023) that exceed requirements for the upcoming surveys. This motivates us to develop image processing techniques to recover full sampling, as a step in the lensing analysis that precedes shape measurement (and even source selection), so that these shear calibration techniques can be applied to Roman data. A study of the fundamental mathematical issues can be found in Appendix B of Paper I.

The shear response is a property not just of the shape measurement algorithm, but of the sample selection as well, since applying a shear to a galaxy could cause it to cross a selection threshold (C. Hirata & Seljak, 2003; Kaiser et al., 2000). The same tools that have been developed to measure the shear response can be extended to incorporate the response from source selection (e.g. E. S. Sheldon et al., 2020, 2023). Furthermore, in a tomographic weak lensing analysis, the assignment of a galaxy to a particular tomographic bin is itself a form of selection, and thus one needs to derive the shear response of the photometry in each filter used for constructing the tomographic bins (e.g. Gatti, Sheldon, et al., 2021; Myles et al., 2021; Troxel et al., 2018). The next-generation weak lensing surveys have specified "shape measurement" filters (J129+H158+F184 in the case of Roman) as well as additional filters that are used for photometric redshifts (Y106 for Roman). This means that although the source galaxies do not need to be *resolved* in the photo-*z*-only filters, one still needs to either recover *full sampling* in these filters (and use the aforementioned frameworks) or develop an alternative framework for determining the statistical shear response. (This

issue was not fully understood at the time the Roman Reference Survey was designed.) Therefore, we have investigated recovery of a fully sampled mosaic in Roman Y106 band as well.

The recent joint Roman+Rubin simulations (Troxel et al., 2023), built on top of the Legacy Survey of Space and Time (LSST) Dark Energy Science Collaboration (DESC) Data Challenge 2 (DC2) simulations (Korytov et al., 2019; Kovacs et al., 2022; LSST Dark Energy Science Collaboration et al., 2021; LSST Dark Energy Science Collaboration (LSST DESC), 2021), provide an opportunity to test out algorithms to recover full sampling as part of an integrated simulation and processing pipeline suite, and explore the implications for Roman weak lensing analyses. This is the first in a series of papers that develops and tests an implementation of the IMCOM algorithm (Rowe et al., 2011) on a simulation of part of the Roman Reference Survey. In "Paper I", we focus on the characteristics of the simulation, relevant mathematical background, image combination machinery, and basic properties of the outputs. "Paper II" covers statistical analyses of the output images, including the ellipticities of simulated stars, correlation functions, noise power spectra, and noise-induced biases. Both papers use a 48×48 arcmin region from the simulations, large enough to contain ~ 2 Roman fields of view and a representative portion of the tiling pattern (see Fig. 6.8).

As discussed in Mandelbaum et al. (2023), in order for a reconstructed image to have a well-defined PSF the image coaddition algorithm needs to be linear and the weights on each exposure need to be independent of signals of sky scene (e.g., inverse-variance weights including source Poisson noise break the linearity assumption). To produce a well-defined coadded PSF, Rowe et al. (2011) presented the linear image combination algorithm IMCOM. IMCOM finds an optimal matrix $\mathbf{T}$ mapping from input (native) to output (coadd) pixels by minimizing the cost function which consists of the "leakage" (squared L^2 norm of the difference between the output PSF compared to a user-specified "target" PSF) and the output noise variance. The relative weight of the leakage and noise in the objective is controlled by a Lagrange multiplier κ in IMCOM; the logic in the iterative solver for κ can

be configured for different outcomes (e.g., to minimize noise subject to leakage being less than a specified value).

Imcom is fundamentally different from most other image reconstruction techniques in the sense that users are able to design their desired PSF for a given area and noise correlation level. Qualitatively, it is a process that transforms the input images with PSFs into a combined image with a common PSF in every pixel for a given area. If one would like a reconstructed image to be well-sampled and to have an isotropic and homogeneous PSF (indeed the case that is explored in Paper I to avoid PSFs with diffraction spikes), the size of the output PSF needs to be larger than the original PSF; hence the reconstructed image would be lower resolution than a "typical" coadd image. Despite this trade-off, the size of the output PSF is still much smaller than that of a ground-based PSF (see Table 4 of Paper I), meaning that this method still takes advantage of space-based imaging. Readers may refer to Rowe et al. (2011) and §2 of Paper I for the full details of the algorithm and the motivation in the current context of Roman, respectively.

6.3.1 Statement of the Problem

A variety of methods have been explored in the literature for combining multiple images of the sky into a single "coadded" image. If the coadded image is to be used as the starting point for a standard weak lensing analysis, one wants it to be both oversampled and have a well-defined PSF in the sense of Mandelbaum et al. (2023): the output image should be the true astronomical scene convolved with a PSF. We will go further here and ask for an algorithm that produces a specific desired output PSF Γ that is uniform and circular — thus we choose the output PSF and design a coaddition scheme to achieve it, rather than running a coaddition code and accepting the measured PSF at the end. This is advantageous for survey uniformity and mitigation of additive biases, but as we will see this is only possible under certain circumstances.

Thus in the context of this paper, the goal of the coaddition pipeline is to take in several input images of the sky, which are at some native pixel scale s_{in} and in general

have their own rotations, distortions, PSFs, and masks; and produce a well-sampled output image at an output pixel scale s_{out}, and with a uniform, round output PSF. Implicit in this statement of charge is that we are trying to accomplish at once several tasks that are sometimes distinct steps in an image processing pipeline:

1. *Interpolation* over masked pixels (e.g., cosmic ray hits, bad columns, or hot, dead, or unstable pixels).

2. *Resampling* onto a common grid.

3. *Rounding* and *homogenization* of the output point spread function (for some weak lensing pipelines; this step could also be performed last or not at all).

4. *Averaging* of the intensities from each input image to yield a single output image.

For oversampled data, it may be reasonable to treat these as separate, since operations such as resampling, convolution, and (sometimes) filling in a single missing sample, can be carried out on an oversampled function without introducing biases. However, they may be viewed in a unified framework if all of the operations used are linear. In this case, each step is a matrix operation, leading to an output image that is a linear combination of input images, with the mapping described by an $m \times n$ matrix **T**, where m is the number of output pixels and n is the number of input pixels. These statements apply to many of the common algorithms that have been applied to ground-based weak lensing data sets (either for shapes, source selection, or photo-zs): for example, linear predictive codes for interpolating bad pixels (Bosch et al., 2018, §4.5); Lanczos-3 (Bosch et al. 2018, §3.3) or polynomial (E. M. Huff et al., 2014, §4.4) interpolation for resampling; and pixel-domain (G. M. Bernstein & Jarvis, 2002, §7) or Fourier-domain (E. M. Huff et al., 2014, §4.1) rounding kernels, and PSF Gaussianization (Hildebrandt et al. 2012,§3; Kuijken et al. 2015, §4.2).

None of steps #1–3 are possible individually on undersampled data without introducing biases or making additional assumptions about the astronomical scene. However, the end goal of constructing a well-sampled output image with uniform PSF with some matrix **T**

may still be possible, even if **T** cannot be factored into the individual steps. The Fourier-domain algorithm of Lauer (1999) and the iterative algorithm of Fruchter 2011 are examples that combine some of these steps for some types of input data. The Imcom technique of Rowe et al. (2011) searches for a matrix **T** that accomplishes all 4 steps with minimum noise and target PSF error (as measured with quadratic metrics).[16] It is computationally expensive but can work with rolls, geometric distortions, varying input PSFs, and complex masks, and thus is a promising choice for a space-based weak lensing survey with *Roman*. Imcom returns a residual estimate for the output PSF; this allows us to identify cases where the desired output PSF is impossible to build (e.g., due to aliasing with insufficient dithers, or contains Fourier modes not represented in the input image).

We note that the Drizzle algorithm (Fruchter & Hook, 2002) that is commonly used to combine undersampled space-based images is itself a linear operation that can be described using a coaddition matrix **T**. In the case of Drizzle, **T** is sparse; the entry $T_{\alpha i}$ is determined by the overlap of output pixel α with a "shrunken" version of input pixel i. The Drizzle matrix **T** is within the search space for Imcom, and therefore by Imcom's target metrics of sum-of-squares error in the PSF and noise, Imcom will always perform at least as well as Drizzle (usually much better). But by choosing a particular sparse **T**, the Drizzle algorithm has a lower memory footprint and much faster run time, and therefore is likely to remain useful in the weak lensing analysis as a "quick look" tool (this is also how it was used in the DC2 simulation; Troxel et al. 2023) and for flagging purposes.

While Rowe et al. (2011) demonstrated their method on some test problems with $\sim 6 \times 6$ arcsec postage stamps, and the method has also been demonstrated on laboratory data (Shapiro et al., 2013), the method has not yet been applied to *Roman* simulations over an area large enough to measure the statistical properties of the coadded images. The availability of the Rubin Data Challenge 2 (DC2) + *Roman* simulation suite, and updated knowledge of Roman properties including characterization of the flight detectors, makes

---

[16] We want each output pixel to depend only on input pixels within a few arc seconds of its position. In practice, this is implemented by splitting the image into postage stamps; see § 4.1 for details.

this an excellent time to embark on such a simulation. The qualitative and quantitative objectives for this simulation are as follows:

1. Wrap the algorithm in a driver that can tile the sky and pipe the appropriate (simulated) observations to the linear algebra kernel and re-assemble the output into a community standard format such as FITS.

2. Find an example (not necessarily final) set of parameters for the Imcom algorithm that avoid basic problems such as noise amplification or ghosting across postage stamp boundaries (or reduce them to acceptable levels).

3. Characterize how chip gaps and cosmetic defects map into the assembled mosaics.

4. Use injected sources to test the output normalization, astrometry, size, shape, and higher moments of the final coadd PSF after propagation through Imcom.

5. Measure the correlation function of the ellipticities at scales overlapping the range likely to be included in the *Roman* weak lensing analysis.

6. Measure the noise properties of the output image for both uncorrelated and correlated input noise.

7. Compare the noise measured on the output images to the predictions from the Exposure Time Calculator (C. M. Hirata et al., 2012) and analytical descriptions in the literature (e.g. G. Bernstein, 2002).

8. Determine the as-realized computing time requirements for the coadd on a modern computing cluster (in order to inform both resource estimates and priorities for further optimization).

9. Compare the moments (i.e., shape and size) of bright unsaturated stars (suitable for PSF characterization) in the output images with the measurements performed on Drizzled coadd from DC2+*Roman* simulations.

Most of these objectives can only be achieved by simulating > 1 field of view. This paper presents the initial set of coaddition simulations and first look results; follow-on papers will go into more detail on some of the individual objectives.

6.3.2 Implementation of Imcom on Simulated Roman Images

Paper I re-implemented Imcom with a PYTHON interface and C back-end so that the pipeline is compatible with the image simulations. Paper I describes the implementation of Imcom and updates from the original version (e.g., how to compute input PSF correlations. see §4 of Paper I). It then applied Imcom on various input layers of 48×48 arcmin footprint (including realistic *Roman* single-exposure images produced in Troxel et al., 2023; the description of different input layers is in §3 and Table 1 of Paper I). The target PSF specified in Paper I is the Airy disk convolved with a Gaussian kernel whose width depends on the bandpass (Paper I Table 4), and Imcom is configured to produce (if possible) an output PSF within 0.1% of the target PSF in an L^2 norm sense. This implies that the root-sum-square of the error in the moments is 0.1% if the moments are defined in an orthonormal basis such as shapelets (Refregier, 2003). Paper I demonstrates several aspects of Imcom on Roman simulations:

- reconstruction of Nyquist-sampled images;
- homogenization and isotropization of well-defined co-add PSF; and
- minimization of noise covariances in coadded images.

Throughout this section, we use the quantity called "fidelity" as the basic quality indicator of the Imcom output, and many statistics are reported as a function of the fidelity. This defines how well the output PSF recovered the target PSF we specified. Mathematically, fidelity depends on the difference between the output and target PSF,

$$L_\alpha(s) = \sum_{i=0}^{n-1} T_{\alpha i} G_i (R_\alpha - r_i + s) - \Gamma_\alpha(s), \tag{6.4}$$

where the index α indicates an output pixel; i indicates an input pixel; G_i is the PSF in the ith input pixel; and R_α and r_i are the output and input pixel positions. The fidelity

is defined as the square norm of the output PSF residual scaled to the square norm of the target PSF, and re-written as an inverse logarithmic measure:

$$\text{Fidelity} \equiv -10\log_{10}\frac{U_\alpha}{C} \equiv -10\log_{10}\frac{\int [L_\alpha(\mathbf{s})]^2 d^2\mathbf{s}}{\int [\Gamma(\mathbf{s})]^2 d^2\mathbf{s}}. \tag{6.5}$$

The fidelity is usually — but not always — better (larger) if there are more exposures. The fidelity map in our simulation footprint for each bandpass we simulated can be found in Fig. 6.8.

Figure 6.8 shows the number of exposures in the coadd region (0.64 deg^2) as the coverage map and the fidelity achieved in the coadd process. The tiling pattern here is from the reference survey design, and more detail in the tiling pattern can be found in Troxel et al., 2023. We can see that less coverage in the $Y106$ band (most undersampled) results in the lowest fidelity among other bands, while the fidelity in the $F184$ band is better because it is the better-sampled bandpass. The sampling quality, on the other hand, can be quantified as the modulation transfer function (MTF) of the input PSF and the resulting coadd PSF, which is the absolute value of the Fourier transform. Figure 6.9 shows the MTF of the input PSF (top panel) from `galsim.roman` module and the output PSF (bottom panel) produced from the coadd process. We can see that none of the bandpasses satisfies the Nyquist frequency, whereas the output PSF is well-sampled for all the bandpasses, given the fidelity of the output PSF. As a comparison of Imcom with Drizzle, Figure 6.10 shows an example of a simulated coadded star in $Y106$ band processed through two algorithms. As discussed earlier, Imcom attempts to coadd images in a way that regularizes the PSF to match the target PSF, the Imcom star looks more uniform and homogeneous compared to the Drizzle star, which attempts to stack images at a give position.

6.3.3 Analysis of the Simulated Images and Implications for Weak Lensing

6.3.3.1 Simulated Data

This study utilizes the simulated data products from Paper I, which covers 0.64 square degrees in four filters: Y106, J129, H158, and F184 from shortest to longest wavelength. The
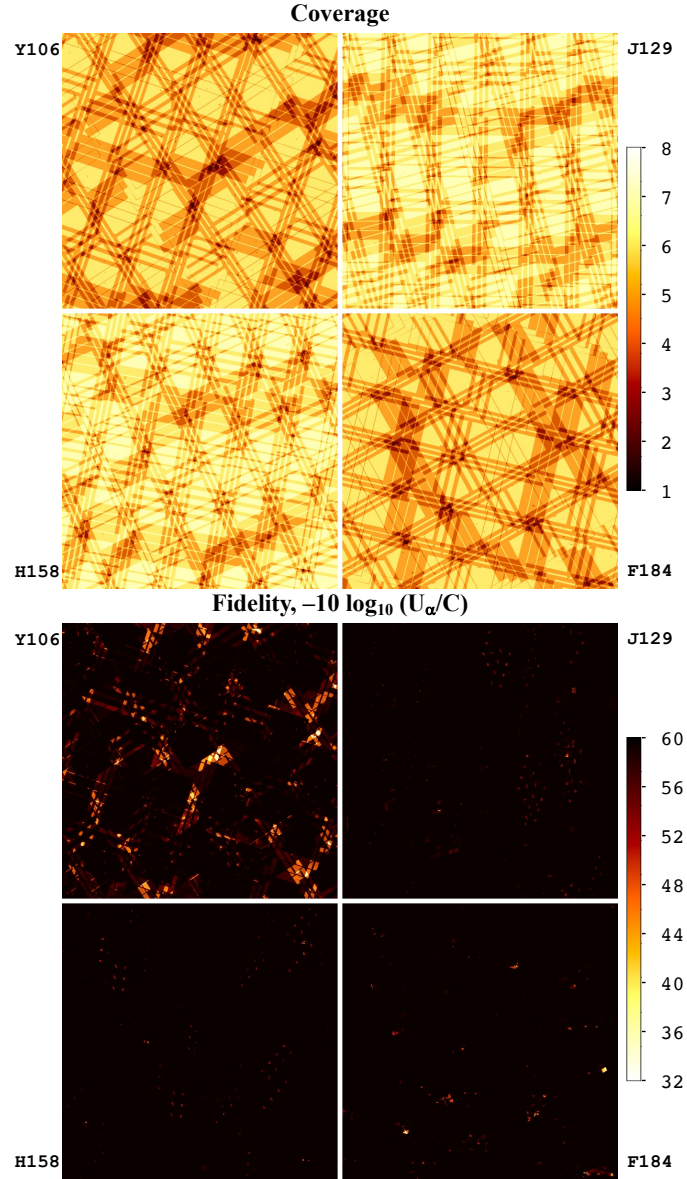
FIGURE 6.8: *Top*: The coverage (number of exposures) in each of the 4 bands in the 48×48 arcmin region considered in this paper. Each sub-panel shows one of the filters. The 18-chip "pawprint" feature of the *Roman* focal plane is easily visible, as is the presence of two roll angles from the two passes in each filter. *Bottom*: The fidelity map over the 48×48 arcmin region simulated in each of the 4 bands. The lowest values are seen in Y106 since it has the most undersampled PSF, and the number of dither positions is lower than in J129. Note that the same features in the coverage map also appear here: the output PSF is not as well matched to the target in regions of intersecting chip gaps.
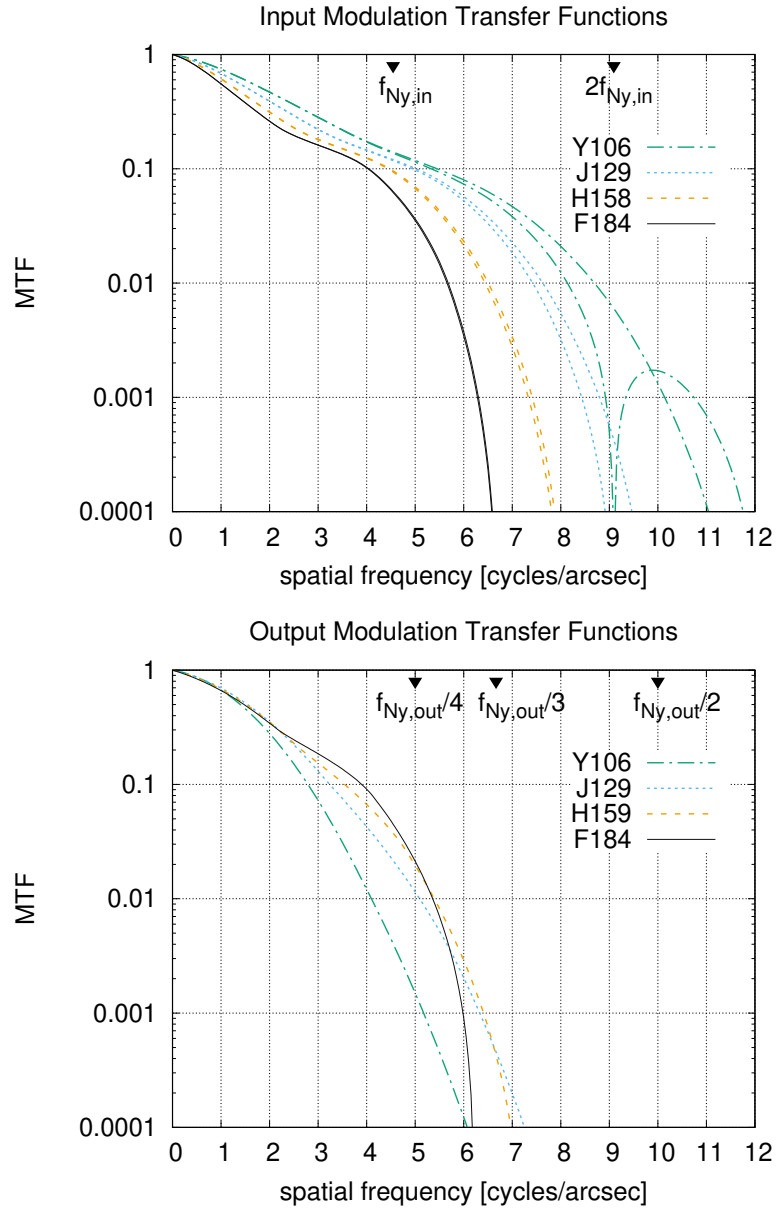
FIGURE 6.9: The input and output modulation transfer functions (MTFs: absolute value of the Fourier transform of the PSF). The upper panel shows the MTFs as computed in the Exposure Time Calculator (C. M. Hirata et al., 2012) based on the requirement aberrations. Two curves are shown for each filter, either for wave vector aligned with the pixel grid or at a 45° angle; for F184, the difference is not visible on the plot. The Nyquist frequency at the native (input) pixel scale is marked. The lower panel shows the output PSFs, with fractions of the Nyquist frequency at the output pixel scale s_{out} marked. Note that all of the input images are undersampled (the MTF is nonzero for spatial frequencies extending past $f_{Ny,in}$) but the output images are well sampled, with the MTF dropping to negligible levels ($< 10^{-4}$) by $\sim 0.36 f_{Ny,out}$ in all filters.
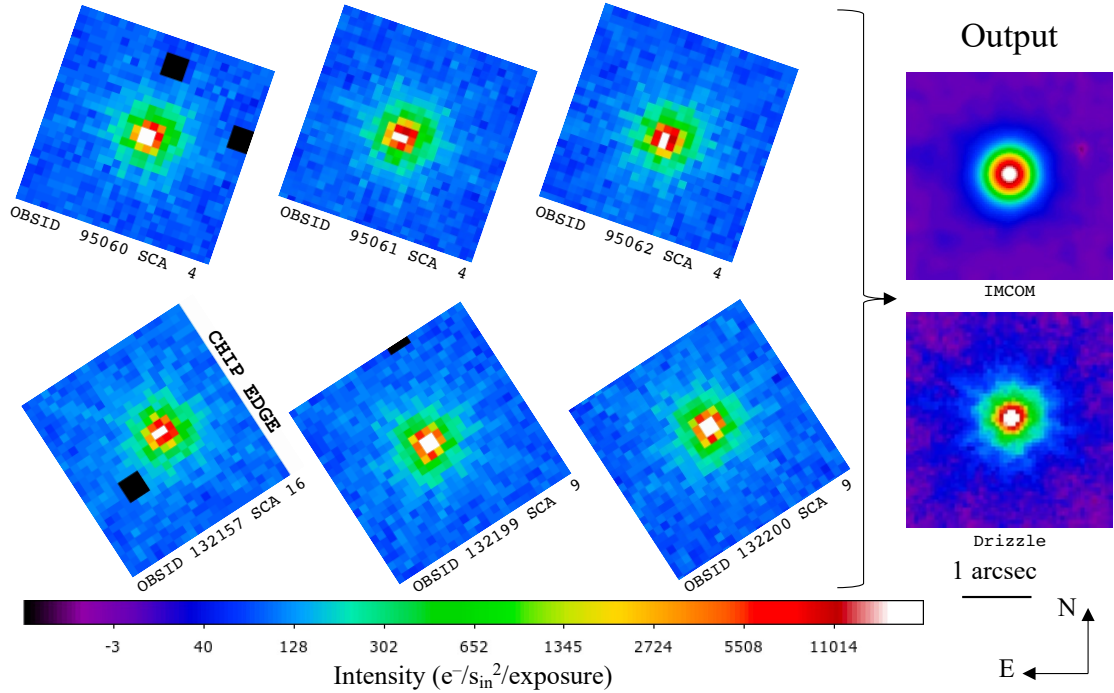
FIGURE 6.10: An example of a simulated coadded star in the Y106 band. The left part of the figure shows the 6 images of the star, at the as-observed roll angles in the two passes, in the "simple" DC2 simulation. The right panel shows the coadded map. The IMCOM coadd (this project) is shown at top; the drizzled coadd is shown below. A logarithmic color stretch is used. The sky level (61 e/p) is present in the inputs but has been removed in the outputs. The black squares in the inputs are masked pixels (for the IMCOM run).

sky inputs are from the Large Synoptic Survey Telescope Dark Energy Science Collaboration Data Challenge 2 (LSST DESC DC2; Korytov et al. 2019; Kovacs et al. 2022; LSST Dark Energy Science Collaboration et al. 2021; LSST Dark Energy Science Collaboration (LSST DESC) 2021). Table 1 in Paper I illustrates various input images that have been fed into the IMCOM algorithm, which can be classified as follows.

- *Sky image* (layer names: **SCI**, **truth**): The images were generated through the *Roman* image simulations pipeline (Troxel et al. 2021, 2023) utilizing the truth catalogs of stars and galaxies from the LSST DESC CosmoDC2 simulations (Korytov et al., 2019; Kovacs et al., 2022). The layer labeled **SCI** includes saturation and simple detector physics models such as read noise and dark current, simulated in GALSIM, while the

layer labeled **truth** refers to noiseless images; star and galaxy profiles are drawn at designated locations.

- *Point sources* (layer names: **gsstar14**, **cstar14**): These are grids of sources located at HEALPix resolution 14 (`nside=2`^{14}) pixels (Górski et al., 2005). Each source is a δ-function convolved with a simulated *Roman* PSF; the PSFs are simulated in Troxel et al., 2023 through GALSIM using flat spectral energy distribution (SED). **gsstar14** refers to images where the sources were drawn using GALSIM, while **cstar14** refers to images where they were drawn with internal routines in the coaddition code. We call them "injected stars" throughout this paper.

- *Noise images* (layer names: **whitenoise1**, **1fnoise2**): We generate realizations of white noise (**whitenoise1**) and $1/f$ noise (**1fnoise2**). The white noise is uncorrelated between pixels and has unit variance. The $1/f$ noise is scale-invariant in the time stream and is then re-formatted into a 2-dimensional image according to the pixel readout order (Mosby et al., 2020). It has unit variance per logarithmic range in frequency.

Examples of the injected stars and noise realizations are shown in Fig. 6.11. And examples of a variety of objects identified in the co-added sky images are shown in Fig. 8 of Paper I.

6.3.3.2 Measurement of noise correlations

We first investigate the noise fields, giving an overview of noise effects (§ 6.3.3.2.1), and then describing the 2D (§ 6.3.3.2.2) and 1D azimuthally averaged (§ 6.3.3.2.3) noise power spectra.

6.3.3.2.1 Noise Overview

Noise is a significant source of error for the precision necessary to observe weak gravitational lensing of galaxies. The impact of noise on the measurement of a shear signal can be parameterized into two types of systematic observational errors: additive and multiplicative biases (e.g. Heymans, Van Waerbeke, et al., 2006). If the true signal is given by γ_{true}, noise
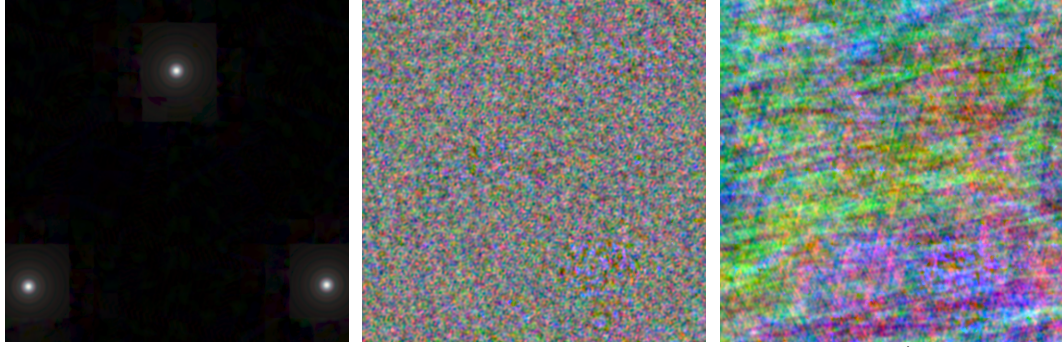
FIGURE 6.11: Coadded injected GALSIM stars (left), white noise (center) and $1/f$ noise (right) realizations, displayed as 3-color F184 (red)/J129 (green)/Y106 (blue) combinations. Each image shows a 700×700 output pixel (17.5×17.5 arcsec) region of the coadded images, from the **gsstar14**, **whitenoise1**, and **1fnoise2** layers, respectively. The color scale is a fourth-root stretch (0 to 0.2 input flux per input pixel) in the injected star image (left); and for the noise realizations it is linear, spanning ± 1.25 (center) or ± 4 (right) in input units. Note that the input white noise layer leads to output noise correlated on the scale of the input pixels, whereas the $1/f$ noise layer shows the characteristic striping at each of the 2 input rolls. These rolls are at different angles in each filter, hence the color pattern. The region shown is $270 \leq x < 970$, $301 \leq y < 1001$ of block (2,30).

(or other) biases give a γ_{meas} of

$$\gamma_{\text{meas}} = (1 + m)\gamma_{\text{true}} + c. \tag{6.6}$$

The additive bias (also called "spurious shear") is given by the constant c, and manifests as a shear signal that is present even when the true population of galaxies is unlensed. The factor of m gives the multiplicative bias (also called "calibration error"). Multiplicative bias occurs when a real lensing signal is detected, but the measurement is larger or smaller than the true signal by some factor (Bacon et al., 2001; Erben et al., 2001; C. Hirata & Seljak, 2003). The next-generation weak lensing surveys have stringent requirements for both types of errors (Cropper et al., 2013; Euclid Collaboration et al., 2020; Massey et al., 2013; Paulin-Henriksson et al., 2009; The LSST Dark Energy Science Collaboration et al., 2021; Troxel et al., 2021).

To quantify the impact that noise might have on observations and determine whether these requirements will be met, we measure and analyze noise correlations in the coadded images from two types of input noise fields: white noise and $1/f$ noise (see §3.4 of Pa-

per I). Real noise has both of these components, as well as some smaller additional terms (Rauscher, 2015). We focus on the noise power spectrum in the output images, since both the lowest-order noise-induced bias and the variance of the measured shapes are proportional to second moments of the noise (i.e., depend on $(S/N)^{-2}$; G. M. Bernstein and Jarvis 2002) and are therefore captured by the power spectrum. We then compare this power spectrum to the expected output noise power spectrum if we ignored sampling issues. Appendix B of Paper II describes in detail the impact of anisotropic noise (such as $1/f$ noise and non-ideal white noise) on ellipticity measurements.

Different properties of a galaxy are affected by noise at different wave numbers. If a large scale uniform (zero wavenumber) noise offset is present in an image, the error in this flux would impact the estimated photometric flux from the galaxy, but not the position or shape. An astrometric measurement will, however, be affected by an overall tilt (gradient of the noise, or in Fourier space the noise weighted by one factor of wavenumber); this would bias the centroid towards one direction or another. The shape of a galaxy will only be biased if the second derivative of the noise field is biased towards a preferred direction. In Fourier space, the ellipticity error thus comes from the noise weighted by two powers of the wave number (the impact of noise on shapes is discussed more in § 6.3.3.3.5). Photometry, astrometry, and shape measurements are thus dependent on higher and higher spatial frequencies respective to one another. This is demonstrated quantitatively in Appendix B of Paper II, including the factor of wave vector squared ($u^2 - v^2$ for g_1 and $2uv$ for g_2) appearing in the noise-induced error in the shapes.

6.3.3.2.2 2D noise power spectra

We take the convention that the power spectrum $P(u,v)$ of a field is given by the 2D Fourier Transform of the correlation function $\xi(\Delta x, \Delta y)$:

$$P(u,v) = \int \xi(\Delta x, \Delta y) \mathrm{e}^{-2\pi \mathrm{i}(u\Delta x + v\Delta y)} \, \mathrm{d}\Delta x \, \mathrm{d}\Delta y, \tag{6.7}$$

where $\xi(\Delta x, \Delta y) = \langle S(x,y)S(x',y') \rangle$ is the correlation function of the noise field S with pixel coordinates given by (x,y) in Cartesian space and (u,v) in Fourier space. In the case of

discrete data, we replace the integral with a sum over pixels; we preserve the convention that P has units of $S^2 \times$ area (e.g., for a field sampled at the output pixel scale s_{out} as considered here, we sum over pixels and multiply by s_{out}^2).

We accomplish this by making use of the Numpy Fast Fourier Transform (FFT) function (Harris et al., 2020). Each noise field in each $N \times N$ pixel block (here $N = 2600$) is FFTed and normalized by the size of the blocks and the size of the output pixels:

$$P_{2D}(u, v) = \frac{s_{\text{out}}^2}{N^2} \left| \sum_{j_x, j_y} S_{j_x, j_y} e^{-2\pi i s_{\text{out}}(u j_x + v j_y)} \right|^2 , \qquad (6.8)$$

where u and v are sampled at integer multiples of $1/(N s_{\text{out}})$. The two-dimensional power spectra that result from this are further binned into 8×8 bins, resulting in power spectra that are 325×325 pixels covering the range of u and v from -20 to $+20$ cycles arcsec^{-1} (the Nyquist limit for $s_{\text{out}} = 0.025$ arcsec/pixel) at spacing

$$\Delta u = \Delta v = \frac{1}{325 s_{\text{out}}} = 0.123 \text{ cycles arcsec}^{-1}. \qquad (6.9)$$

For each observation filter, we then averaged together the power spectra from each of the 2304 blocks (the total 48×48 arcmin^2 region). The resulting average power spectrum for the full mosaic in each observing filter can be seen in Fig. 6.12. Note that this procedure included the padding regions that appear in more than one block, so these regions are over-represented in the averaged power spectrum. Since the padding regions are not special relative to the detectors or tiling strategy, we do not think this is a major issue.

In the absence of sampling issues and if the input and output PSFs were all identical, input white noise should lead to output white noise and a constant power spectrum for the 2D image. Since we have an output PSF that is larger than the input PSF in real space (narrower in Fourier space), we expect that the high-wave number Fourier modes will have reduced power (proportional to the square of the Fourier transform of the output PSF). The examples in Figure 6.12 clearly show this behavior. Note that the spectra are plotted on a log scale, so that although several features are visible, any features outside of the central

maxima have very little power. The circular region in the center of the 2D power spectra comes from the output PSF: the Airy disc convolved with a Gaussian. In the Y106 and J129 bands, where the Gaussian dominates the cutoff of the PSF, we see a smooth fade into uncorrelated wavenumber space. In the H158 band and especially the F184 band, the Airy disk defines the limit of the PSF, so beyond this limit the image contains only noise — this causes Imcom to set the background to zero, causing the hard edge of the circle.

We can confirm this by comparing measurements of the image with expectations. The band limit (maximum number of cycles per unit angle) for a diffraction-limited telescope is given by D/λ, where D is the telescope diameter and λ the wavelength of light. For the F184 band,

$$\frac{D}{\lambda} = \frac{2.37\,\mathrm{m}}{1.84\,\mu\mathrm{m}} = 1.29 \times 10^6\,\mathrm{cycles\,rad^{-1}} = 6.25\,\mathrm{cycles\,arcsec^{-1}}. \tag{6.10}$$

This is indeed the radius of the circle on the F184 band image, confirming that this feature is caused by the Fourier modes outside the circular regions being beyond the target PSF band limits.

The large "+ signs" extended throughout the images correspond to the directions of the postage stamp boundaries. (Note that the input images are at various roll angles, so these features must instead be associated with the output.) The step function-like feature of the postage stamp boundaries becomes a continuous line in Fourier space, so we see these extended + signs in the power spectra.

The spots in the F184 band are a small print-through of the initial pixel positions in the input images into the final output images. The first ring of 8 points is located at a radius of ~ 9 cycles arcsec^{-1} from the center, i.e., roughly the inverse of the input pixel scale $s_\mathrm{in} = 0.11$ arc§As expected, the directions of the 8 points corresponds to the 4 grid directions of the input exposures.

For the $1/f$ noise power spectra in Figure 6.13, we have combined two sets of images with horizontal banding at different roll angles, so the output noise image will have at least two distinct preferred directions (see the right panel of Fig. 6.11). These features appear
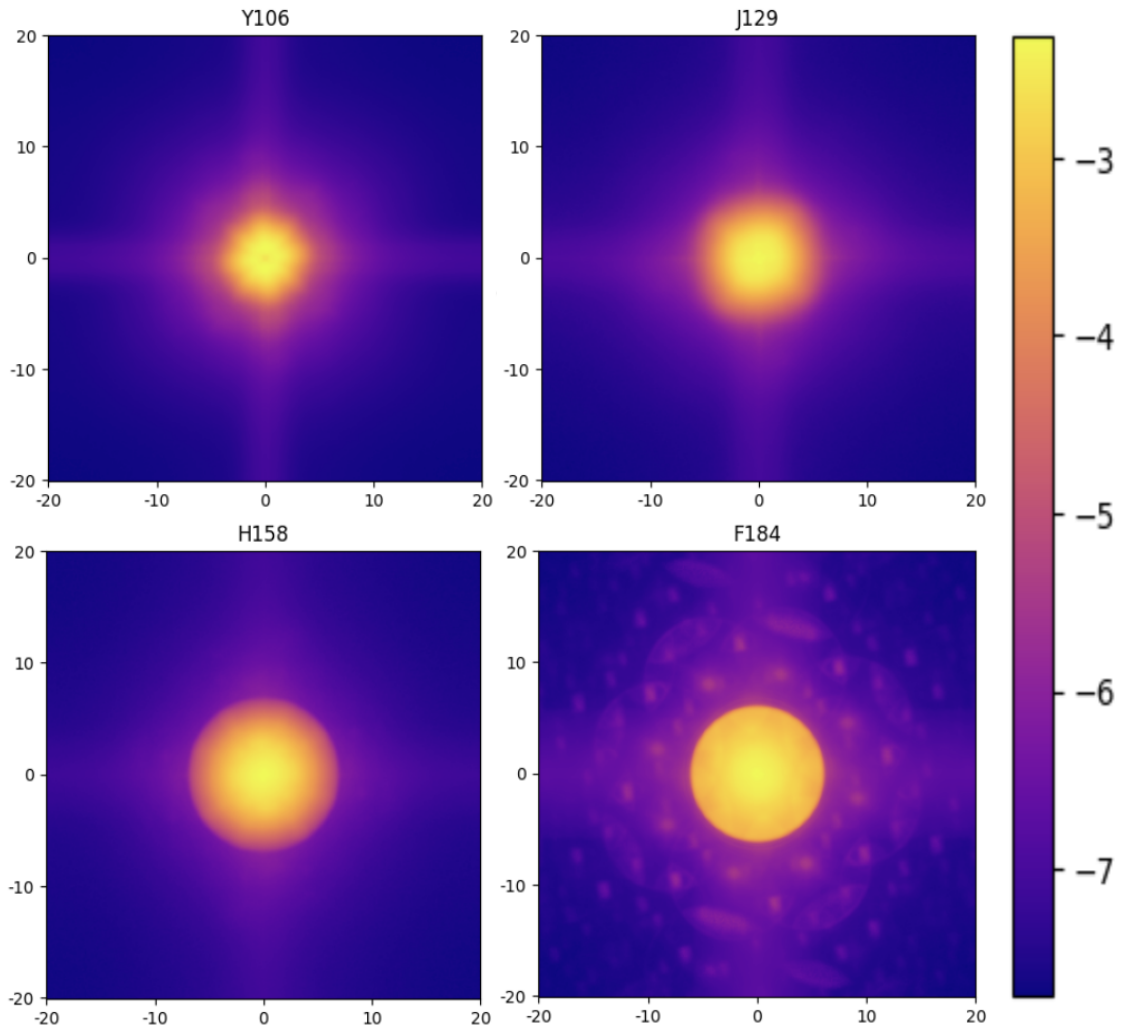
FIGURE 6.12: 2D averaged power spectrum of the white noise field of each band, plotted on a logarithmic color scale. The horizontal and vertical axes show wave vector components (u and v respectively) ranging from -20 to $+20$ cycles arcsec^{-1}. The color scale shows the power $P(u, v)$ in units of arcsec^2 (Eq. 6.7). The minimum and maximum values of each power spectrum are as follows: 6.6×10^{-8} to 6.7×10^{-3} for Y106; 3.4×10^{-8} to 3.5×10^{-3} for J129; 5.9×10^{-8} to 3.2×10^{-3} for H158; and 2.0×10^{-8} to 4.8×10^{-3} for F184.

strongly in each panel of Figure 6.13 as a distinct X through the centers of the images. The roll angles are slightly different in each band in order to maximize coverage, leading to different orientations of the X's in each image.

As in the white noise spectra, the boundary between postage stamps contained in the images creates step-like features in the noise fields, which manifest as two distinct perpendicular Fourier modes in the power spectra. However, this feature is clearly more prominent in the $1/f$ noise than in the white noise. In $1/f$ noise, we have striping across entire channels within the detector, which then crosses over postage stamp boundaries. The correlations between postage stamp boundary-caused features extend over much larger scales in real space, corresponding to sharper features in Fourier space. Thus we see the postage stamp boundary feature (the large + sign) more distinctly in these images.

The $1/f$ bands also display the same reduction of power at large wave number as in the white noise, and the sharp circular boundary in H158 and especially F184 caused by the band limit of the PSFs.

In addition to features coinciding with behaviors seen in the white noise images, we see one additional pattern appear in the $1/f$ noise that is not present in white noise data. Figure 6.13 shows this feature most clearly in the J129 band: alternating bright and dark vertical fringes across the center of the 2D power spectrum image. We measure the spacing between fringes to be 0.8 cycles arcsec^{-1}, or one cycle per 1.25 arcsec postage stamp. We therefore believe that the fringes result from steps at the postage stamp edges, with a sense that is coherent across multiple postage stamps (due to the large correlation length of the $1/f$ noise).

While these rough analytical arguments allow us to identify specific features in the output 2D power spectra with properties of the input images and Imcom algorithm, the quantitative details — how much power appears in each feature, and how this varies as a function of sampling going from Y106 (bluest/worst sampled) to F184 (reddest/best sampled) — must be determined via simulations.
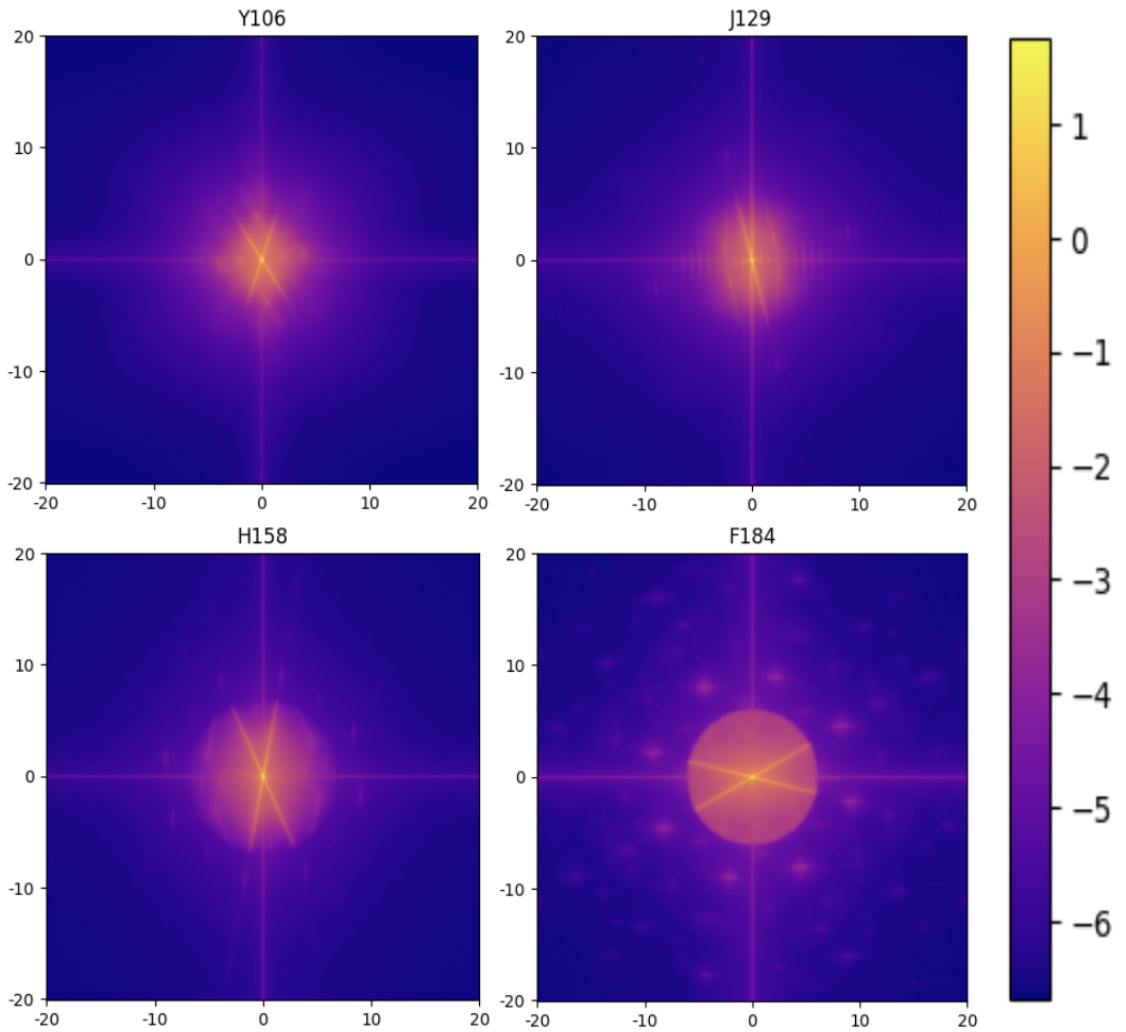
FIGURE 6.13: The 2D averaged power spectrum of the coadded $1/f$ noise field of each band, plotted on a logarithmic color scale. The horizontal and vertical axes show wave vector components (u and v respectively) ranging from -20 to $+20$ cycles arcsec^{-1}. The color scale shows the power $P(u,v)$ in units of arcsec^2 (Eq. 6.7). The minimum and maximum values of each power spectrum are as follows: 1.8×10^{-6} to 5.4×10^1 for Y106; 8.5×10^{-7} to 4.6×10^1 for J129; 6.9×10^{-7} to 4.8×10^1 for H158; and 2.1×10^{-7} to 5.6×10^1 for F184. The X-shape, + sign, spots (in H158 and F184), and vertical fringes (in J129) are discussed in the main text.

6.3.3.2.3 Azimuthally averaged power spectra

In addition to the two-dimensional power spectra, we generate for each filter a set of one-dimensional azimuthally averaged power spectra. First, the two-dimensional power spectra of each block are saved from the previous step of analysis. We then calculate the mean exposure coverage in each block, and group the power spectra into one of 5 bins in mean coverage. Since the root-mean-square of noise in the output noise images shows the mean exposure coverage dependence, it is good to check how noise correlations depend on the coverage as well (see § 5.3 of Paper I for more details). These power spectra are also separated by observing filter, as exposure coverage varies significantly depending on the band in which observations are taken. We average together the 2D power spectra for blocks within a given mean coverage bin into a single 2D power spectrum, which is then azimuthally averaged over thin annuli, using the method from Casey et al. (2023). For this work we used 162 radial bins, effectively taking rings of width one pixel in the power spectrum map (Eq. 6.9) and averaging the values of the power at each circular aperture of wavenumbers.

Figure 6.14 shows the mean coverage-binned 1D power spectra for the output white and $1/f$ noise images in each observation filter. Rather than just $P(\nu)$, we plot $2\pi\nu P(\nu)$ so that the area under the curve corresponds to the variance in the output pixels. We additionally include in each figure a purely analytical model of the 1D power spectrum, based on $N_{\mathrm{in}} = 5$ input exposures and ignoring pixelization/sampling issues. Derivations of the analytical models for the output noise power spectra can be found in Appendix A of Paper II.

For all bands and for both types of noise, the peak power and width of the power spectrum depends consistently on the mean coverage in the image. Exposures with small mean coverage values have the highest peaks and the slowest dropoffs down to zero power at large wave number. Our analytic expectation represents an idealized case, and the behavior as compared with the spectra for the mean coverage bins shows that with decreasing mean coverage, we move farther above the ideal power spectrum. However, we note that in all
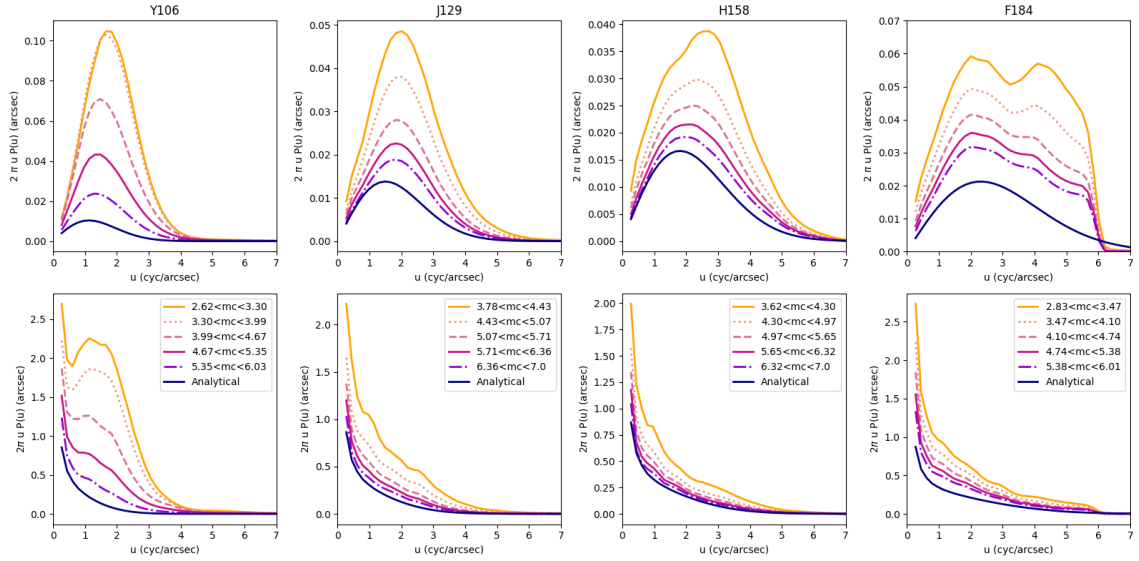
FIGURE 6.14: Top row: 1D power spectra for the output white noise fields in each filter. Bottom row: 1D power spectra for the output $1/f$ noise fields in each filter. Each filter's spectra are divided into five even-width bins of mean coverage ("mc" in short), and plotted against the analytical expectation for noise power spectra for combining 5 exposures in the absence of sampling issues (see Appendix A for derivations).

of these cases the noise power spectrum is above the analytic expectation for most wave numbers.

In the white noise 1D power spectra, several features are evident in all bands. Each of the observation bands shows that the contributions to the power spectrum (weighted by $2\pi v$) go up, rise to some peak, and come back down to zero, qualitatively consistent with the analytic expectation. Noise increase due to aliasing often gets worse as one moves to larger wave number (the zero-mode corresponds to total flux, which is conserved in the absence of intrapixel sensitivity variation). This can result in $2\pi v P(v)$ having a steeper dependence than $\propto v$ at small v, as seen prominently for Y106 (the most undersampled filter) in Fig. 6.14. Figure 6.15 shows the central feature in the 2D power spectrum from input white noise for each filter with the color scale significantly stretched to show this behavior.

In contrast, the $1/f$ noise spectra have a distinct peak in the center of the image, caused by the overlaps in the Fourier modes from the roll angles. The power spectrum as a function
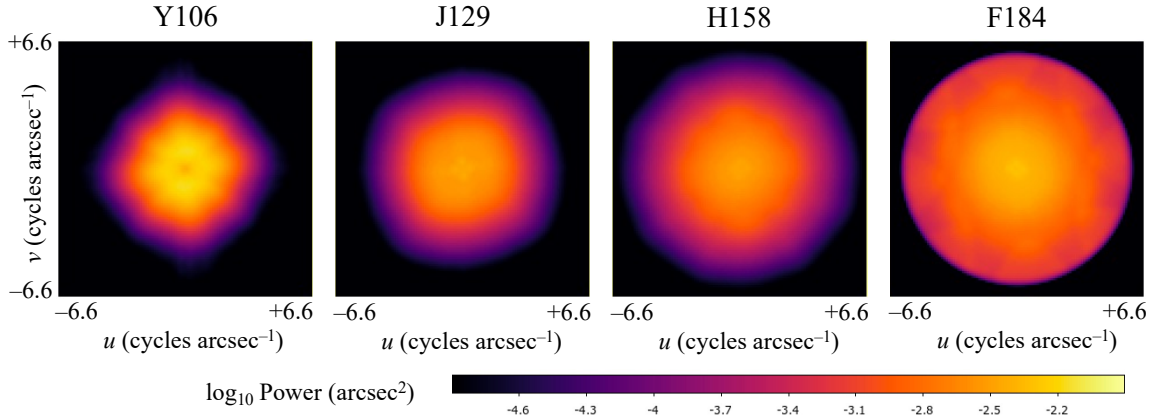
FIGURE 6.15: Zoomed in image of the central features in the input white noise power spectra. By stretching the color scale we can see more clearly that the zero-wavenumber modes do not contribute the most to power in the output noise, particularly in Y106.

of frequency on one dimension goes like $1/f$, so for small wave numbers the power should reach very large values — a result that is clearly visible in the spectra for all bands. The analytic estimation for the $1/f$ noise spectra in the absence of pixelization/sampling effects (Appendix A of Paper II) is qualitatively correct for the redder filters, but the normalization is slightly low, and it misses the "bump" caused by aliasing in the bluer filters (especially Y106).

Analyzing these power spectra allows us to understand the correlations between features caused by noise in the simulated images being operated on by IMCOM. In Section 6.3.3.3.5, we provide a more detailed discussion of the quantitative links between these power spectra and weak lensing measurement biases.

6.3.3.3 Moments Analysis of the coadded images

In this section, we present the quantitative analysis of the simulated coadded images of multiple layers. This includes object centroid, ellipticity and size measured by computing image moments of objects located in grids, and simulated fields with and without noise.

6.3.3.3.1 Moments of the injected sources

Our first set of tests is conducted on the grids of simulated stars. Our main objective is to show the properties of the output PSFs and demonstrate that these properties have an

expected dependency on how divergent the output PSF is from the target. The expected properties are exactly known since we chose the target PSF to be the Airy disk convolved with the Gaussian kernel.

Our simulation footprint contains $54\,597$ unique simulated stars, each at the center of a HEALPix[17] (Górski et al., 2005) resolution 14 pixel. For each injected star, we cut out a 99×99 output pixel (2.475×2.475 arcsec) postage stamp from the output block containing that star (for the "block" definition refer to Fig. 4 of Paper I). We consider the first the GalSim noiseless star layer (**gstar14**).[18] We measure the 1st and 2nd-order moments of the simulated sources in the output images using the `galsim.hsm` module (C. Hirata & Seljak, 2003; Mandelbaum et al., 2005), which implements the fitting of an adaptive elliptical Gaussian to the image (e.g. G. M. Bernstein & Jarvis, 2002).[19] The 1st moments (centroids) can be compared with the expected position based on the World Coordinate System (WCS) of the coadded image; the result is reported as the astrometric error. The 2nd moments (covariance of the Gaussian: a 2×2 matrix **M**) are reported as three real numbers: the shear-invariant width

$$\sigma = \sqrt[4]{M_{xx}M_{yy} - M_{xy}^2}, \tag{6.11}$$

and the shape components

$$(g_1, g_2) = \frac{(M_{xx} - M_{yy}, 2M_{xy})}{M_{xx} + M_{yy} + 2\sqrt{M_{xx}M_{yy} - M_{xy}^2}} \tag{6.12}$$

that are zero for a perfectly circular object and generally satisfy $g_1^2 + g_2^2 < 1$ for a positive definite second moment matrix. (The use of "g" for the latter indicates consistency with the

---

[17] http://healpix.sourceforge.net

[18] There is also a **cstar14** layer: this should in principle be the same except for approximations used to draw the stars. We have computed the correlation function $\xi_+(\theta)$ from the nearest-neigbor (≈ 0.2 arcmin) to the diagonal (1 degree) in all 4 bands, and found values ranging from consistent with zero up through 2.1×10^{-9}. Given that this difference is small compared to *Roman* requirements, we present only the GalSim-drawn stars (which are independent of any of the Imcom routines) in the main text to avoid clutter.

[19] The `galsim.hsm` module can implement PSF corrections to galaxy shapes using the method of C. Hirata and Seljak (2003) and Mandelbaum et al. (2005), but this functionality is not used in this section since we are only measuring the stars.
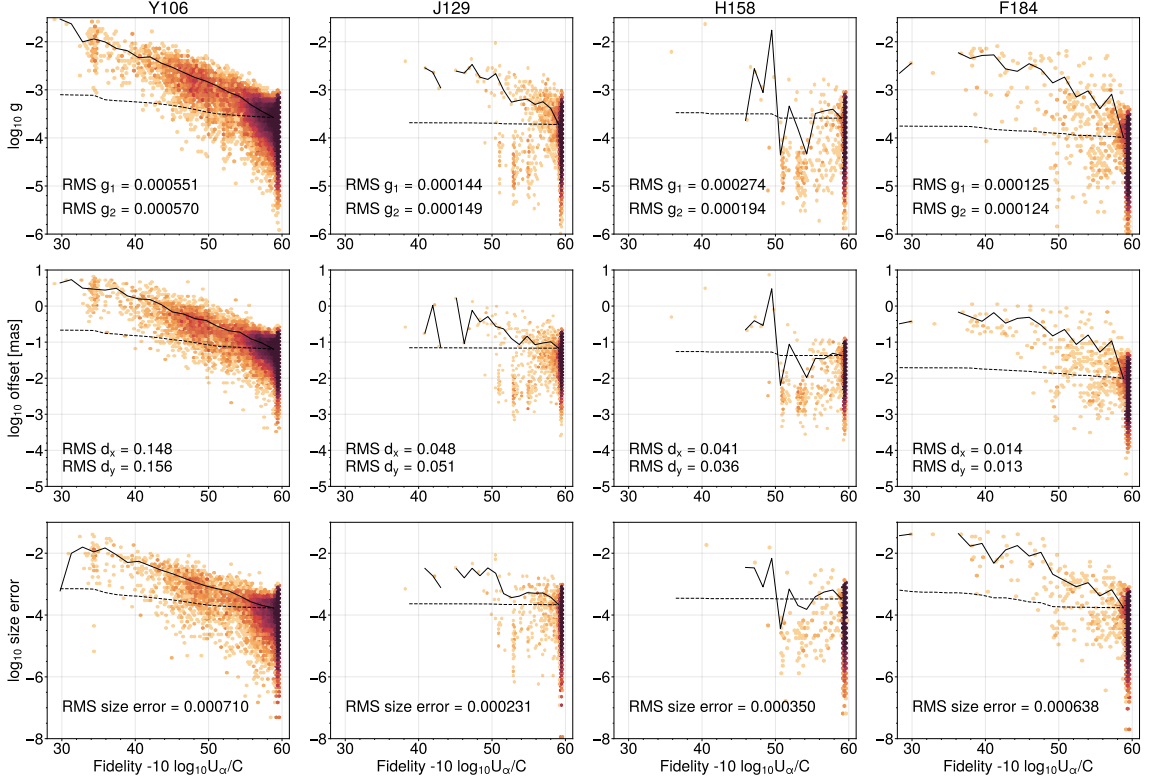
FIGURE 6.16: The distributions (in an arcsinh scale) of moments of the injected stars drawn in the input images, coadded in IMCOM, and then measured by the `galsim.hsm` module in each of the filters, with no noise. **Top**: the ellipticity $g = \sqrt{g_1^2 + g_2^2}$ of the injected GALSIM stars. **Middle**: the astrometric displacement from the coordinates where the star was injected. **Bottom**: the relative size error of the GALSIM stars and target PSF. The definition of size in this figure is Eqn. 6.11. The horizontal axis is the output PSF fidelity (larger means a better match to the target PSF; see § 6.3.3.1). The solid line shows the RMS ellipticity (top), RMS astrometric displacement (middle), and RMS fractional size error (bottom) in each fidelity bin. The dashed line is the same thing but is cumulative (i.e., the RMS for all stars in regions with that fidelity or better). This would be applicable to cases where we impose a mask based on the fidelity.

conventions of Schneider and Seitz 1995.) We also report the mean fidelity $\langle -\log_{10}(U_\alpha/C) \rangle$ for the pixels in the central 20×20 output pixel (i.e., 0.5×0.5 arcsec) region surrounding the star. This is a measure of how well IMCOM estimates it has done at building an output image with the desired PSF in that region of the survey.

Figure 6.16 shows measured ellipticity, astrometric error and fractional size difference of the sources drawn by GALSIM. It is expected that the anisotropy of shapes decreases as the fidelity of the output image is maximized. Most of the postage stamps (for the "stamp"

205

definition refer to Fig. 4 of Paper I) achieved high fidelity (above 50) in all bandpasses except Y106. This is likely due to the bandpasses being the most undersampled and that the algorithm is unable to find the transformation matrix that the leakage and noise correlations are minimal (this is also shown in Fig. 11 of Paper I). In all bandpasses, however, the total RMS ellipticity of the coadded injected stars in each shape component is $\lesssim 5.7 \times 10^{-4}$ which is the PSF ellipticity requirement on angular multipole scales $(32 < \ell < 3200)$ determined by the SRD. Here we also demonstrate that the astrometric error of the sources induced by Imcom is a small contribution to the relative error budget in the astrometric calibration (< 1.3 mas) defined by the SRD. Finally, the bottom panel of Fig. 6.16 shows the fractional size error of the injected stars relative to the target PSF. We cannot directly compare the RMS size error in each bandpass to the required PSF size error in the SRD ($\lesssim 3.6 \times 10^{-4}$)[20] because our RMS errors are computed at individual points, whereas the size error requirement is computed at scales $\ell < 3200$ (or smoothed at a scale of ~ 4 arcmin, i.e., where there are 3200^2 pixels on the full celestial sphere). We see that the size errors are largest in Y106 and F184. If we bin the stars into pixels, we see that the size error declines to $(1.58, 0.59, 1.01, 2.09) \times 10^{-4}$ in Y106/J129/H158/F184 respectively in 1×1 arcmin pixels; and then it declines to $(0.46, 0.39, 0.70, 1.46) \times 10^{-4}$ in 4×4 arcmin pixels. Thus we see that the image combination step is using only a small fraction $(1.46/3.6)^2 = 16\%$ of the overall PSF size error budget in a root-sum-square sense.

The spatial distribution of the second moment errors, averaged in 1 arcmin^2 pixels, is shown in Fig. 6.17. Most of the area has ellipticity errors at the $\lesssim 10^{-4}$ level; one sees a few outliers, with corresponding errors in the size. The large outliers seen in Y106 and F184 correspond to low-coverage regions (see Fig. 6.8 of Paper I). What matters most for weak lensing purposes are the 2-point statistical features of these maps; the correlation function will be investigated in § 6.3.3.3.3.

We note that these quantities are also measured on the sources drawn by our internal

---

[20] The requirement on relative size error σ_T/T (where $T = M_{xx} + M_{yy} = 2\sigma^2/(1 - g^2) \approx 2\sigma^2$) can be propagated to $\sigma_\mathrm{œ}/\sigma \sim \sigma_T/2T$.
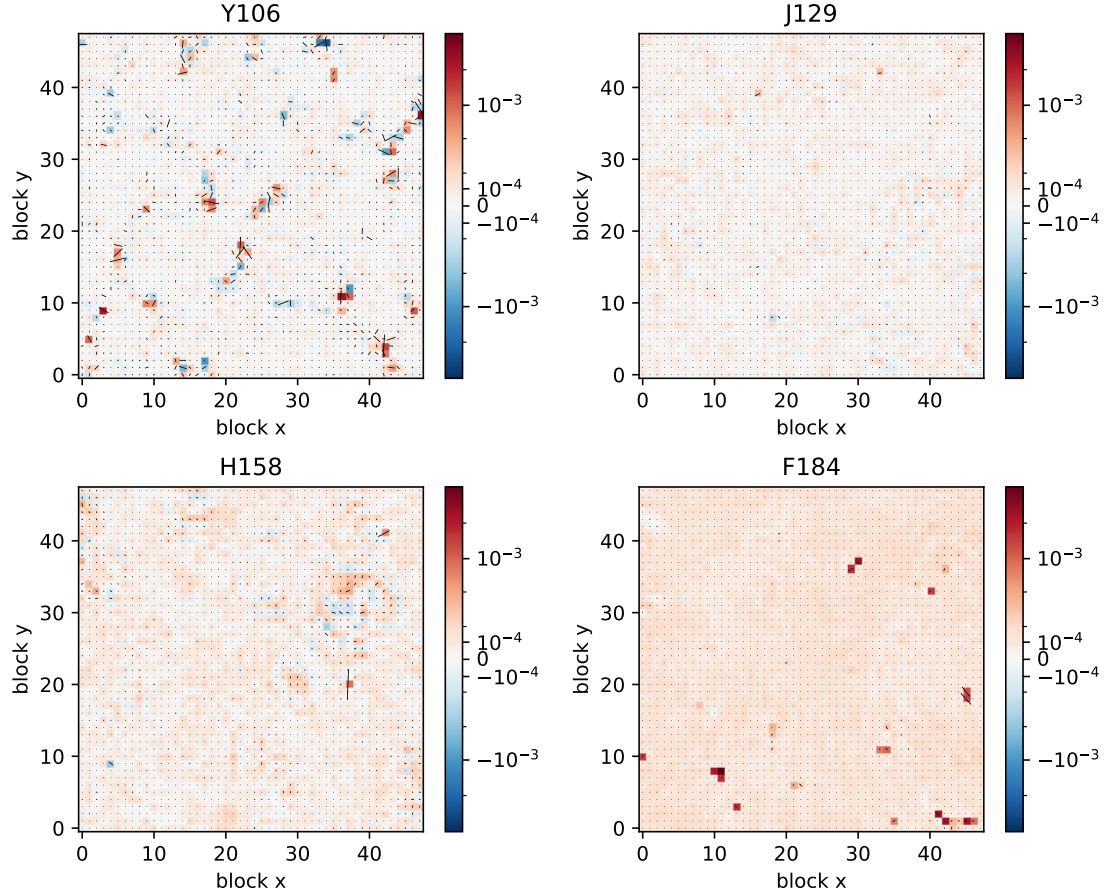
FIGURE 6.17: A spatial map of the size error (color scale) shape (whiskers) of the injected stars. Each panel shows the 48×48 arcmin footprint of the simulation in one of the 4 filters. Stars are averaged into pixels (1 arcmin² each). The color scale shows size error ($\sigma_{\text{star}}/\sigma_{\text{target}} - 1$) on an arcsinh scale, and the whiskers are scaled so that a length of 1 pixel corresponds to $g = 5 \times 10^{-4}$. This is presented on a square grid, however we have checked that the main features are also present if gridded in HEALPix and so they are not gridding artifacts.

"croutines" and we find consistent results as GALSIM sources.

6.3.3.3.2 Measurement of stars in the simulated images

For precise measurements of galaxy properties, of particular interest is the propagation of the PSF through coaddition algorithms. In principle, IMCOM tries to remove any anisotropy or inhomogeneity from the coadded PSF and coadd stars should result in being round. However, since the leakage (square norm of the difference of output and target PSF) is not exactly zero there is some residual ellipticity of the coadded stars even in the absence

of noise. Although stars in the coadded images are not utilized directly for modeling the PSF (with Imcom, the PSF determination step must be performed on single-epoch images prior to coaddition[21]), the coadded stars are an important test of PSF propagation and any ellipticity that we see at the end will have implications for galaxy measurement.

Stars are identified in the coadded sky images based on the truth locations of these stars. We use the simple simulated sky images for *Roman* simulated in Troxel et al. (2021), which utilized the LSST DESC DC2 simulations (The LSST Dark Energy Science Collaboration et al., 2021). Its stellar catalog was based on *Galfast* (JuriÄ, 2018; Jurić et al., 2008) simulations. We cut out postage stamps around the truth locations and measure the star properties using the `galsim.hsm` module (which allows the flux, centroid, and second moments to float). The truth catalog contains locations, magnitudes estimated in *Roman* bandpasses from object flux based on objects' SEDs, and whether the star is a candidate for PSF modeling. The criteria for being a candidate star defined in Troxel et al. (2023) are that:

- no pixel in the simulated star stamp is saturated in at least one exposure of the star (saturation was chosen at 10^5 e in the images with *simple* detector models); and
- the star has a detection signal-to-noise $(S/N)_{det}$ above 50, as defined by $(S/N)_{det} = 0.015 \times (\text{total flux})$, where 0.015 was the typical background inverse noise level. (The observed signal-to-noise ratio including source Poisson noise is slightly lower.)

The S/N level was chosen here to be permissive to allow more restrictive selections later. We used this criteria for selecting clean stellar samples to conduct our measurement. We additionally select stars whose magnitudes are fainter than 18 in all bandpasses since we found that some single-exposure images contained saturated stars. (In the real survey, some information might be obtained from saturated stars because the detectors are read non-destructively and the early, non-saturated reads can be used; however, it is possible that the PSF would be different since one does not average over telescope motion during the full exposure, and in any case the present simulations do not include the early reads.)

---

[21] Imcom requires PSF models for each exposure to calculate correlations between PSFs.

With these selections, we consider 2623 (Y106), 2674 (J129), 2588 (H158), 2647 (F184) stars in our simulation footprint. For each star in each of the Imcom images (**SCI** and **truth**), we cut out 99×99 output pixels postage stamps resulting in a stamp 2.475 arcsec on each side, whereas we extract 43×43 pixels around the truth centroid of a star in Drizzle images resulting in a stamp 2.473 arcsec on each side. Although the cutouts from Drizzle coadded "SCI" images (Drizzle: **SCI**) are directly comparable with those of Imcom coadded "SCI" images (Imcom: **SCI**), the measurements of stars on "truth" images are not. While we cut out postage stamps from Imcom coadded "truth" images (Imcom: **truth**), Drizzle coadded images of the "truth" layer were not simulated by Troxel et al. (2023) at the time of this project. Examples of Imcom and Drizzle images are shown in Fig. 6.18.

Compared to the measurement of injected stars (§6.3.3.3.1), the measurement on the cutout of stars is expected to contain complications that could directly affect the shape and size of an object. These complications include background and simulated-detector noise, blending, and chromaticity (since the injected sources are drawn with the same SED passed to Imcom, but the simulated stars are drawn with their "true" SEDs). The simulated stars therefore test more of the sources of systematic biases in weak lensing surveys. Some of these effects can be seen in Figure 6.19 as outliers from the stellar locus in each bandpass. Fig. 6.19 additionally displays stellar locus of the same stars in Drizzle images, which is located at a smaller size than Imcom stars. This is expected because Drizzle does not smear the PSF. However, there is a large dispersion in sizes especially in the bluer, more undersampled bands. The Drizzle algorithm is designed to preserve total flux in its "raining down" procedure (Fruchter & Hook, 2002), but the spatial spread in the output image will depend on the specific locations of the pixels. Even though the output PSF from Imcom is larger than Drizzle (especially in Y106), it is designed to be uniform: it must be large enough so that that output resolution could be achieved even in a part of the image where the pixels interlace each other differently (see Paper I, Fig. 7). The Imcom output PSF is still much smaller than ground-based PSF and the narrowness of the locus will help with star-galaxy separation in the real mission.
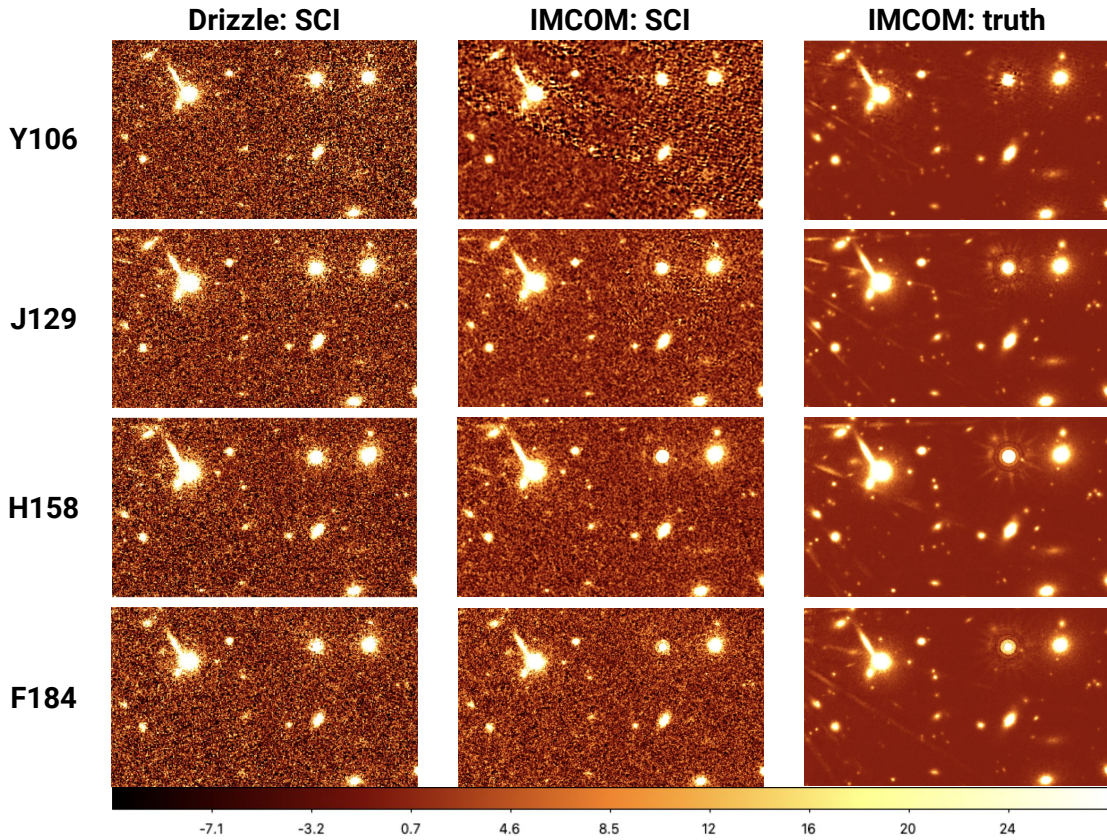
FIGURE 6.18: Coadded images of **SCI** and **truth** layers for a selected region for Y106, J129, H158 and F184 bandpasses. *Left*: DRIZZLE co-added **SCI** image, *Middle*: IMCOM co-added **SCI** image. *Right*: IMCOM co-added **truth** image. The flux in DRIZZLE images are scaled by $(0.11/0.0575)^2$ to account for the difference in the output pixel size and normalized to show the same color range. The area that is shown here is 32.7×19.2 arcsec centered around RA= 53.006 deg and Dec= -40.027. Note that this is near the center of our simulated output region.
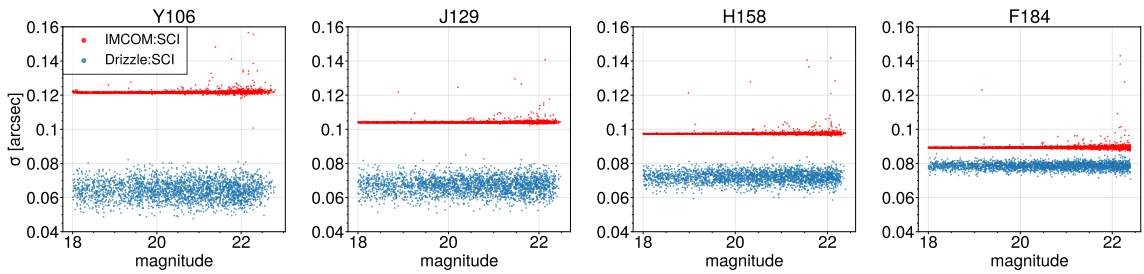
FIGURE 6.19: Size-magnitude diagram for the selected stars (mag> 18) in our simulated IMCOM and DRIZZLE images. The size of the stars is measured with the adaptive moments method (G. M. Bernstein & Jarvis, 2002). Note that IMCOM produces a larger output PSF, but it is much more uniform (see main text).
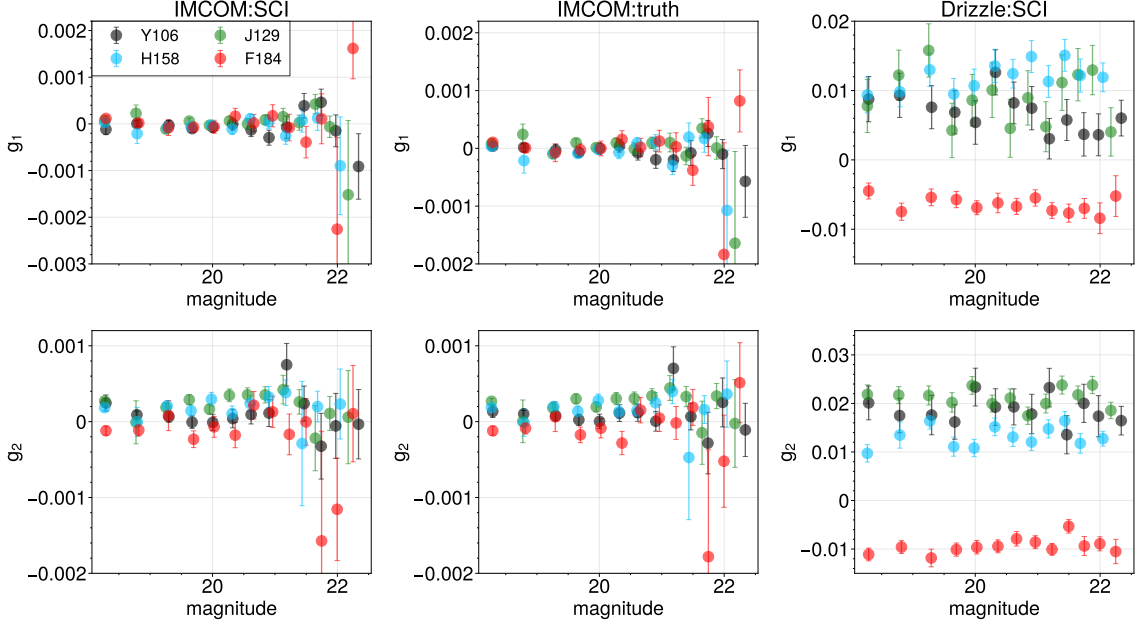
FIGURE 6.20: The mean ellipticity (g_1, g_2) of PSF candidate stars as a function of star magnitude of corresponding bandpass is shown. Four colored data points in a panel show the values from the stars found in Y106, J129, H158, F184 images. These stars were cut out from mosaics of coadded images using the coordinates from truth star catalog. The magnitude is also taken from the truth catalog. The ellipticity is measured with adaptive moments method in GALSIM and the error bar is a standard error of the mean. ***Top***: the ellipticity (g_1) from the cutouts of three sets of images (IMCOM and DRIZZLE coadded **SCI** images, IMCOM coadded **truth** images. ***Bottom***: g_2 for the same set of stars. We use the DRIZZLE images produced in Troxel et al. 2023.

Figure 6.20 shows the measured ellipticity of stars found in simulated images as a function of object magnitude. The mean ellipticity components g_1 and g_2 in IMCOM are at the level of a $\lesssim$few$\times 10^{-4}$ for all bandpasses. By comparison, the measured shapes on DRIZZLE images are consistently different from zero by an amount of order $\sim 10^{-2}$ (DRIZZLE: **SCI**). It shows that the DRIZZLE process is not able to average out the shape of PSFs, regardless of the fact that output pixel size is larger in DRIZZLE images (0.0575 arcsec/pixel) than IMCOM (0.025 arcsec/pixel) and pixel size does have an effect on the measured PSF ellipticity (Fig. E1 of Troxel et al. 2021).

Figure 6.21 shows the residual ellipticity measured on the cutouts of stars from "SCI" and "truth" images, and the ellipticity compared to the target PSF for IMCOM (which in this case is only different from zero due to numerical precision). The difference between "SCI"
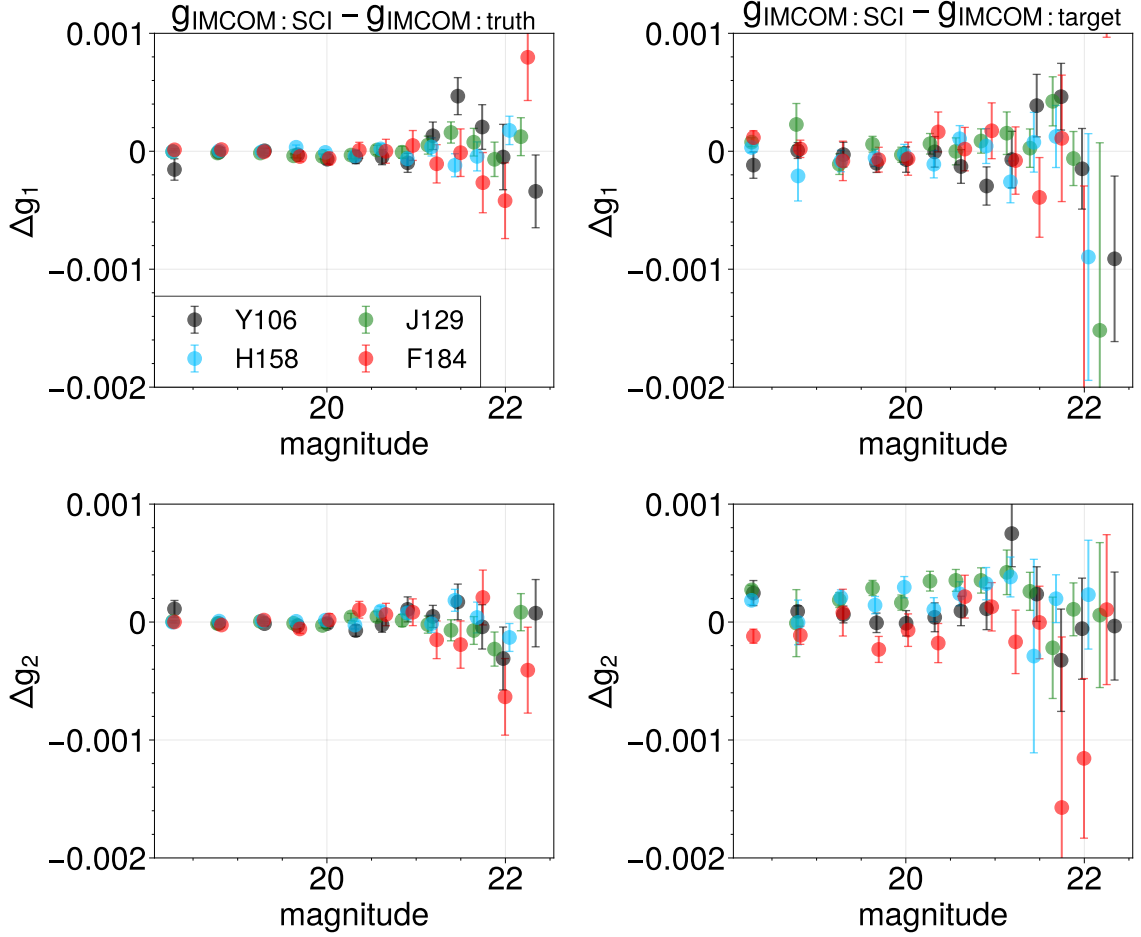
FIGURE 6.21: The residual ellipticity (g_1: ***Top***, g_2: ***Bottom***) of the stars extracted from several layers of simulated images is presented. ***Left***: the difference in the shapes from IMCOM coadded **SCI** and **truth** images. This shows the effect of simple noise models on the ellipticity as **SCI** images include them and **truth** images do not. ***Right***: the difference in the shapes from the IMCOM coadded **SCI** images and target PSF we chose in our IMCOM simulations. This shows the cumulative effect of noise in sky images and output PSF fidelity.

and "truth" shows the residual shape introduced by the simple detector physics noise model (which includes dark current, saturation, and read and Poisson noise). Here, the average residual ellipticity is $\lesssim 2 \times 10^{-4}$ for bright stars and $\lesssim 8 \times 10^{-4}$ for faint stars, verifying that IMCOM shows a tolerance to simple noise models on star shapes. We also investigated whether achieving the target fidelity can affect star shapes of different magnitudes. The right column of Fig. 6.21 that shows the cumulative effect of noise and fidelity indicates that for g_1 the residual behavior is consistent with the simple noise model case (top left

panel of the same figure) whereas Δg_2 shows a non-zero residual ellipticity over a range of magnitude. Although this is likely caused by the output PSF that did not exactly match the target, the leakage into star shapes is less than the PSF ellipticity error requirement.

Additionally, we have estimated the magnitudes of the stars from the total image intensity for best-fit elliptical Gaussian in GALSIM. These magnitudes are estimated on the stars of both IMCOM and DRIZZLE "SCI" images. Figure 6.22 shows the relative error of the measured magnitude compared to the truth for each filter. It is estimated from the photon flux in the following way. The measured number of photons (N_{star}) can be used to measure the magnitudes of the stars, using

$$ m_{AB} = -2.5 \log_{10} \frac{N_{star}}{N_{zero\ point}} - m_{correct}, \tag{6.13} $$

where $N_{zero\ point}$ is the number of photons that *Roman* would observe for a 0 AB magnitude source (Oke & Gunn, 1983) and $m_{correct}$ is an aperture correction term to account for the fluxes in the wings of stars, because the diffraction wings of the PSF are not captured by the best-fit Gaussian; thus the HSM fluxes are less than the "total" (integrated to ∞) fluxes. We compute the zero point based on the model throughput curve of *Roman* that was used in the simulation:

$$ N_{zero\ point} = \int (3.631 \times 10^{-23}\,\mathrm{W\,m^{-2}\,Hz^{-1}}) A_{eff}(\lambda) t_{obs} \frac{\mathrm{d}\nu}{h\nu}, \tag{6.14} $$

where A_{eff} is the effective collecting area of the telescope for a given bandpass, $t_{obs} = 139.8\,\mathrm{s}$ is the exposure time, and $h\nu$ is the energy of photons (where h is Planck's constant). The effective collecting area for a given bandpass can be integrated over the bandpass[22], and $\int (A_{eff}/\lambda)\mathrm{d}\lambda = 0.5915, 0.6051, 0.5978, 0.3929\,\mathrm{m^2}$ for Y106, J129, H158, and F184 respectively. We then correct for $m_{correct}$ by measuring the flux and magnitude on the target PSF for each bandpass; the corrections are 0.0977, 0.1471, 0.2180, 0.3018 mag for Y106, J129, H158, and F184 respectively.

---

[22] https://roman.gsfc.nasa.gov/science/WFI_technical.html Our effective area is calculated using the values from early design phase to be internally consistent with the area used in Troxel et al., 2023 simulations.
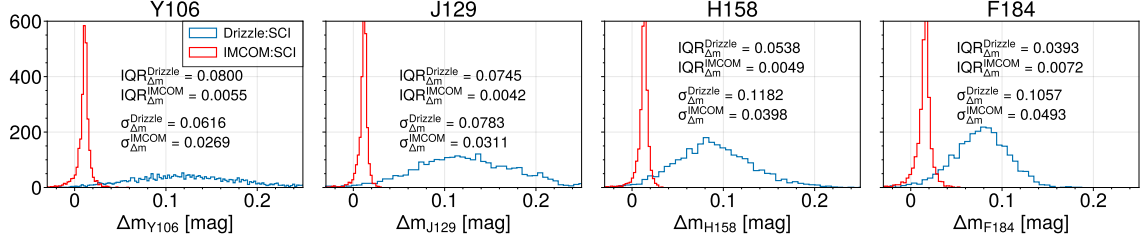
FIGURE 6.22: The deviation of measured magnitudes of the stars in DRIZZLE and IMCOM images from the magnitudes from the truth catalog for all the bandpasses is shown. The magnitude of the stars is estimated from the flux measurement using `galsim.hsm`. Since the flux units in GALSIM are photons/cm^2/s, we multiply the flux measured on IMCOM star cutouts by $(0.025/0.11)^2$ to obtain flux from surface brightness. There is no need for this scaling for DRIZZLE cutouts because DRIZZLE operates on fluxes rather than surface brightnesses. The number of photons is then converted to the AB magnitude through Eq. (6.13). The texts in each panel display the interquartile range (IQR) to indicate the spread that is unaffected by outliers, and the standard deviation of the sample.

Since we specify the target PSF in IMCOM to be the Airy disk convolved with the Gaussian kernel, the adaptive moments method captures the fluxes from these stars quite well. Their RMS residual magnitudes are 28, 32, 41, 51 mmag in Y/J/H/F band whereas the SRD states relative photometric calibration in each filter to be better than 10 mmag. We should note that this measurement includes neighboring fluxes from nearby sources (which are *not* included in the SRD requirement) and stars with low fidelity (outliers in Fig. 6.19). A visual inspection of outliers from the size-magnitude diagram in Y106 showed that most are due to leaking flux from neighboring objects (not necessarily fully blended). For the adaptive moment magnitudes measured on DRIZZLE images, on the other hand, as the dispersion in the difference suggests, the coadded PSF obtained through DRIZZLE is not uniform across our footprint and the magnitude measurement is not reliable in the strongly undersampled case (Y106). (We note that DRIZZLE preserves *total flux* by construction; but the fraction of the flux captured by the adaptive moment method depends on the PSF.) Even for the weakly undersampled cases, the mean of the residual magnitude is one order of magnitude worse than the IMCOM case.

In this section, we have only explored the moments on single-band images; the moments measured on multi-band (synthetic wide-band) images will be analyzed in § 6.3.3.4.

6.3.3.3.3 Correlation functions of stars in various outputs

We have so far looked at one-point statistics of observed properties of stars in the coadded images of various input layers. In the end, however, it is crucial to verify that systematic biases related to undersampling and the image reconstruction process do not contaminate the cosmological signal (e.g., Fig. 12 of Troxel et al., 2023 for their estimated $\xi_\pm$ over 20 deg^2 simulated sky). We approach this by measuring two-point statistics, especially shape-shape correlations of these stars. The calculations of two-point correlation functions were performed using the publicly available TreeCorr package (Jarvis et al., 2004).

In Fig. 6.23, we measure shape-shape correlations (ξ_+) of observed stars in Imcom coadded injected stars and "SCI" layers, and in Drizzle coadded "SCI" image. We also show a simple comparison of these star shape correlations to *Roman* PSF mitigation requirements. Here we compute the approximate requirement on ξ_+ from the requirements on additive errors in SRD in each angular multipole moment bin. We rewrite the Hankel transform of angular power spectra C_ℓ as a Riemann sum (Givans et al., 2022):

$$\xi_+ = \int_0^\infty \frac{\ell \, d\ell}{2\pi} J_0(\ell\theta)(C_{EE}(\ell) + C_{BB}(\ell))$$

$$\approx \sum_{\ell \text{ bins}} 2\gamma^2 \langle J_0(\ell\theta) \rangle, \tag{6.15}$$

where J_0 is the Bessel function of first kind. It is clear here that the shape correlations of Imcom coadded stars are at a statistically acceptable level compared to the requirement. The most idealized case is shown as the correlations of injected stars, drawn with exactly the same input PSF given to Imcom: here any deviations of the measured shapes from isotropy and homogeneity can be attributed to the algorithm itself. We confirm that the level of correlations is two orders of magnitude smaller than the estimated systematic requirement. As can be seen in Fig. 6.23, disparities exist between ξ_+ on Imcom: **SCI** and Imcom: **injected stars** since the stars drawn in the noiseless injected source layer are isolated and the PSFs are made with a flat SED, while the stars drawn in Troxel et al. (2023) are fully chromatic. We should note that we do not expect the measurement using Drizzle stars to be consistent

with zero since DRIZZLE does not attempt to smooth the output PSF to be isotropic.

It is worth mentioning that the ξ_+ presented here is the contamination solely from star or PSF shapes — error contributions from residual PSF shape/size errors and shape measurement are not included. We consider the shapes of the injected stars as e_{PSF} and those of stars in sky image as e_{star}. Typically we characterize the additive shear systematics as the following in terms of observed shear, PSF modeling errors and noise:

$$\gamma^{\text{obs}} = \gamma^{\text{true}} + \delta e_{\text{PSF}}^{\text{sys}} + \delta e_{\text{noise}}; \tag{6.16}$$

here $\delta e_{\text{PSF}}^{\text{sys}}$ (additive shear systematic biases due to PSF modeling) can be decomposed into

$$\delta e_{\text{PSF}}^{\text{sys}} = \alpha e_{\text{PSF}} + \beta(e_{\text{star}} - e_{\text{PSF}}) + \eta(e_{\text{star}} \frac{T_{\text{star}} - T_{\text{PSF}}}{T_{\text{star}}}) \tag{6.17}$$

following Paulin-Henriksson et al. (2009) and Jarvis et al. (2016). Our test in this section only quantifies the contribution to e_{PSF} from residuals in the image combination process, but not the coefficients α, β, and η. This will be investigated in a future paper. We will, however, quantify the contribution to the observed shear due to additive noise biases (δe_{noise}) in § 6.3.3.3.5.

Fig. 6.23 additionally demonstrates the tangential shear around the positions of simulated (in the "SCI" image) stars and the injected stars. While we expect these signals to be zero given that we have not put large scale structure in the position catalog and they seem to be below the additive shear error requirement (only in $2.0 < \log_{10} \ell < 2.5$ due to the relevant scale of galaxy-galaxy lensing), γ_{t} signal around injected stars might be underestimated because the angular distance between sources is discrete.

6.3.3.3.4 Correlations of fourth moments

In addition to the PSF second moments, T. Zhang, Almoubayyed, et al., 2023 demonstrated that the correlation function of the spin-2 components of the PSF higher moments (e.g., fourth moment) can cause shear additive bias to cosmic shear correlation function, contingent on the shear estimation method used in the analysis. We measure the standard-

216
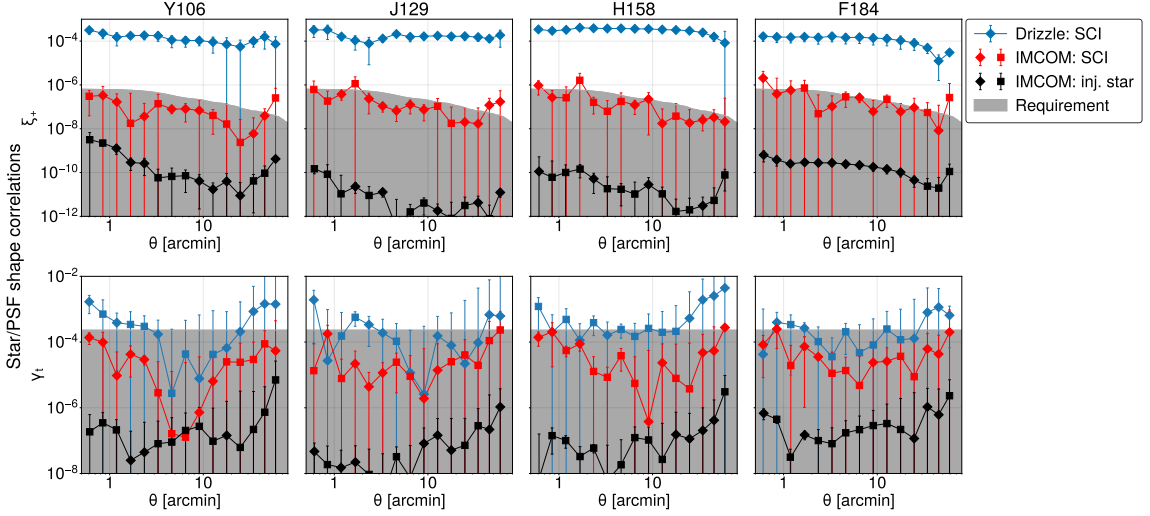
FIGURE 6.23: **Top**: Auto-correlation (ξ_+) of observed star ellipticity from various coadded images. This includes DRIZZLE and IMCOM images with simple detector noise models (see § 2 for detailed explanation), and GALSIM-drawn injected stars from IMCOM images. The ellipticity was measured with adaptive moments. Dark grey shaded region shows the required ξ_+ signal approximated with the requirements on additive shear errors from SRD. Each panel displays the signals corresponding to each bandpass, and "diamond" marker is the positive signal while "square" is the negative signal but taken absolute value. **Bottom**: Cross-correlation of the sky coordinates and the observed ellipticity of the same sources. Readers may refer to Fig. 6.17 for the residual ellipticity around the positions where there are fewer dither positions.

ized higher moments defined in T. Zhang, Li, et al., 2023,

$$M_{pq} = \frac{\int \mathrm{d}x \, \mathrm{d}y \, u^p \, v^q \, \omega(x, y) \, I(x, y)}{\int \mathrm{d}x \, \mathrm{d}y \, \omega(x, y) \, I(x, y)}. \tag{6.18}$$

Here the (u, v) are transformed coordinates from the image coordinate (x, y), such that the second moment shapes in Eq. (6.12) vanish, and the second moment size in Eq. (6.11) is normalized to 1; p and q are the integer moment indices. For fourth moments, $p + q = 4$. Here $\omega(x, y) = e^{-x \cdot \mathbf{M}^{-1} x / 2}$ is the adaptive weight function given by HSM (C. Hirata & Seljak, 2003), and $I(x, y)$ is the image of the PSF. The complex spin-2 fourth moment is defined as

$$M_{\mathrm{PSF}}^{(4)} = M_{40} - M_{04} + 2\mathrm{i}(M_{31} + M_{13}). \tag{6.19}$$

In Figure 6.24, we show the correlation function $\xi_\pm$ of the PSF fourth moments, measured on the coadded image of the injected stars drawn from the GALSIM routine. This is
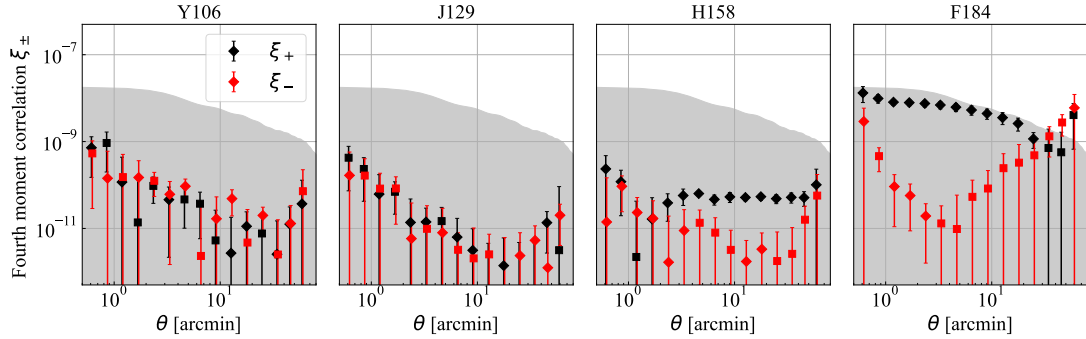
FIGURE 6.24: Auto-correlation ($\xi_\pm$) of the fourth moment spin-2 components ($M_{\mathrm{PSF}}^{(4)}$), measured by the injected stars drawn from the GALSIM routine. Each panel displays the signals corresponding to each bandpass, and "diamond" marker is the positive signal while "square" is the negative signal but taken absolute value. The grey-shaded region shows the requirement on the fourth moment ξ_+, computed from the SRD and the assumption that the fourth moment leakage will be 6-times larger than that of second moments. The PSF fourth moments correlation functions are safely within the requirement for Y106, J129, and H158 band, and are on par with the requirement for the F184 band.

presented with an approximated requirement for the fourth moments correlation function from the SRD, by assuming the fourth moment leakage factor $\alpha^{(2)}$ is 6 times larger than the second moment leakage factor (α in Eq. 6.17). This decision is supported by the results of T. Zhang, Li, et al., 2023. The fourth moment correlation function of the injected stars are safely within the requirement for the Y106, J129, and H158 band, showing that the higher moments of the anisotropy of the IMCOM PSF will not cause significant additive bias in these bands. However, the correlation functions in F184 are only slightly below the requirement for the most angular range and are above the requirement (though not by a statistically significant amount) for the largest scales. This indicates that the PSF fourth moments could potentially contaminate the real cosmological signal in F184. In fact, the fourth moments correlation function is ~ 3 order-of-magnitude larger than the second moment correlation in terms of signal-to-requirement fraction, mainly because IMCOM PSFs have extremely low large-scale coherence in the second moment shapes, which is not necessarily the same for the fourth moments.

This result suggests that the PSF fourth moments should be actively monitored in the *Roman* HLIS cosmological analysis. Further work is however required for investigat-

ing the leakage of PSF fourth moments into the galaxy shape for the *Roman* HLIS, by cross-correlating the galaxy shape with the star moments (characterization of the α, β, η coefficients in Eq. 6.17). A larger-area simulation will also be valuable here for better understanding the leakage at scales larger than 60 arcmin.

6.3.3.3.5 Estimation of additive noise bias

A concern with measuring shapes on a coadded image is that noise correlations can result in a bias in the shape measurement even if the PSF has been made round and is exactly known (G. M. Bernstein & Jarvis, 2002; Gurvich & Mandelbaum, 2016; Herbonnet et al., 2017; C. M. Hirata et al., 2004; Kaiser et al., 2000; Mandelbaum et al., 2015; Melchior & Viola, 2012; Okura & Futamase, 2018; Refregier et al., 2012). For example, if there are noise correlations in the x-direction, then there are different centroid uncertainties in the x and y directions; this propagates into different biases in object moments $\langle x^2 \rangle$ and $\langle y^2 \rangle$, and hence a bias in the ellipticity g_1. There are in fact a number of such terms, each resulting from the fact that the ellipticity is a non-linear function of the data, and leading overall to a bias proportional to ν^{-2} where ν is the detection significance (see, e.g., the detailed discussion in G. M. Bernstein and Jarvis 2002, §8.2). This results in the *additive noise bias*; the aforementioned leading terms result from the second derivative of the measured shape with respect to the input image, and so we refer to it as the "second-order" additive noise bias. (There are third-order and higher terms as well.) A more detailed treatment will be presented in a future paper; here our aim is a first look at the second-order noise bias of the ellipticities of injected stars.

One may construct a Monte Carlo estimate of the additive bias as follows:

$$\Delta g = \frac{1}{2} \sum_{\alpha\beta} \frac{\partial^2 g}{\partial I_\alpha \, \partial I_\beta} \mathrm{Cov}(I_\alpha, I_\beta)$$

$$\approx \left\langle A \left[\frac{g(I + \epsilon N) + g(I - \epsilon N)}{2} - g(I) \right] \right\rangle, \tag{6.20}$$

where I is the image of the object; N is a noise image; A and ϵ are scaling factors; and the $\langle \rangle$ denotes an average over the Monte Carlo noise realizations. If the shape measurement

of the object is performed on a coadded image, then I should be the coadded image and N should be a coadded noise realization (and thus includes any correlations imprinted by the coaddition procedure).

If the object image is normalized to have unit flux, and N is normalized to be a noise image with unit input variance per input pixel, then the proper scaling is

$$A\epsilon^2|_{\text{white noise}} = \frac{1}{\nu_{\text{SE}}^2 \Omega_{\text{psf}}/s_{\text{in}}^2},$$ (6.21)

where ν_{SE} is the single-epoch signal-to-noise ratio and $\Omega_{\text{psf}}/s_{\text{in}}^2$ is the input PSF effective area in pixels (shown in Table 4 of Paper I). Then Eq. (6.20) returns an estimate of the second-order additive noise bias. In principle, the use of multiple Monte Carlo realizations of the noise should allow us to reduce the uncertainty in Eq. (6.20). But even a single realization is unbiased and can be used in a correlation function code such as TreeCorr to estimate the additive noise bias correlation function.

There may also be noise bias from the input $1/f$ noise. Typically the $1/f$ noise is specified by a "knee frequency" f_{knee} (with the pixels time-ordered, so units of Hz) where the $1/f$ noise power spectrum is equal to the white noise component power spectrum. For readout, the 4096×4096 pixel arrays used by Roman split into 32 channels of 4096 rows and 128 columns each. The pixels in each row are read out with a cadence of 5 μs; after all the pixels in one row are read out, we move to the next row (so the time to read each row is $128 \times 5 = 640\,\mu$s plus overheads). This pattern is shown in, e.g., Fig. 2 of Freudenburg et al. (2020), and maps $1/f$ noise into a "banding" pattern (Fig. 3 of Paper I). Since our input $1/f$ noise fields are normalized to unit variance per logarithmic range in f, the appropriate normalization for the $1/f$ noise fields is

$$A\epsilon^2|_{1/f \text{ noise}} = \frac{1}{\nu_{\text{SE}}^2 \Omega_{\text{psf}}/s_{\text{in}}^2} \frac{f_{\text{knee}}}{\Delta f_{\text{band}}} \frac{\sigma_{\text{read}}^2}{\sigma_{\text{tot}}^2},$$ (6.22)

where Δf_{band} is the bandwidth for the white noise (equal to half the sampling rate, so 100 kHz for Roman); and $\sigma_{\text{read}}^2/\sigma_{\text{tot}}^2$ is the fraction of the noise variance coming from read noise

(as opposed to Poisson noise).

For both types of noise, we first attempted to mesure at single-epoch signal-to-noise ratio $\nu_{\mathrm{SE}} = 10$; if the shape measurement did not converge (see Table 6.7 for statistics on how often this happened) then we computed $A\epsilon^2$ using $\nu_{\mathrm{SE}} = 10^{1.5} = 31.6$.

We report the noise-induced additive bias (c_1, c_2) for different noise models applied on the noise-less shapes of the GALSIM-made injected stars in Table 6.7. As can be seen, the magnitude of additive biases surpasses the total additive systematic budget of 2.7×10^{-4} according to the SRD. Furthermore, we correlated Δg (which is the effect of noise in object ellipticity), and as can be seen in Fig. 6.25 noise-induced additive bias does show correlations over many scales. Hence, in the future, there will be a need to correct for these noise biases with a more comprehensive set of noise images if IMCOM is used for image processing for *Roman*. Possible correction schemes range from numerical approaches based on shearing a noise field (as done in METACALIBRATION; E. S. Sheldon and Huff 2017); subtraction based on second derivatives of the weighted shape estimator (Li & Mandelbaum, 2023); or using analytic models such as Appendix A of Paper II (presumably allowing the overall normalization to be empirically determined, as suggested in G. M. Bernstein and Jarvis 2002). It may be best in a cosmology analysis to implement more than one of these approaches as an internal check. It is clear that for the current set of IMCOM settings, the noise-induced biases are larger than residual PSF biases, suggesting that we might benefit from tuning the balance between leakage and noise in the future.

We also show in Table 6.7 the additive noise biases predicted by second-order biasing theory for Gaussian model objects Eq. (B26), derived in Appendix B of Paper II. (Note that all radii and power spectra must be scaled to the output pixel scale s_{out} in order to use that result.) The predicted biases are in the correct direction where significant and have approximately the right magnitude (the two largest biases in the table are greater than the prediction by 20% and 37%, although only the latter is statistically significant). The remaining discrepancy may be due to the assumption of a Gaussian profile used in the analytic bias prediction.

Table 6.7: The mean values of the noise-induced additive bias (c_1 and c_2) for various input noise models and bandpasses. These are normalized to single-epoch signal-to-noise ratio $\nu_{SE} = 10$ and knee frequency $f_{knee} = 1\,kHz$, and are before any mitigations. (A very small fraction of objects was assigned $\nu_{SE} = 31.6$ (if `galsim.hsm` did not converge for $\nu_{SE} = 10$) and re-normalized to $\nu_{SE} = 10$. These are shown in the table and are out of 54 597 stars in total.) The errors calculated here are the standard error of the mean. The last two columns show predicted bias according to the formulae in Appendix A of Paper II and the measured noise power spectra from Section 6.3.3.2.

Noise models	Bands	Measured bias		Number with	Predicted bias	
		$c_1 \times 10^4$	$c_2 \times 10^4$	$\nu_{SE} = 31.6$	$c_1 \times 10^4$	$c_2 \times 10^4$
white noise	Y106	5.44 ± 1.33	-6.02 ± 1.25	867	4.77	-5.01
white noise	J129	-0.81 ± 0.42	-3.10 ± 0.40	40	-0.81	-1.89
white noise	H158	1.24 ± 0.30	-0.59 ± 0.30	29	0.40	-0.51
white noise	F184	1.14 ± 0.46	0.71 ± 0.46	21	0.26	0.80
$1/f$ noise	Y106	7.68 ± 0.38	1.42 ± 0.38	44	5.62	0.62
$1/f$ noise	J129	3.80 ± 0.15	0.78 ± 0.08	15	2.34	0.54
$1/f$ noise	H158	2.87 ± 0.10	0.16 ± 0.06	9	1.49	0.11
$1/f$ noise	F184	-2.19 ± 0.08	-0.56 ± 0.08	9	-1.10	-0.26
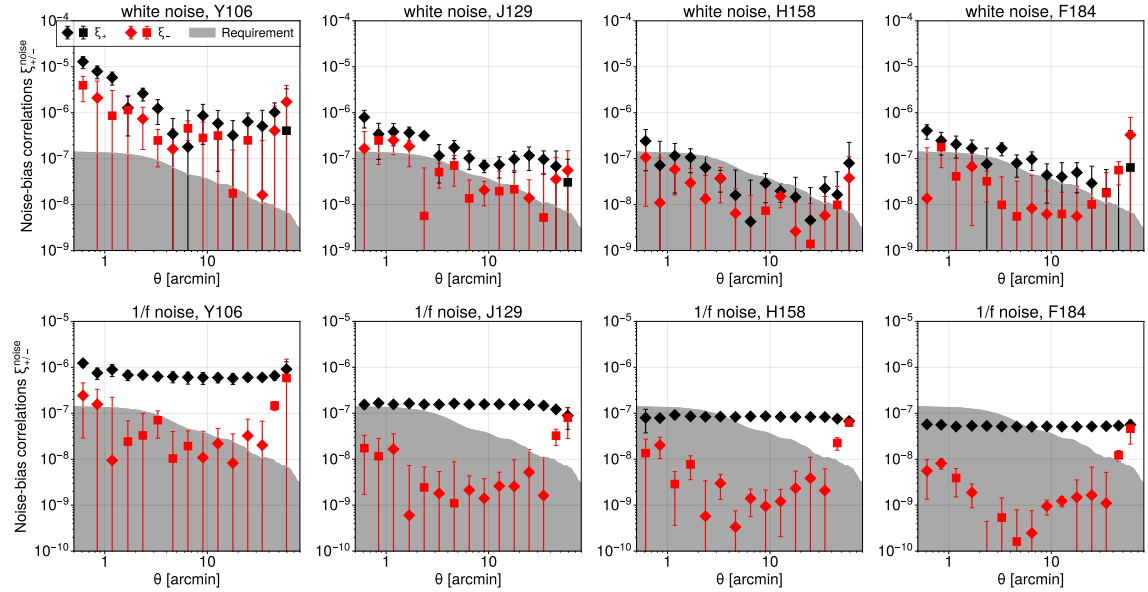
FIGURE 6.25: Auto-correlations of the noise bias (Δg) estimated with white noise (**top**) and 1/f (**bottom**) noise models for all the four bandpasses are shown. "diamond" marker is the positive signal while "square" is the negative signal but taken absolute value. These are normalized to single-epoch signal-to-noise ratio $\nu_{SE} = 10$ and (for the $1/f$ noise case) a knee frequency of $f_{knee} = 1\,kHz$. Note that white noise biases generally scale as $\propto 1/\nu_{SE}^2$ and $1/f$ noise biases scale as $\propto f_{knee}/\nu_{SE}^2$; this means that their correlation functions scale as $\propto 1/\nu_{SE}^4$ and $\propto f_{knee}^2/\nu_{SE}^4$, respectively. These are the "raw" biases, with no attempt at mitigation.

6.3.3.4 Synthetic wide band images

Synthetic wide band images, created by stacking several standard-width filters, are often used as an intermediate product in weak lensing analyses (e.g., $r+i+z$ in DES (DES Collaboration et al., 2018, 2021)). They can be used for making a deep detection image, or as a reference for forced photometry in individual filters for photometric redshifts. (This could include filters on other observatories, e.g., Vera Rubin Observatory data if one were to make a Y106+J129+H158+F184 image with *Roman.*) One could also make a shape catalog from the combined Y106+J129+H158+F184 imaging; such a catalog would have the advantages of providing a deeper catalog and reducing noise biases,[23] but the disadvantage that with only one catalog using all the data one can only measure a shape auto-correlation (we would not have the option of cross-correlating two different versions of the shape catalog from different data). It is also possible that one would use both the single-band and the synthetic wide band shape catalogs to test for different systematics — for example, the individual bands allow for cross-correlations to test for PSF systematics associated with the tiling pattern (which is different in each filter; D. Spergel et al. 2015), but the wide-band image has lower noise bias.

We have built a set of wide band images in post-processing as follows. First, the output images in each filter a are smoothed to a common output PSF $\Gamma_{\rm out}$ by convolving with a kernel K_a. Ideally, we want the coadd PSF Γ_a convolved with this kernel to be the output PSF, $\Gamma_a \otimes K_a \approx \Gamma_{\rm out}$; in practice, we do this by writing

$$\tilde{K}_a(\boldsymbol{u}) = \frac{\tilde{\Gamma}_a^*(\boldsymbol{u})\tilde{\Gamma}_{\rm out}(\boldsymbol{u})}{|\tilde{\Gamma}_{\rm out}(\boldsymbol{u})|^2 + \epsilon^2}. \tag{6.23}$$

Without the ϵ term, this kernel would exactly transform the PSF Γ_a into $\Gamma_{\rm out}$; but we set $\epsilon = 10^{-4}$ in the denominator to avoid division by a near-zero quantity. The kernel is clipped to a 201×201 output pixel region. We choose the output PSF $\Gamma_{\rm out}$ to be an Airy disc

---

[23] Noise biases usually scale as ν^{-2}, where ν is the significance; so if one were to average N exposures and then measure the ellipticity of a galaxy, the noise bias is a factor of N smaller than if one measures the ellipticity in each exposure and takes the average. The calculation gets somewhat more complicated if one is considering different filters with different ν, but the result that noise bias is reduced in the combined image should hold for most galaxy SEDs.

convolved with a Gaussian as in Paper I; the Airy disc parameters are $\lambda/D = 0.112$ arcsec (the size for J129), obscuration 0.31, and the Gaussian has a scale length of $\sigma = 0.1051$ arcsec (the largest of the Gaussian widths used in Paper I). The full width at half maximum of this output PSF is 0.287 arc§

Next, the images are added with some weights:

$$H_{\text{out}}(x, y) = \sum_a w_a C_a \sum_{\Delta x, \Delta y} K_a(\Delta x, \Delta y) H_a(x - \Delta x, y - \Delta y), \tag{6.24}$$

where H_a is the input image in band a, and H_{out} is the output image. The normalization factors C_a convert the input units (electrons per s_{in}^2 per exposure) into surface brightness units (μJy s_{out}^{-2}, or μJy per output pixel) using the effective area curves provided by the *Roman* project.[24] The weights (summing to $\sum_a w_a = 1$) are proportional to the inverse square depths given by Akeson et al. (2019): 0.294, 0.323, 0.294, and 0.089 for the Y106, J129, H158, and F184 bands respectively. Examples of the synthetic wide images are shown in Fig. 6.26.

These images are then used again to extract stars to measure their properties, especially the two-point correlation functions. We measure the centroids and shapes of the stars using adaptive moments, and Figure 6.27 shows their shape-shape and shape-position correlation functions. Although these signals suggest that the star ellipticity correlations are within the requirement defined in SRD, we do not see an improvement in removing the residual contamination compared to the cases with individual bandpasses shown in Fig. 6.23.

6.3.3.5 Summary and Discussion

In this paper, we have analyzed the coadded images that are produced in Paper I. The layers that were simulated in Paper I include the *simulated sky image* produced in Troxel et al. (2023), the *injected point sources* (δ-function convolved with *Roman* PSF), and two types of *noise fields* (white noise and 1/f noise). We have measured the following statistics on these images that are relevant to better characterize the weak lensing shear systematics:

---

[24] https://roman.gsfc.nasa.gov/science/RRI/Roman_effarea_20210614.xlsx

"simple" "truth"

center at (515,1590)

center at (725,400)

-0.0001 0.00029 0.0011 0.0027 0.0059 0.012 0.025 0.05 0.1

μ Jy s_{out}^{-2}
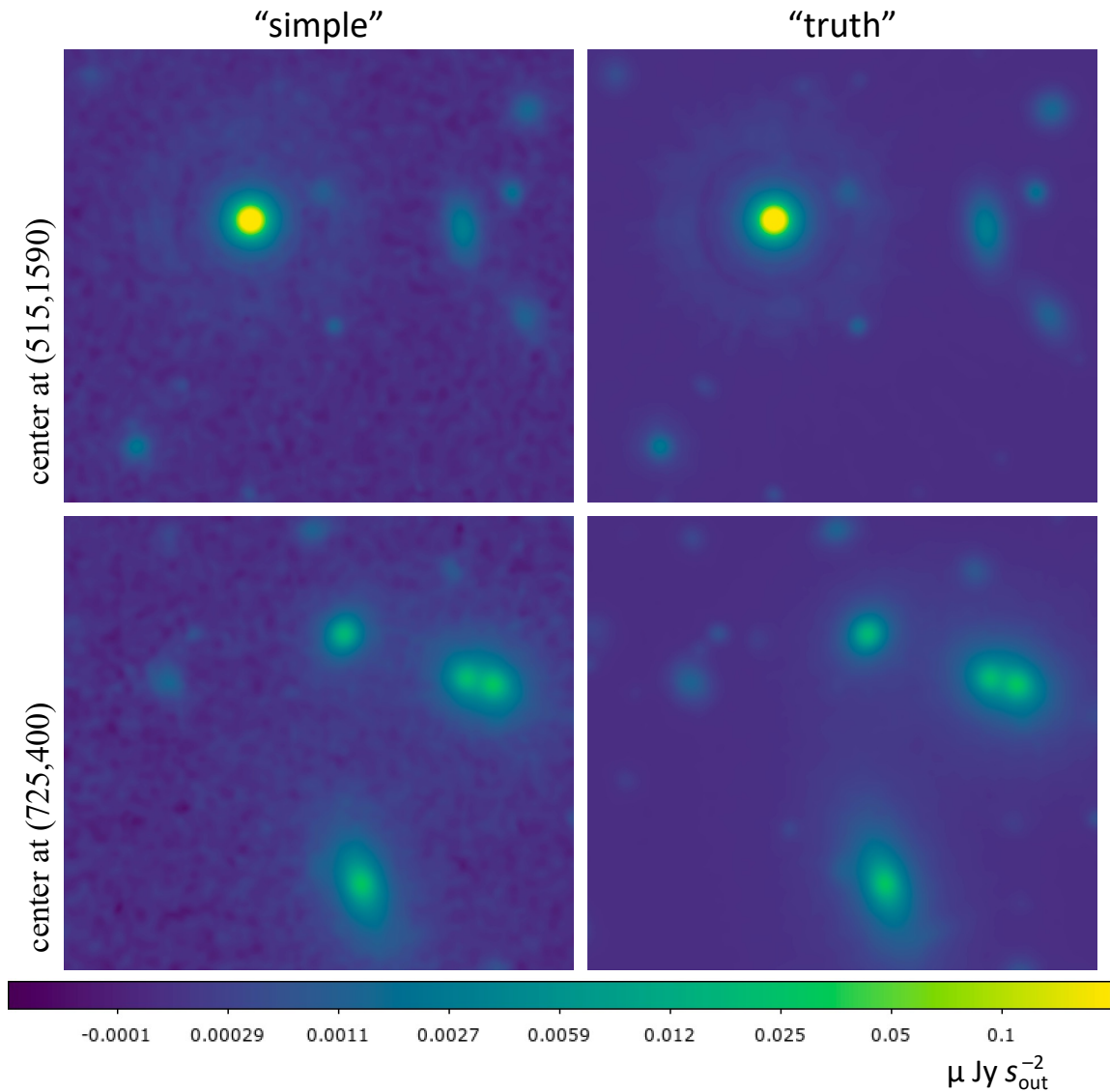
FIGURE 6.26: Two examples of fields in the synthetic wide band images (§ 6.3.3.4), from block (0,14). The left column shows the "simple" detector model, the right column shows "truth" (the noiseless image). The top row contains a bright star that saturates on the color scale (reaching 0.90 μJy s_{out}^{-2} at its center), with a log stretch to show the wings of the output PSF. Both images show a 450×400 output pixel (11.25×10 arcsec) region.
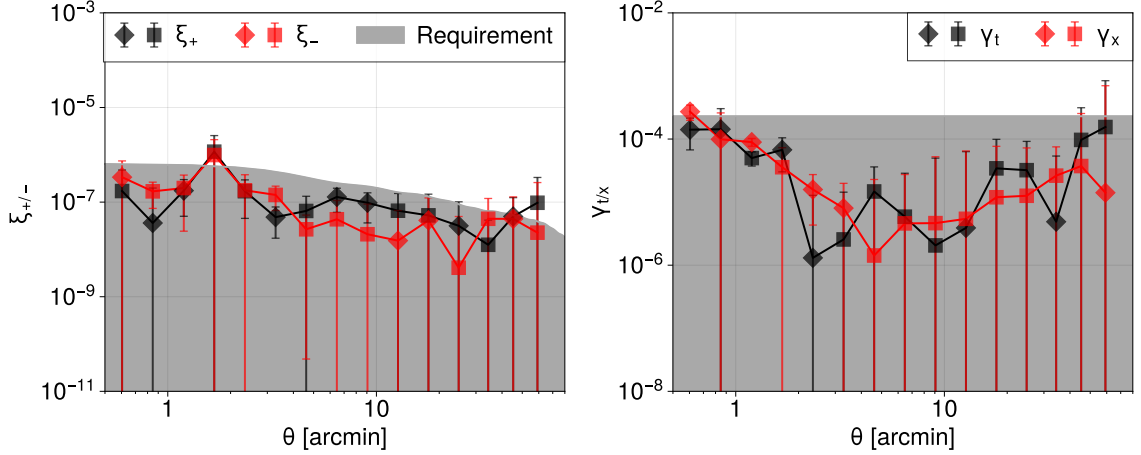
FIGURE 6.27: Shape-shape (**Left**) and shape-position (**Right**) correlation functions of stars observed in the synthetic wide band images. The grey region shows the estimated requirement on the signals from the PSF ellipticity additive error requirement in the SRD. "diamond" marker is the positive signal while "square" is the negative signal but taken absolute value.

- the power spectra of coadded white noise and $1/f$ noise, as measured in the output images;

- one point statistics of magnitude, astrometric error, 2nd moments (shape and size), and 4th order moments of the injected stars (an idealized case with no blending or chromaticity effects) and stars in the coadded sky image; and

- two-point statistics (shape-shape $\xi_{\pm}$ and position-shape $\gamma_{t/x}$) of shapes and/or positions of the same sources.

If *Roman* images are to be processed using IMCOM, it is essential to understand the implications of noise biasing on measurements of galaxy shapes. Noise power spectra are directly involved in the calculation of shape measurement bias (Appendix A of Paper II), so we first investigated the power spectra of the coadded white and $1/f$ noise fields. In both cases, the noise power spectra of the coadded images decline to zero beyond $\sim$ 5–6 cycles arcsec^{-1}, depending on the band. Specific features in the 2-dimensional and azimuthally averaged 1-dimensional power spectra indicate correlations in the noise fields that will impact shape measurements. We find that the most prominent features in the noise power spectra come from: band limits on the output PSFs, input image pixel positions, and the

postage stamp boundaries and angular size. By comparing with analytic models of the expected 1-dimensional power spectra for well-sampled images (following derivations found in Appendix A of Paper II), we recover some of the expected qualitative features, but the noise power spectra are generally above the simple expectation. This highlights the importance of using full simulations of the image processing steps to predict the output noise and associated biases, rather than using simple formulae appropriate for well-sampled data. Each filter performs slightly differently, with the increase in power spectrum relative to the simplistic expectation being worst in Y106. This is unsurprising since it has the worst coverage and sampling of all the filters (see Paper I for further discussion of coverage regions).

We have additionally presented the average astrometric offset from input catalog positions and the shape and size deviation from target PSF measured on injected stars (coadded PSF), and compared them to the PSF requirements documented in the *Roman* SRD. We have shown (Fig. 6.16) that they are well within the requirements in a root-mean-square sense in the four bandpasses in the Reference survey design (Y106, J129, H158, F184). The Imcom algorithm, although much more computationally expensive, has yielded large gains in output PSF quality relative to the current "industry standard" for combining space images (Drizzle).

Since what matters to weak lensing studies in the end is the level of contamination each systematic effect has in shape correlations, we have measured two-point correlation functions of shapes (2nd moments: Fig. 6.23) of the injected and simulated (sky image) stars and 4th order moments (Fig. 6.24) of injected stars. While the PSF shape-shape correlations are well below the mission requirement for all the bandpasses, the 4th moment-4th moment correlations in F184 is on the verge of falling short (other 4th moment correlations are not of concern).

We finally investigated the additive bias imprinted on the shapes of the injected stars by both white and $1/f$ noise in the input images, by adding the appropriate noise fields in and re-measuring the shapes. We find biases that exceed *Roman* requirements when scaled

to signal-to-noise ratio per observation $\nu_{SE} = 10$, indicating that noise bias will have to be corrected in *Roman* analyses (as is already planned for *Roman* and other weak lensing projects). Appendix B of Paper II develops an analytic model for the noise bias, which we find is in agreement with the observed trends.

While this set of simulations represents a major step toward use of the Imcom algorithm to the *Roman* weak lensing program, there are several more studies that should be carried out prior to implementation in an operational pipeline. These include:

1. *Computational efficiency*: The existing implementation is computationally expensive, and would require $\sim 10^9$ CPU-hours to run on the full baseline HLIS survey if there were no speed-ups, whereas Drizzle would require $\sim 10^5$ CPU hours (extrapolated from the implementation in Troxel et al. 2023). On the algorithm side, one could investigate optimizing postage stamp and padding parameters (see Paper I), or re-arranging the linear algebra operations in Imcom if we can search over a limited range in the Lagrange multiplier κ.[25] On the hardware/firmware side, one could make use of ongoing advances in graphics processing unit-accelerated linear algebra.

2. *Extended source injection*: The tests with injected stars in this paper used point sources since these are a "stress test" for undersampling effects. However, we also want to implement grids of extended sources so that we can test Metacalibration (E. Huff & Mandelbaum, 2017; E. S. Sheldon & Huff, 2017) or analytic differentiation (Li & Mandelbaum, 2023) techniques wrapped around an algorithm that operates on an Imcom coadd.

3. *Error propagation*: We would like to study propagation of astrometric errors, relative flux calibration between images, and PSF model errors through the image coaddition pipeline. This will involve the insertion of specialized layers with these types of errors injected.

---

[25] The variable κ is the Lagrange multiplier that controls the relative weighting of leakage and noise in the optimization of the coaddition matrix **T**; see Rowe et al. (2011). In particular, with a limited range one could avoid the expensive eigendecomposition step in favor of matrix inversions.

4. *Laboratory noise fields*: The analysis of the laboratory noise fields from this project, and an assessment of their implications for additive noise bias, is ongoing. Additional noise fields from the focal plane level and Wide Field Instrument level tests will be incorporated as they become available.

5. *Poisson noise bias corrections*: While IMCOM coaddition is a linear operation on the input pixels, shape measurement algorithms are non-linear operations on the data and hence are subject to noise biases. The current implementation allows one to coadd simulated noise relatizations, and therefore one can generate simulated output noise, as needed by tools such as Deep Metacalibration (Z. Zhang et al., 2023).[26] Such realizations would also allow a Monte Carlo evaluation of the noise bias terms in twice-differentiable shape measurement algorithms (e.g., Li, Li, and Massey 2022; Li and Mandelbaum 2023). The performance of the method has not been tested on simulations with source Poisson noise. But further work will be needed to address biases arising from self-Poisson noise of the source galaxies (e.g., Appendix D of Li & Mandelbaum, 2023).

6. *Chromatic effects*: When running image combination in mosaic mode, one has to choose a "reference" intraband SED in order to have a well-defined PSF, but of course the sources in the field have a range of SEDs. Chromatic terms in the PSF will arise from diffraction, dispersion in the filter substrate, chromatic wavefront from mirror, filter, and detector coatings, and depth-dependent absorption effects in the detectors (Mosby et al., 2020). Additionally, there is a field-dependent filter bandpass due to angle of incidence effects, which results in objects redder than the reference SED having a normalization that is larger for input exposures near the field center and smaller for input exposures near the corners of the field. We plan to test how these chromatic effects propagate through IMCOM and assess how they should be corrected.

7. *Deep fields*: Like other weak lensing surveys, the *Roman* HLIS requires deep fields for

---

[26] Note that Deep Metacalibration explicitly avoids the need to apply a shear to a "wide survey" noise field.

photo-z, selection, and noise bias calibration. Some shear calibration algorithms also require deep fields (Z. Zhang et al., 2023). The Imcom algorithm will run on deep fields, but since the current version has $O(n^3)$ (where n is the number of input pixels), a deep survey with 10 as many exposures but only 1% of the area of the wide survey actually requires $10^3 \times 0.01 = 10$ times as many operations to run Imcom as the wide survey if done by brute force. One solution to mitigate this is to coadd subsets of the deep field exposures to obtain full sampling at a common PSF, and then do a pixel-by-pixel coadd, but other options should be investigated for feasibility and performance. Another opportunity for the deep fields, since the observations include large dithers, would be to mitigate field-dependent bandpass effects. This would involve extending the linear algebra formalism in Rowe et al. (2011) to simultaneously reconstruct both an image through the "mean" bandpass in each filter and a "first principal component" (PC1) bandpass.[27]

8. *Other survey strategies*: The Reference survey strategy was developed to support hardware trades for the *Roman* mission, and the actual survey design may be different (see, e.g., Eifler et al. 2021 for one proposal). Simulations similar to those in this series of papers should be carried out for the possible alternative survey designs to ensure the data will be usable.

This is the Accepted Manuscript version of an article for publication in Monthly Notices of the Royal Astronomical Society. IOP Publishing Ltd is not responsible for any errors or omissions in this version of the manuscript or any version derived from it. The version of Record is available online at the following doi: 10.1093/mnras/stae182 and 10.1093/mnras/stae177.

---

[27] Mathematically, this would involve turning the optical transfer function $\tilde{G}_i(\boldsymbol{u})$ into a length 2 vector for the sensitivity to the mean and PC1 bandpasses. The **A** and **B** matrices would involve dot products of these vectors as well as integrals over the Fourier plane.

7

Conclusion

This is a remarkable time for cosmology in the history of astronomy and physics. With exceptional technologies to observe the Universe, we are witnessing a paradigm shift in how we understand nature and the Universe. Since the early 20th century, we have been discovering more evidence of unknown matter and energy – dark matter and dark energy, which cannot yet be fully described by the fundamental theory of particle physics. While the standard cosmological model, which incorporates dark matter and dark energy, explains the observational evidence of the history and structure of the Universe very well, it is not complete due to "tensions" in the model that is derived from different cosmological probes.

In this thesis, we have pedagogically reviewed the fundamental principles and intricate methodologies of observational cosmology. A significant focus was placed on the theory and practice of weak gravitational lensing, discussing how cosmic shear serves as a powerful cosmological probe through its sensitivity to the matter distribution in the Universe. Because of its subtle effect, however, measuring the cosmic shear signal is extremely challenging, and the results can be easily misleading without accounting for various systematics. The practical applications of the effort to measure this were examined in the context of the Dark Energy Survey Year-6, highlighting the capabilities and innovations brought forth by the

DES Collaboration. We navigated through the complexities of producing the catalogs of galaxy shear and redshift alongside the effort to measure cosmological parameters with cosmic shear. With the implementation of an image processing pipeline that is also intended for future surveys such as LSST, my work resulted in a more accurate measurement of galaxy shapes (competitive with the LSST mission requirement) and produced the largest weak lensing shape catalog to date, achieving more than 150 million galaxy shapes (Yamamoto et al. in prep.). We are currently progressing toward inferring the cosmological parameters from the two-point correlation of galaxy shapes in the catalog and eventually from the "3x2pt" analysis, greatly enhancing the constraining power of the clustering amplitude.

As we finish up with DES data, we must prepare for the Stage-IV surveys, such as Rubin's LSST and Roman's HLIS, which require more stringent systematics control. We have delved into the challenges associated with weak lensing and measuring cosmic shear from space-based telescopes. One of the main challenges is that individual images will be undersampled. Current weak lensing analysis tools rely on the fact that images are properly sampled. To demonstrate, I applied a shear calibration tool I use in current surveys and showed that the shear calibration bias cannot be mitigated without properly treating the under-sampled images (Yamamoto et al., 2023). This result motivated us to reconstruct well-sampled images from under-sampled images simulated for Roman with IMage COMbination (IMCOM). We have demonstrated in Hirata, Yamamoto, et al., 2024 the feasibility of the methodology and succeeded in achieving well-characterized PSF, which is essential in accomplishing precision cosmology with Roman. Yamamoto et al., 2024 has further proved that this technique only uses a small portion of the error budget for shear calibration bias.

While there need to be further efforts to enable weak lensing science and maximize the scientific return with Roman and LSST, my Ph.D. research constitutes an essential step without which Roman and LSST weak lensing science may fall short of realizing its full potential. When future surveys begin acquiring an unprecedented amount and quality of data, we will be ready to explore the nature of dark matter and dark energy. New data

will expand our boundaries of knowledge and technological prowess, and they will test the robustness of our current understanding of the Universe – Λ-CDM model.

Bibliography

Abazajian, K. N., Adshead, P., Ahmed, Z., Allen, S. W., Alonso, D., Arnold, K. S., Baccigalupi, C., Bartlett, J. G., Battaglia, N., Benson, B. A., Bischoff, C. A., Borrill, J., Buza, V., Calabrese, E., Caldwell, R., Carlstrom, J. E., Chang, C. L., Crawford, T. M., Cyr-Racine, F.-Y., . . . Kimmy Wu, W. L. (2016). CMB-S4 Science Book, First Edition. *arXiv e-prints*, arXiv:1610.02743. https://doi.org/10.48550/arXiv.1610.02743

Abbott, T., Abdalla, F. B., Allam, S., Amara, A., Annis, J., Armstrong, R., Bacon, D., Banerji, M., Bauer, A. H., Baxter, E., Becker, M. R., Benoit-Lévy, A., Bernstein, R. A., Bernstein, G. M., Bertin, E., Blazek, J., Bonnett, C., Bridle, S. L., Brooks, D., . . . Dark Energy Survey Collaboration. (2016). Cosmology from cosmic shear with Dark Energy Survey Science Verification data. \\prd, *94*(2), 022001. https://doi.org/10.1103/PhysRevD.94.022001

Abdalla, E., Abellán, G. F., Aboubrahim, A., Agnello, A., Akarsu, Ö., Akrami, Y., Alestas, G., Aloni, D., Amendola, L., Anchordoqui, L. A., Anderson, R. I., Arendse, N., Asgari, M., Ballardini, M., Barger, V., Basilakos, S., Batista, R. C., Battistelli, E. S., Battye, R., . . . Zumalacárregui, M. (2022). Cosmology intertwined: A review of the particle physics, astrophysics, and cosmology associated with the cosmological tensions and anomalies. *Journal of High Energy Astrophysics*, *34*, 49–211. https://doi.org/10.1016/j.jheap.2022.04.002

Ade, P., Aguirre, J., Ahmed, Z., Aiola, S., Ali, A., Alonso, D., Alvarez, M. A., Arnold, K., Ashton, P., Austermann, J., Awan, H., Baccigalupi, C., Baildon, T., Barron, D., Battaglia, N., Battye, R., Baxter, E., Bazarko, A., Beall, J. A., . . . Simons Observatory Collaboration. (2019). The Simons Observatory: Science goals and forecasts. \\jcap, *2019*(2), 056. https://doi.org/10.1088/1475-7516/2019/02/056

Aihara, H., Arimoto, N., Armstrong, R., Arnouts, S., Bahcall, N. A., Bickerton, S., Bosch, J., Bundy, K., Capak, P. L., Chan, J. H. H., Chiba, M., Coupon, J., Egami, E., Enoki, M., Finet, F., Fujimori, H., Fujimoto, S., Furusawa, H., Furusawa, J., . . . Yuma, S. (2018). The Hyper Suprime-Cam SSP Survey: Overview and survey design. \\pasj, *70*, S4. https://doi.org/10.1093/pasj/psx066

Akeson, R., Armus, L., Bachelet, E., Bailey, V., Bartusek, L., Bellini, A., Benford, D., Bennett, D., Bhattacharya, A., Bohlin, R., Boyer, M., Bozza, V., Bryden, G., Calchi Novati, S., Carpenter, K., Casertano, S., Choi, A., Content, D., Dayal, P., . . . Zimmerman, N. (2019, February). The Wide Field Infrared Survey Telescope: 100 Hubbles for the 2020s. https:

//doi.org/10.48550/arXiv.1902.05569
ADS Bibcode: 2019arXiv190205569A.

Albrecht, A., Bernstein, G., Cahn, R., Freedman, W. L., Hewitt, J., Hu, W., Huth, J., Kamionkowski, M., Kolb, E. W., Knox, L., Mather, J. C., Staggs, S., & Suntzeff, N. B. (2006). Report of the Dark Energy Task Force. *arXiv e-prints*, astro–ph/0609591. https://doi.org/10.48550/arXiv.astro-ph/0609591

Albrecht, A., & Steinhardt, P. J. (1982). Cosmology for Grand Unified Theories with Radiatively Induced Symmetry Breaking. *Phys. Rev. Lett.*, *48*(17), 1220–1223. https://doi.org/10.1103/PhysRevLett.48.1220

Alonso, D., Sanchez, J., Slosar, A., & LSST Dark Energy Science Collaboration. (2019). A unified pseudo-Cℓ framework. *Monthly Notices of the Royal Astronomical Society*, *484*, 4127–4151. https://doi.org/10.1093/mnras/stz093
ADS Bibcode: 2019MNRAS.484.4127A.

Amon, A., Gruen, D., Troxel, M. A., MacCrann, N., Dodelson, S., Choi, A., Doux, C., Secco, L. F., Samuroff, S., Krause, E., Cordero, J., Myles, J., DeRose, J., Wechsler, R. H., Gatti, M., Navarro-Alsina, A., Bernstein, G. M., Jain, B., Blazek, J., . . . Weller, J. (2022). Dark Energy Survey Year 3 Results: Cosmology from Cosmic Shear and Robustness to Data Calibration. *Phys. Rev. D*, *105*(2), 023514. https://doi.org/10.1103/PhysRevD.105.023514

Anderson, J., & King, I. R. (2000). Toward High-Precision Astrometry with WFPC2. I. Deriving an Accurate Point-Spread Function. *Publications of the Astronomical Society of the Pacific*, *112*, 1360–1382. https://doi.org/10.1086/316632
ADS Bibcode: 2000PASP..112.1360A.

Angulo, R. E., Zennaro, M., Contreras, S., Aricò, G., Pellejero-Ibañez, M., & Stücker, J. (2021). The BACCO simulation project: Exploiting the full power of large-scale structure for cosmology. *Monthly Notices of the Royal Astronomical Society*, *507*, 5869–5881. https://doi.org/10.1093/mnras/stab2018
ADS Bibcode: 2021MNRAS.507.5869A.

Antilogus, P., Astier, P., Doherty, P., Guyonnet, A., & Regnault, N. (2014). The brighter-fatter effect and pixel correlations in CCD sensors. *J. Inst.*, *9*(03), C03048–C03048. https://doi.org/10.1088/1748-0221/9/03/C03048

Aricò, G., Angulo, R. E., Contreras, S., Ondaro-Mallea, L., Pellejero-Ibañez, M., & Zennaro, M. (2021). The BACCO simulation project: A baryonification emulator with neural networks. *Monthly Notices of the Royal Astronomical Society*, *506*, 4070–4082. https://doi.org/10.1093/mnras/stab1911
ADS Bibcode: 2021MNRAS.506.4070A.

Aricò, G., Angulo, R. E., Zennaro, M., Contreras, S., Chen, A., & Hernández-Monteagudo, C. (2023). DES Y3 cosmic shear down to small scales: Constraints on cosmology and baryons. *A&A*, *678*, A109. https://doi.org/10.1051/0004-6361/202346539

Armstrong, R., Sheldon, E., Huff, E., Bosch, J., Rykoff, E., Mandelbaum, R., Kannawadi, A., Melchior, P., Lupton, R., Becker, M. R., Al-Sayyed, Y., & Collaboration, T. L. D. E. S. (2024, July). The little coadd that could: Estimating shear from coadded images. https://doi.org/10.48550/arXiv.2407.01771

Asgari, M., Mead, A. J., & Heymans, C. (2023). The halo model for cosmology: A pedagogical review. *TheOJA*, *6*, 10.21105/astro.2303.08752. https://doi.org/10.21105/astro.2303.08752

Aubourg, É., Bailey, S., Bautista, J. E., Beutler, F., Bhardwaj, V., Bizyaev, D., Blanton, M., Blomqvist, M., Bolton, A. S., Bovy, J., Brewington, H., Brinkmann, J., Brownstein, J. R., Burden, A., Busca, N. G., Carithers, W., Chuang, C.-H., Comparat, J., Croft, R. A. C., ... BOSS Collaboration. (2015). Cosmological implications of baryon acoustic oscillation measurements. \prd, *92*(12), 123516. https://doi.org/10.1103/PhysRevD.92.123516

Bacon, D. J., Refregier, A., Clowe, D., & Ellis, R. S. (2001). Numerical simulations of weak lensing measurements. *Monthly Notices of the Royal Astronomical Society*, *325*(3), 1065–1074. https://doi.org/10.1046/j.1365-8711.2001.04507.x

Bacon, D. J., Refregier, A. R., & Ellis, R. S. (2000). Detection of weak gravitational lensing by large-scale structure. \mnras, *318*(2), 625–640. https://doi.org/10.1046/j.1365-8711.2000.03851.x

Bartelmann, M., & Schneider, P. (2001). Weak Gravitational Lensing. *Physics Reports*, *340*(4-5), 291–472. https://doi.org/10.1016/S0370-1573(00)00082-X

Baumann, D. (2022). *Cosmology*. Cambridge University Press.

Baumann, D., Jackson, M. G., Adshead, P., Amblard, A., Ashoorioon, A., Bartolo, N., Bean, R., Beltrán, M., de Bernardis, F., Bird, S., Chen, X., Chung, D. J. H., Colombo, L., Cooray, A., Creminelli, P., Dodelson, S., Dunkley, J., Dvorkin, C., Easther, R., ... Zaldarriaga, M. (2009, June). Probing Inflation with CMB Polarization. In S. Dodelson, D. Baumann, A. Cooray, J. Dunkley, A. Fraisse, M. G. Jackson, A. Kogut, L. Krauss, M. Zaldarriaga, & K. Smith (Eds.), *CMB Polarization Workshop: Theory and Foregrounds: CMBPol Mission Concept Study* (pp. 10–120, Vol. 1141). https://doi.org/10.1063/1.3160885

Becker, M. R., Troxel, M. A., MacCrann, N., Krause, E., Eifler, T. F., Friedrich, O., Nicola, A., Refregier, A., Amara, A., Bacon, D., Bernstein, G. M., Bonnett, C., Bridle, S. L., Busha, M. T., Chang, C., Dodelson, S., Erickson, B., Evrard, A. E., Frieman, J., ... Collaboration, T. D. (2016). Cosmic Shear Measurements with DES Science Verification Data. *Phys. Rev. D*, *94*(2), 022002. https://doi.org/10.1103/PhysRevD.94.022002

Becker, M. R. (2013). Cosmic shear E/B-mode estimation with binned correlation function data. *Monthly Notices of the Royal Astronomical Society*, *435*, 1547–1562. https://doi.org/10.1093/mnras/stt1396
ADS Bibcode: 2013MNRAS.435.1547B.

Becker, M. R., & Rozo, E. (2016). Fourier band-power E/B-mode estimators for cosmic shear. *Monthly Notices of the Royal Astronomical Society*, *457*, 304–312. https://doi.org/10.1093/mnras/stv3018
ADS Bibcode: 2016MNRAS.457..304B.

Benítez, N. (2000). Bayesian Photometric Redshift Estimation. *The Astrophysical Journal*, *536*, 571–583. https://doi.org/10.1086/308947
ADS Bibcode: 2000ApJ...536..571B.

Bennett, C. L., Banday, A. J., Gorski, K. M., Hinshaw, G., Jackson, P., Keegstra, P., Kogut, A., Smoot, G. F., Wilkinson, D. T., & Wright, E. L. (1996). Four-Year COBE DMR Cosmic Microwave Background Observations: Maps and Basic Results. \apjl, *464*, L1. https://doi.org/10.1086/310075

Bernstein, G. M., Armstrong, R., Plazas, A. A., Walker, A. R., Abbott, T. M. C., Allam, S., Bechtol, K., Benoit-Lévy, A., Brooks, D., Burke, D. L., Rosell, A. C., Kind, M. C., Carretero, J., Cunha, C. E., Costa, L. N. D., DePoy, D. L., Desai, S., Diehl, H. T., Eifler, T. F., ... DES Collaboration. (2017). Astrometric Calibration and Performance of the Dark Energy Camera. *PASP*, *129*(977), 074503. https://doi.org/10.1088/1538-3873/aa6c55

Bernstein, G. M., & Jarvis, M. (2002). Shapes and Shears, Stars and Smears: Optimal Measurements for Weak Lensing. *The Astronomical Journal*, *123*, 583–618. https://doi.org/10.1086/338085
ADS Bibcode: 2002AJ....123..583B.

Bernstein, G. (2002). Advanced Exposure-Time Calculations: Undersampling, Dithering, Cosmic Rays, Astrometry, and Ellipticities. *PASP*, *114*(791), 98. https://doi.org/10.1086/337997

Bernstein, G. M. (2010). Shape measurement biases from underfitting and ellipticity gradients. *Monthly Notices of the Royal Astronomical Society*, *406*(4), 2793–2804. https://doi.org/10.1111/j.1365-2966.2010.16883.x

Bernstein, G. M., & Armstrong, R. (2014). Bayesian lensing shear measurement. *Monthly Notices of the Royal Astronomical Society*, *438*, 1880–1893. https://doi.org/10.1093/mnras/stt2326
ADS Bibcode: 2014MNRAS.438.1880B.

Bernstein, G. M., Armstrong, R., Krawiec, C., & March, M. C. (2016). An accurate and practical method for inference of weak gravitational lensing from galaxy images. *Monthly Notices of the Royal Astronomical Society*, *459*(4), 4467–4484. https://doi.org/10.1093/mnras/stw879

Bertin, E. (2006). Automatic Astrometric and Photometric Calibration with SCAMP. *351*, 112
ADS Bibcode: 2006ASPC..351..112B.

Bertin, E. (2011). Automated Morphometry with SExtractor and PSFEx. *442*, 435
ADS Bibcode: 2011ASPC..442..435B.

Bertin, E., & Arnouts, S. (1996). SExtractor: Software for source extraction. *Astronomy and Astrophysics Supplement Series*, *117*, 393–404. https://doi.org/10.1051/aas:1996164
ADS Bibcode: 1996A&AS..117..393B.

Bertin, E. (2010). SWarp: Resampling and Co-adding FITS Images Together. *Astrophysics Source Code Library*, ascl:1010.068
ADS Bibcode: 2010ascl.soft10068B.

Bisnovatyi-Kogan, G. S., & Tsupko, O. Y. (2017). Gravitational Lensing in Presence of Plasma: Strong Lens Systems, Black Hole Lensing and Shadow. *Universe*, *3*(3), 57. https://doi.org/10.3390/universe3030057

Blazek, J., MacCrann, N., Troxel, M. A., & Fang, X. (2019). Beyond linear galaxy alignments. *Phys. Rev. D*, *100*(10), 103506. https://doi.org/10.1103/PhysRevD.100.103506

Bond, J. R., & Szalay, A. S. (1983). The collisionless damping of density fluctuations in an expanding universe. \apj, *274*, 443–468. https://doi.org/10.1086/161460

Bosch, J., Armstrong, R., Bickerton, S., Furusawa, H., Ikeda, H., Koike, M., Lupton, R., Mineo, S., Price, P., Takata, T., Tanaka, M., Yasuda, N., AlSayyad, Y., Becker, A. C., Coulton, W., Coupon, J., Garmilla, J., Huang, S., Krughoff, K. S., . . . Yamanoi, H. (2018). The Hyper Suprime-Cam software pipeline. *Publications of the Astronomical Society of Japan*, *70*(SP1), S5. https://doi.org/10.1093/pasj/psx080

Brainerd, T. G., Blandford, R. D., & Smail, I. (1996). Weak Gravitational Lensing by Galaxies. \apj, *466*, 623. https://doi.org/10.1086/177537

Brammer, G., Koekemoer, A. M., & Kiziltan, B. (2003, January). *Using MultiDrizzle to combine Dithered WFPC2 Images*.
ADS Bibcode: 2003hstc.conf..325B.

Bridle, S., & King, L. (2007). Dark energy constraints from cosmic shear power spectra: Impact of intrinsic alignments on photometric redshift requirements. *New J. Phys.*, *9*(12), 444–444. https://doi.org/10.1088/1367-2630/9/12/444

Bridle, S., Shawe-Taylor, J., Amara, A., Applegate, D., Balan, B., Joel, S. T., Bernstein, G., Dahle, H., Erben, T., Gill, M., Heavens, A., Heymans, C., High, F. W., Hoekstra, H., Jarvis, M., Kirk, D., Kitching, T., Kneib, J.-P., Kuijken, K., . . . Wittman, D. (2009). Handbook for the GREAT08 Challenge: An image analysis competition for cosmological lensing. *Annals of*

Applied Statistics, *3*, 6–37. https://doi.org/10.1214/08-AOAS222
ADS Bibcode: 2009AnApS...3....6B.

Brout, D., Scolnic, D., Popovic, B., Riess, A. G., Carr, A., Zuntz, J., Kessler, R., Davis, T. M., Hinton, S., Jones, D., Kenworthy, W. D., Peterson, E. R., Said, K., Taylor, G., Ali, N., Armstrong, P., Charvu, P., Dwomoh, A., Meldorf, C., . . . Wiseman, P. (2022). The Pantheon+ Analysis: Cosmological Constraints. \apj, *938*(2), 110. https://doi.org/10.3847/1538-4357/ac8e04

Buchs, R., Davis, C., Gruen, D., DeRose, J., Alarcon, A., Bernstein, G. M., Sánchez, C., Myles, J., Roodman, A., Allen, S., Amon, A., Choi, A., Masters, D. C., Miquel, R., Troxel, M. A., Wechsler, R. H., Abbott, T. M. C., Annis, J., Avila, S., . . . Vikram, V. (2019). Phenotypic redshifts with self-organizing maps: A novel method to characterize redshift distributions of source galaxies for weak lensing. *Monthly Notices of the Royal Astronomical Society*, *489*(1), 820–841. https://doi.org/10.1093/mnras/stz2162

Burke, D. L., Rykoff, E. S., Allam, S., Annis, J., Bechtol, K., Bernstein, G. M., Drlica-Wagner, A., Finley, D. A., Gruendl, R. A., James, D. J., Kent, S., Kessler, R., Kuhlmann, S., Lasker, J., Li, T. S., Scolnic, D., Smith, J., Tucker, D. L., Wester, W., . . . DES Collaboration. (2018). Forward Global Photometric Calibration of the Dark Energy Survey. *The Astronomical Journal*, *155*, 41. https://doi.org/10.3847/1538-3881/aa9f22
ADS Bibcode: 2018AJ....155...41B.

Campos, A., Samuroff, S., & Mandelbaum, R. (2023). An empirical approach to model selection: Weak lensing and intrinsic alignments. *Monthly Notices of the Royal Astronomical Society*, *525*(2), 1885–1901. https://doi.org/10.1093/mnras/stad2213

Carlstrom, J. E., Holder, G. P., & Reese, E. D. (2002). Cosmology with the Sunyaev-Zel'dovich Effect. \araa, *40*, 643–680. https://doi.org/10.1146/annurev.astro.40.060401.093803

Carroll, S. M. (2019). *Spacetime and Geometry: An Introduction to General Relativity*. Cambridge University Press.

Casey, K. J., Greco, J. P., Peter, A. H. G., & Davis, A. B. (2023). Discovery of a red backsplash galaxy candidate near M81. *Monthly Notices of the Royal Astronomical Society*, *520*(3), 4715–4729. https://doi.org/10.1093/mnras/stad352

Chabanier, S., Millea, M., & Palanque-Delabrouille, N. (2019). Matter power spectrum: From Ly \ensuremath\alpha forest to CMB scales. \mnras, *489*(2), 2247–2253. https://doi.org/10.1093/mnras/stz2310

Chang, C., Jarvis, M., Jain, B., Kahn, S. M., Kirkby, D., Connolly, A., Krughoff, S., Peng, E. .-., & Peterson, J. R. (2013). The effective number density of galaxies for weak lensing measurements in the LSST project. *Monthly Notices of the Royal Astronomical Society*, *434*, 2121–2135. https://doi.org/10.1093/mnras/stt1156
ADS Bibcode: 2013MNRAS.434.2121C.

Chisari, N. E., Codis, S., Laigle, C., Dubois, Y., Pichon, C., Devriendt, J., Slyz, A., Miller, L., Gavazzi, R., & Benabed, K. (2015). Intrinsic alignments of galaxies in the Horizon-AGN cosmological hydrodynamical simulation. *Mon. Not. R. Astron. Soc.*, *454*(3), 2736–2753. https://doi.org/10.1093/mnras/stv2154

Chisari, N. E., Mead, A. J., Joudaki, S., Ferreira, P., Schneider, A., Mohr, J., Tröster, T., Alonso, D., McCarthy, I. G., Martin-Alvarez, S., Devriendt, J., Slyz, A., & van Daalen, M. P. (2019). Modelling baryonic feedback for survey cosmology. *TheOJA*, *2*(1), 10.21105/astro.1905.06082. https://doi.org/10.21105/astro.1905.06082

Coulton, W. R., Armstrong, R., Smith, K. M., Lupton, R. H., & Spergel, D. N. (2018). Exploring the Brighter-fatter Effect with the Hyper Suprime-Cam. *AJ*, *155*(6), 258. https://doi.org/10.3847/1538-3881/aac08d

Cropper, M., Hoekstra, H., Kitching, T., Massey, R., Amiaux, J., Miller, L., Mellier, Y., Rhodes, J., Rowe, B., Pires, S., Saxton, C., & Scaramella, R. (2013). Defining a weak lensing experiment in space. *Monthly Notices of the Royal Astronomical Society*, *431*(4), 3103–3126. https://doi.org/10.1093/mnras/stt384

Dawson, W. A., Schneider, M. D., Tyson, J. A., & Jee, M. J. (2016). THE ELLIPTICITY DISTRIBUTION OF AMBIGUOUSLY BLENDED OBJECTS. *ApJ*, *816*(1), 11. https://doi.org/10.3847/0004-637X/816/1/11

de Jong, R. S., Agertz, O., Berbel, A. A., Aird, J., Alexander, D. A., Amarsi, A., Anders, F., Andrae, R., Ansarinejad, B., Ansorge, W., Antilogus, P., Anwand-Heerwart, H., Arentsen, A., Arnadottir, A., Asplund, M., Auger, M., Azais, N., Baade, D., Baker, G., . . . Zucker, D. (2019). 4MOST: Project overview and information for the First Call for Proposals. *The Messenger*, *175*, 3–11. https://doi.org/10.18727/0722-6691/5117

Delgado, A. M., Hadzhiyska, B., Bose, S., Springel, V., Hernquist, L., Barrer, M., Pakmor, R., Ferlito, F., Kannan, R., Hernández-Aguayo, C., White, S. D. M., & Frenk, C. (2023). The MillenniumTNG Project: Intrinsic alignments of galaxies and halos. *Monthly Notices of the Royal Astronomical Society*, *523*(4), 5899–5914. https://doi.org/10.1093/mnras/stad1781

DeRose, J., Wechsler, R. H., Becker, M. R., Busha, M. T., Rykoff, E. S., MacCrann, N., Erickson, B., Evrard, A. E., Kravtsov, A., Gruen, D., Allam, S., Avila, S., Bridle, S., Brooks, D., Buckley-Geer, E., Carnero Rosell, A., Carrasco Kind, M., Carretero, J., Castander, F. J., . . . Vikram, V. (2019, January). The Buzzard Flock: Dark Energy Survey Synthetic Sky Catalogs. https://doi.org/10.48550/arXiv.1901.02401
ADS Bibcode: 2019arXiv190102401D.

Derylo, G., Diehl, H. T., & Estrada, J. (2006). 0.250mm-thick CCD packaging for the Dark Energy Survey Camera array. *6276*, 627608. https://doi.org/10.1117/12.672505
ADS Bibcode: 2006SPIE.6276E..08D.

DES Collaboration, Abbott, T. M. C., Abdalla, F. B., Alarcon, A., Aleksić, J., Allam, S., Allen, S., Amara, A., Annis, J., Asorey, J., Avila, S., Bacon, D., Balbinot, E., Banerji, M., Banik, N., Barkhouse, W., Baumer, M., Baxter, E., Bechtol, K., . . . Zuntz, J. (2018). Dark Energy Survey Year 1 Results: Cosmological Constraints from Galaxy Clustering and Weak Lensing. *Phys. Rev. D*, *98*(4), 043526. https://doi.org/10.1103/PhysRevD.98.043526

DES Collaboration, Abbott, T. M. C., Acevedo, M., Aguena, M., Alarcon, A., Allam, S., Alves, O., Amon, A., Andrade-Oliveira, F., Annis, J., Armstrong, P., Asorey, J., Avila, S., Bacon, D., Bassett, B. A., Bechtol, K., Bernardinelli, P. H., Bernstein, G. M., Bertin, E., . . . Zhang, Y. (2024). The Dark Energy Survey: Cosmology Results With \raisebox-0.5ex\textasciitilde1500 New High-redshift Type Ia Supernovae Using The Full 5-year Dataset. *arXiv e-prints*, arXiv:2401.02929. https://doi.org/10.48550/arXiv.2401.02929

DES Collaboration, Abbott, T. M. C., Adamow, M., Aguena, M., Allam, S., Amon, A., Annis, J., Avila, S., Bacon, D., Banerji, M., Bechtol, K., Becker, M. R., Bernstein, G. M., Bertin, E., Bhargava, S., Bridle, S. L., Brooks, D., Burke, D. L., Rosell, A. C., . . . Vila-Verde, G. (2021). The Dark Energy Survey Data Release 2. *ApJS*, *255*(2), 20. https://doi.org/10.3847/1538-4365/ac00b3

DES Collaboration, Abbott, T. M. C., Aguena, M., Alarcon, A., Allam, S., Alves, O., Amon, A., Andrade-Oliveira, F., Annis, J., Avila, S., Bacon, D., Baxter, E., Bechtol, K., Becker, M. R., Bernstein, G. M., Bhargava, S., Birrer, S., Blazek, J., Brandao-Souza, A., . . . Zuntz, J. (2022). Dark Energy Survey Year 3 Results: Cosmological Constraints from Galaxy Clustering and Weak Lensing. *Phys. Rev. D*, *105*(2), 023520. https://doi.org/10.1103/PhysRevD.105.023520

Dodelson, S. (2003). *Modern Cosmology*.

Dodelson, S. (2017, June). *Gravitational Lensing*.
ADS Bibcode: 2017grle.book.....D.

Doré, O., Hirata, C., Wang, Y., Weinberg, D., Baronchelli, I., Benson, A., Capak, P., Choi, A., Eifler, T., Hemmati, S., Ho, S., Izard, A., Jain, B., Jarvis, M., Kiessling, A., Krause, E., Massara, E., Masters, D., Merson, A., . . . Zu, Y. (2018, April). WFIRST Science Investigation Team "Cosmology with the High Latitude Survey" Annual Report 2017.

Edge, A., Sutherland, W., Kuijken, K., Driver, S., McMahon, R., Eales, S., & Emerson, J. P. (2013). The VISTA Kilo-degree Infrared Galaxy (VIKING) Survey: Bridging the Gap between Low and High Redshift. *The Messenger*, *154*, 32–34
ADS Bibcode: 2013Msngr.154...32E.

Eifler, T., Simet, M., Krause, E., Hirata, C., Huang, H.-J., Fang, X., Miranda, V., Mandelbaum, R., Doux, C., Heinrich, C., Huff, E., Miyatake, H., Hemmati, S., Xu, J., Rogozenski, P., Capak, P., Choi, A., Doré, O., Jain, B., . . . Wu, H.-Y. (2021). Cosmology with the Roman Space Telescope: Synergies with the Rubin Observatory Legacy Survey of Space

and Time. *Monthly Notices of the Royal Astronomical Society*, *507*(1), 1514–1527. https://doi.org/10.1093/mnras/stab533

Eisenstein, D. J., Zehavi, I., Hogg, D. W., Scoccimarro, R., Blanton, M. R., Nichol, R. C., Scranton, R., Seo, H.-J., Tegmark, M., Zheng, Z., Anderson, S. F., Annis, J., Bahcall, N., Brinkmann, J., Burles, S., Castander, F. J., Connolly, A., Csabai, I., Doi, M., . . . York, D. G. (2005). Detection of the Baryon Acoustic Peak in the Large-Scale Correlation Function of SDSS Luminous Red Galaxies. \apj, *633*(2), 560–574. https://doi.org/10.1086/466512

Erben, T., Waerbeke, L. V., Bertin, E., Mellier, Y., & Schneider, P. (2001). How accurately can we measure weak gravitational shear? *A&A*, *366*(3), 717–735. https://doi.org/10.1051/0004-6361:20010013

Esteves, J. H., Utsumi, Y., Snyder, A., Schutt, T., Broughton, A., Trbalic, B., Mau, S., Rasmussen, A., Plazas Malagón, A. A., Bradshaw, A., Marshall, S., Digel, S., Chiang, J., Rykoff, E., Waters, C., Soares-Santos, M., & Roodman, A. (2023). Photometry, Centroid and Point-spread Function Measurements in the LSST Camera Focal Plane Using Artificial Stars. *PASP*, *135*(1053), 115003. https://doi.org/10.1088/1538-3873/ad0a73

Euclid Collaboration, Paykari, P., Kitching, T., Hoekstra, H., Azzollini, R., Cardone, V. F., Cropper, M., Duncan, C. A. J., Kannawadi, A., Miller, L., Aussel, H., Conti, I. F., Auricchio, N., Baldi, M., Bardelli, S., Biviano, A., Bonino, D., Borsato, E., Bozzo, E., . . . Zucca, E. (2020). Euclid preparation. VI. Verifying the performance of cosmic shear experiments. *Astronomy and Astrophysics*, *635*, A139. https://doi.org/10.1051/0004-6361/201936980 ADS Bibcode: 2020A&A...635A.139E.

Everett, S., Yanny, B., Kuropatkin, N., Huff, E. M., Zhang, Y., Myles, J., Masegian, A., Elvin-Poole, J., Allam, S., Bernstein, G. M., Sevilla-Noarbe, I., Splettstoesser, M., Sheldon, E., Jarvis, M., Amon, A., Harrison, I., Choi, A., Hartley, W. G., Alarcon, A., . . . Collaboration), ((2022). Dark Energy Survey Year 3 Results: Measuring the Survey Transfer Function with Balrog. *ApJS*, *258*(1), 15. https://doi.org/10.3847/1538-4365/ac26c1

Fang, X., Eifler, T., & Krause, E. (2020). 2D-FFTLog: Efficient computation of real space covariance matrices for galaxy clustering and weak lensing. *Monthly Notices of the Royal Astronomical Society*, *497*(3), 2699–2714. https://doi.org/10.1093/mnras/staa1726

Fang, X., Krause, E., Eifler, T., & MacCrann, N. (2020). Beyond Limber: Efficient computation of angular power spectra for galaxy clustering and weak lensing. *Journal of Cosmology and Astroparticle Physics*, *2020*, 010. https://doi.org/10.1088/1475-7516/2020/05/010 ADS Bibcode: 2020JCAP...05..010F.

Fenech Conti, I., Herbonnet, R., Hoekstra, H., Merten, J., Miller, L., & Viola, M. (2017). Calibration of weak-lensing shear in the Kilo-Degree Survey. *Monthly Notices of the Royal Astronomical Society*, *467*, 1627–1651. https://doi.org/10.1093/mnras/stx200 ADS Bibcode: 2017MNRAS.467.1627F.

Feroz, F., Hobson, M. P., & Bridges, M. (2009). MultiNest: An efficient and robust Bayesian inference tool for cosmology and particle physics. *Monthly Notices of the Royal Astronomical Society*, *398*(4), 1601–1614. https://doi.org/10.1111/j.1365-2966.2009.14548.x

Finner, K., Lee, B., Chary, R.-R., Jee, M. J., Hirata, C., Congedo, G., Taylor, P., & HyeongHan, K. (2023). Near-IR Weak-lensing (NIRWL) Measurements in the CANDELS Fields. I. Point-spread Function Modeling and Systematics. *ApJ*, *958*(1), 33. https://doi.org/10.3847/1538-4357/acfafd

Flaugher, B., Diehl, H. T., Honscheid, K., Abbott, T. M. C., Alvarez, O., Angstadt, R., Annis, J. T., Antonik, M., Ballester, O., Beaufore, L., Bernstein, G. M., Bernstein, R. A., Bigelow, B., Bonati, M., Boprie, D., Brooks, D., Buckley-Geer, E. J., Campa, J., Cardiel-Sas, L., . . . DES Collaboration. (2015). The Dark Energy Camera. \aj, *150*(5), 150. https://doi.org/10.1088/0004-6256/150/5/150

Fluri, J., Kacprzak, T., Lucchi, A., Schneider, A., Refregier, A., & Hofmann, T. (2022). Full w CDM analysis of KiDS-1000 weak lensing maps using deep learning. *Physical Review D*, *105*, 083518. https://doi.org/10.1103/PhysRevD.105.083518
ADS Bibcode: 2022PhRvD.105h3518F.

Foreman, S., Coulton, W., Villaescusa-Navarro, F., & Barreira, A. (2020). Baryonic effects on the matter bispectrum. *Monthly Notices of the Royal Astronomical Society*, *498*(2), 2887–2911. https://doi.org/10.1093/mnras/staa2523

Foreman-Mackey, D., Hogg, D. W., Lang, D., & Goodman, J. (2013). Emcee: The MCMC Hammer. *Publications of the Astronomical Society of the Pacific*, *125*(925), 306–312. https://doi.org/10.1086/670067

Fortuna, M. C., Hoekstra, H., Johnston, H., Vakili, M., Kannawadi, A., Georgiou, C., Joachimi, B., Wright, A. H., Asgari, M., Bilicki, M., Heymans, C., Hildebrandt, H., Kuijken, K., & Von Wietersheim-Kramsta, M. (2021). KiDS-1000: Constraints on the intrinsic alignment of luminous red galaxies. *A&A*, *654*, A76. https://doi.org/10.1051/0004-6361/202140706

Fosalba, P., Gaztañaga, E., Castander, F. J., & Crocce, M. (2015). The MICE Grand Challenge light-cone simulation - III. Galaxy lensing mocks from all-sky lensing maps. *Monthly Notices of the Royal Astronomical Society*, *447*, 1319–1332. https://doi.org/10.1093/mnras/stu2464
ADS Bibcode: 2015MNRAS.447.1319F.

Freudenburg, J. K. C., Givans, J. J., Choi, A., Hirata, C. M., Bennett, C., Cheung, S., Cillis, A., Cottingham, D., Hill, R. J., Mah, J., & Meier, L. (2020). Brighter-fatter Effect in Near-infrared Detectors—III. Fourier-domain Treatment of Flat Field Correlations and Application to WFIRST. *PASP*, *132*(1013), 074504. https://doi.org/10.1088/1538-3873/ab9503

Fruchter, A. S., & Hook, R. N. (2002). Drizzle: A Method for the Linear Reconstruction of Undersampled Images. *PUBL ASTRON SOC PAC*, *114*(792), 144–152. https://doi.org/10.1086/338393

Fruchter, A. S. (2011). A New Method for Band-limited Imaging with Undersampled Detectors. *PASP*, *123*(902), 497. https://doi.org/10.1086/659313

Gaia Collaboration. (2018). Gaia Data Release 2. Summary of the contents and survey properties. *Astronomy and Astrophysics*, *616*, A1. https://doi.org/10.1051/0004-6361/201833051 ADS Bibcode: 2018A&A...616A...1G.

García-García, C., Zennaro, M., Aricò, G., Alonso, D., & Angulo, R. E. (2024, March). Cosmic shear with small scales: DES-Y3, KiDS-1000 and HSC-DR1. https://doi.org/10.48550/arXiv.2403.13794

Gatti, M., Giannini, G., Bernstein, G. M., Alarcon, A., Myles, J., Amon, A., Cawthon, R., Troxel, M., DeRose, J., Everett, S., Ross, A. J., Rykoff, E. S., Elvin-Poole, J., Cordero, J., Harrison, I., Sanchez, C., Prat, J., Gruen, D., Lin, H., . . . Wilkinson, R. D. (2021). Dark Energy Survey Year 3 Results: Clustering Redshifts – Calibration of the Weak Lensing Source Redshift Distributions with redMaGiC and BOSS/eBOSS. *Monthly Notices of the Royal Astronomical Society*, *510*(1), 1223–1247. https://doi.org/10.1093/mnras/stab3311

Gatti, M., Sheldon, E., Amon, A., Becker, M., Troxel, M., Choi, A., Doux, C., MacCrann, N., Alsina, A. N., Harrison, I., Gruen, D., Bernstein, G., Jarvis, M., Secco, L. F., Ferté, A., Shin, T., McCullough, J., Rollins, R. P., Chen, R., . . . Wilkinson, R. D. (2021). Dark Energy Survey Year 3 Results: Weak Lensing Shape Catalogue. *Monthly Notices of the Royal Astronomical Society*, *504*(3), 4312–4336. https://doi.org/10.1093/mnras/stab918

Givans, J. J., Choi, A., Porredon, A., Freudenburg, J. K. C., Hirata, C. M., Hill, R. J., Bennett, C., Foltz, R., & Meier, L. (2022). Quantum Yield and Charge Diffusion in the Nancy Grace Roman Space Telescope Infrared Detectors. *PASP*, *134*(1031), 014001. https://doi.org/10.1088/1538-3873/ac46ba

Górski, K. M., Hivon, E., Banday, A. J., Wandelt, B. D., Hansen, F. K., Reinecke, M., & Bartelmann, M. (2005). HEALPix: A Framework for High-Resolution Discretization and Fast Analysis of Data Distributed on the Sphere. *The Astrophysical Journal*, *622*, 759–771. https://doi.org/10.1086/427976 ADS Bibcode: 2005ApJ...622..759G.

Graham, M. L., Connolly, A. J., Wang, W., Schmidt, S. J., Morrison, C. B., Ivezić, Ž., Fabbro, S., Côté, P., Daniel, S. F., Jones, R. L., Jurić, M., Yoachim, P., & Kalmbach, J. B. (2020). Photometric Redshifts with the LSST. II. The Impact of Near-infrared and Near-ultraviolet Photometry. *AJ*, *159*(6), 258. https://doi.org/10.3847/1538-3881/ab8a43

Grogin, N. A., Kocevski, D. D., Faber, S. M., Ferguson, H. C., Koekemoer, A. M., Riess, A. G., Acquaviva, V., Alexander, D. M., Almaini, O., Ashby, M. L. N., Barden, M., Bell, E. F., Bournaud, F., Brown, T. M., Caputi, K. I., Casertano, S., Cassata, P., Castellano, M., Challis, P., . . . Yun, M. S. (2011). CANDELS: The Cosmic Assembly Near-infrared Deep Extragalactic Legacy Survey. *The Astrophysical Journal Supplement Series*, *197*, 35. https://doi.org/10.1088/0067-0049/197/2/35
ADS Bibcode: 2011ApJS..197...35G.

Gurvich, A., & Mandelbaum, R. (2016). The impact of correlated noise on galaxy shape estimation for weak lensing. *Monthly Notices of the Royal Astronomical Society*, *457*(4), 3522–3534. https://doi.org/10.1093/mnras/stw174

Guth, A. H. (1981). Inflationary universe: A possible solution to the horizon and flatness problems. *Phys. Rev. D*, *23*(2), 347–356. https://doi.org/10.1103/PhysRevD.23.347

Guyonnet, A., Astier, P., Antilogus, P., Regnault, N., & Doherty, P. (2015). Evidence for self-interaction of charge distribution in charge-coupled devices. *A&A*, *575*, A41. https://doi.org/10.1051/0004-6361/201424897

Handley, W. J., Hobson, M. P., & Lasenby, A. N. (2015). PolyChord: Nested sampling for cosmology. *Monthly Notices of the Royal Astronomical Society: Letters*, *450*(1), L61–L65. https://doi.org/10.1093/mnrasl/slv047

Harnois-Déraps, J., Martinet, N., & Reischke, R. (2021). Cosmic shear beyond 2-point statistics: Accounting for galaxy intrinsic alignment with projected tidal fields. *Monthly Notices of the Royal Astronomical Society*, *509*(3), 3868–3888. https://doi.org/10.1093/mnras/stab3222

Harris, C. R., Millman, K. J., van der Walt, S. J., Gommers, R., Virtanen, P., Cournapeau, D., Wieser, E., Taylor, J., Berg, S., Smith, N. J., Kern, R., Picus, M., Hoyer, S., van Kerkwijk, M. H., Brett, M., Haldane, A., del Río, J. F., Wiebe, M., Peterson, P., . . . Oliphant, T. E. (2020). Array programming with NumPy. *Nature*, *585*, 357–362. https://doi.org/10.1038/s41586-020-2649-2
ADS Bibcode: 2020Natur.585..357H.

Hartley, W. G., Choi, A., Amon, A., Gruendl, R. A., Sheldon, E., Harrison, I., Bernstein, G. M., Sevilla-Noarbe, I., Yanny, B., Eckert, K., Diehl, H. T., Alarcon, A., Banerji, M., Bechtol, K., Buchs, R., Cantu, S., Conselice, C., Cordero, J., Davis, C., . . . (DES Collaboration). (2022). Dark Energy Survey Year 3 Results: Deep Field optical + near-infrared images and catalogue. *Monthly Notices of the Royal Astronomical Society*, *509*(3), 3547–3579. https://doi.org/10.1093/mnras/stab3055

Hébert, C.-A., Meyers, J. E., Do, M. H., Burchat, P. R., & Collaboration, t. L. D. E. S. (2024, March). Generation of realistic input parameters for simulating atmospheric point-spread functions at astronomical observatories.

Hemmati, S., Capak, P., Masters, D., Davidzon, I., Dorè, O., Kruk, J., Mobasher, B., Rhodes, J., Scolnic, D., & Stern, D. (2019). Photometric Redshift Calibration Requirements for WFIRST Weak-lensing Cosmology: Predictions from CANDELS. *The Astrophysical Journal*, *877*, 117. https://doi.org/10.3847/1538-4357/ab1be5
ADS Bibcode: 2019ApJ...877..117H.

Herbonnet, R., Buddendiek, A., & Kuijken, K. (2017). Shear nulling after PSF Gaussianisation: Moment-based weak lensing measurements with subpercent noise bias. *A&A*, *599*, A73. https://doi.org/10.1051/0004-6361/201629263

Heymans, C., Grocutt, E., Heavens, A., Kilbinger, M., Kitching, T. D., Simpson, F., Benjamin, J., Erben, T., Hildebrandt, H., Hoekstra, H., Mellier, Y., Miller, L., Van Waerbeke, L., Brown, M. L., Coupon, J., Fu, L., Harnois-Déraps, J., Hudson, M. J., Kuijken, K., . . . Velander, M. (2013). CFHTLenS tomographic weak lensing cosmological parameter constraints: Mitigating the impact of intrinsic galaxy alignments. *mnras*, *432*(3), 2433–2453. https://doi.org/10.1093/mnras/stt601

Heymans, C., Tröster, T., Asgari, M., Blake, C., Hildebrandt, H., Joachimi, B., Kuijken, K., Lin, C.-A., Sánchez, A. G., van den Busch, J. L., Wright, A. H., Amon, A., Bilicki, M., de Jong, J., Crocce, M., Dvornik, A., Erben, T., Fortuna, M. C., Getman, F., . . . Wolf, C. (2021). KiDS-1000 Cosmology: Multi-probe weak gravitational lensing and spectroscopic galaxy clustering constraints. *åp*, *646*, A140. https://doi.org/10.1051/0004-6361/202039063

Heymans, C., Van Waerbeke, L., Miller, L., Erben, T., Hildebrandt, H., Hoekstra, H., Kitching, T. D., Mellier, Y., Simon, P., Bonnett, C., Coupon, J., Fu, L., Harnois Déraps, J., Hudson, M. J., Kilbinger, M., Kuijken, K., Rowe, B., Schrabback, T., Semboloni, E., . . . Velander, M. (2012). CFHTLenS: The Canada-France-Hawaii Telescope Lensing Survey. *Monthly Notices of the Royal Astronomical Society*, *427*, 146–166. https://doi.org/10.1111/j.1365-2966.2012.21952.x
ADS Bibcode: 2012MNRAS.427..146H.

Heymans, C., Van Waerbeke, L., Bacon, D., Berge, J., Bernstein, G., Bertin, E., Bridle, S., Brown, M. L., Clowe, D., Dahle, H., Erben, T., Gray, M., Hetterscheidt, M., Hoekstra, H., Hudelot, P., Jarvis, M., Kuijken, K., Margoniner, V., Massey, R., . . . Wittman, D. (2006). The Shear Testing Programme - I. Weak lensing analysis of simulated ground-based observations. *Monthly Notices of the Royal Astronomical Society*, *368*, 1323–1339. https://doi.org/10.1111/j.1365-2966.2006.10198.x
ADS Bibcode: 2006MNRAS.368.1323H.

Heymans, C., White, M., Heavens, A., Vale, C., & van Waerbeke, L. (2006). Potential sources of contamination to weak lensing measurements: Constraints from N-body simulations. *Monthly Notices of the Royal Astronomical Society*, *371*, 750–760. https://doi.org/10.1111/j.1365-2966.2006.10705.x
ADS Bibcode: 2006MNRAS.371..750H.

High, F. W., Rhodes, J., Massey, R., & Ellis, R. (2007). Pixelation Effects in Weak Lensing. *Publications of the Astronomical Society of the Pacific*, *119*, 1295–1307. https://doi.org/10.1086/523112
ADS Bibcode: 2007PASP..119.1295H.

Hikage, C., Takada, M., Hamana, T., & Spergel, D. (2011). Shear power spectrum reconstruction using the pseudo-spectrum method. *Monthly Notices of the Royal Astronomical Society*, *412*, 65–74. https://doi.org/10.1111/j.1365-2966.2010.17886.x
ADS Bibcode: 2011MNRAS.412...65H.

Hildebrandt, H., Erben, T., Kuijken, K., van Waerbeke, L., Heymans, C., Coupon, J., Benjamin, J., Bonnett, C., Fu, L., Hoekstra, H., Kitching, T. D., Mellier, Y., Miller, L., Velander, M., Hudson, M. J., Rowe, B. T. P., Schrabback, T., Semboloni, E., & Benítez, N. (2012). CFHTLenS: Improving the quality of photometric redshifts with precision photometry*. *Monthly Notices of the Royal Astronomical Society*, *421*(3), 2355–2367. https://doi.org/10.1111/j.1365-2966.2012.20468.x

Hildebrandt, H., Viola, M., Heymans, C., Joudaki, S., Kuijken, K., Blake, C., Erben, T., Joachimi, B., Klaes, D., Miller, L., Morrison, C. B., Nakajima, R., Verdoes Kleijn, G., Amon, A., Choi, A., Covone, G., de Jong, J. T. A., Dvornik, A., Fenech Conti, I., . . . Van Waerbeke, L. (2017). KiDS-450: Cosmological parameter constraints from tomographic weak gravitational lensing. *Monthly Notices of the Royal Astronomical Society*, *465*(2), 1454–1498. https://doi.org/10.1093/mnras/stw2805

Hirata, C., & Seljak, U. (2003). Shear calibration biases in weak-lensing surveys. *Monthly Notices of the Royal Astronomical Society*, *343*, 459–480. https://doi.org/10.1046/j.1365-8711.2003.06683.x
ADS Bibcode: 2003MNRAS.343..459H.

Hirata, C. M., Gehrels, N., Kneib, J.-P., Kruk, J., Rhodes, J., Wang, Y., & Zoubian, J. (2012, April). The WFIRST Galaxy Survey Exposure Time Calculator. https://doi.org/10.48550/arXiv.1204.5151

Hirata, C. M., Mandelbaum, R., Seljak, U., Guzik, J., Padmanabhan, N., Blake, C., Brinkmann, J., Budávari, T., Connolly, A., Csabai, I., Scranton, R., & Szalay, A. S. (2004). Galaxy–galaxy weak lensing in the Sloan Digital Sky Survey: Intrinsic alignments and shear calibration errors. *Monthly Notices of the Royal Astronomical Society*, *353*(2), 529–549. https://doi.org/10.1111/j.1365-2966.2004.08090.x

Hirata, C. M., & Seljak, U. (2004). Intrinsic alignment-lensing interference as a contaminant of cosmic shear. *Phys. Rev. D*, *70*(6), 063526. https://doi.org/10.1103/PhysRevD.70.063526

Hirata, C. M., Yamamoto, M., Laliotis, K., Macbeth, E., Troxel, M. A., Zhang, T., Cao, K., Choi, A., Givans, J., Heitmann, K., Ishak, M., Jarvis, M., Kovacs, E., Long, H., Mandelbaum, R., Park, A., Porredon, A., Walter, C. W., & Wood-Vasey, W. M. (2024, January). Simulating image

coaddition with the Nancy Grace Roman Space Telescope: I. Simulation methodology and general results.

Hoekstra, H., Kannawadi, A., & Kitching, T. D. (2021). Accounting for object detection bias in weak gravitational lensing studies. *Astronomy and Astrophysics*, *646*, A124. https://doi.org/10.1051/0004-6361/202038998
ADS Bibcode: 2021A&A...646A.124H.

Hoffmann, K., Secco, L. F., Blazek, J., Crocce, M., Tallada-Crespí, P., Samuroff, S., Prat, J., Carretero, J., Fosalba, P., Gaztanaga, E., & Castander, F. J. (2022). Modeling Intrinsic Galaxy Alignment in the MICE Simulation. *Phys. Rev. D*, *106*(12), 123510. https://doi.org/10.1103/PhysRevD.106.123510

Howell, S. B. (2006). *Handbook of CCD Astronomy* (2nd ed.). Cambridge University Press. https://doi.org/10.1017/CBO9780511807909

Hoyle, B., Gruen, D., Bernstein, G. M., Rau, M. M., De Vicente, J., Hartley, W. G., Gaztanaga, E., DeRose, J., Troxel, M. A., Davis, C., Alarcon, A., MacCrann, N., Prat, J., Sánchez, C., Sheldon, E., Wechsler, R. H., Asorey, J., Becker, M. R., Bonnett, C., . . . DES Collaboration. (2018). Dark Energy Survey Year 1 Results: Redshift distributions of the weak-lensing source galaxies. *Monthly Notices of the Royal Astronomical Society*, *478*(1), 592–610. https://doi.org/10.1093/mnras/sty957

Hu, W. (1999). Power Spectrum Tomography with Weak Lensing. *ApJ*, *522*(1), L21. https://doi.org/10.1086/312210

Hubble, E. (1929). A Relation between Distance and Radial Velocity among Extra-Galactic Nebulae. *Proceedings of the National Academy of Science*, *15*(3), 168–173. https://doi.org/10.1073/pnas.15.3.168

Huff, E., & Mandelbaum, R. (2017, February). Metacalibration: Direct Self-Calibration of Biases in Shear Measurement. https://doi.org/10.48550/arXiv.1702.02600

Huff, E. M., Hirata, C. M., Mandelbaum, R., Schlegel, D., Seljak, U., & Lupton, R. H. (2014). Seeing in the dark - I. Multi-epoch alchemy. *Monthly Notices of the Royal Astronomical Society*, *440*, 1296–1321. https://doi.org/10.1093/mnras/stu144
ADS Bibcode: 2014MNRAS.440.1296H.

Huterer, D., & Takada, M. (2005). Calibrating the Nonlinear Matter Power Spectrum: Requirements for Future Weak Lensing Surveys. *Astroparticle Physics*, *23*(4), 369–376. https://doi.org/10.1016/j.astropartphys.2005.02.006

Ivezić, Ž., Kahn, S. M., Tyson, J. A., Abel, B., Acosta, E., Allsman, R., Alonso, D., & AlSayyad, Y. e. a. (2018, May). LSST: From Science Drivers to Reference Design and Anticipated Data Products. https://doi.org/10.3847/1538-4357/ab042c

Jarvis, M., Bernstein, G., & Jain, B. (2004). The Skewness of the Aperture Mass Statistic. *Monthly Notices of the Royal Astronomical Society*, *352*(1), 338–352. https://doi.org/10.1111/j.1365-2966.2004.07926.x

Jarvis, M., Bernstein, G. M., Amon, A., Davis, C., Léget, P. F., Bechtol, K., Harrison, I., Gatti, M., Roodman, A., Chang, C., Chen, R., Choi, A., Desai, S., Drlica-Wagner, A., Gruen, D., Gruendl, R. A., Hernandez, A., MacCrann, N., Meyers, J., . . . Collaboration, D. E. S. (2020). Dark Energy Survey Year 3 Results: Point-Spread Function Modeling. *Monthly Notices of the Royal Astronomical Society*, *501*(1), 1282–1299. https://doi.org/10.1093/mnras/staa3679

Jarvis, M., Sheldon, E., Zuntz, J., Kacprzak, T., Bridle, S. L., Amara, A., Armstrong, R., Becker, M. R., Bernstein, G. M., Bonnett, C., Chang, C., Das, R., Dietrich, J. P., Drlica-Wagner, A., Eifler, T. F., Gangkofner, C., Gruen, D., Hirsch, M., Huff, E. M., . . . Wechsler, R. H. (2016). The DES Science Verification weak lensing shear catalogues. *Monthly Notices of the Royal Astronomical Society*, *460*, 2245–2281. https://doi.org/10.1093/mnras/stw990
ADS Bibcode: 2016MNRAS.460.2245J.

Jarvis, M., Jain, B., Bernstein, G., & Dolney, D. (2006). Dark Energy Constraints from the CTIO Lensing Survey. *apj*, *644*(1), 71–79. https://doi.org/10.1086/503418

Jee, M. J., Tyson, J. A., Hilbert, S., Schneider, M. D., Schmidt, S., & Wittman, D. (2016). Cosmic Shear Results from the Deep Lens Survey. II. Full Cosmological Parameter Constraints from Tomography. *apj*, *824*(2), 77. https://doi.org/10.3847/0004-637X/824/2/77

Jeffrey, N., Gatti, M., Chang, C., Whiteway, L., Demirbozan, U., Kovacs, A., Pollina, G., Bacon, D., Hamaus, N., Kacprzak, T., Lahav, O., Lanusse, F., Mawdsley, B., Nadathur, S., Starck, J. L., Vielzeuf, P., Zeurcher, D., Alarcon, A., Amon, A., . . . DES Collaboration. (2021). Dark Energy Survey Year 3 results: Curved-sky weak lensing mass map reconstruction. *Monthly Notices of the Royal Astronomical Society*, *505*, 4626–4645. https://doi.org/10.1093/mnras/stab1495
ADS Bibcode: 2021MNRAS.505.4626J.

Joachimi, B., Semboloni, E., Bett, P. E., Hartlap, J., Hilbert, S., Hoekstra, H., Schneider, P., & Schrabback, T. (2013). Intrinsic galaxy shapes and alignments I: Measuring and modelling COSMOS intrinsic galaxy ellipticities. *Monthly Notices of the Royal Astronomical Society*, *431*(1), 477–492. https://doi.org/10.1093/mnras/stt172

Joachimi, B., Semboloni, E., Hilbert, S., Bett, P. E., Hartlap, J., Hoekstra, H., & Schneider, P. (2013). Intrinsic galaxy shapes and alignments II: Modelling the intrinsic alignment contamination of weak lensing surveys. *Monthly Notices of the Royal Astronomical Society*, *436*(1), 819–838. https://doi.org/10.1093/mnras/stt1618

Joachimi, B., Cacciato, M., Kitching, T. D., Leonard, A., Mandelbaum, R., Schäfer, B. M., Sifón, C., Hoekstra, H., Kiessling, A., Kirk, D., & Rassat, A. (2015). Galaxy alignments: An overview. *Space Sci Rev*, *193*(1-4), 1–65. https://doi.org/10.1007/s11214-015-0177-4

JuriÄ, M. (2018). Galfast: Milky Way mock catalog generator. *Astrophysics Source Code Library*, ascl:1810.001
ADS Bibcode: 2018ascl.soft10001J.

Jurić, M., Ivezić, Ž., Brooks, A., Lupton, R. H., Schlegel, D., Finkbeiner, D., Padmanabhan, N., Bond, N., Sesar, B., Rockosi, C. M., Knapp, G. R., Gunn, J. E., Sumi, T., Schneider, D. P., Barentine, J. C., Brewington, H. J., Brinkmann, J., Fukugita, M., Harvanek, M., . . . York, D. G. (2008). The Milky Way Tomography with SDSS. I. Stellar Number Density Distribution. *The Astrophysical Journal*, *673*, 864–914. https://doi.org/10.1086/523619
ADS Bibcode: 2008ApJ...673..864J.

Kacprzak, T., Bridle, S., Rowe, B., Voigt, L., Zuntz, J., Hirsch, M., & MacCrann, N. (2014). S\'{e}rsic galaxy models in weak lensing shape measurement: Model bias, noise bias and their interaction. *Monthly Notices of the Royal Astronomical Society*, *441*(3), 2528–2538. https://doi.org/10.1093/mnras/stu588

Kacprzak, T., Fluri, J., Schneider, A., Refregier, A., & Stadel, J. (2023). CosmoGridV1: A simulated wCDM theory prediction for map-level cosmological inference. *Journal of Cosmology and Astroparticle Physics*, *2023*, 050. https://doi.org/10.1088/1475-7516/2023/02/050
ADS Bibcode: 2023JCAP...02..050K.

Kacprzak, T., Zuntz, J., Rowe, B., Bridle, S., Refregier, A., Amara, A., Voigt, L., & Hirsch, M. (2012). Measurement and Calibration of Noise Bias in Weak Lensing Galaxy Shape Estimation. *Monthly Notices of the Royal Astronomical Society*, *427*(4), 2711–2722. https://doi.org/10.1111/j.1365-2966.2012.21622.x

Kaiser, N. (1992). Weak Gravitational Lensing of Distant Galaxies. *The Astrophysical Journal*, *388*, 272. https://doi.org/10.1086/171151
ADS Bibcode: 1992ApJ...388..272K.

Kaiser, N., & Squires, G. (1993). Mapping the Dark Matter with Weak Gravitational Lensing. *The Astrophysical Journal*, *404*, 441. https://doi.org/10.1086/172297
ADS Bibcode: 1993ApJ...404..441K.

Kaiser, N., Squires, G., & Broadhurst, T. (1995). A Method for Weak Lensing Observations. *ApJ*, *449*, 460. https://doi.org/10.1086/176071

Kaiser, N., Wilson, G., & Luppino, G. A. (2000). Large-Scale Cosmic Shear Measurements. *arXiv e-prints*, astro–ph/0003338. https://doi.org/10.48550/arXiv.astro-ph/0003338

Kannawadi, A., Hoekstra, H., Miller, L., Viola, M., Conti, I. F., Herbonnet, R., Erben, T., Heymans, C., Hildebrandt, H., Kuijken, K., Vakili, M., & Wright, A. H. (2019). Towards emulating cosmic shear data: Revisiting the calibration of the shear measurements for the Kilo-Degree Survey. *A&A*, *624*, A92. https://doi.org/10.1051/0004-6361/201834819

Kannawadi, A., Rosenberg, E., & Hoekstra, H. (2021). Mitigating the effects of undersampling in weak lensing shear estimation with metacalibration. *Monthly Notices of the Royal Astronomical Society*, *502*(3), 4048–4063. https://doi.org/10.1093/mnras/stab211

Kiessling, A., Cacciato, M., Joachimi, B., Kirk, D., Kitching, T. D., Leonard, A., Mandelbaum, R., Schäfer, B. M., Sifón, C., Brown, M. L., & Rassat, A. (2015). Galaxy alignments: Theory, modelling and simulations. *Space Sci Rev*, *193*(1-4), 67–136. https://doi.org/10.1007/s11214-015-0203-6

Kilbinger, M. (2015). Cosmology with cosmic shear observations: A review. *Reports on Progress in Physics*, *78*, 086901. https://doi.org/10.1088/0034-4885/78/8/086901
ADS Bibcode: 2015RPPh...78h6901K.

Kilbinger, M., Fu, L., Heymans, C., Simpson, F., Benjamin, J., Erben, T., Harnois-Déraps, J., Hoekstra, H., Hildebrandt, H., Kitching, T. D., Mellier, Y., Miller, L., Van Waerbeke, L., Benabed, K., Bonnett, C., Coupon, J., Hudson, M. J., Kuijken, K., Rowe, B., . . . Velander, M. (2013). CFHTLenS: Combined probe cosmological model comparison using 2D weak gravitational lensing. *mnras*, *430*(3), 2200–2220. https://doi.org/10.1093/mnras/stt041

Kirk, D., Brown, M. L., Hoekstra, H., Joachimi, B., Kitching, T. D., Mandelbaum, R., Sifón, C., Cacciato, M., Choi, A., Kiessling, A., Leonard, A., Rassat, A., & Schäfer, B. M. (2015). Galaxy alignments: Observations and impact on cosmology. *Space Sci Rev*, *193*(1-4), 139–211. https://doi.org/10.1007/s11214-015-0213-4

Kitching, T. D., Rowe, B., Gill, M., Heymans, C., Massey, R., Witherick, D., Courbin, F., Georgatzis, K., Gentile, M., Gruen, D., Kilbinger, M., Li, G. L., Mariglis, A. P., Meylan, G., Storkey, A., & Xin, B. (2013). Image Analysis for Cosmology: Results from the GREAT10 Star Challenge. *The Astrophysical Journal Supplement Series*, *205*, 12. https://doi.org/10.1088/0067-0049/205/2/12
ADS Bibcode: 2013ApJS..205...12K.

Koekemoer, A. M., Faber, S. M., Ferguson, H. C., Grogin, N. A., Kocevski, D. D., Koo, D. C., Lai, K., Lotz, J. M., Lucas, R. A., McGrath, E. J., Ogaz, S., Rajan, A., Riess, A. G., Rodney, S. A., Strolger, L., Casertano, S., Castellano, M., Dahlen, T., Dickinson, M., . . . Yun, M. S. (2011). CANDELS: The Cosmic Assembly Near-infrared Deep Extragalactic Legacy Survey—The Hubble Space Telescope Observations, Imaging Data Products, and Mosaics. *The Astrophysical Journal Supplement Series*, *197*, 36. https://doi.org/10.1088/0067-0049/197/2/36
ADS Bibcode: 2011ApJS..197...36K.

Korytov, D., Hearin, A., Kovacs, E., Larsen, P., Rangel, E., Hollowed, J., Benson, A. J., Heitmann, K., Mao, Y.-Y., Bahmanyar, A., Chang, C., Campbell, D., DeRose, J., Finkel, H., Frontiere, N., Gawiser, E., Habib, S., Joachimi, B., Lanusse, F., . . . (The LSST Dark Energy Science Collaboration. (2019). CosmoDC2: A Synthetic Sky Catalog for Dark Energy Science with LSST. *The Astrophysical Journal Supplement Series*, *245*, 26. https://doi.org/10.3847/1538-4365/ab510c
ADS Bibcode: 2019ApJS..245...26K.

Kovacs, E., Mao, Y.-Y., Aguena, M., Bahmanyar, A., Broussard, A., Butler, J., Campbell, D., Chang, C., Fu, S., Heitmann, K., Korytov, D., Lanusse, F., Larsen, P., Mandelbaum, R., Morrison, C. B., Payerne, C., Ricci, M., Rykoff, E., Sánchez, F. J., . . . Collaboration, T. L. D. E. S. (2022). Validating Synthetic Galaxy Catalogs for Dark Energy Science in the LSST Era. *The Open Journal of Astrophysics*, *5*. https://doi.org/10.21105/astro.2110.03769

Krause, E., Eifler, T. F., Zuntz, J., Friedrich, O., Troxel, M. A., Dodelson, S., Blazek, J., Secco, L. F., MacCrann, N., Baxter, E., Chang, C., Chen, N., Crocce, M., DeRose, J., Ferte, A., Kokron, N., Lacasa, F., Miranda, V., Omori, Y., . . . Weller, J. (2017, June). Dark Energy Survey Year 1 Results: Multi-Probe Methodology and Simulated Likelihood Analyses. https://doi.org/10.48550/arXiv.1706.09359

Krist, J. E., Hook, R. N., & Stoehr, F. (2011, September). 20 years of Hubble Space Telescope optical modeling using Tiny Tim. In M. A. Kahan (Ed.), *SPIE Optical Engineering + Applications* (81270J). https://doi.org/10.1117/12.892762

Kuijken, K., Heymans, C., Dvornik, A., Hildebrandt, H., de Jong, J. T. A., Wright, A. H., Erben, T., Bilicki, M., Giblin, B., Shan, H.-Y., Getman, F., Grado, A., Hoekstra, H., Miller, L., Napolitano, N., Paolilo, M., Radovich, M., Schneider, P., Sutherland, W., . . . Kleijn, G. A. V. (2019). The fourth data release of the Kilo-Degree Survey: Ugri imaging and nine-band optical-IR photometry over 1000 square degrees. *A&A*, *625*, A2. https://doi.org/10.1051/0004-6361/201834918

Kuijken, K., Heymans, C., Hildebrandt, H., Nakajima, R., Erben, T., de Jong, J. T. A., Viola, M., Choi, A., Hoekstra, H., Miller, L., van Uitert, E., Amon, A., Blake, C., Brouwer, M., Buddendiek, A., Conti, I. F., Eriksen, M., Grado, A., Harnois-Déraps, J., . . . van Waerbeke, L. (2015). Gravitational lensing analysis of the Kilo-Degree Survey. \mnras, *454*(4), 3500–3532. https://doi.org/10.1093/mnras/stv2140

Laigle, C., McCracken, H. J., Ilbert, O., Hsieh, B. C., Davidzon, I., Capak, P., Hasinger, G., Silverman, J. D., Pichon, C., Coupon, J., Aussel, H., Le Borgne, D., Caputi, K., Cassata, P., Chang, Y. .-., Civano, F., Dunlop, J., Fynbo, J., Kartaltepe, J. S., . . . Zabl, J. (2016). The COSMOS2015 Catalog: Exploring the 1 < z < 6 Universe with Half a Million Galaxies. *The Astrophysical Journal Supplement Series*, *224*, 24. https://doi.org/10.3847/0067-0049/224/2/24
ADS Bibcode: 2016ApJS..224...24L.

Lamman, C., Tsaprazi, E., Shi, J., Šarčević, N. N., Pyne, S., Legnani, E., & Ferreira, T. (2024). The IA Guide: A Breakdown of Intrinsic Alignment Formalisms. *TheOJA*, *7*, 10.21105/astro.2309.08605. https://doi.org/10.21105/astro.2309.08605

Lange, J. U. (2023, June). NAUTILUS: Boosting Bayesian importance nested sampling with deep learning. https://doi.org/10.48550/arXiv.2306.16923

Lauer, T. R. (1999). Combining Undersampled Dithered Images. *Publications of the Astronomical Society of the Pacific*, *111*, 227–237. https://doi.org/10.1086/316319
ADS Bibcode: 1999PASP..111..227L.

Laureijs, R., Amiaux, J., Arduini, S., Auguères, J. .-., Brinchmann, J., Cole, R., Cropper, M., & Dabin, C. e. a. (2011). Euclid Definition Study Report. *arXiv e-prints*, arXiv:1110.3193. https://doi.org/10.48550/arXiv.1110.3193

Lee, J., Acevedo, M., Sako, M., Vincenzi, M., Brout, D., Sanchez, B., Chen, R., Davis, T. M., Jarvis, M., Scolnic, D., Qu, H., Galbany, L., Kessler, R., Lasker, J., Sullivan, M., Wiseman, P., Aguena, M., Allam, S., Alves, O., . . . Collaboration), ((2023). The Dark Energy Survey Supernova Program: Corrections on Photometry Due to Wavelength-dependent Atmospheric Effects. *AJ*, *165*(6), 222. https://doi.org/10.3847/1538-3881/acca15

Léget, P.-F., Astier, P., Regnault, N., Jarvis, M., Antilogus, P., Roodman, A., Rubin, D., & Saunders, C. (2021). Improving the astrometric solution of the Hyper Suprime-Cam with anisotropic Gaussian processes. *A&A*, *650*, A81. https://doi.org/10.1051/0004-6361/202140463

Lemos, P., Challinor, A., & Efstathiou, G. (2017). The effect of Limber and flat-sky approximations on galaxy weak lensing. *Journal of Cosmology and Astroparticle Physics*, *2017*, 014. https://doi.org/10.1088/1475-7516/2017/05/014
ADS Bibcode: 2017JCAP...05..014L.

Lesgourgues, J. (2011). The Cosmic Linear Anisotropy Solving System (CLASS) I: Overview. *arXiv e-prints*, arXiv:1104.2932. https://doi.org/10.48550/arXiv.1104.2932

Lewis, A., & Challinor, A. (2006). Weak gravitational lensing of the CMB. \physrep, *429*(1), 1–65. https://doi.org/10.1016/j.physrep.2006.03.002

Lewis, A., Challinor, A., & Lasenby, A. (2000). Efficient Computation of Cosmic Microwave Background Anisotropies in Closed Friedmann-Robertson-Walker Models. \apj, *538*(2), 473–476. https://doi.org/10.1086/309179

Li, X., Li, Y., & Massey, R. (2022). Weak gravitational lensing shear measurement with FPFS: Analytical mitigation of noise bias and selection bias. *Monthly Notices of the Royal Astronomical Society*, *511*, 4850–4860. https://doi.org/10.1093/mnras/stac342
ADS Bibcode: 2022MNRAS.511.4850L.

Li, X., & Mandelbaum, R. (2023). Analytical weak-lensing shear responses of galaxy properties and galaxy detection. *Monthly Notices of the Royal Astronomical Society*, *521*, 4904–4926. https://doi.org/10.1093/mnras/stad890
ADS Bibcode: 2023MNRAS.521.4904L.

Li, X., Miyatake, H., Luo, W., More, S., Oguri, M., Hamana, T., Mandelbaum, R., Shirasaki, M., Takada, M., Armstrong, R., Kannawadi, A., Takita, S., Miyazaki, S., Nishizawa, A. J., Plazas Malagon, A. A., Strauss, M. A., Tanaka, M., & Yoshida, N. (2022). The three-year shear catalog of the Subaru Hyper Suprime-Cam SSP Survey. *Publications of the Astronomical Society of Japan*, *74*, 421–459. https://doi.org/10.1093/pasj/psac006
ADS Bibcode: 2022PASJ...74..421L.

Lilly, S. J., Le Brun, V., Maier, C., Mainieri, V., Mignoli, M., Scodeggio, M., Zamorani, G., Carollo, M., Contini, T., Kneib, J.-P., Le Fèvre, O., Renzini, A., Bardelli, S., Bolzonella, M., Bongiorno, A., Caputi, K., Coppa, G., Cucciati, O., de la Torre, S., ... Taniguchi, Y. (2009). The zCOSMOS 10k-Bright Spectroscopic Sample. *The Astrophysical Journal Supplement Series*, *184*, 218–229. https://doi.org/10.1088/0067-0049/184/2/218
ADS Bibcode: 2009ApJS..184..218L.

Lima, M., Cunha, C. E., Oyaizu, H., Frieman, J., Lin, H., & Sheldon, E. S. (2008). Estimating the redshift distribution of photometric galaxy samples. *Monthly Notices of the Royal Astronomical Society*, *390*, 118–130. https://doi.org/10.1111/j.1365-2966.2008.13510.x
ADS Bibcode: 2008MNRAS.390..118L.

Limber, D. N. (1953). The Analysis of Counts of the Extragalactic Nebulae in Terms of a Fluctuating Density Field. *The Astrophysical Journal*, *117*, 134. https://doi.org/10.1086/145672
ADS Bibcode: 1953ApJ...117..134L.

Linde, A. D. (1982). A new inflationary universe scenario: A possible solution of the horizon, flatness, homogeneity, isotropy and primordial monopole problems. *Physics Letters B*, *108*, 389–393. https://doi.org/10.1016/0370-2693(82)91219-9
ADS Bibcode: 1982PhLB..108..389L.

LoVerde, M., & Afshordi, N. (2008). Extended Limber approximation. *Phys. Rev. D*, *78*(12), 123506. https://doi.org/10.1103/PhysRevD.78.123506

LSST Dark Energy Science Collaboration. (2012). Large Synoptic Survey Telescope: Dark Energy Science Collaboration. *arXiv e-prints*, arXiv:1211.0310. https://doi.org/10.48550/arXiv.1211.0310

LSST Dark Energy Science Collaboration, Abolfathi, B., Armstrong, R., Awan, H., Babuji, Y. N., Bauer, F. E., Beckett, G., Biswas, R., Bogart, J. R., Boutigny, D., Chard, K., Chiang, J., Cohen-Tanugi, J., Connolly, A. J., Daniel, S. F., Digel, S. W., Drlica-Wagner, A., Dubois, R., Gawiser, E., ... Wood-Vasey, W. M. (2021, January). DESC DC2 Data Release Note.

https://doi.org/10.48550/arXiv.2101.04855
ADS Bibcode: 2021arXiv210104855L.

LSST Dark Energy Science Collaboration (LSST DESC). (2021). The LSST DESC DC2 Simulated Sky Survey. *The Astrophysical Journal Supplement Series*, *253*, 31. https://doi.org/10.3847/1538-4365/abd62c
ADS Bibcode: 2021ApJS..253...31L.

LSST Science Collaboration. (2009, December). LSST Science Book, Version 2.0. https://doi.org/10.48550/arXiv.0912.0201
ADS Bibcode: 2009arXiv0912.0201L.

MacCrann, N., Becker, M. R., McCullough, J., Amon, A., Gruen, D., Jarvis, M., Choi, A., Troxel, M. A., Sheldon, E., Yanny, B., Herner, K., Dodelson, S., Zuntz, J., Eckert, K., Rollins, R. P., Varga, T. N., Bernstein, G. M., Gruendl, R. A., Harrison, I., . . . Wilkinson, R. D. (2021). DES Y3 results: Blending shear and redshift biases in image simulations. *Monthly Notices of the Royal Astronomical Society*, *509*(3), 3371–3394. https://doi.org/10.1093/mnras/stab2870

Mandelbaum, R., Hirata, C. M., Seljak, U., Guzik, J., Padmanabhan, N., Blake, C., Blanton, M. R., Lupton, R., & Brinkmann, J. (2005). Systematic errors in weak lensing: Application to SDSS galaxy-galaxy weak lensing. *Monthly Notices of the Royal Astronomical Society*, *361*, 1287–1322. https://doi.org/10.1111/j.1365-2966.2005.09282.x
ADS Bibcode: 2005MNRAS.361.1287M.

Mandelbaum, R., Jarvis, M., Lupton, R. H., Bosch, J., Kannawadi, A., Murphy, M. D., Zhang, T., & Collaboration, t. L. D. E. S. (2023). PSFs of coadded images. *TheOJA*, *6*, 10.21105/astro.2209.09253. https://doi.org/10.21105/astro.2209.09253

Mandelbaum, R., Rowe, B., Armstrong, R., Bard, D., Bertin, E., Bosch, J., Boutigny, D., Courbin, F., Dawson, W. A., Donnarumma, A., Fenech Conti, I., Gavazzi, R., Gentile, M., Gill, M. S. S., Hogg, D. W., Huff, E. M., Jee, M. J., Kacprzak, T., Kilbinger, M., . . . Zuntz, J. (2015). GREAT3 results – I. Systematic errors in shear estimation and the impact of real galaxy morphology. *Monthly Notices of the Royal Astronomical Society*, *450*(3), 2963–3007. https://doi.org/10.1093/mnras/stv781

Mandelbaum, R., Rowe, B., Bosch, J., Chang, C., Courbin, F., Gill, M., Jarvis, M., Kannawadi, A., Kacprzak, T., Lackner, C., Leauthaud, A., Miyatake, H., Nakajima, R., Rhodes, J., Simet, M., Zuntz, J., Armstrong, B., Bridle, S., Coupon, J., . . . Schrabback, T. (2014). THE THIRD GRAVITATIONAL LENSING ACCURACY TESTING (GREAT3) CHALLENGE HANDBOOK. *ApJS*, *212*(1), 5. https://doi.org/10.1088/0067-0049/212/1/5

Massey, R., Heymans, C., Bergé, J., Bernstein, G., Bridle, S., Clowe, D., Dahle, H., Ellis, R., Erben, T., Hetterscheidt, M., High, F. W., Hirata, C., Hoekstra, H., Hudelot, P., Jarvis, M., Johnston, D., Kuijken, K., Margoniner, V., Mandelbaum, R., . . . van Waerbeke, L. (2007). The Shear

Testing Programme 2: Factors affecting high-precision weak-lensing analyses. *Monthly Notices of the Royal Astronomical Society*, *376*, 13–38. https://doi.org/10.1111/j.1365-2966.2006.11315.x

ADS Bibcode: 2007MNRAS.376...13M.

Massey, R., Hoekstra, H., Kitching, T., Rhodes, J., Cropper, M., Amiaux, J., Harvey, D., Mellier, Y., Meneghetti, M., Miller, L., Paulin-Henriksson, S., Pires, S., Scaramella, R., & Schrabback, T. (2013). Origins of weak lensing systematics, and requirements on future instrumentation (or knowledge of instrumentation). *Monthly Notices of the Royal Astronomical Society*, *429*(1), 661–678. https://doi.org/10.1093/mnras/sts371

Massey, R., Rhodes, J., Leauthaud, A., Capak, P., Ellis, R., Koekemoer, A., Réfrégier, A., Scoville, N., Taylor, J. E., Albert, J., Bergé, J., Heymans, C., Johnston, D., Kneib, J.-P., Mellier, Y., Mobasher, B., Semboloni, E., Shopbell, P., Tasca, L., & Van Waerbeke, L. (2007). COSMOS: Three-dimensional Weak Lensing and the Growth of Structure. \apjs, *172*(1), 239–253. https://doi.org/10.1086/516599

McCarthy, I. G., Salcido, J., Schaye, J., Kwan, J., Elbers, W., Kugel, R., Schaller, M., Helly, J. C., Braspenning, J., Frenk, C. S., van Daalen, M. P., Vandenbroucke, B., Conley, J. T., Font, A. S., & Upadhye, A. (2023). The FLAMINGO project: Revisiting the S8 tension and the role of baryonic physics. *Monthly Notices of the Royal Astronomical Society*, *526*, 5494–5519. https://doi.org/10.1093/mnras/stad3107

ADS Bibcode: 2023MNRAS.526.5494M.

McCarthy, I. G., Schaye, J., Bird, S., & Le Brun, A. M. C. (2017). The BAHAMAS project: Calibrated hydrodynamical simulations for large-scale structure cosmology. *Monthly Notices of the Royal Astronomical Society*, *465*, 2936–2965. https://doi.org/10.1093/mnras/stw2792

ADS Bibcode: 2017MNRAS.465.2936M.

Mead, A. J., Brieden, S., Tröster, T., & Heymans, C. (2021). Hmcode-2020: Improved modelling of non-linear cosmological power spectra with baryonic feedback. *Monthly Notices of the Royal Astronomical Society*, *502*(1), 1401–1422. https://doi.org/10.1093/mnras/stab082

Mead, A. J., Peacock, J. A., Heymans, C., Joudaki, S., & Heavens, A. F. (2015). An accurate halo model for fitting non-linear cosmological power spectra and baryonic feedback models. *Monthly Notices of the Royal Astronomical Society*, *454*, 1958–1975. https://doi.org/10.1093/mnras/stv2036

ADS Bibcode: 2015MNRAS.454.1958M.

Melchior, P., Böhnert, A., Lombardi, M., & Bartelmann, M. (2010). Limitations on shapelet-based weak-lensing measurements. *A&A*, *510*, A75. https://doi.org/10.1051/0004-6361/200912785

Melchior, P., Moolekamp, F., Jerdee, M., Armstrong, R., Sun, A. .-., Bosch, J., & Lupton, R. (2018). Scarlet: Source separation in multi-band images by Constrained Matrix Factorization. *Astronomy and Computing*, *24*, 129–142. https://doi.org/10.1016/j.ascom.2018.07.001

Melchior, P., Suchyta, E., Huff, E., Hirsch, M., Kacprzak, T., Rykoff, E., Gruen, D., Armstrong, R., Bacon, D., Bechtol, K., Bernstein, G. M., Bridle, S., Clampitt, J., Honscheid, K., Jain, B., Jouvel, S., Krause, E., Lin, H., MacCrann, N., . . . Wester, W. (2015). Mass and galaxy distributions of four massive galaxy clusters from Dark Energy Survey Science Verification data. *Monthly Notices of the Royal Astronomical Society*, *449*(3), 2219–2238. https://doi.org/10.1093/mnras/stv398

Melchior, P., & Viola, M. (2012). Means of confusion: How pixel noise affects shear estimates for weak gravitational lensing. *Monthly Notices of the Royal Astronomical Society*, *424*(4), 2757–2769. https://doi.org/10.1111/j.1365-2966.2012.21381.x

Meyers, J. E., & Burchat, P. R. (2015). IMPACT OF ATMOSPHERIC CHROMATIC EFFECTS ON WEAK LENSING MEASUREMENTS. *ApJ*, *807*(2), 182. https://doi.org/10.1088/0004-637X/807/2/182

Miller, L., Heymans, C., Kitching, T. D., Van Waerbeke, L., Erben, T., Hildebrandt, H., Hoekstra, H., Mellier, Y., Rowe, B. T. P., Coupon, J., Dietrich, J. P., Fu, L., Harnois-Deraps, J., Hudson, M. J., Kilbinger, M., Kuijken, K., Schrabback, T., Semboloni, E., Vafaei, S., & Velander, M. (2013). Bayesian Galaxy Shape Measurement for Weak Lensing Surveys - III. Application to the Canada-France-Hawaii Telescope Lensing Survey. *Monthly Notices of the Royal Astronomical Society*, *429*(4), 2858–2880. https://doi.org/10.1093/mnras/sts454

Miller, L., Kitching, T. D., Heymans, C., Heavens, A. F., & Van Waerbeke, L. (2007). Bayesian Galaxy Shape Measurement for Weak Lensing Surveys -I. Methodology and a Fast Fitting Algorithm. *Monthly Notices of the Royal Astronomical Society*, *382*(1), 315–324. https://doi.org/10.1111/j.1365-2966.2007.12363.x

Miralda-Escude, J. (1991). Gravitational Lensing by Clusters of Galaxies: Constraining the Mass Distribution. *The Astrophysical Journal*, *370*, 1. https://doi.org/10.1086/169789 ADS Bibcode: 1991ApJ...370....1M.

Miyatake, H., Sugiyama, S., Takada, M., Nishimichi, T., Li, X., Shirasaki, M., More, S., Kobayashi, Y., Nishizawa, A. J., Rau, M. M., Zhang, T., Takahashi, R., Dalal, R., Mandelbaum, R., Strauss, M. A., Hamana, T., Oguri, M., Osato, K., Luo, W., . . . Wang, S.-Y. (2023). Hyper Suprime-Cam Year 3 results: Cosmology from galaxy clustering and weak lensing with HSC and SDSS using the emulator based halo model. \prd, *108*(12), 123517. https://doi.org/10.1103/PhysRevD.108.123517

Morganson, E., Gruendl, R. A., Menanteau, F., Kind, M. C., Chen, Y.-C., Daues, G., Drlica-Wagner, A., Friedel, D. N., Gower, M., Johnson, M. W. G., Johnson, M. D., Kessler, R., Paz-Chinchón, F., Petravick, D., Pond, C., Yanny, B., Allam, S., Armstrong, R., Barkhouse,

W., . . . DES Collaboration. (2018). The Dark Energy Survey Image Processing Pipeline. *PASP*, *130*(989), 074501. https://doi.org/10.1088/1538-3873/aab4ef

Mosby, G., Rauscher, B. J., Bennett, C., Cheng, E. S., Cheung, S., Cillis, A., Content, D., Cottingham, D., Foltz, R., Gygax, J., Hill, R. J., Kruk, J. W., Mah, J., Meier, L., Merchant, C., Miko, L., Piquette, E. C., Waczynski, A., & Wen, Y. (2020). Properties and characteristics of the Nancy Grace Roman Space Telescope H4RG-10 detectors. *Journal of Astronomical Telescopes, Instruments, and Systems*, *6*, 046001. https://doi.org/10.1117/1.JATIS.6.4.046001 ADS Bibcode: 2020JATIS...6d6001M.

Myles, J., Alarcon, A., Amon, A., Sánchez, C., Everett, S., DeRose, J., McCullough, J., Gruen, D., Bernstein, G. M., Troxel, M. A., Dodelson, S., Campos, A., MacCrann, N., Yin, B., Raveri, M., Amara, A., Becker, M. R., Choi, A., Cordero, J., . . . Wester, W. (2021). Dark Energy Survey Year 3 Results: Redshift Calibration of the Weak Lensing Source Galaxies. *Monthly Notices of the Royal Astronomical Society*, *505*(3), 4249–4277. https://doi.org/10.1093/mnras/stab1515

Nelder, J. A., & Mead, R. (1965). A Simplex Method for Function Minimization. *The Computer Journal*, *7*(4), 308–313. https://doi.org/10.1093/comjnl/7.4.308

Oke, J. B., & Gunn, J. E. (1983). Secondary standard stars for absolute spectrophotometry. *The Astrophysical Journal*, *266*, 713–717. https://doi.org/10.1086/160817 ADS Bibcode: 1983ApJ...266..713O.

Okura, Y., & Futamase, T. (2018). Analytical noise bias correction for weak lensing shear analysis with ERA. *Monthly Notices of the Royal Astronomical Society*, *479*(4), 4971–4983. https://doi.org/10.1093/mnras/sty1746

Particle Data Group, Workman, R. L., Burkert, V. D., Crede, V., Klempt, E., Thoma, U., Tiator, L., Agashe, K., Aielli, G., Allanach, B. C., Amsler, C., Antonelli, M., Aschenauer, E. C., Asner, D. M., Baer, H., Banerjee, S., Barnett, R. M., Baudis, L., Bauer, C. W., . . . Zyla, P. A. (2022). Review of Particle Physics. *Progress of Theoretical and Experimental Physics*, *2022*(8), 083C01. https://doi.org/10.1093/ptep/ptac097

Paturel, G., Petit, C., Prugniel, P., Theureau, G., Rousseau, J., Brouty, M., Dubois, P., & Cambrésy, L. (2003). HYPERLEDA. I. Identification and designation of galaxies. *Astronomy and Astrophysics*, *412*, 45–55. https://doi.org/10.1051/0004-6361:20031411 ADS Bibcode: 2003A&A...412...45P.

Paulin-Henriksson, S., Refregier, A., & Amara, A. (2009). Optimal point spread function modeling for weak lensing: Complexity and sparsity. *A&A*, *500*(2), 647–655. https://doi.org/10.1051/0004-6361/200811061

Peacock, J., & Heymans, C. (2009). Lecture notes in Advanced Cosmology.

Penzias, A. A., & Wilson, R. W. (1965). A Measurement of Excess Antenna Temperature at 4080 Mc/s. \apj, *142*, 419–421. https://doi.org/10.1086/148307

Percival, W. J., Friedrich, O., Sellentin, E., & Heavens, A. (2022). Matching Bayesian and frequentist coverage probabilities when using an approximate data covariance matrix. *Monthly Notices of the Royal Astronomical Society*, *510*, 3207–3221. https://doi.org/10.1093/mnras/stab3540
ADS Bibcode: 2022MNRAS.510.3207P.

Perlmutter, S., & Riess, A. (1999, July). Cosmological parameters from supernovae: Two groups' results agree. In D. O. Caldwell (Ed.), *COSMO-98* (pp. 129–142, Vol. 478). https://doi.org/10.1063/1.59382

Planck Collaboration, Aghanim, N., Akrami, Y., Ashdown, M., Aumont, J., Baccigalupi, C., Ballardini, M., Banday, A. J., Barreiro, R. B., Bartolo, N., Basak, S., Battye, R., Benabed, K., Bernard, J. .-., Bersanelli, M., Bielewicz, P., Bock, J. J., Bond, J. R., Borrill, J., ... Zonca, A. (2020). Planck 2018 results. VI. Cosmological parameters. *åp*, *641*, A6. https://doi.org/10.1051/0004-6361/201833910

Planck Collaboration, Akrami, Y., Ashdown, M., Aumont, J., Baccigalupi, C., Ballardini, M., Banday, A. J., Barreiro, R. B., Bartolo, N., Basak, S., Benabed, K., Bersanelli, M., Bielewicz, P., Bond, J. R., Borrill, J., Bouchet, F. R., Boulanger, F., Bucher, M., Burigana, C., ... Zonca, A. (2020). Planck 2018 results. IV. Diffuse component separation. *åp*, *641*, A4. https://doi.org/10.1051/0004-6361/201833881

Plazas, A. A., Bernstein, G. M., & Sheldon, E. S. (2014). On-Sky Measurements of the Transverse Electric Fields' Effects in the Dark Energy Camera CCDs. *Publications of the Astronomical Society of the Pacific*, *126*, 750. https://doi.org/10.1086/677682
ADS Bibcode: 2014PASP..126..750P.

Plazas, A. A., & Bernstein, G. M. (2012). Atmospheric dispersion effects in weak lensing measurements. *Publications of the Astronomical Society of the Pacific*, *124*(920), 1113–1123. https://doi.org/10.1086/668294

Pujol, A., Kilbinger, M., Sureau, F., & Bobin, J. (2019). A highly precise shear bias estimator independent of the measured shape noise. *Astronomy and Astrophysics*, *621*, A2. https://doi.org/10.1051/0004-6361/201833740
ADS Bibcode: 2019A&A...621A...2P.

Rauscher, B. J. (2015). Teledyne H1RG, H2RG, and H4RG Noise Generator. *PASP*, *127*(957), 1144. https://doi.org/10.1086/684082

Refregier, A. (2003). Shapelets — I. A method for image analysis. *Monthly Notices of the Royal Astronomical Society*, *338*(1), 35–47. https://doi.org/10.1046/j.1365-8711.2003.05901.x

Refregier, A., Kacprzak, T., Amara, A., Bridle, S., & Rowe, B. (2012). Noise bias in weak lensing shape measurements. *Monthly Notices of the Royal Astronomical Society*, *425*, 1951–1957. https://doi.org/10.1111/j.1365-2966.2012.21483.x
ADS Bibcode: 2012MNRAS.425.1951R.

Riess, A. G., Filippenko, A. V., Challis, P., Clocchiatti, A., Diercks, A., Garnavich, P. M., Gilliland, R. L., Hogan, C. J., Jha, S., Kirshner, R. P., Leibundgut, B., Phillips, M. M., Reiss, D., Schmidt, B. P., Schommer, R. A., Smith, R. C., Spyromilio, J., Stubbs, C., Suntzeff, N. B., & Tonry, J. (1998). Observational Evidence from Supernovae for an Accelerating Universe and a Cosmological Constant. \aj, *116*(3), 1009–1038. https://doi.org/10.1086/300499

Riess, A. G., Yuan, W., Macri, L. M., Scolnic, D., Brout, D., Casertano, S., Jones, D. O., Murakami, Y., Anand, G. S., Breuval, L., Brink, T. G., Filippenko, A. V., Hoffmann, S., Jha, S. W., D'arcy Kenworthy, W., Mackenty, J., Stahl, B. E., & Zheng, W. (2022). A Comprehensive Measurement of the Local Value of the Hubble Constant with 1 km s-1 Mpc-1 Uncertainty from the Hubble Space Telescope and the SH0ES Team. *The Astrophysical Journal*, *934*, L7. https://doi.org/10.3847/2041-8213/ac5c5b
ADS Bibcode: 2022ApJ...934L...7R.

Rowe, B. (2010). Improving PSF modelling for weak gravitational lensing using new methods in model selection. *Monthly Notices of the Royal Astronomical Society*, *404*, 350–366. https://doi.org/10.1111/j.1365-2966.2010.16277.x
ADS Bibcode: 2010MNRAS.404..350R.

Rowe, B., Hirata, C., & Rhodes, J. (2011). Optimal Linear Image Combination. *The Astrophysical Journal*, *741*, 46. https://doi.org/10.1088/0004-637X/741/1/46
ADS Bibcode: 2011ApJ...741...46R.

Rowe, B., Jarvis, M., Mandelbaum, R., Bernstein, G. M., Bosch, J., Simet, M., Meyers, J. E., Kacprzak, T., Nakajima, R., Zuntz, J., Miyatake, H., Dietrich, J. P., Armstrong, R., Melchior, P., & Gill, M. S. S. (2015, February). GalSim: The modular galaxy image simulation toolkit. https://doi.org/10.48550/arXiv.1407.7676

Rubin, V. C., Ford, W. K., Jr., & Thonnard, N. (1980). Rotational properties of 21 SC galaxies with a large range of luminosities and radii, from NGC 4605 (R=4kpc) to UGC 2885 (R=122kpc). *The Astrophysical Journal*, *238*, 471–487. https://doi.org/10.1086/158003
ADS Bibcode: 1980ApJ...238..471R.

Salcido, J., McCarthy, I. G., Kwan, J., Upadhye, A., & Font, A. S. (2023). SP(k) – A hydrodynamical simulation-based model for the impact of baryon physics on the non-linear matter power spectrum. *Monthly Notices of the Royal Astronomical Society*, *523*(2), 2247–2262. https://doi.org/10.1093/mnras/stad1474

Samsing, J., & Kim, A. G. (2011). Dithering Strategies and Point-Source Photometry. *PASP*, *123*(902), 470. https://doi.org/10.1086/659244

Samuroff, S., Mandelbaum, R., Blazek, J., Campos, A., MacCrann, N., Zacharegkas, G., Amon, A., Prat, J., Singh, S., Elvin-Poole, J., Ross, A. J., Alarcon, A., Baxter, E., Bechtol, K., Becker, M. R., Bernstein, G. M., Rosell, A. C., Kind, M. C., Cawthon, R., . . . To, C. (2023). The Dark Energy Survey Year 3 and eBOSS: Constraining galaxy intrinsic alignments across luminosity and colour space. *Monthly Notices of the Royal Astronomical Society*, *524*(2), 2195–2223. https://doi.org/10.1093/mnras/stad2013

Sanchez, J., Mendoza, I., Kirkby, D. P., Burchat, P. R., & LSST Dark Energy Science Collaboration. (2021). Effects of overlapping sources on cosmic shear estimation: Statistical sensitivity and pixel-noise bias. *Journal of Cosmology and Astroparticle Physics*, *2021*, 043. https://doi.org/10.1088/1475-7516/2021/07/043
ADS Bibcode: 2021JCAP...07..043S.

Sánchez, C., Raveri, M., Alarcon, A., & Bernstein, G. M. (2020). Propagating sample variance uncertainties in redshift calibration: Simulations, theory, and application to the COS-MOS2015 data. *Monthly Notices of the Royal Astronomical Society*, *498*, 2984–2999. https://doi.org/10.1093/mnras/staa2542
ADS Bibcode: 2020MNRAS.498.2984S.

Scaramella, R., Amiaux, J., Mellier, Y., Burigana, C., Carvalho, C. S., Cuillandre, J.-C., Silva, A. D., Derosa, A., Dinis, J., Maiorano, E., Maris, M., Tereno, I., Laureijs, R., Boenke, T., Buenadicha, G., Dupac, X., Venancio, L. M. G., Gómez-Álvarez, P., Hoar, J., . . . Whittaker, L. (2022). Euclid preparation - I. The Euclid Wide Survey. *A&A*, *662*, A112. https://doi.org/10.1051/0004-6361/202141938

Schaye, J., Kugel, R., Schaller, M., Helly, J. C., Braspenning, J., Elbers, W., McCarthy, I. G., van Daalen, M. P., Vandenbroucke, B., Frenk, C. S., Kwan, J., Salcido, J., Bahé, Y. M., Borrow, J., Chaikin, E., Hahn, O., Huško, F., Jenkins, A., Lacey, C. G., & Nobels, F. S. J. (2023). The FLAMINGO project: Cosmological hydrodynamical simulations for large-scale structure and galaxy cluster surveys. \mnras, *526*(4), 4978–5020. https://doi.org/10.1093/mnras/stad2419

Schneider, P., Eifler, T., & Krause, E. (2010). COSEBIs: Extracting the full E-/B-mode information from cosmic shear correlation functions. *Astronomy and Astrophysics*, *520*, A116. https://doi.org/10.1051/0004-6361/201014235
ADS Bibcode: 2010A&A...520A.116S.

Schneider, P., Van Waerbeke, L., & Mellier, Y. (2002). B-modes in cosmic shear from source redshift clustering. *A&A*, *389*(3), 729–741. https://doi.org/10.1051/0004-6361:20020626

Schneider, P., van Waerbeke, L., Kilbinger, M., & Mellier, Y. (2002). Analysis of two-point statistics of cosmic shear - I. Estimators and covariances. *A&A*, *396*(1), 1–19. https://doi.org/10.1051/0004-6361:20021341

Schneider, P., & Seitz, C. (1995). Steps towards nonlinear cluster inversion through gravitational distortions. I. Basic considerations and circular clusters. *Astronomy and Astrophysics*, *294*, 411–431. https://doi.org/10.48550/arXiv.astro-ph/9407032
ADS Bibcode: 1995A&A...294..411S.

Schrabback, T., Erben, T., Simon, P., Miralles, J. .-., Schneider, P., Heymans, C., Eifler, T., Fosbury, R. A. E., Freudling, W., Hetterscheidt, M., Hildebrandt, H., & Pirzkal, N. (2007). Cosmic shear analysis of archival HST/ACS data. I. Comparison of early ACS pure parallel data to the HST/GEMS survey. *åp*, *468*(3), 823–847. https://doi.org/10.1051/0004-6361:20065898

Scodeggio, M., Guzzo, L., Garilli, B., Granett, B. R., Bolzonella, M., de la Torre, S., Abbas, U., Adami, C., Arnouts, S., Bottini, D., Cappi, A., Coupon, J., Cucciati, O., Davidzon, I., Franzetti, P., Fritz, A., Iovino, A., Krywult, J., Le Brun, V., . . . Percival, W. J. (2018). The VIMOS Public Extragalactic Redshift Survey (VIPERS). Full spectroscopic data and auxiliary information release (PDR-2). *Astronomy and Astrophysics*, *609*, A84. https://doi.org/10.1051/0004-6361/201630114
ADS Bibcode: 2018A&A...609A..84S.

Scolnic, D., Brout, D., Carr, A., Riess, A. G., Davis, T. M., Dwomoh, A., Jones, D. O., Ali, N., Charvu, P., Chen, R., Peterson, E. R., Popovic, B., Rose, B. M., Wood, C. M., Brown, P. J., Chambers, K., Coulter, D. A., Dettman, K. G., Dimitriadis, G., . . . Zheng, W. (2022). The Pantheon+ Analysis: The Full Data Set and Light-curve Release. *\apj*, *938*(2), 113. https://doi.org/10.3847/1538-4357/ac8b7a

Secco, L. F., Samuroff, S., Krause, E., Jain, B., Blazek, J., Raveri, M., Campos, A., Amon, A., Chen, A., Doux, C., Choi, A., Gruen, D., Bernstein, G. M., Chang, C., DeRose, J., Myles, J., Ferté, A., Lemos, P., Huterer, D., . . . To, C. (2022). Dark Energy Survey Year 3 Results: Cosmology from Cosmic Shear and Robustness to Modeling Uncertainty. *Phys. Rev. D*, *105*(2), 023515. https://doi.org/10.1103/PhysRevD.105.023515

Seitz, C., & Schneider, P. (1997). Steps towards nonlinear cluster inversion through gravitational distortions. III. Including a redshift distribution of the sources. *Astronomy and Astrophysics*, *318*, 687–699. https://doi.org/10.48550/arXiv.astro-ph/9601079
ADS Bibcode: 1997A&A...318..687S.

Seljak, U., & Zaldarriaga, M. (1996). A Line-of-Sight Integration Approach to Cosmic Microwave Background Anisotropies. *\apj*, *469*, 437. https://doi.org/10.1086/177793

Semboloni, E., Hoekstra, H., Schaye, J., van Daalen, M. P., & McCarthy, I. G. (2011). Quantifying the effect of baryon physics on weak lensing tomography. *Monthly Notices of the Royal Astronomical Society*, *417*, 2020–2035. https://doi.org/10.1111/j.1365-2966.2011.19385.x
ADS Bibcode: 2011MNRAS.417.2020S.

Shapiro, C., Rowe, B. T. P., Goodsall, T., Hirata, C., Fucik, J., Rhodes, J., Seshadri, S., & Smith, R. (2013). Weak Gravitational Lensing Systematics from Image Combination. *Publications*

of the Astronomical Society of the Pacific, *125*, 1496. https://doi.org/10.1086/674415
ADS Bibcode: 2013PASP..125.1496S.

Sharma, S., Bland-Hawthorn, J., Johnston, K. V., & Binney, J. (2011). Galaxia: A Code to Generate a Synthetic Survey of the Milky Way. *The Astrophysical Journal*, *730*, 3. https://doi.org/10.1088/0004-637X/730/1/3
ADS Bibcode: 2011ApJ...730....3S.

Sheldon, E. (2015). NGMIX: Gaussian mixture models for 2D images. *Astrophysics Source Code Library*, ascl:1508.008
ADS Bibcode: 2015ascl.soft08008S.

Sheldon, E. S., Becker, M. R., Jarvis, M., Armstrong, R., & Collaboration, L. D. E. S. (2023). Metadetection Weak Lensing for the Vera C. Rubin Observatory. *The Open Journal of Astrophysics*, *6*. https://doi.org/10.21105/astro.2303.03947

Sheldon, E. S., Becker, M. R., MacCrann, N., & Jarvis, M. (2020). Mitigating Shear-dependent Object Detection Biases with Metacalibration. *ApJ*, *902*(2), 138. https://doi.org/10.3847/1538-4357/abb595

Sheldon, E. S., & Huff, E. M. (2017). Practical Weak-lensing Shear Measurement with Metacalibration. *ApJ*, *841*(1), 24. https://doi.org/10.3847/1538-4357/aa704b

Shirasaki, M., Hamana, T., Takada, M., Takahashi, R., & Miyatake, H. (2019). Mock galaxy shape catalogues in the Subaru Hyper Suprime-Cam Survey. *Monthly Notices of the Royal Astronomical Society*, *486*, 52–69. https://doi.org/10.1093/mnras/stz791
ADS Bibcode: 2019MNRAS.486...52S.

Singh, S., Mandelbaum, R., & More, S. (2015). Intrinsic alignments of SDSS-III BOSS LOWZ sample galaxies. *Monthly Notices of the Royal Astronomical Society*, *450*(2), 2195–2216. https://doi.org/10.1093/mnras/stv778

Spergel, D., Gehrels, N., Baltay, C., Bennett, D., Breckinridge, J., Donahue, M., Dressler, A., Gaudi, B. S., Greene, T., Guyon, O., Hirata, C., Kalirai, J., Kasdin, N. J., Macintosh, B., Moos, W., Perlmutter, S., Postman, M., Rauscher, B., Rhodes, J., . . . Zhao, F. (2015). Wide-Field InfrarRed Survey Telescope-Astrophysics Focused Telescope Assets WFIRST-AFTA 2015 Report. *arXiv e-prints*, arXiv:1503.03757. https://doi.org/10.48550/arXiv.1503.03757

Spergel, D. N., Verde, L., Peiris, H. V., Komatsu, E., Nolta, M. R., Bennett, C. L., Halpern, M., Hinshaw, G., Jarosik, N., Kogut, A., Limon, M., Meyer, S. S., Page, L., Tucker, G. S., Weiland, J. L., Wollack, E., & Wright, E. L. (2003). First-Year Wilkinson Microwave Anisotropy Probe (WMAP) Observations: Determination of Cosmological Parameters. *apjs*, *148*(1), 175–194. https://doi.org/10.1086/377226

Springel, V., White, S. D. M., Jenkins, A., Frenk, C. S., Yoshida, N., Gao, L., Navarro, J., Thacker, R., Croton, D., Helly, J., Peacock, J. A., Cole, S., Thomas, P., Couchman, H., Evrard, A., Colberg, J., & Pearce, F. (2005). Simulations of the formation, evolution and clustering of galaxies and quasars. \nat, *435*(7042), 629–636. https://doi.org/10.1038/nature03597

Suchyta, E., Huff, E. M., Aleksić, J., Melchior, P., Jouvel, S., MacCrann, N., Ross, A. J., Crocce, M., Gaztanaga, E., Honscheid, K., Leistedt, B., Peiris, H., Rykoff, E. S., Sheldon, E., Abbott, T., Abdalla, F. B., Allam, S., Banerji, M., Benoit-Lévy, A., . . . Zhang, Y. (2016). No galaxy left behind: Accurate measurements with the faintest objects in the Dark Energy Survey. *Monthly Notices of the Royal Astronomical Society*, *457*(1), 786–808. https://doi.org/10.1093/mnras/stv2953

Sunyaev, R. A., & Zeldovich, Y. B. (1970). Small-Scale Fluctuations of Relic Radiation. \apss, *7*(1), 3–19. https://doi.org/10.1007/BF00653471

Tenneti, A., Singh, S., Mandelbaum, R., Di Matteo, T., Feng, Y., & Khandai, N. (2015). Intrinsic alignments of galaxies in the MassiveBlack-II simulation: Analysis of two-point statistics. *Monthly Notices of the Royal Astronomical Society*, *448*(4), 3522–3544. https://doi.org/10.1093/mnras/stv272

The LSST Dark Energy Science Collaboration, Mandelbaum, R., Eifler, T., Hložek, R., Collett, T., Gawiser, E., Scolnic, D., Alonso, D., Awan, H., Biswas, R., Blazek, J., Burchat, P., Chisari, N. E., Dell'Antonio, I., Digel, S., Frieman, J., Goldstein, D. A., Hook, I., Ivezić, Ž., . . . Troxel, M. A. (2021, September). The LSST Dark Energy Science Collaboration (DESC) Science Requirements Document.

Trotta, R. (2017, January). Bayesian Methods in Cosmology. https://doi.org/10.48550/arXiv.1701.01467

Troxel, M. A., & Ishak, M. (2015). The Intrinsic Alignment of Galaxies and its Impact on Weak Gravitational Lensing in an Era of Precision Cosmology. *Physics Reports*, *558*, 1–59. https://doi.org/10.1016/j.physrep.2014.11.001

Troxel, M. A., Lin, C., Park, A., Hirata, C., Mandelbaum, R., Jarvis, M., Choi, A., Givans, J., Higgins, M., & Sanchez, B. (2023). A joint Roman Space Telescope and Rubin Observatory synthetic wide-field imaging survey. *Monthly Notices of the Royal Astronomical Society*, *522*(2), 2801–2820.

Troxel, M. A., Long, H., Hirata, C. M., Choi, A., Jarvis, M., Mandelbaum, R., Wang, K., Yamamoto, M., Hemmati, S., & Capak, P. (2021). A synthetic Roman Space Telescope High-Latitude Imaging Survey: Simulation suite and the impact of wavefront errors on weak gravitational lensing. *Monthly Notices of the Royal Astronomical Society*, *501*(2), 2044–2070. https://doi.org/10.1093/mnras/staa3658

Troxel, M. A., MacCrann, N., Zuntz, J., Eifler, T. F., Krause, E., Dodelson, S., Gruen, D., Blazek, J., Friedrich, O., Samuroff, S., Prat, J., Secco, L. F., Davis, C., Ferté, A., DeRose, J., Alarcon, A., Amara, A., Baxter, E., Becker, M. R., . . . DES Collaboration. (2018). Dark Energy Survey Year 1 results: Cosmological constraints from cosmic shear. *Physical Review D*, *98*, 043528. https://doi.org/10.1103/PhysRevD.98.043528
ADS Bibcode: 2018PhRvD..98d3528T.

Van Alfen, N., Campbell, D., Blazek, J., Leonard, C. D., Lanusse, F., Hearin, A., Mandelbaum, R., & Collaboration, T. L. D. E. S. (2023, November). An Empirical Model For Intrinsic Alignments: Insights From Cosmological Simulations.

Van Waerbeke, L., Mellier, Y., & Hoekstra, H. (2005). Dealing with systematics in cosmic shear studies: New results from the VIRMOS-Descart survey. *åp*, *429*, 75–84. https://doi.org/10.1051/0004-6361:20041513

Van Waerbeke, L., Mellier, Y., Radovich, M., Bertin, E., Dantel-Fort, M., McCracken, H. J., Le Fèvre, O., Foucaud, S., Cuillandre, J. .-., Erben, T., Jain, B., Schneider, P., Bernardeau, F., & Fort, B. (2001). Cosmic shear statistics and cosmology. *åp*, *374*, 757–769. https://doi.org/10.1051/0004-6361:20010766

Vincenzi, M., Brout, D., Armstrong, P., Popovic, B., Taylor, G., Acevedo, M., Camilleri, R., Chen, R., Davis, T. M., Hinton, S. R., Kelsey, L., Kessler, R., Lee, J., Lidman, C., Möller, A., Qu, H., Sako, M., Sanchez, B., Scolnic, D., . . . Weaverdyck, N. (2024). The Dark Energy Survey Supernova Program: Cosmological Analysis and Systematic Uncertainties. *arXiv e-prints*, arXiv:2401.02945. https://doi.org/10.48550/arXiv.2401.02945

Vogelsberger, M., Genel, S., Springel, V., Torrey, P., Sijacki, D., Xu, D., Snyder, G. F., Nelson, D., & Hernquist, L. (2014). Introducing the Illustris Project: Simulating the coevolution of dark and visible matter in the Universe. *Monthly Notices of the Royal Astronomical Society*, *444*(2), 1518–1547. https://doi.org/10.1093/mnras/stu1536

Voigt, L. M., & Bridle, S. L. (2010). Limitations of model-fitting methods for lensing shear estimation. *Monthly Notices of the Royal Astronomical Society*, *404*(1), 458–467. https://doi.org/10.1111/j.1365-2966.2010.16300.x

Walter, C. W. (2015). The Brighter-Fatter and other Sensor Effects in CCD Simulations for Precision Astronomy. *J. Inst.*, *10*(05), C05015–C05015. https://doi.org/10.1088/1748-0221/10/05/C05015

Weaver, J. R., Kauffmann, O. B., Ilbert, O., McCracken, H. J., Moneti, A., Toft, S., Brammer, G., Shuntov, M., Davidzon, I., Hsieh, B. C., Laigle, C., Anastasiou, A., Jespersen, C. K., Vinther, J., Capak, P., Casey, C. M., McPartland, C. J. R., Milvang-Jensen, B., Mobasher, B., . . . Zamorani, G. (2022). COSMOS2020: A Panchromatic View of the Universe to z~10 from Two Complementary Catalogs. *The Astrophysical Journal Supplement Series*,

258, 11. https://doi.org/10.3847/1538-4365/ac3078
ADS Bibcode: 2022ApJS..258...11W.

Wechsler, R. H., & Tinker, J. L. (2018). The Connection between Galaxies and their Dark Matter Halos. *Annu. Rev. Astron. Astrophys.*, *56*(1), 435–487. https://doi.org/10.1146/annurev-astro-081817-051756

Weinberg, D. H., Mortonson, M. J., Eisenstein, D. J., Hirata, C., Riess, A. G., & Rozo, E. (2013). Observational probes of cosmic acceleration. \physrep, *530*(2), 87–255. https://doi.org/10.1016/j.physrep.2013.05.001

Wittman, D. M., Tyson, J. A., Kirkman, D., Dell'Antonio, I., & Bernstein, G. (2000). Detection of weak gravitational lensing distortions of distant galaxies by cosmic dark matter at large scales. \nat, *405*(6783), 143–148. https://doi.org/10.1038/35012001

Yamamoto, M., Laliotis, K., Macbeth, E., Zhang, T., Hirata, C. M., Troxel, M. A., Cao, K., Choi, A., Givans, J., Heitmann, K., Ishak, M., Jarvis, M., Kovacs, E., Long, H., Mandelbaum, R., Park, A., Porredon, A., Walter, C. W., & Wood-Vasey, W. M. (2024, January). Simulating image coaddition with the Nancy Grace Roman Space Telescope: II. Analysis of the simulated images and implications for weak lensing.

Yamamoto, M., Troxel, M. A., Jarvis, M., Mandelbaum, R., Hirata, C., Long, H., Choi, A., & Zhang, T. (2023). Weak Gravitational Lensing Shear Estimation with Metacalibration for the Roman High-Latitude Imaging Survey. *Monthly Notices of the Royal Astronomical Society*, *519*(3), 4241–4252. https://doi.org/10.1093/mnras/stac2644

York, D. G., Adelman, J., Anderson, J., John E., Anderson, S. F., Annis, J., Bahcall, N. A., Bakken, J. A., Barkhouser, R., Bastian, S., Berman, E., Boroski, W. N., Bracker, S., Briegel, C., Briggs, J. W., Brinkmann, J., Brunner, R., Burles, S., Carey, L., Carr, M. A., . . . SDSS Collaboration. (2000). The Sloan Digital Sky Survey: Technical Summary. \aj, *120*(3), 1579–1587. https://doi.org/10.1086/301513

Zhang, J., & Komatsu, E. (2011). Cosmic shears should not be measured in conventional ways. *Monthly Notices of the Royal Astronomical Society*, *414*(2), 1047–1058. https://doi.org/10.1111/j.1365-2966.2011.18436.x

Zhang, T., Almoubayyed, H., Mandelbaum, R., Meyers, J. E., Jarvis, M., Kannawadi, A., Schmitz, M. A., Guinot, A., & LSST Dark Energy Science Collaboration. (2023). Impact of point spread function higher moments error on weak gravitational lensing - II. A comprehensive study. *Monthly Notices of the Royal Astronomical Society*, *520*, 2328–2350. https://doi.org/10.1093/mnras/stac3350
ADS Bibcode: 2023MNRAS.520.2328Z.

Zhang, T., Li, X., Dalal, R., Mandelbaum, R., Strauss, M. A., Kannawadi, A., Miyatake, H., Nicola, A., Malagón, A. A. P., Shirasaki, M., Sugiyama, S., Takada, M., & More, S.

(2023). A general framework for removing point-spread function additive systematics in cosmological weak lensing analysis. *Monthly Notices of the Royal Astronomical Society*, *525*(2), 2441–2471. https://doi.org/10.1093/mnras/stad1801

Zhang, Z., Sheldon, E. S., & Becker, M. R. (2023). Deep-field Metacalibration. *The Open Journal of Astrophysics*, *6*. https://doi.org/10.21105/astro.2206.07683

Zonca, A., Singer, L., Lenz, D., Reinecke, M., Rosset, C., Hivon, E., & Gorski, K. (2019). Healpy: Equal area pixelization and spherical harmonics transforms for data on the sphere in Python. *The Journal of Open Source Software*, *4*, 1298. https://doi.org/10.21105/joss.01298 ADS Bibcode: 2019JOSS....4.1298Z.

Zuntz, J., Sheldon, E., Samuroff, S., Troxel, M. A., Jarvis, M., MacCrann, N., Gruen, D., Prat, J., Sánchez, C., Choi, A., Bridle, S. L., Bernstein, G. M., Dodelson, S., Drlica-Wagner, A., Fang, Y., Gruendl, R. A., Hoyle, B., Huff, E. M., Jain, B., . . . Zhang, Y. (2018). Dark Energy Survey Year 1 Results: Weak Lensing Shape Catalogues. *Monthly Notices of the Royal Astronomical Society*, *481*(1), 1149–1182. https://doi.org/10.1093/mnras/sty2219

Zuntz, J., Kacprzak, T., Voigt, L., Hirsch, M., Rowe, B., & Bridle, S. (2013). IM3SHAPE: A maximum-likelihood galaxy shear measurement code for cosmic gravitational lensing. *Monthly Notices of the Royal Astronomical Society*, *434*(2), 1604–1618. https://doi.org/10.1093/mnras/stt1125

Zuntz, J., Paterno, M., Jennings, E., Rudd, D., Manzotti, A., Dodelson, S., Bridle, S., Sehrish, S., & Kowalkowski, J. (2015). CosmoSIS: Modular cosmological parameter estimation. *Astronomy and Computing*, *12*, 45–59. https://doi.org/10.1016/j.ascom.2015.05.005